UNIVERSIDAD COMPLUTENSE DE MADRID

FACULTAD DE CIENCIAS FÍSICAS

TESIS DOCTORAL

Dynamic and topological properties of perdiocally driven nanostructures
Propiedades dinámicas y topológicas de nanoestructuras con campos AC

MEMORIA PARA OPTAR AL GRADO DE DOCTOR

PRESENTADA POR

Álvaro Gómez León

Directora

Gloria Platero

Madrid, 2014

Dynamical and topological properties of periodically driven nanostructures

Tesis doctoral presentada por:

Álvaro Gómez León

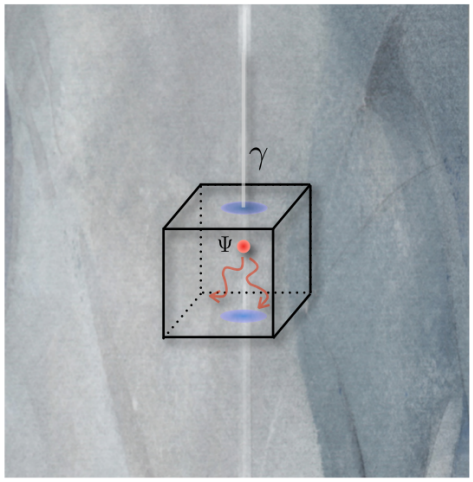

Madrid, Diciembre de 2013.

Universidad Complutense de Madrid

Facultad de C.C. Físicas
Instituto de Ciencia de Materiales de Madrid (CSIC)

Directora: **Gloria Platero**

Propiedades dinámicas y topológicas de nano-estructuras con campos AC

Tesis doctoral presentada por:

Álvaro Gómez León

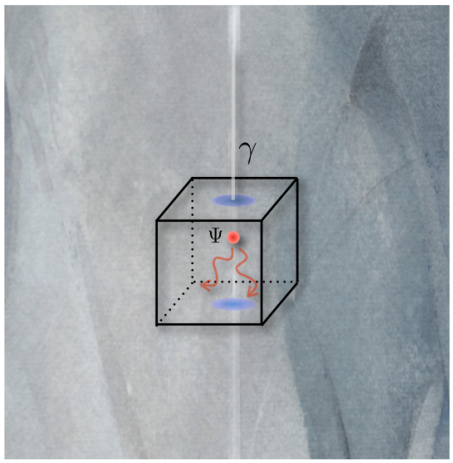

Madrid, Diciembre de 2013.

Universidad Complutense de Madrid

Facultad de C.C. Físicas
Instituto de Ciencia de Materiales de Madrid (CSIC)

Directora: **Gloria Platero**

To my parents, for their constant support and for encouraging me to always find answers.

Everything is vague to a degree you do not realize till you have tried to make it precise.

(Bertrand Russell)

Contents

Resumen

En esta tesis estudiamos sistemas cuánticos llevados fuera del equilibrio a través de campos externos periódicos en el tiempo.

Durante los últimos cuatro años, en los cuales se ha realizado esta tesis, hemos trabajado con sistemas muy diferentes, como por ejemplo: puntos cuánticos, grafeno, superconductores topológicos y cadenas de Ising. A pesar de esto, siempre hemos mantenido un objetivo común: entender como se ven afectadas sus diferentes propiedades físicas cuando son llevados fuera del equilibrio a través de una interacción con campos externos (periódicos en el tiempo). En concreto, en esta tesis se presentan los resultados correspondientes a puntos cuánticos fuera del equilibrio acoplados campos magnéticos AC y de grafeno acoplado a campos eléctricos AC. Creemos que la profunda descripción de estos dos sistemas, presentada en este trabajo, permite entender fácilmente la mayoría de trabajos en este campo y da una perspectiva general de como realizar el estudio de este tipo de sistemas.

Cuando comenzamos esta tesis, no había actividad en el campo de fases topológicas y campos AC. Básicamente la teoría de Floquet era utilizada en trabajos relacionados con dinámica de electrones en pozos cuánticos[1, 2], puntos cuánticos[3, 4, 5, 6, 7] and super-redes[8]. Por otro lado, debido a la gran complejidad de estos sistemas fuera de equilibrio, la utilización de métodos numéricos era la principal fuente de análisis. Esto permitió que profundizásemos en la teoría de Floquet y en las técnicas utilizadas para el análisis numérico. Simultáneamente, durante los últimos años ha ocurrido una ligera revolución en la física de estado sólido, primero con el descubrimiento de los aislantes topológicos[9], y unos años depués, con varias propuestas para manipular e inducir estos nuevos estados de la materia a través de campos externos[10, 11]. Cuando comencé a leer esos trabajos me interesé profundamente por la frontera entre fases topológicas y sistemas fuera del equilibrio, y es cuando además, comenzamos a colaborar con numerosos grupos, que son los que me han ayudado a introducirme en los diferentes campos descritos en esta tesis. Para la escritura de esta tesis he seguido un orden cronológico de mis trabajos, ya que creo que así es más sencillo entender los problemas y soluciones que se han planteado a lo largo de el desarrollo de este campo.

En nuestros primeros trabajos, comenzamos por estudiar sistemas sencillos: puntos cuánticos simples y dobles, con pocos niveles participando en la dinámica y en la descripción de partícula libre. Estos puntos cuánticos estaban acoplados a ciertos campos externos magnéticos que variaban de manera periódica con el tiempo, de manera que estudiamos la dinámica de espín. En este momento es cuando uno

puede darse cuenta de lo complicado que puede llegar a ser un sistema, inicialmente sencillo, una vez que pasa a estar fuera de equilibrio. El problema principal es, que para ciertas configuraciones de campos, una solución analítica es imposible. Un ejemplo clásico es el sistema de dos niveles estudiado por Bloch y Rabi[12], que no puede ser resuelto para polarización lineal, y requiere del uso de ciertas aproximaciones, como por ejemplo la de onda rotante (RWA).

Durante el estudio de este tipo de sistemas, nos centramos en algunos efectos particulares que aparecen en sistemas con campos AC, como por ejemplo la destrucción coherente de túnel (CDT). Esto nos permitió demostrar que el uso de campos AC magnéticos, en vez de eléctricos, permite controlar simultáneamente el grado de libertad espacial (permitiendo a la carga moverse o no), y el grado de libertad de espín del electrón[13]. Este resultados nos llevo a intentar entender como podría medirse experimentalmente este tipo de efectos, y si estos se verían afectados por ciertos tipos de decoherencia. Para ello, desarrollamos una ecuación maestra en base de Floquet, que permitía obtener una medida del transporte de carga a través del sistema, cuando este se acopla a contactos metálicos[14].

A la vez que estudiábamos la dinámica electrónica en puntos cuánticos fuera de equilibrio, comenzamos a trabajar en los aspectos topológicos de diversos sistemas físicos. Para comenzar, aplicamos estos conceptos a los puntos cuánticos que estábamos estudiando, centrándonos en efectos no adiabáticos. Esto nos permitió demostrar que las correlaciones entre el espín y la posición de la carga electrónica afectaban en gran medida a la topología de las fases presentes en el sistema[15].

A partir de este punto decidimos profundizar en mayor medida en el estudio de fases topológicas, y en los posibles sistemas que podrían presentar mayor riqueza en cuanto a estas. Uno de nuestros primeros objetivos fue intentar clasificar todas las posibles fases existentes en sistemas acoplados a campos AC (sin interacciones), ya que la clasificación de sistemas en equilibrio había sido completada y había cierto debate a como aplicar estos conceptos a sistemas fuera del equilibrio. En la ref.[16] propusimos como clasificar las diferentes fases utilizando técnicas similares a las de sistemas en equilibrio, demostrando que la utilización de campos dependientes del tiempo permitía incrementar el número de fases accesibles a sistemas en equilibrio, e inclusive simular algunos aspectos de sistemas en dimensiones superiores. Cabe destacar que uno de los aspectos más importantes de nuestro método, es que permite entender en términos de truncado de dimensiones la transición de un sistema evolucionado adiabáticamente a uno que lo hace no adiabáticamente. En trabajos posteriores nos hemos dedicado principalmente a estudiar estas propiedades en sistemas realistas, como por ejempo grafeno, para el cual hemos descrito en términos generales las posibles fases topológicas que pueden ser inducidas con los campos externos[17]. En este último trabajo también incluimos una descripción de como sería posible aniquilar puntos de Dirac mediante variaciones en el campo externo aplicado, o como incrementar el número de conos de Dirac en el sistema fuera de equilibrio. Finalmente, en ref.[18], estudiamos una fase caracterizada por un invariante Chern que puede ser inducida en grafeno, la cual permite simular el modelo de

Haldane con némeros Chern mayores que la unidad.

En nuestros últimos trabajos, hemos estudiado el efecto de los campos AC en sistemas con interacciones. Esto incluye cadenas de Ising (las cuales están íntimamente relacionadas con superconductores de tipo p)[19] y fases con excitaciones fraccionadas, como la fase obtenida en la ref.[20], para la cual obtenemos un efecto Hall cuántico fraccionado en la red hexagonal cuando el sistema está en presencia de un campo externo AC. Estos últimos trabajos no están incluidos en esta tesis debido a su reciente finalización. De todos modos, creemos que los resultados y técnicas aquí presentadas, permitan que los lectores sean capaces de entenderlos fácilmente.

Abstract

In this thesis we present a study of quantum systems which are periodically driven out of equilibrium. Although during this four years period we have studied several physical systems such as quantum dots, graphene, topological superconductors and Ising chains, a main idea has been always behind: To understand the physics of quantum systems periodically driven out of equilibrium by external fields. Here we review some of the results for quantum dots and graphene, and try to give a general perspective for the treatment of these systems.

When we started this thesis, there was not activity in the field of periodically driven systems and topological phases. Mainly, works in electron dynamics in quantum wells[1, 2], quantum dots[3, 4, 5, 6, 7] and super-lattices[8], all driven by AC electric fields, considered the use of Floquet theory. In addition, due to the great complexity of systems out of equilibrium, mainly numerical approaches were considered. The calmed scenario at that time, allowed me to deeply study the Floquet formalism and the ideas governing periodically driven systems. Fortunately, a couple of years later a boom happened in the field, first in condensed matter physics with the discovery of topological insulators, and a few years later with some proposals to manipulate the topological states of matter by external means. At that point I became really interested on the boundary between topology and AC driven systems, and we started to collaborate with several groups with whom I have learned many things, that allowed me to address all the different topics presented here. The thesis will follow the chronological order of my works, because I think it will allow to address all topics in a self-sustained and comprehensive way.

When we started our work, we considered simple systems as starting point: Single and double quantum dots, each with a few energy levels involved, and in its most simple form, as non interacting qubits. The quantum dots were coupled to a set of external time-dependent magnetic fields, and we studied the spin dynamics of the electrons. It turned out that although the systems were quite simple, they could not been exactly solved for general fields configurations. The most classical example was studied by Rabi and Bloch[12], in which a periodically driven two level system is considered that can be exactly solved for circular polarization of the field, but not for linear one. It requires the use of some approximations, as e.g., the so called rotating wave approximation (RWA). Nevertheless, dealing with this system I learned some interesting dynamical effects, such as the coherent destruction of tunneling (CDT), which allowed us to demonstrate that the use of AC magnetic, instead of AC electric fields, provided a way to control the electron charge and spin

dynamics simultaneously[13].

The latter results increased my interest in the understanding of the electron dynamics, and its relation with observables. Thus, we considered to address this problem using a master equation approach to measure the current through the system[14]. A few works were made in the field of periodically driven open systems, so using them as a guideline[21, 22], we developed a full master equation in Floquet formalism. It allowed us to prove the relation between current and electron dynamics controlled by the external field.

Simultaneously to the development of the master equation for the quantum dots I started my learning of topology in physics. I tried to apply these concepts to our current setups under study, the quantum dots, finding that it was not trivial at all. Although the single quantum dot in the RWA approximation resembled the famous result of Berry[23], the double quantum dot was not that simple. The analysis of the topological features resulted in a complex interplay between the spin and the spatial dynamics, with rich topological phase diagrams[15].

At this point we became more interested in the field of topology, and decided to change the systems under study to those in which the topological properties could be more involved such as in D-dimensional lattices. Our first problem under consideration was the topological classification of periodically driven systems[16], which was under current debate. We followed a classification scheme analogous to the one of time independent systems i.e., in terms of the presence of certain anti-unitary symmetries, but combined with Floquet formalism. Finally, we applied our theoretical results to different setups such as graphene and Ising chains. For the case of graphene we fully analyzed all possible topological properties, providing a complete description of the different phases which can be obtained due to the driving field. We also proposed an alternative way to merge Dirac points using external electric fields[17], as well as a way to obtain a plateau structure for Chern insulators equivalent to the one of the quantum Hall effect, but in the absence of magnetic fields[18].

In our latest works we have studied the effect of interactions in systems out of equilibrium. This includes a 1D Ising chain periodically driven by magnetic fields, which importantly, can be mapped to a p-wave superconductor[19], and the case of doped graphene, which has been proposed as the first experimental setup in which a fractional Chern insulator could be observed[20]. These last topics are not included in this thesis because they have been recently finished. However, we expect that the techniques and results presented here will help the reader to easily understand these last works.

Acknowledgments

Durante la realización de esta tesis de doctorado, en la cual he pasado cuatro años en el Instituto de Ciencia de Materiales de Madrid (ICMM), he compartido muchísimas experiencias con gran cantidad de gente. Por eso me gustaría dedicar unas pocas lineas a agradecer a todos y cada uno de ellos esos momentos de diversión, de risas y de discusiones que me han aportado momentos tan valiosos.

Primero, quisiera agradecer a mi directora de tesis Gloria todo ese cariño que siempre me ha tenido, su continuada ayuda durante la elaboración de todos nuestros trabajos, y sobre todo, la plena confianza en mi trabajo, que creo que ha ayudado en gran medida a que me convierta en el científico que he llegado a ser.

I also would like to thank: To Professor Philip Stamp, for inviting my to the University of British Columbia in several ocassions, for teaching me about decoherence, and for his friendship and hospitality when I was in Vancouver. I also acknowledge to Professor Tobias Brandes, for his invitation to give a talk at the Technische Universität of Berlin, all his comments about my work and his sympathy, to Professor Markus Büttiker for his interest in my work, his invitation to the University of Geneva and for his hospitality, to Professor Diego Frustaglia for his introduction to spin-orbit rings, to Dr. Pierre Deplace for introducing me to graphene and the funny nights playing jazz and doing physics at my home, and to Dr. Victor Bastidas for his help when I was in Berlin and the discussions on spin systems out of equilibrium.

También quiero agradecer compañeros de trabajo: A Sigmund por iniciarme en la teoría de sistemas fuera del equilibrio y por echarme una mano siempre que lo he necesitado. A Rafa por haber ser el posdoc con el que siempre te puedes echar unas risas, su ayuda con los puntos cuánticos y por el cachondeo en el viaje a Corcega. A Mathias, por poner siempre ese punto divertido a las situaciones y haberme ayudado en todo desde que empecé. A Mónica, por preguntar siempre tantas cosas haciendo ver todo mucho más interesante. A Fernando, Ángel y Robert por esas risas en el despacho y por las discusiones de física tan interesantes que me han planteado. A Fernando "junior" por soportar que siempre le robase el ordenador y por acogerme en su casa de Berlín. A María por hacer tan divertido ese congreso en Oporto y su alegría continuada. A Hector por echarme una mano con el grafeno cuando lo he necesitado. A Laura, por hacer que me esforzase en explicar correctamente los aislantes topológicos y su buen rollo. A Kike, por esas risas que nos hemos echado con él en las comidas. A Fito, por poner siempre tanta pasión a la física, introducirme en el efecto Hall cuántico fraccionado y por esas *jam sessions* de guitarra que nos hemos echado. A los miembros del grupo de música del instituto con los que he

pasado tantos ensayos y días especiales: Miguel, Luis, Álvaro, Alex, Pep, Ainhoa, Gladys y Arturo. A Felix Santos, por enseñarme a comprender la música con la misma claridad que la física. A Blas y Noel por esas noches músicales tan divertidas que no olvido. A todos los compañeros del *basket* de los jueves: Julián, Covadonga, Oscar, Yurena, Elena...

Como no, también tengo que agradecer a los amigos con los que llevo tanto tiempo compartiendo cosas: A Jorge y Jose por haber pasado tantos años juntos siendo tan amigos y compartiendo tantas aficiones y momentos. A Bea por todo su cariño y apoyo, y por ayudarme a desconectar del trabajo cuando lo he necesitado. A David, Yizeh, Juan, Nacho y Juanmi por todas esas noches de farra que hemos tenido desde primero de carrera. A Raúl y Antonio por haber sido los Séneca mas cachondos que me he encontrado en toda la carrera. A Jeong Sook por haber sido tan buena compañera de piso y amiga. A Maiko por el cariño que siempre me ha tenido y por lo divertida que es con beber una sola cerveza.

Por último, me gustaría agradecer a toda mi familia, principalmente a mis padres Armando y Esperanza, por todo ese cariño y esa ayuda que siempre me han proporcionado cuando la he necesitado, y por interesarse siempre por el trabajo que estaba realizando, aunque yo no supiese transmitírselo tan bien como me gustaría. También agradezco a mis tíos Ignacio y Elena por ese cariño que siempre me han demostrado y esas maravillosas vacaciones que cada año me han permitido pasar en su "balneario" y navegando en el barco. También a mis tíos Fred y Celia, porque aunque siempre hemos vivido tan separados, cada vez que hemos tenido la oportunidad de vernos ha sido como si fuésemos una familia que se ve a diario. Por último, a mis tíos Jose Antonio y Margarita, ya que han sido los artífices de esas divertidas Nocheviejas que hemos tenido en Galicia.

Finalmente, agradezco a mis primos todo ese cariño que siempre me han dado: A Carmen por ser siempre tan divertida e ingeniosa, consiguiendo que me sorprenda cada vez que la veo. A Antonio por esas conversaciones tan profundas que siempre hemos tenido, y porque no, ¡por tocar la batería conmigo siempre que hay ocasión!. A Carolina por haberme llevado por toda Venezuela cada vez que he ido a visitarla. Por último, a Natalia, Ricardo y Carlos por esas reuniones de primos tan divertidas que hemos tenido.

List of Publications

Part of the work presented in this thesis has given rise to the following publications and preprints:

1. *"Charge localization and dynamical spin locking in double quantum dots driven by ac magnetic fields"*, **Á. Gómez-León**, G. Platero, Physical Review B (Rapid Communications) **84**, 121310 (2011).
2. "*Transport blocking and topological phases using ac magnetic fields*", **Á. Gómez-León** and G. Platero, Physical Review B **85** (24), 245319 (2012).
3. "*Topological phases in adiabatic and nonadiabatic driven systems*", **Á. Gómez-León** and G. Platero, Physical Review B **86** (11), 115318 (2012).
4. "*Floquet topological quantum phase transitions in the transverse Wen-plaquette model*" , V. M. Bastidas, C. Emary, G. Schaller, **Á. Gómez-León**, G. Platero and T. Brandes, arXiv preprint: 1302.0781 (2013).
5. "*Floquet-Bloch theory and topology in periodically driven lattices*", **Á. Gómez-León** and G Platero, Physical Review Letters **110**, 200403 (2013).
6. "*Merging of Dirac points and Floquet topological transitions in AC driven graphene*" P. Delplace, **Á. Gómez-León** and G. Platero, arXiv preprint:1304.6272 (2013).
7. "*Engineering the Anomalous quantum Hall effect with electric fields*" **Á. Gómez-León**, P. Delplace and G Platero, arXiv preprint: 1309.5402 (2013).
8. "*Floquet Fractional Chern Insulator in Doped Graphene*" A. G. Grushin**, Á. Gómez-León** and T. Neupert, arXiv preprint: 1309.3571 (2013).

1 Introduction

1.1 Time evolution: Geometry and Topology in Quantum Systems

As an introduction to some of the topics treated in this thesis, in this chapter we briefly explain some of the fundamental concepts in differential geometry used in this thesis, from a perspective of quantum mechanics and condensed matter physics. We shall discuss the mathematical structure and symmetries of the Schrödinger equation, the concept of parallel transportation and its natural appearance in quantum mechanics[24].

1.1.1 Mathematical description of quantum mechanics and the kinematic symmetry

Quantum physics concerns the study of small scale systems, where the physics laws governing the world are those of quantum mechanics. In its simple form, we could say that in quantum mechanics everything is described in terms wave functions/fields. The general equations describing the evolution of fields are the Klein-Gordon equation (for bosons) and the Dirac equation (for fermions), although in order to describe the physics of condensed matter systems it is commonly used its low energy limit, known as the Schrödinger equation. The reason for the use of the low energy limit is that the energy scales considered in the laboratories are of the order of electron volts, which are very small compared with the term mc^2[1].

In order to introduce a basic framework for the description of the geometrical and topological properties, we now briefly comment the mathematical structure of quantum mechanics: In quantum mechanics *pure physical states* are represented by non zero elements of a Hilbert space $\mathbb{H}$, called *state vectors*. Each vector $|\psi\rangle \in \mathbb{H} - \{0\}$ defines a one dimensional vector subspace of $\mathbb{H}$, which is called a *ray*:

$$\lambda_\psi := \{|\phi\rangle \in \mathbb{H} \ : \ |\phi\rangle = c|\psi\rangle, \ c \in \mathbb{C}\}\,. \tag{1.1.1}$$

All the states associated to a ray (i.e., the set of all states connected through the equivalence relation $|\psi\rangle \sim c|\psi\rangle$, where $c \in \mathbb{C}$), represent the same physical state,

[1] Nevertheless, we shall see in the last sections of this thesis how also condensed matter systems can be also described by emergent Dirac equations.

because the measurement of an observable $\langle\psi|\hat{O}|\psi\rangle/\langle\psi|\psi\rangle$ remains invariant. Thus, the collection of all pure states can be identified with the set of all rays in $\mathbb{H}$, and this is called the *projective Hilbert space* $\mathcal{P}(\mathbb{H})$.

Alternatively, one can characterize the pure states in terms of unit rays. They consist on normalized state vectors, or equivalently, in the intersection of the rays with a unit radius N-dimensional sphere:

$$S(\mathbb{H}) := \{|\psi\rangle \in \mathbb{H} \ : \ \langle\psi|\psi\rangle = 1\}, \tag{1.1.2}$$

$$\hat{\lambda}_\psi := \left\{|\phi\rangle \in \mathbb{H} \ : \ |\phi\rangle = e^{i\chi}|\psi\rangle, \ \chi \in \mathbb{R}\right\}, \tag{1.1.3}$$

Importantly, this picture provides a clearer view of the $U(1)$ symmetry of quantum mechanics, since they are all connected through phase transformations $e^{i\chi}$. Then, a ray represents the set of all possible phase transformations for a state vector $|\psi\rangle$. This last picture is specially useful due to its direct connection with a *fiber bundle* structure, in which the $U(1)$ invariance represents the *fibers* of a base manifold given by the projective Hilbert space $\mathcal{P}(\mathbb{H})$.

From the previous arguments, we could say that phase factors and rays are two different aspects of state vectors, and this separation comes from the implicit $U(1)$ symmetry of the Schrödinger equation[2]. Even further, it seems that the phases $e^{i\chi}$ are unimportant, however, we will see that they play an important role when different states interfere.

Importantly, this separation between rays and $U(1)$ transformations has lead to a very natural description of quantum mechanics in terms of *fiber bundles[25, 26, 24].* Roughly speaking, fiber bundles are useful to describe in geometrical terms the interplay between some intrinsic degrees of freedom, as for example those arising from the $U(1)$ symmetry, and the evolution of the system over a base manifold. To properly define the fiber bundle one needs a base manifold, which in our case is given by the projection operators $\Lambda_\psi := |\psi\rangle\langle\psi|$ (invariant under $U(1)$ phase transformations), and a set of fibers attached at each point of the base manifold. The base manifold coincides with the projective Hilbert space:

$$\mathcal{P}(\mathbb{H}) = \{\Lambda_\psi \ : \ |\psi\rangle \in S(\mathbb{H})\}, \tag{1.1.4}$$

and the mapping $\pi : \ |\psi\rangle \to \Lambda_\psi = |\psi\rangle\langle\psi|$ from the Hilbert space to the projective Hilbert space provides the relation between the phases and the evolution over the base manifold. Finally, the fibers representing the $U(1)$ symmetry can be geometrically described by circles S^1 at each point[3] (see Figure 1.1.1 for a schematic representation).

[2]Note that this symmetry is always present in all quantum mechanical systems.

[3]The $U(1)$ fibers represent a rotation of a unit vector over the complex plane, and that is the reason why it can be visualized as a circle. Formally speaking $U(1) \simeq \mathbb{T}$ being $\mathbb{T}$ the circle group.

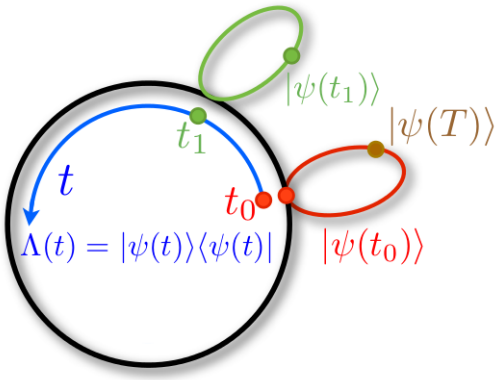

Figure 1.1.1: Time evolution for the projective $\Lambda(t)$ and the total Hilbert space. Clearly, closed curves in the projective space (black circle) does not imply to obtain the same final state vector, which can be different in a $U(1)$ phase rotation. This is represented as a different point (red and brown) over the fiber at $\Lambda(0) = \Lambda(T)$.

Now let us consider a more physical approach to the $U(1)$ symmetry. The time dependent Schrödinger equation relates the time evolution of the wave function $|\Psi(t)\rangle$ with its Hamiltonian as follows:

$$H(x,t)\,|\Psi(x,t)\rangle = i\partial_t|\Psi(x,t)\rangle. \tag{1.1.5}$$

Interestingly, Equation 1.1.5 has the so called *kinematic symmetry*, which is the invariance under time dependent phase transformations previously considered:

$$|\Psi(x,t)\rangle \to e^{i\alpha(t)}|\Psi(x,t)\rangle, \tag{1.1.6}$$

This invariance comes from the fact that observables $\mathcal{O}$ in quantum mechanics must be independent of the frame considered, i.e., $|\langle\Psi(x,t)\,|\mathcal{O}|\Psi(x,t)\rangle| = |\langle\Psi'(x,t)\,|\mathcal{O}|\Psi'(x,t)\rangle|$, leading to the equivalence relation between Hamiltonians:

$$\begin{aligned} H(x,t)\,e^{i\alpha(t)}|\Psi(x,t)\rangle &= i\partial_t\left(e^{i\alpha(t)}|\Psi(x,t)\rangle\right) \\ &= e^{i\alpha(t)}\left(-\dot{\alpha}(t)\,|\Psi(x,t)\rangle + i\partial_t|\Psi(x,t)\rangle\right) \end{aligned} \tag{1.1.7}$$

$$H(x,t) + \dot{\alpha}(t) \sim H(x,t)\,. \tag{1.1.8}$$

Thus, Hamiltonians are defined up to a shift of a time dependent function $\dot{\alpha}(t)$. The importance of this symmetry is that a physical system is not uniquely defined by a Hamiltonian, but for the equivalence class of all Hamiltonians related by the kinematic symmetry. An important physical implication is for example that absolute energies are not observables, and just energy differences can be measured in experiments. In addition, when the system evolves it will lead to the appearance of geometric phases and topological terms, which constrain the physical quantities to concrete values, as for example in the quantum Hall effect.

1.1.2 Parallel transportation and geometric phases

Let us consider a quantum mechanical system, this can be subjected to external changes, for example as consequence of a coupling with the environment or due to an external controlled tuning. In this case, the changes are described by a set of time dependent parameters $\mathbf{R}(t) = (R_1(t), R_2(t), \ldots)$ which define a smooth manifold M. Changes in the environment are then described by curves $\mathbf{C} : t \in [0, T] \to M$, and as we proof next, parallel transportation plays an important role in this context, and it is mathematically described by the concepts previously introduced.

1.1.2.1 Adiabatic approximation

Let us assume that at $t = 0$ the state is an eigenstate of the Hamiltonian $H(R(0))$ with eigenvalue $E_n(R(0))$. If the Hamiltonian commutes for all different times $[H(t), H(t')] = 0$, its time evolution is just given by :

$$\psi_n(t) = e^{-i\int_0^t E_n(R(t_1))dt_1}\psi(0). \tag{1.1.9}$$

However, this is not true in general, and the time evolution can make the system *jump* from one state to another. The adiabatic approximation lays in between both cases, i.e., it considers that the state does not jump to other energy states, but the Hamiltonian does not commute at different times. Importantly, it can be proved that the adiabatic approximation cannot be exactly fulfilled, and as we stress during this thesis, a complete study of the dynamics is important.

Let us consider an evolving state vector $\psi(t)$ in the basis of instantaneous eigenstates $\{|n; R(t)\rangle\}$:

$$\psi(t) = \sum_m c_m(t)\,|m, R(t)\rangle. \tag{1.1.10}$$

If the state adiabatically evolves, one can assume that:

$$\psi(t) \sim c_n(t)\,|n, R(t)\rangle,\ c_n(0) = 1, \tag{1.1.11}$$

meaning that the state does not jump to other energy levels, although it contains a time dependence. Inserting Equation 1.1.11 in the time dependent Schrödinger equation we arrive at:

$$\left[\frac{d}{dt}c_n(t) + iE_n(R(t))\,c_n(t)\right]|n, R(t)\rangle = -c_n(t)\,\frac{d}{dt}|n, R(t)\rangle. \tag{1.1.12}$$

Multiplying by $|m \neq n, R(t)\rangle$ on the left side we finally get:

$$\langle m, R(t)\,|\frac{d}{dt}|n, R(t)\rangle = 0, \tag{1.1.13}$$

which is the necessary and sufficient condition for the adiabatic approximation to be valid. Equation 1.1.13 represents the simplest way to understand the differences

between adiabatic a non-adiabatic evolution in terms of orthogonality between instantaneous eigenstates under small time variations. Nevertheless, in this thesis we shall consider further examples to clearly understand the meaning of adiabatic evolution, and how the system can dramatically change when adiabaticity is not fulfilled.

If we instead consider the projectors $\Lambda_\psi(t) = |\psi(t)\rangle\langle\psi(t)|$ defined above, a periodic evolution performs a closed curve in M, which makes the projectors:

$$\Lambda_\psi(0) \to \Lambda_\psi(t) \to \Lambda_\psi(T) = \Lambda_\psi(0), \tag{1.1.14}$$

to evolve in closed curves as well. Importantly, it does not mean that the states perform closed loops, since in general they fulfill:

$$\psi(T) = e^{-i\alpha_\psi}\psi(0). \tag{1.1.15}$$

For the case of time independent Hamiltonians, the phase is $\alpha_\psi = E_n T$, and it is called dynamical phase factor because it can be removed by a gauge transformation. However, we shall show that for general time dependent Hamiltonians a geometric phase factor also appears, and this cannot be removed by a gauge transformation.

If one considers Equation 1.1.11 as a solution of the time dependent Schrödinger equation, and multiplies by $|n, R(t)\rangle$ on the left:

$$\frac{d}{dt}c_n(t) + c_n(t)\langle n, R(t)|\partial_t|n, R(t)\rangle = -ic_n(t)E_n(R(t)), \tag{1.1.16}$$

the solution is given by:

$$c_n(t) = e^{-i\int_0^t E_n(t_1)dt_1}e^{i\gamma_n(t)}, \tag{1.1.17}$$

$$\gamma_n(t) \equiv \int_{R(0)}^{R(t)}\langle n, R(t_1)|d|n, R(t_1)\rangle dt_1, \tag{1.1.18}$$

where d is the exterior derivative with respect to the parameter which characterizes the adiabatic changes. Importantly $\gamma_n(t)$ does not depend on the explicit time dependence of the parameters, but just on the curve traced over the parameter space. This is a important feature, related with certain strength against small errors in experiments[27, 28, 29]. However, the independence on the explicit time evolution is a pure consequence of the adiabatic approximation, and in general, the geometric phase does depend on the explicit time dependence[30, 15]. This insensitivity to small errors when the adiabatic regime is well satisfied has lead to several proposals for its use in quantum computation[31] as a way to perform logical quantum gates. Nevertheless, it requires the use of non abelian phases, which are much more difficult to control.[4].

[4]Non abelian phases are obtained when the evolving state belongs to a degenerate subspace. This feature makes the geometric phase to be no longer phase factor, but a matrix. Thus, the inequivalent ground states and the transitions between them can be used to define qubits and logic gates respectively.

1.1.2.2 Berry connection and curvature tensor

Now, let us write Equation 1.1.18 in terms of the 1-form:

$$\gamma_n(t) \equiv \oint \hat{A}, \tag{1.1.19}$$

$$\hat{A} \equiv i\langle n, \mathbf{R}|d|n, \mathbf{R}\rangle = i\langle n, R_\mu|\frac{\partial}{\partial R_\mu}|n, R_\mu\rangle dR_\mu, \tag{1.1.20}$$

where the summation in repeated indexes is considered and d is the exterior derivative. This is the well known Berry connection, which accounts of the parallel transportation over a manifold defined by the set of parameters $M = \{R_1, R_2, \ldots\}$. The connection is usually described as a gauge field responsible of the covariance of the system at all points of the parameter space, i.e., *covariance implies the same physics, independently of the observer.* A well known example is the covariance of the electromagnetic field, whose gauge fields are the scalar and vector potential.

Geometric phases are gauge invariant[24], although the connection is not. In order to express in terms of a gauge invariant quantity the geometric phase $\gamma_n(t)$, we can define the 2-form curvature tensor, equivalent to the field tensor of electromagnetism:

$$\hat{F}^n = d\hat{A}^n = \frac{\partial A^n_\mu}{\partial R^\nu} dR^\nu \wedge dR^\mu, \tag{1.1.21}$$

such that using Stokes theorem we arrive at:

$$\gamma_n(\mathbf{C}) = \oint_{\mathbf{C}} \hat{A}^n = \int_{\mathbf{S}} d\hat{A}^n = \int_{\mathbf{S}} \hat{F}^n, \tag{1.1.22}$$

where the surface $\mathbf{S}$ is arbitrary chosen as long as it is bounded by the closed curve $\mathbf{C}$, i.e., $\partial\mathbf{S} = \mathbf{C}$.

1.1.2.3 Underlying geometric picture in parallel transportation

In order to understand the geometric content of the previously introduced quantities, we proceed to illustrate them: As we have described all along this section, the effect of time dependent external sources in the quantum system might have profound consequences. Importantly, some of its effects can be described in terms of geometrical objects, and the underlying principle is the one of parallel transportation. Parallel transportation describes how a vector frame changes its orientation when it is moved over a smooth manifold. This is shown in Figure 1.1.2, where a vector frame (green arrows) is transported over the surface of a sphere maintaining the axis parallel each small step. After a closed loop the vector frame is rotated a total angle α due to the curved surface.

If we compare Figure 1.1.2 with the mathematical structure introduced previously, the vector frame which is transported is given by the rays/vector states of the

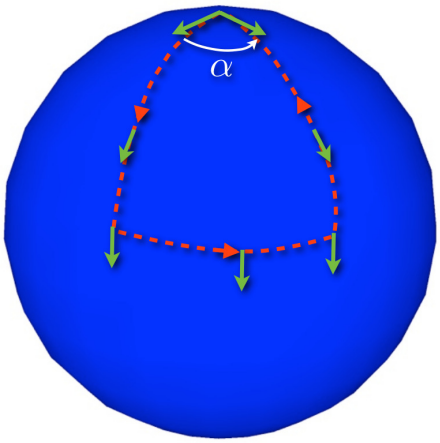

Figure 1.1.2: Parallel transportation of a vector frame over a 2-sphere. A closed loop (red dotted line) in which the observer/vector state is always pointing south through the geodesic (green arrow) leads to a final state vector rotated an angle α in comparison with the initial one. The angle of rotation only depends on the trajectory followed over the sphere.

Schrödinger equation – which are only defined at a single point on the sphere. The sphere represents some external parameters which are varied, as e.g., a magnetic field or some environmental degrees of freedom. Thus, the Berry connection tell us how to compare the different rays/states at different points, in a way that the physics laws are the same everywhere. Finally, the Berry curvature describes the local curvature felt by the vector frame at its origin. Here a beautiful analogy can be made with the *local flatness theorem* in general relativity[32], which states that every reference frame is equivalent at first order to a flat space. Then, if an observer wants to find out about the local space-time curvature, he needs to measure second derivatives of the signature, i.e., the effect of a gravitational field or accelerations. In our case, non vanishing second derivatives of the state vectors means a non local flatness. Finally, in order to connect with the topological properties – i.e., large scale distances –, the observer can *walk* over the whole manifold, and then guess the topology of the total space. This is related with the integration of the Berry curvature over the whole parameter space. This last measurement exactly is the so called first Chern number c_1.

1.2 Floquet Theory

The interest in the study of driven systems arises for one main reason: The interaction with external fields allows to externally manipulate the properties of the system in a controllable way. On the other hand, the interaction with time dependent external fields makes the system energy to be a non conserved quantity. This last feature

is the principal source of problems in the study of these systems, which requires to keep track of the energy flow between external sources and system. Nevertheless, this problem can be partially solved with the use of periodically varying fields, which allows to use Floquet theory and greatly simplifies the system analysis.

The time periodicity of the field induces a discrete translational symmetry in the Hamiltonian $H(t) = H(t+T)$, where $T = 2\pi/\omega$ is the period of the driving field. The advantage of Floquet theory is that it takes into account the system time translational symmetry, and provides an *ansatz* for symmetry-reduced solutions, where the effect of the driving is easily analyzed.

In quantum mechanics, a symmetry operation is described by an operator which leaves invariant the time dependent Schrödinger equation:

$$\left(H(t) - i\hbar\frac{\partial}{\partial t}\right)|\Psi(t)\rangle = 0. \tag{1.2.1}$$

Mathematically speaking it means that the symmetry operator commutes or anti-commutes with the operator $H(t) - i\hbar\partial_t$, leaving the measurement of an observable $|\langle\Psi|\tilde{O}|\Psi\rangle|$ invariant. Requiring hermiticity for $H - i\hbar\partial_t$, it constrains the possibilities to unitarity or anti-unitarity operators[5].

For a Hamiltonian with a periodic time dependence, the symmetry operation corresponds to a discrete translation by one period of the driving:

$$\mathfrak{S}_T : t \to t + T, \tag{1.2.2}$$

and because the symmetry operations must conserve the norm of any wave function, the eigenvalues of $\mathfrak{S}_T$ must be pure phase factors. If $|\psi(t)\rangle$ is an eigenfunction with eigenvalue $e^{-i\theta}$, $(\theta \in \mathbb{R})$, the action of the symmetry is given by:

$$\mathfrak{S}_T|\psi(t)\rangle = |\psi(t+T)\rangle = e^{-i\theta}|\psi(t)\rangle, \tag{1.2.3}$$

meaning that $|\psi(t)\rangle$ has the same periodicity than the Hamiltonian. These states are called in the literature Floquet states, and their eigenvalues $\theta \equiv \epsilon T/\hbar$ are expressed in terms of ϵ, called quasi-energies. The quasi-energies are time independent by definition, and physically describe the total phase acquired by a quantum state when the system evolves over a period. In addition, as the symmetry operator and the Schrödinger equation must share a common basis of eigenfunctions, we can state that a time periodic Hamiltonian will have a complete set of solutions $\{|\Psi(t)\rangle\}$ in Floquet form:

$$|\Psi(t)\rangle = e^{-i\epsilon t/\hbar}|\psi(t)\rangle,\ |\psi(t+T)\rangle = |\psi(t)\rangle, \tag{1.2.4}$$

and a general solution of the time dependent Schrödinger equation will be given in terms of a linear combination of Floquet states. Inserting Equation 1.2.4 in the time

[5]The differences between unitary and anti-unitary symmetries will be analyzed further in the chapter related with topological properties of quantum systems.

dependent Schrödinger equation (Equation 1.2.1) we obtain the eigenvalue equation for the Floquet states (also called Floquet equation):

$$\mathcal{H}(t)|\psi(t)\rangle = \epsilon|\psi(t)\rangle, \tag{1.2.5}$$

where the Floquet operator is given by:

$$\mathcal{H}(t) \equiv H(t) - i\hbar\partial_t. \tag{1.2.6}$$

It is important to note that the main advantage of the Floquet *ansatz* (Equation 1.2.4) is that it provides a mapping of the time dependent Schrödinger equation to an eigenvalue equation for the Floquet states.

1.2.1 Sambe space

A practical advantage of Floquet formalism is that the time periodicity of Floquet states allows for a representation of the eigenvalue equation in terms of a basis made of time independent states. The main advantage of this approach relies in the simplicity of the numerical calculations (which avoid numerical integration), and as we shall prove in the next chapter, also helps in the understanding of the topological properties and their dependence on the driving regime.

Let us consider a vector state $|\Psi(t)\rangle$ or a Floquet state $|\psi(t)\rangle$, it is clear that both are elements of the same Hilbert space $\mathbb{H}$. However, $|\psi(t)\rangle$ can be conveniently expanded in Fourier series considering the time periodicity of the Floquet states:

$$|\psi(t)\rangle = \sum_{n=-\infty}^{\infty} e^{in\omega t}|\psi_n\rangle. \tag{1.2.7}$$

Importantly, the Hilbert space of T-periodic functions $\mathcal{T}$ can be defined in terms of a basis $\{u_n(t) = e^{in\omega t},\ n \in \mathbb{Z}\}$ with scalar product:

$$(f(t), g(t)) = \frac{1}{T}\int_0^T f(t)^* g(t)\, dt. \tag{1.2.8}$$

This provides an adequate orthonormalized and complete basis for the Floquet states:

$$(u_n(t), u_m(t)) = \delta_{n,m}, \tag{1.2.9}$$

$$\frac{1}{T}\sum_n u_n(t)^* u_n(t') = \delta_T(t - t'), \tag{1.2.10}$$

where δ_T denotes the delta function $\mathrm{mod}(T)$.

Then, the Sambe space[33] is built by taking the direct product of both Hilbert spaces $\mathcal{S} = \mathbb{H} \times \mathcal{T}$, and considering that the Floquet states are decomposed in the product of both basis $|\psi_{n,\alpha}\rangle = |u_n\rangle \times |\psi_\alpha\rangle \in \mathbb{H} \times \mathcal{T}$, where we have denoted

$u_n(t) = \langle t|u_n\rangle$. Note that $|u_n\rangle$ contains the information of the dynamics, while $|\psi_\alpha\rangle$ contains the spatial and intrinsic degrees of freedom, labeled by α. Finally, the scalar product is given in terms of the composition of scalar products for each Hilbert space:

$$\langle\langle \phi(t)|\phi'(t)\rangle\rangle = \frac{1}{T}\int_0^T \langle\phi(t)|\phi'(t)\rangle dt. \tag{1.2.11}$$

In conclusion, the introduction of the composite Hilbert space allows to express all quantities in terms of a time independent basis, paying the price of an increased matrix dimensionality.

1.2.2 Geometric phases in Floquet states

Floquet states, in the same way as Bloch states, have a $U(1)$ gauge invariance. It makes the quasi-energies a multivalued function, analogous to the quasi-momentum in solids, which define a first Brillouin zone (FBZ) that we shall call Floquet sideband (FSB). In addition, as we commented above, the quasi-energies share some properties with the energies in undriven systems, due to the eigenvalue equation. These two ingredients, and the fact that the quasi-energy is exactly the phase acquired by the Floquet state during a driving cycle, allows to study in simple means the geometrical properties of periodically driven systems. To prove it, let us consider the variation of the quasi-energies with respect to the frequency of the driving field ω:

$$\begin{aligned}
\frac{\partial\epsilon_\alpha}{\partial\omega} &= \frac{\partial}{\partial\omega}\left(\langle\langle\psi_\alpha(t)|\mathcal{H}(t)|\psi_\alpha(t)\rangle\rangle\right) \\
&= \epsilon_\alpha\left(\langle\langle\frac{\partial}{\partial\omega}\psi_\alpha(t)|\psi_\alpha(t)\rangle\rangle + \langle\langle\psi_\alpha(t)|\frac{\partial}{\partial\omega}\psi_\alpha(t)\rangle\rangle\right) + \langle\langle\psi_\alpha(t)|\frac{\partial\mathcal{H}(t)}{\partial\omega}|\psi_\alpha(t)\rangle\rangle \\
&= \langle\langle\psi_\alpha(t)|\frac{\partial\mathcal{H}(t)}{\partial\omega}|\psi_\alpha(t)\rangle\rangle,
\end{aligned} \tag{1.2.12}$$

where we have used $\frac{\partial}{\partial\omega}\left(\langle\langle\psi_\alpha(t)|\psi_\alpha(t)\rangle\rangle\right) = \langle\langle\frac{\partial}{\partial\omega}\psi_\alpha(t)|\psi_\alpha(t)\rangle\rangle + \langle\langle\psi_\alpha(t)|\frac{\partial}{\partial\omega}\psi_\alpha(t)\rangle\rangle = 0$. This result is just a consequence of the Hellmann-Feynman theorem. However, we can re-parametrize the Floquet operator using $\mathcal{H}(t) = H(t) - i\partial_t$ and $\omega t = \tau$, we arrive at:

$$\mathcal{H}(t) = H(\tau) - i\omega\partial_\tau, \tag{1.2.13}$$

$$\frac{\partial\mathcal{H}(t)}{\partial\omega} = -i\partial_\tau = -i\frac{1}{\omega}\partial_t. \tag{1.2.14}$$

Thus, the time derivative operator is linked to the ω-derivative of the Floquet operator. Finally, considering the expression for the geometric phase:

$$\begin{aligned}
\gamma_G^\alpha &= \int_0^T \langle\psi_\alpha(t)|i\partial_t|\psi_\alpha(t)\rangle dt = -\omega T\langle\langle\psi_\alpha(t)|\frac{\partial\mathcal{H}(t)}{\partial\omega}|\psi_\alpha(t)\rangle\rangle \\
&= -2\pi\frac{\partial\epsilon_\alpha}{\partial\omega},
\end{aligned} \tag{1.2.15}$$

we get the expression for γ_G^α in terms of the quasi-energies variation with ω. This expression will be useful to understand the topological phase transitions from high to low frequency regime in a single quantum dot.

1.2.3 Mean energy

In addition, another useful quantity can be defined in Floquet systems, this is the mean energy. It is related with the topological properties as has been recently pointed out [34]. As out of equilibrium systems are not energy conserving, energy is not a good quantum number and cannot be defined. However, the mean energy or energy average in a period contains some interesting properties very related with the geometric phase. It is defined as follows:

$$\bar{E}_\alpha = \langle\langle \Psi_\alpha(t) | H(t) | \Psi_\alpha(t) \rangle\rangle = \frac{1}{T}\int_0^T \langle u_\alpha(t) | H(t) | u_\alpha(t) \rangle dt,$$

where $|\Psi_\alpha(t)\rangle = e^{-i\epsilon_\alpha t}|u_\alpha(t)\rangle$. To understand its relation with the geometric phase, let us write the Hamiltonian in terms of the Floquet operator:

$$\begin{aligned} \bar{E}_\alpha &= \frac{1}{T}\int_0^T \langle u_\alpha(t) | \left(\mathcal{H}(t) + i\partial_t\right) | u_\alpha(t) \rangle dt \\ &= \epsilon_\alpha + \frac{1}{T}\int_0^T \langle u_\alpha(t) | i\partial_t | u_\alpha(t) \rangle dt \\ &= \epsilon_\alpha - \omega\frac{\partial \epsilon_\alpha}{\partial \omega}, \end{aligned} \tag{1.2.16}$$

or also can be written as:

$$\bar{E}_\alpha = \epsilon_\alpha - \sum_n n\omega \langle u_{\alpha,n} | u_{\alpha,n} \rangle. \tag{1.2.17}$$

Equation 1.2.16 shows that the mean energy consists in two contributions: the quasi-energy, plus the geometric phase. In addition, Equation 1.2.17 shows that it also consists in the quasi-energy plus an energy contribution associated with the number of photons attached to the dressed state. Importantly, this quantity is independent of the side-band under consideration.

2 AC magnetic fields and single quantum dots

2.1 General case

Before we discuss the results of this thesis, we shall analyze a single quantum dot with one electronic level participating in the dynamics. It will allow the reader to familiarize with Floquet formalism in its simplest form.

Single quantum dots are artificial atoms, or 0 dimensional quantum boxes. Their electronic, optical and transport properties can be externally modulated by means of gate and bias voltages. Importantly for our purposes, they allow to study e.g. the spin dynamics of a single electron without an interplay with the spatial degree of freedom. The single level occupancy is achieved through a Coulomb blockade mechanism, in which the bias and voltage gates are adequately fixed. This can be understood as follows: Let us assume that the Fermi level on the right/left leads fulfill $\mu_R < \mu_L$. In absence of a magnetic field, all electronic levels with energy below μ_R are filled (Figure 2.1.1, left). If we now tune the Fermi energy in the left contact μ_L, it is possible to enclose a single electronic level within the transport window, given by $E \in [\mu_L, \mu_R]$. Then, only two states (double degeneracy due to the spin degree of freedom) participate in the dynamics (Figure 2.1.1). Finally, Coulomb interaction rises the double occupied energy levels, such that they are shifted above μ_L and energy U_C. Then, the double occupied levels do not participate in the dynamics and a single particle description of the problem is enough (Figure 2.1.1, right).

The application of an external DC magnetic field creates a Zeeman splitting, lifting the spin degeneracy of the electronic level (breaking Kramers degeneracy). It allows to define a two level system also called qubit (Figure 2.1.1, right). The spin dynamics of the two level system can be described in terms of the Pauli matrices:

$$\sigma_x = \begin{pmatrix} 0 & 1 \\ 1 & 0 \end{pmatrix}, \ \sigma_y = \begin{pmatrix} 0 & -i \\ i & 0 \end{pmatrix}, \text{ and } \sigma_z = \begin{pmatrix} 1 & 0 \\ 0 & -1 \end{pmatrix}, \tag{2.1.1}$$

and the Hamiltonian:

$$H_{SD} = -\vec{\mu} \cdot \vec{B} = \frac{1}{2} \begin{pmatrix} B_z & 0 \\ 0 & -B_z \end{pmatrix}, \tag{2.1.2}$$

$$\vec{\mu} = -g\mu_B \vec{J}/\hbar, \tag{2.1.3}$$

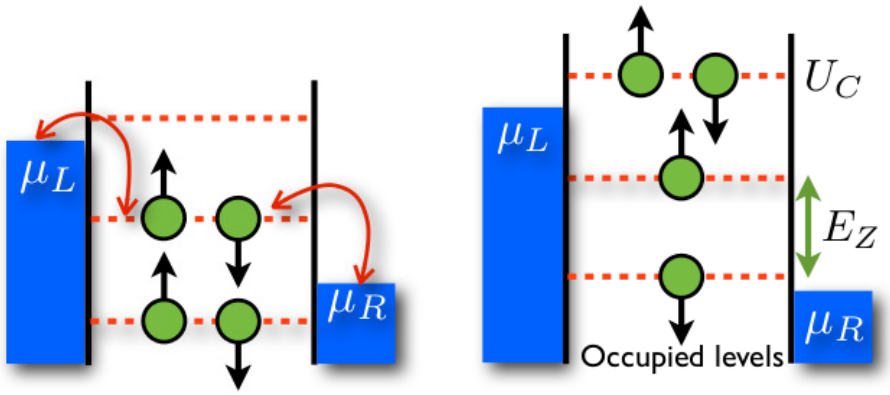

Figure 2.1.1: Single quantum dot configuration in absence of external magnetic fields and Coulomb interaction (left). The bias and gate voltage configuration allows to adjust the number of electronic levels within the transport window $E \in [\mu_L, \mu_R]$. (right) The application of an external magnetic field, which creates a Zeeman splitting, splits the spin degeneracy of the electrons, and can define a qubit $\{|\uparrow\rangle, |\downarrow\rangle\}$. In addition, the presence of Coulomb interaction lifts the double occupied level out of the transport window and then a single particle description is appropriate.

where g is the Landé factor, μ_B the Bohr magneton, and $\vec{J}$ the total angular momentum which coincides with the spin $\vec{S}$ for a localized electron. We have assumed that the external magnetic field is aligned with the z-axis, and the energy units for the Zeeman term: $g\mu_B/\hbar = 1$.

For the present time independent configuration, the system's solution consist on two energy levels with an energy splitting:

$$E_z = B_z. \tag{2.1.4}$$

However, the calculation becomes more involved if the include a perpendicular time dependent magnetic field $\vec{B}_\perp(t)$. The crossed magnetic field produces spin rotations between the spin up/down levels, leading to a time dependent dynamics. The time dependent Hamiltonian is:

$$H(t)_{SD} = -\vec{\mu} \cdot \vec{B}(t) = \frac{1}{2} \begin{pmatrix} B_z & B_\perp(t) \\ B_\perp^*(t) & -B_z \end{pmatrix}. \tag{2.1.5}$$

Importantly, the specific time dependence of the field strongly affects to the mathematical resolution of the problem. Here we shall consider the cases of linearly and circularly polarized fields.

2.1.1 Circular polarization

This is a widely studied problem, and in addition, contains some important features such as the mapping to a time independent problem, and the presence of non-trivial topological properties. First, we describe the magnetic field polarization for a circular field according to the angles of a 2-sphere $S^2 = \{\varphi, \theta\}$, where $\varphi = [0, 2\pi]$, and $\theta = [0, \pi]$ are the azimutal and polar angles respectively (see Figure 2.1.2).

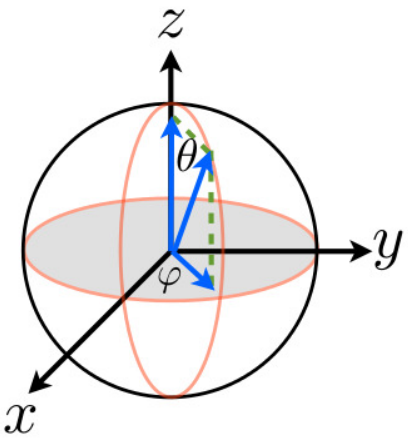

Figure 2.1.2: External magnetic field parametrization according to the azimutal and polar angles of a 2-sphere.

Next, we assume that the rotation of the field lies in the x-y plane, i.e., $\varphi = \varphi(t)$. It means that we assume a time independent Zeeman splitting along the z-axis. Finally, we assume that the azimutal angle $\varphi(t)$ changes linearly with time $\varphi(t) = \omega t$. Then, the Hamiltonian for the spin in the rotating magnetic field is:

$$\begin{aligned} H_C(t) &= \vec{B}\cdot\vec{\sigma} = \frac{1}{2}\begin{pmatrix} B_z & B_\perp\cos(\omega t) - iB_\perp\sin(\omega t) \\ B_\perp\cos(\omega t) + iB_\perp\sin(\omega t) & -B_z \end{pmatrix} \\ &= \frac{|\vec{B}|}{2}\begin{pmatrix} \cos(\theta) & \sin(\theta)\, e^{-i\varphi(t)} \\ \sin(\theta)\, e^{i\varphi(t)} & -\cos(\theta) \end{pmatrix}, \qquad (2.1.6) \\ |\vec{B}| &\equiv \sqrt{B_\perp^2 + B_z^2},\ \theta = \arctan\left(\frac{B_\perp}{B_z}\right),\ \varphi(t) = \omega t. \qquad (2.1.7) \end{aligned}$$

Before we solve this problem, we should comment its historical relevance, mainly in two different fields. On one side, this problem was studied by Bloch and Rabi[12] in order to understand the effect of an applied harmonic field on a two level system. On the other hand, Berry[23] studied the same problem from a very different point of view, which is the concept of parallel transportation in quantum mechanics. We shall discuss both points of view in this section, although the importance of parallel transportation will be studied further in the next sections, in the context of topological insulating states of matter.

As we commented above, the circular polarization configuration can be exactly solved through a mapping to a time independent reference frame. Although it does not require the use of Floquet formalism, we shall use it for consistence with the main topic of this thesis, and for comparison with the direct resolution. We also consider a Floquet approach which does not lead to an exact solution, but helps in the understanding of the different frequency regimes – adiabatic and diabatic driving. Finally, the comparison between the Floquet and the direct resolution will clarify the similarities and differences between energies and quasi-energies.

2.1.1.1 Direct resolution of the time dependent Schrödinger equation:

Here, we solve the system dynamics without invoking the Floquet ansatz. It will allow to analyze the differences and similarities between quasi-energies and energies.

The equation governing the time evolution of the system is the time dependent Schrödinger equation:

$$H_C\left(t\right)\left|\Psi_\alpha\left(t\right)\right\rangle = i\partial_t|\Psi_\alpha\left(t\right)\rangle, \tag{2.1.8}$$

being α the index labeling the basis of spin up/down state. Now, let us consider a unitary transformation $U_C\left(t\right) = e^{-i\varphi(t)\sigma_z/2}$ to a co-rotating frame:

$$\tilde{H}_C = U_C^\dagger\left(t\right)\cdot H_C\left(t\right)\cdot U_C\left(t\right) = \frac{|\vec{B}|}{2}\left[\sin\left(\theta\right)\sigma_x + \cos\left(\theta\right)\sigma_z\right]. \tag{2.1.9}$$

Importantly, as $U_C\left(t\right)$ is a time dependent unitary transformation, an extra term $-iU_C^\dagger\left(t\right)\partial_t U_C\left(t\right)$ must be included due to the time derivative to preserve gauge invariance. In the rotating frame, the Hamiltonian is time independent and we must solve the eigenvalue equation:

$$\left[\tilde{H}_C - iU_C^\dagger\left(t\right)\partial_t U_C\left(t\right)\right]|\psi_\alpha\rangle = E_\alpha|\psi_\alpha\rangle. \tag{2.1.10}$$

The solutions in the lab frame are:

$$\begin{aligned} |\Psi_\alpha\left(t\right)\rangle &= e^{-iE_\alpha t}e^{-i\omega t\frac{\sigma_z}{2}}|\psi_\alpha\rangle, \quad |\psi_\alpha\rangle = \left\{\begin{pmatrix}\cos\left(\frac{\beta}{2}\right)\\ \sin\left(\frac{\beta}{2}\right)\end{pmatrix}, \begin{pmatrix}\sin\left(\frac{\beta}{2}\right)\\ -\cos\left(\frac{\beta}{2}\right)\end{pmatrix}\right\}, \\ E_\pm &= \pm\frac{1}{2}\sqrt{|\vec{B}|^2+\omega^2-2\omega|\vec{B}|\cos\left(\theta\right)}, \end{aligned} \tag{2.1.11}$$

where $\beta = \arccos\left[\left(\cos\left(\theta\right)-\omega/|\vec{B}|\right)/\sqrt{\sin\left(\theta\right)^2+\left(\cos\left(\theta\right)-\omega/|\vec{B}|\right)^2}\right]$. Note that the energies $E_\pm$ do not cross unless $\omega = |\vec{B}|$. This is the hallmark of the topological phase transition from adiabatic to diabatic regime as we will show below, and as expected, it requires a gap closure.

2.1.1.2 Floquet Resolution

If we instead consider the Floquet ansatz, the Floquet states are obtained by solving the next eigenvalue equation:

$$\mathcal{H}_C(t)\,|u_\alpha(t)\rangle = \epsilon_\alpha |u_\alpha(t)\rangle, \tag{2.1.12}$$

where $\mathcal{H}_C(t) \equiv H_C(t) - i\partial_t$ is the Floquet operator, $|u_\alpha(t)\rangle$ the Floquet state and ϵ_α the corresponding quasi-energy.

In order to clearly understand the dynamics at different frequencies and the validity range of the approximations, we first represent the Floquet operator in Sambe space:

$$\mathcal{H}_C^{(n,m)} = \frac{|\vec{B}|}{2}\left\{\cos(\theta)\,\sigma_z\delta_{n,m} + \sin(\theta)\,\sigma_+\delta_{n,m+1} + \sin(\theta)\,\sigma_-\delta_{n,m-1}\right\} - \delta_{n,m}n\omega. \tag{2.1.13}$$

Equation 2.1.13 represents the infinite set of Floquet side-bands in Sambe space and the couplings among them, which directly depend on the ratio $|\vec{B}|\sin(\theta)/\omega$. First, we must notice that decoupled Floquet bands means to neglect the terms proportional to $\sigma_\pm$. Thus, high frequency approximation holds as far as the Floquet bands are almost decoupled, which requires the condition $\omega \gg |\vec{B}|\sin(\theta)$ to be fulfilled. If this is the case, we approach the time evolution by the time independent effective Hamiltonian:

$$H_C^{\text{eff}} = \frac{|\vec{B}|}{2}\cos(\theta)\,\sigma_z, \tag{2.1.14}$$

in which we have considered the side-band zero. Note that Equation 2.1.14 is just the Hamiltonian of the single spin coupled to the constant magnetic field. The reason for the AC field term to vanish is that, in this limit, the spin cannot be aligned with the external magnetic field due to its fast rate of change, and in consequence it "feels" the time average field, which is zero. In Figure 2.1.3(left) we plot the behavior of the side-bands in high frequency[1]. So far, this approximate resolution for the high frequency regime shows the condition to obtain an effective Hamiltonian in terms of quasi-energies decoupled quasi-energies. This will be very useful when the system is not exactly solvable in Chapters 4-5.

Now, we obtain the exact solution using the Floquet ansatz. This is obtained by means of the mapping to a co-rotating frame considered above (Equation 2.1.9). The time independent Floquet operator in the rotating frame is given by:

$$\left[\tilde{H}_C - iU_C^\dagger(t)\,\partial_t U_C(t) - i\partial_t\right]|\tilde{u}_\alpha(t)\rangle = \epsilon_\alpha|\tilde{u}_\alpha(t)\rangle, \tag{2.1.15}$$

where $|\tilde{u}_\alpha(t)\rangle = U_C^\dagger(t)\,|u_\alpha(t)\rangle$ are the eigenstates in the rotating frame, and the Floquet operator is explicitly given by:

$$\tilde{\mathcal{H}}_C(t) \equiv \frac{|\vec{B}|}{2}\sin(\theta)\,\sigma_x + \frac{1}{2}\left[|\vec{B}|\cos(\theta) - \omega\right]\sigma_z - i\partial_t. \tag{2.1.16}$$

[1]The shift of the exact crossing from $\theta = \pi/2$ to lower values is due to a finite coupling between side-bands.

Note that the effect of the driving in Equation 2.1.16 is the renormalization of the Zeeman splitting to $B_z - \omega$. In this frame the Floquet equation can be exactly solved, and its eigenstates are:

$$|\tilde{u}_\alpha(t)\rangle = e^{-i(E_\alpha - \epsilon_\alpha)t}|\tilde{u}_\alpha\rangle \quad (2.1.17)$$

$$|u_\alpha(t)\rangle = e^{-i\omega t\sigma_z/2}e^{-i(E_\alpha - \epsilon_\alpha)t}|\tilde{u}_\alpha\rangle, \quad (2.1.18)$$

in the co-rotating and lab frame respectively, where $E_\pm$ is defined in Equation 2.1.11, and $|\tilde{u}_+\rangle = \left(\cos\left(\frac{\beta}{2}\right), \sin\left(\frac{\beta}{2}\right)\right)^T$, $|\tilde{u}_-\rangle = \left(\sin\left(\frac{\beta}{2}\right), -\cos\left(\frac{\beta}{2}\right)\right)^T$ the corresponding eigenvectors. The parameter β is defined below Equation 2.1.11 as well. Finally, we can obtain the quasi-energies by the requirement of time periodicity for the Floquet states $|u_\alpha(T)\rangle = |u_\alpha(0)\rangle$, which fixes their possible values to:

$$\epsilon_\pm = n\omega \mp \frac{\omega}{2} + E_\pm,\ n \in \mathbb{Z}. \quad (2.1.19)$$

Note that the Brillouin zone like structure has naturally arose for the quasi-energies, where n can take any integer value and all quasi-energies with different n are just copies shifted $n\omega$. Finally, the Floquet states have a very simple time dependence in the lab frame:

$$|u_\alpha(t)\rangle = e^{-i\omega t\frac{\sigma_z}{2}}e^{i\left(n-\frac{\alpha}{2}\right)\omega t}|u_\alpha(0)\rangle. \quad (2.1.20)$$

It is important to realize that the quasi-energies (Equation 2.1.19) differ from the energies (Equation 2.1.11) in a shift $\pm\omega/2$, resulting in an exact crossing for all values of (ω, θ) (Figure 2.1.3). This difference means that the energies $E_\pm$ are different objects than the quasi-energies. However, it is clear that both are related, and this can be clearly stated for this system as follows: A vanishing gap between energies requires $E_+ - E_- = 0$, which can be written in terms of the quasi-energies as:

$$E_+ - E_- = \epsilon_+ - \epsilon_- + \omega = 0 \quad (2.1.21)$$

Hence, the gap closure happens when the frequency ω equals the gap between quasi-energies. Figure 2.1.3 (middle) shows the case when the frequency equals the gap, which occurs when the different side-bands touch. This will be further discussed in Chapters 4 and 5, in terms of the Δ_π gap closure, which characterizes the breakdown of the high frequency effective Hamiltonian.

Finally, in order to compare the Floquet states (Equation 2.1.20) with the solutions of the time dependent Schrödinger equation (Equation 2.1.11), we rewrite $|\Psi_\alpha(t)\rangle$ in terms of the quasi-energies:

$$\begin{aligned} |\Psi_\alpha(t)\rangle &= e^{-i\left(-n\omega+\alpha\frac{\omega}{2}+\epsilon_\alpha\right)t}e^{-i\omega t\frac{\sigma_z}{2}}|\psi_\alpha\rangle \\ &= e^{-i\epsilon_\alpha t}e^{i\left(n\omega-\alpha\frac{\omega}{2}\right)t}e^{-i\omega t\frac{\sigma_z}{2}}|\psi_\alpha\rangle \\ &= e^{-i\epsilon_\alpha t}|u_\alpha(t)\rangle, \end{aligned} \quad (2.1.22)$$

It proves that the Floquet states, which only differ in a phase factor, are equally valid for the calculation of geometrical and topological quantities.

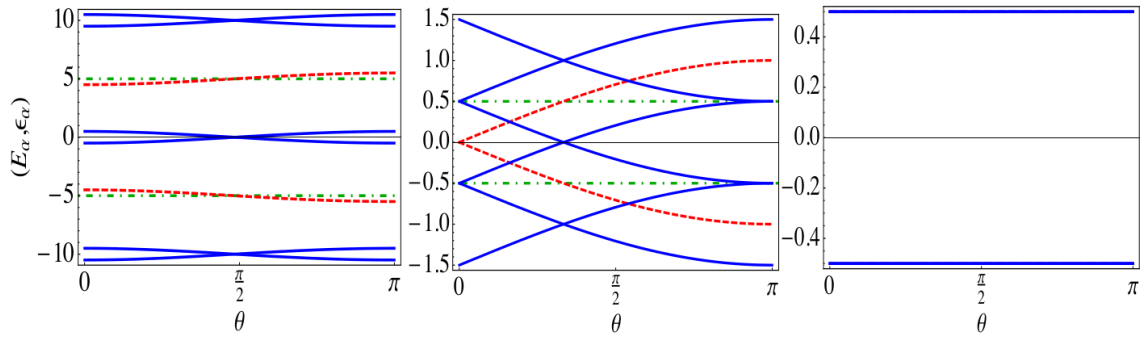

Figure 2.1.3: Comparison between exact energies (dashed red color) and quasi-energies (blue) at different frequencies. Left plot shows the high frequency case ($\omega = 10|\vec{B}|$), in which three equivalent side-bands are shown with boundaries in dot-dashed green lines. It shows how the energies are gapped while the quasi-energies are not. Center plot shows the resonant case when the side-bands touch and the gap of the energies is closed ($\omega = |\vec{B}|$). This is the topological phase transition from diabatic to adiabatic regime. Right plot shows the adiabatic limit $\omega \to 0$ in which energies and quasi-energies match.

2.1.1.3 Topological transition from adiabatic to diabatic regime.

As we already know the exact Floquet states, we proceed to calculate the geometrical and topological properties. The Berry connection 1-form is obtained by means of the exterior derivative:

$$\begin{aligned} \hat{A}_\alpha &= \langle u_\alpha | id | u_\alpha \rangle = \langle u_\alpha | i\partial_t | u_\alpha \rangle dt + \langle u_\alpha | i\partial_\theta | u_\alpha \rangle d\theta \\ &= A_{\alpha,t} dt + A_{\alpha,\theta} d\theta, \qquad (2.1.23) \\ A_{\alpha,t} &= \frac{\omega}{2} \left[\langle u_\alpha | \sigma_z | u_\alpha \rangle - (2n - \alpha) \right] \\ &= \frac{\omega}{2} \left[\alpha \cos(\beta) - (2n - \alpha) \right], \qquad (2.1.24) \\ A_{\alpha,\theta} &= \langle u_\alpha | i\partial_\theta | u_\alpha \rangle. \qquad (2.1.25) \end{aligned}$$

We did not explicitly write A_θ because it is time independent, and its contribution will be irrelevant for the Berry curvature. Besides, note that the A_t term is the one giving rise to the geometric phase – by definition the geometric phase is its time integral. The Berry curvature is given by:

$$\begin{aligned} F_\alpha &= dA_\alpha = \partial_\theta A_{\alpha,t} d\theta \wedge dt \\ &= \frac{\partial A_{\alpha,t}}{\partial \beta(\theta)} \frac{\partial \beta(\theta)}{\partial \theta} d\theta \wedge dt, \qquad (2.1.26) \end{aligned}$$

and allows to calculate the Chern number, which is given by the integral of the Berry curvature all over the parameter space:

$$\begin{aligned} c_1 &= \frac{1}{2\pi}\int F_\alpha \\ &= \frac{1}{2\pi}\int_0^T dt \int_0^\pi \partial_\beta A_{\alpha,t}\frac{\partial\beta\left(\theta\right)}{\partial\theta}d\theta \\ &= \Theta\left(1-\frac{\omega}{B}\right). \end{aligned} \tag{2.1.27}$$

Equation 2.1.27 encodes the information of a topological transition between two different driving regimes, each of them characterized in terms of a Chern number. The Chern number accounts for the transition from adiabatic regime, in which the spin is able to follow the magnetic field direction, to diabatic regime, where the spin cannot align with the magnetic field and then is subjected to an average magnetic field. To easily understand the condition $\Theta\left(1-\omega/|\vec{B}|\right)$, we just need to look at the definition of the angle β:

$$\beta = \arctan\left[\frac{\sin\left(\theta\right)}{\cos\left(\theta\right)-\omega/|\vec{B}|}\right], \tag{2.1.28}$$

For a non zero Chern number, β needs to be varied from $\beta\in[0,\pi]$, covering the full 2-sphere. This is only possible if $\omega/|\vec{B}|<1$, such that the denominator becomes zero and the argument runs from $(-\infty,\infty)$, as it is seen in Figure 2.1.4. Then, in high frequency regime, the spin "feels" an average static field mimicking a constant Zeeman field, which does not induce Rabi oscillations between spin up/down, and the spinor does not cover the whole 2-sphere. When the system enters in the adiabatic regime, the spin follows the AC field and fully covers the 2-sphere, oscillating between spin up and down.

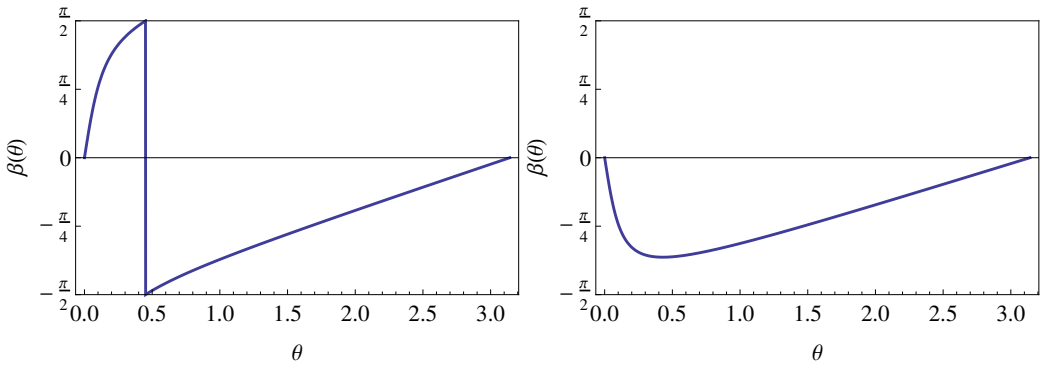

Figure 2.1.4: Domain of the β angle as a function of θ for $\omega/|\vec{B}|<1$ (left), and $\omega/|\vec{B}|>1$ (right). Note how in the adiabatic regime (left) the β angle covers the full π domain.

As a check, we can also calculate the geometric phase using Equation 1.2.15:

$$\gamma_{\alpha=\pm} = -2\pi\partial_\omega\epsilon_\alpha = -2\pi n + \alpha\pi\left[1+\cos\left(\beta\right)\right], \tag{2.1.29}$$

$$\beta \equiv \arccos\left(\frac{|\vec{B}|\cos\left(\theta\right)-\omega}{\sqrt{\left(|\vec{B}|\cos\left(\theta\right)-\omega\right)^2+|\vec{B}|^2\sin\left(\theta\right)^2}}\right). \tag{2.1.30}$$

Equation 2.1.29 is the well known expression for the geometric phase of a spin in a rotating magnetic field, which is tilted a $\beta\left(\theta,\omega\right)$ angle. Importantly, the angle fulfills $\beta \underset{\omega\to 0}{\to} \theta$, and then, non-adiabatic effects can be interpreted in terms of a renormalization of the angle θ. In Figure 2.1.5 we plot the behavior of the geometric phase γ_α in terms of the Zeeman splitting for two different situations.

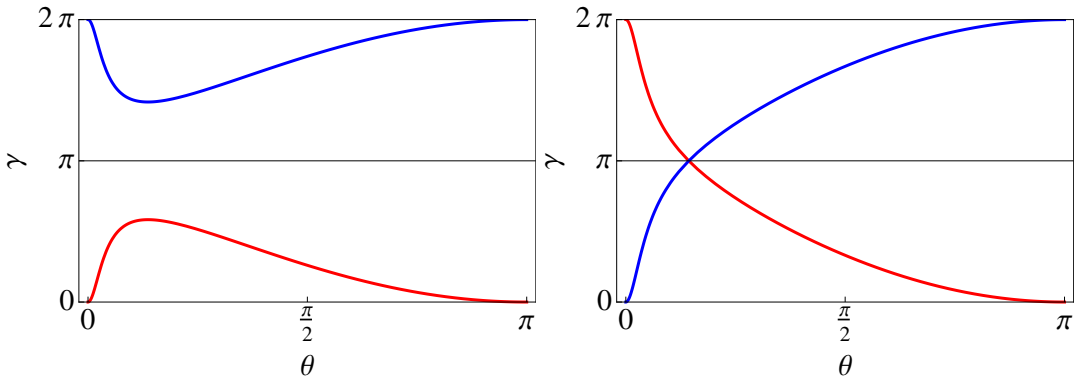

Figure 2.1.5: Geometric phase for a single spin in a circularly polarized magnetic field at different driving regimes. In the high frequency regime, the geometric phase γ_α is zero for all θ (not shown). Left plot shows a frequency value in which the geometric phases are non zero but the system is within the trivial topological phase ($\omega = 1.1|\vec{B}|$). Right plot shows a frequency value in which the system is in the adiabatic regime, with non zero Chern number ($\omega = 0.9|\vec{B}|$).

In the high frequency limit, the geometric phase is almost flat with value $2\pi n,\ n\in\mathbb{Z}$ (not shown). It means that the system is in a trivial phase for high frequency, as we shown above in terms of the Chern number. Figure 2.1.5 (left) shows the case with frequency slightly larger than the field amplitude, i.e., $\omega/|\vec{B}| \gtrsim 1$. Here, the geometric phases are important, and they cannot be neglected in formal calculations, even though the Chern number vanishes. In Figure 2.1.5 (right) the frequency is slightly smaller than the field amplitude. At this point, below the critical point $\omega/|\vec{B}| = 1$, the system is in the non-trivial topological phase. Clearly, the geometric phases change drastically and now their derivative with respect to θ does not change in sign. Moreover, as the Berry curvature (Equation 2.1.26) is proportional to $\partial_\theta A_t$, it is possible, just by looking at Figure 2.1.5, to extract the value of ω at which the topological transition occurs. This happens when the function $\partial_\theta A_t$ is strictly positive or negative for all the θ domain.

Finally, we calculate the mean energy of the system as:

$$\begin{aligned}\bar{E}_\alpha &= \frac{1}{T}\int_0^T \langle\langle u_\alpha(0)|e^{i\omega t\frac{\sigma_z}{2}}H(t)\,e^{-i\omega t\frac{\sigma_z}{2}}|u_\alpha(0)\rangle\rangle dt \\ &= \langle\langle u_\alpha(0)|\frac{|\vec{B}|}{2}\left[\sin(\theta)\,\sigma_x+\cos(\theta)\,\sigma_z\right]|u_\alpha(0)\rangle\rangle \\ &= \alpha\frac{|\vec{B}|}{2}\cos(\beta-\theta)\,. \end{aligned} \tag{2.1.31}$$

Therefore, the mean energy can be used used as an indicator of a topological transition when the frequency is varied, since it accounts for the difference between the non-adiabatic tilting angle $\beta(\omega,\theta)$ of the magnetic field, and the adiabatic one θ.

For completeness, in Figure 2.1.6 we plot the quasi-energies within the zero side-band versus frequency. As the definition of the side-bands depends on the frequency value, a folding of the Brillouin zone like structure happens when ω is decreased. Importantly, it involves a gap closures of the quasi-energies, which according to the previous calculations, are not accompanied by topological transitions (we remain in the adiabatic regime according to Chern number value). Then, gap closures due to side-bands folding does not directly imply a change in the topological properties. We will show during this thesis that the folding of quasi-energies, in difference with the present case, can affect to the topological properties during the transition between diabatic and adiabatic regime. Then, each case must be carefully analyzed. Nevertheless, in all cases studied in this thesis we found that the side-bands inversions affect to the topological properties when these are characterized by weak topological indices[2].

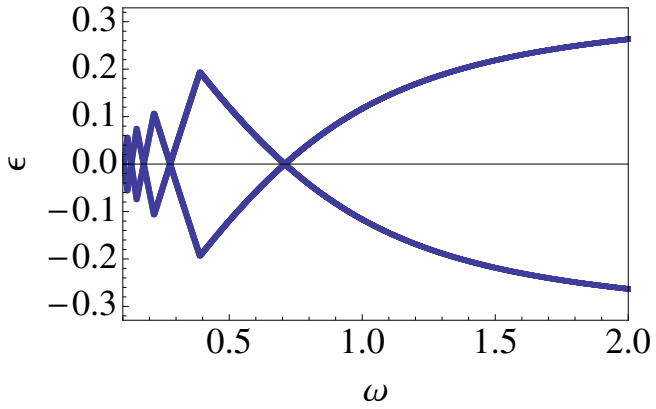

Figure 2.1.6: Floquet side-band folding due to a frequency decrease. Parameters considered $\theta=\pi/4$, and $|\vec{B}|=1$.

[2]Weak topological indices are the ones defined in lower dimensions than the total parameter space dimension.

2.1.1.4 Explanation of the transition from D to D+1 in a single quantum dot.

In the context of the following sections of this thesis, we briefly explain why the transition from diabatic to adiabatic can be interpreted as an increase in the parameter space manifold dimension (this is discussed in detail in Chapter 4). Consider the high frequency expression for the quasi-energies of a single QD in a rotating magnetic field (Equation 2.1.14):

$$H_C^{\text{eff}} = \frac{|\vec{B}|}{2} \cos(\theta)\, \sigma_z. \tag{2.1.32}$$

It consists on a spin placed in a constant Zeeman field with strength $|\vec{B}| \cos(\theta)$. The eigenstates of this Hamiltonian are constant, and independent of the field strength $|\vec{B}|$ or the θ angle. Therefore, parallel transportation of the states is trivial, meaning flat base space which is the reason why at high frequency the curvature vanishes. The effective Hamiltonian H_C^{eff} is not time reversal invariant, because the TRS operation for a spin half system is $\Theta^{-1} H_C^{\text{eff}} \Theta = -H_C^{\text{eff}}$, where $\Theta = e^{-i\pi\sigma_y/2} K$ and K is the complex conjugation operator. TRS acting on a spin eigenstate changes the spin sign $\Theta^{-1} \vec{S} \Theta = -\vec{S}$, because it is an angular momentum and the magnetic field $|\vec{B}|$ is invariant. Then, the Hamiltonian belongs to the Standard (Wigner-Dyson) A (unitary) class, and in 1D it does not possess a topological invariant[3].

When the frequency is decreased, the effective Hamiltonian (Equation 2.1.32) is no longer a good approximation, and we must consider the full time dependent Floquet operator (Equation 2.1.13). This is defined over a two dimensional parameter space, spanned by (θ, t). This 2D system has a non-trivial topological invariant, which is precisely the first Chern number c_1. Then the transition from adiabatic to diabatic regime corresponds to a change in the base manifold dimension.

We must comment that in this system, with a topological invariant in real space, it is evident that the driving in a perpendicular direction to the Zeeman field provides a new spatial component, and thus the increase in the dimensions. However, this feature will be more involved for the case of k-space invariants, where the driving also allows to increase the effective dimension of the FBZ from $\mathbb{T}^n \to \mathbb{T}^{n+1}$.

2.1.2 Linear polarization

Linearly polarized fields are usually considered in experiments. However, in contrast with circular fields, their field amplitude $|\vec{B}|$ depends on time. Besides, an exact solution is not possible for this field configuration, and two different approaches are classically considered. The first one assumes a system near to resonance ($\omega \simeq \Delta E = E_+ - E_-$), such that it is possible to neglect fast oscillating terms, resulting in the

[3]The different topological classes are explained in Chapter 4, and at this point the reader just need to know that a system with the current symmetries in 1D does not have a topological invariant.

previously studied case of circular polarization – This is usually called rotating wave approximation. The complementary approach considers a high frequency field, far from resonance. This last one allows, by means of the interaction picture, to obtain an effective Hamiltonian in which the parameters of the undriven Hamiltonian are renormalized by the external field.

The Hamiltonian for a linearly polarized field is:

$$H_L(t) = \frac{1}{2}\begin{pmatrix} B_z & B_x\cos(\omega t) \\ B_x\cos(\omega t) & -B_z \end{pmatrix} \tag{2.1.33}$$

$$= \frac{|\vec{B}|}{2}\begin{pmatrix} \cos(\theta) & \sin(\theta)\cos(\omega t) \\ \sin(\theta)\cos(\omega t) & -\cos(\theta) \end{pmatrix}, \tag{2.1.34}$$

where we have considered two different parametrizations for the external magnetic field: First in terms of the amplitude $B_{x,z}$, and second in terms of the azimutal angle θ for an easier comparison with the previous results.

For the first approach, we consider the next transformation to the interaction picture:

$$U_L(t) = e^{iB_z\sigma_z t/2}, \tag{2.1.35}$$

$$|u_\alpha(t)\rangle_I = U_L(t)\,|u_\alpha(t)\rangle. \tag{2.1.36}$$

The interaction picture Hamiltonian is given by:

$$H_L^I(t) = U_L(t)\cdot H_L(t)\cdot U_L^\dagger(t) - \frac{B_z}{2}\sigma_z$$

$$= \frac{B_x}{4}\begin{pmatrix} 0 & e^{it(B_z-\omega)} + e^{it(B_z+\omega)} \\ e^{-it(B_z-\omega)} + e^{-it(B_z+\omega)} & 0 \end{pmatrix}, \tag{2.1.37}$$

where it is clear the difference between rotating $e^{it(B_z+\omega)}$ and counter rotating terms $e^{it(B_z-\omega)}$. Near resonance (i.e., when $\omega \simeq B_z$), the counter rotating terms become $e^{it(B_z-\omega)} \sim 1$, while on the other hand, the rotating term would oscillate very fast, averaging to zero. In consequence, one can assume in the co-rotating frame:

$$H_L^I(t) \simeq \frac{B_x}{4}\begin{pmatrix} 0 & e^{it(B_z-\omega)} \\ e^{-it(B_z-\omega)} & 0 \end{pmatrix} \simeq \frac{B_x}{4}\sigma_x. \tag{2.1.38}$$

Thus, in the laboratory frame we have:

$$H_L(t) \simeq \frac{1}{2}\begin{pmatrix} B_z & \frac{B_x}{2}e^{-it\omega} \\ \frac{B_x}{2}e^{it\omega} & -B_z \end{pmatrix}. \tag{2.1.39}$$

Equation 2.1.39 is analogous to the circularly polarized case previously considered, and then one can exactly solve its time evolution.

However, we just claimed that the rotating terms must average to zero without proof. In addition, can be seen numerically that when the field amplitude is increased, the

numerical results disagree with theory, and a constrain for the field amplitude must be included in order to obtain agreement. This constriction comes from the rotating terms, and can be easily understood using the Floquet picture on Equation 2.1.37. In Sambe space, the components of the Floquet operator in the interaction picture are given by (we assume near resonance condition $\omega - B_z \simeq 0$, and $\omega + B_z \simeq 2\omega$):

$$\begin{aligned}\mathcal{H}^I_{L,(n,m)} &= \frac{1}{T}\int_0^T H^I_L(t)\, e^{i\omega t(n-m)}dt - \delta_{n,m} n\omega \\ &= \left(\frac{B_x}{4}\sigma_x - n\omega\right)\delta_{n,m} + \frac{B_x}{4}\sigma_+\delta_{n,m-2} + \frac{B_x}{4}\sigma_-\delta_{n,m+2}, \quad (2.1.40)\end{aligned}$$

where $\sigma_\pm = (\sigma_x \pm i\sigma_y)/2$. It is now clear that the RWA is equivalent to neglect the two last terms of Equation 2.1.40, decoupling the Floquet bands – it leads to a time independent effective Hamiltonian in the rotating frame. However, to neglect the two photon processes it is required that the energy difference between the corresponding Floquet bands n and $n \pm 2$ has to be larger than the coupling between them. In other words, we require $B_x/4 \ll 2\omega$, i.e., $B_x \ll 8\omega$. This is the reason why the Rabi formula breaks down near resonance for large field amplitudes. Physically, the increase of the field amplitude implies an increasing probability of multi-photon processes, which are not included in the RWA picture. The physical effect associated with this corrections to the Rabi formula is the so called Bloch-Siegert shift[35].

The second approach to this problem, considers again a transformation to the interaction picture, but this time the AC field is encoded in the wave functions. The unitary transformation is:

$$\begin{aligned}U'_L(t) &= e^{i\sigma_x \int B_x \cos(\omega t)dt/2} \\ &= e^{i\sigma_x \sin(\omega t)/2\omega}, \quad (2.1.41)\\ |u'_\alpha(t)\rangle_I &= U'_L(t)\,|u_\alpha(t)\rangle. \quad (2.1.42)\end{aligned}$$

The transformation to the interaction picture of Equation 2.1.34 by means of $U'_L(t)$ results in:

$$H^{II}_L(t) = \frac{B_z}{2}\begin{pmatrix} \cos\left(\frac{B_x \sin(\omega t)}{\omega}\right) & -i\sin\left(\frac{B_x \sin(\omega t)}{\omega}\right) \\ i\sin\left(\frac{B_x \sin(\omega t)}{\omega}\right) & -\cos\left(\frac{B_x \sin(\omega t)}{\omega}\right)\end{pmatrix}, \quad (2.1.43)$$

where importantly, B_z is the only parameter that affects to the band gap and width. The parameter B_x/ω is now in the argument of the cosine/sine functions, and controls their rate of change, but does not change their modulus. Thus, B_x/ω can be understood as an *effective frequency* in the interaction picture. This is more evident from the Fourier space representation of the corresponding Floquet operator:

$$\mathcal{H}^{II}_{L,(n,m)} = \frac{B_z}{4}\begin{pmatrix} J_{m-n}\left(\frac{B_x}{\omega}\right) + J_{n-m}\left(\frac{B_x}{\omega}\right) & J_{n-m}\left(\frac{B_x}{\omega}\right) - J_{m-n}\left(\frac{B_x}{\omega}\right) \\ J_{m-n}\left(\frac{B_x}{\omega}\right) - J_{n-m}\left(\frac{B_x}{\omega}\right) & -J_{m-n}\left(\frac{B_x}{\omega}\right) - J_{n-m}\left(\frac{B_x}{\omega}\right)\end{pmatrix} - n\omega\mathcal{I}\delta_{m,n}, \quad (2.1.44)$$

where $\mathcal{I}$ is the identity matrix in the spin space. In view of Equation 2.1.44, we can see that the tuning of the effective frequency (B_x/ω) controls the contribution of multi-photon resonances. In addition, note that in order to obtain an effective time independent Hamiltonian we must require a decoupling between the side-bands. This is independent of the field amplitude B_x (decoupling between Floquet bands requires $\omega \gg B_z/4$) leading the time independent Hamiltonian in high frequency:

$$H_{\text{eff}} = \frac{B_z}{2} J_0\left(\frac{B_x}{\omega}\right)\sigma_z. \tag{2.1.45}$$

Equation 2.1.45 shows the effect of the field amplitude in the Zeeman splitting, which is renormalized by zeroth order Bessel functions of the first kind $J_0(x)$. Note that the linearly polarized field presents richer physics than the circular one, because in high frequency the circular field does not show a renormalization effects. A similar effect, was proposed in another system: two levels separated by a tunneling barrier in the presence of an electric field. There, the tunneling barrier becomes renormalized by $J_0(E/\omega)$ where E is the electric field amplitude. At the zeros of $J_0(E/\omega)$ the tunneling rate is quenched. This situation was termed coherent destruction of tunneling (CDT)[36]. In the present case, it is the Zeeman splitting which is renormalized to zero as $J_0(B_x/\omega)$ becomes zero.

From the two different approaches considered above it is evident that for some frequency ω, the Chern number must change by means of a topological phase transition. The reason is that the RWA leads to a system with non-zero Chern number, while the high frequency approximation leads to a system with vanishing Chern number. In order to understand this transition, we must lower the frequency, at least to the order in which the RWA is valid.

Let us consider the angular parametrization used for the circularly polarized field. The Fourier space representation of the Floquet operator in Equation 2.1.44 is:

$$\mathcal{H}^{II}_{L,(n,m)} = \frac{|\vec{B}|\cos(\theta)}{4}\left\{\left[J_{m-n}(x) + J_{n-m}(x)\right]\sigma_z + i\left[J_{n-m}(x) - J_{m-n}(x)\right]\sigma_y\right\} - n\omega\mathcal{I}\delta_{m,n}, \tag{2.1.46}$$

where we have defined $x = \lambda\sin(\theta)$, and the adiabatic parameter $\lambda = |\vec{B}|/\omega$. Next we perform an exact numerical calculation of the quasi-energies for different frequencies using Equation 2.1.46. We find that similarly to the circularly polarized case, the Floquet side-bands move closer when ω is decreased, and when $|\vec{B}| = \omega$ the gap between them is closed. However, we cannot analytically prove that this point represents a topological phase transition. For this purpose we have calculated numerically the frequency dependence of the Chern number as it is shown in Figure 2.1.7. It shows a change in the Chern number from $c_1 = 0$ to $c_1 = 2$, and hence a topological phase transition when the different side-bands touch.

In order to understand the difference in the value of the Chern number for the circular and linear polarizations, we must look at Hamiltonian in the RWA approximation (Equation 2.1.39). It shows that in comparison with the circular case, the

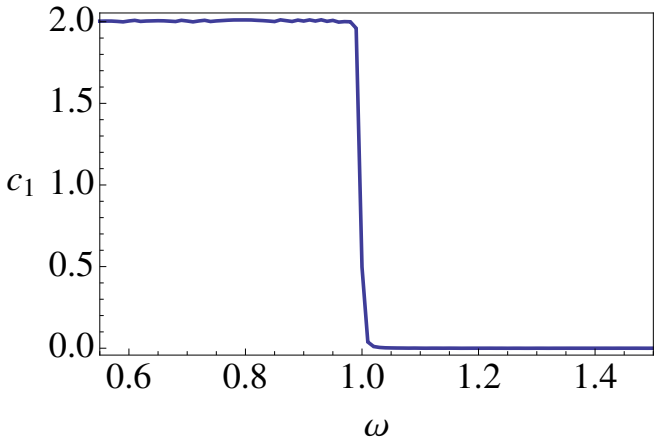

Figure 2.1.7: Numerical calculation of the Chern number using the Sambe space representation of the Floquet eigenvalue equation. It shows that for $\omega = |\vec{B}| = 1$, the system overcomes a topological phase transition to a 2 dimensional parameter space (θ, t), in which the Chern number is $c_1 = 2$. This is an important difference with the circular case, in which $c_1 = 1$.

polar angle $\theta = \arctan[B_z/B_\perp]$ differs in a factor of two due to the $B_x\sigma_x/4$ term. Therefore, when the Berry curvature is integrated in θ for the calculation of the Chern number, the 2-sphere is covered twice, leading to $c_1 = 2$.

For completeness, in Figure 2.1.8 we plot the quasi-energies vs the frequency of the AC field. A comparison with Figure 2.1.6 shows that linear and circular polarization behaves similarly. At high frequency the geometric phase vanishes both plots (i.e., the variation of the quasi-energies $\partial_\omega \epsilon_\alpha \sim 0$), which is related with the decoupling of Floquet side-bands, then, at lower frequencies can be observed the folding of the side-bands.

In summary, in this chapter we have analyzed the differences between circular and linear fields, and the advantages of Floquet theory. The main advantage is that, when the system is not analytically solvable, the side-bands picture allows to efficiently obtain information of the difference frequency regimes. We have show, that linear fields are richer due to the renormalization effects, but also more complicated to study. In addition, we have discussed the different approaches which can be considered in these systems, depending on the regime we are interested in. All approaches are based in different transformations to the interaction picture. It gives rise to different conditions for the existence of a time independent effective Hamiltonian, however, a common feature for all effective Hamiltonians is that the frequency ω is fixed, and becomes difficult to study the change in the spectrum due to frequency variations. Finally, we have shown that numerical methods can be used to slightly overcome this constraint, and study the frequency dependence of some properties.

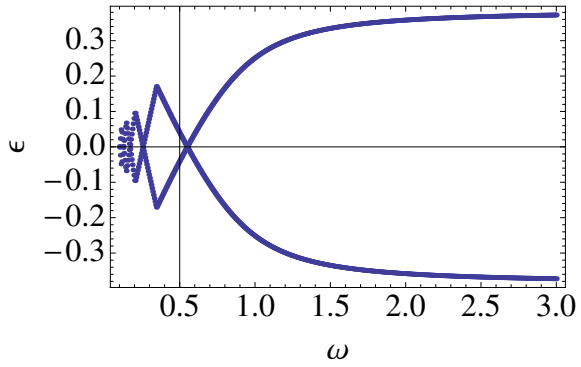

Figure 2.1.8: Quasi-energies vs frequency for a single spin coupled to a linearly polarized field. Note that for $\omega \gg B_z$ the geometric phase $\gamma_\alpha = -2\pi\partial_\omega\epsilon_\alpha \sim 0$, is in agreement with the 1 dimensional parameter space in high frequency. On the other hand, at lower frequency the quasi-energies change with ω, meaning a non vanishing geometric phase. The parameters are: $B_z = B_x/\omega = 1$.

3 Spin and charge dynamics in AC driven double quantum dots

In the previous chapter we have shown that AC fields can be used to tune the dynamical and the topological properties of a single qubit. However, we have restricted our analysis to the dynamics to a localized spin, and in general, quantum systems contain additional degrees of freedom. In this chapter we consider two tunnel coupled quantum dots, and study the interplay between the spin and the spatial degrees of freedom. We show, for different field polarizations, that the AC magnetic fields allow to independently control the spatial and spin degree of freedom. In addition, we will discuss the differences between circular and linear polarization in terms of the spin and charge dynamics. For the characterization of the charge dynamics we study the coupling to the leads and the current through the double quantum dot. Finally, we discuss the topological phases which can be obtained in these systems, and characterize the transition from adiabatic to diabatic regime, when charge and spin dynamics are correlated.

3.1 Linearly polarized AC fields

We consider a double quantum dot (DQD) with single electron occupancy (Figure 3.1.1), coupled to an in-plane linearly polarized AC magnetic field $B_{ac}(t)$ and to a perpendicular DC magnetic field B_z. The Hamiltonian can be written as:

$$
\begin{aligned}
H(t) &= H_0 + H_\tau + H_{dc}^B + H_{ac}^B(t) && (3.1.1)\\
H_0 &= \sum_{i,\sigma} \epsilon_{g,i} c_{\sigma,i}^\dagger c_{\sigma,i}, && (3.1.2)\\
H_\tau &= -t_{LR} \sum_{i\neq j} \left(c_{\sigma,i}^\dagger c_{\sigma,j} + \text{H.c.} \right), && (3.1.3)\\
H_{ac}^B(t) &= \sum_i B_{ac,i} S_{x,i} \sin(\omega t + \phi_i), && (3.1.4)\\
H_{dc}^B &= \sum_i B_{z,i} S_{z,i}, && (3.1.5)
\end{aligned}
$$

where the index $i = L, R$ means left/right dot respectively, $\epsilon_{g,i}$ is the gate voltage in the i dot, $\sigma = \uparrow, \downarrow$ is the spin projection, and t_{LR} the inter-dot tunneling. Note that the magnetic field components also contain a phase difference ϕ, related with

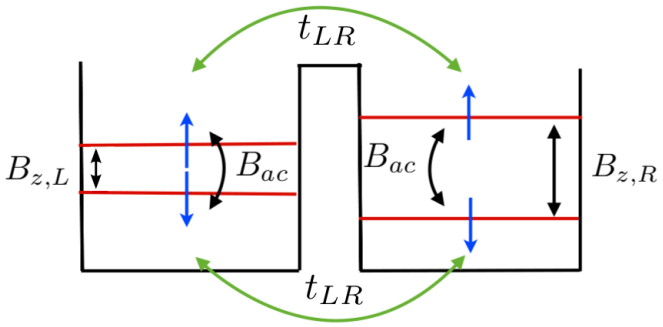

Figure 3.1.1: Double quantum dot with crossed AC and DC magnetic fields $\mathbf{B}_i(t) = (B_{ac,i}(t), 0, B_{z,i})$, where $i = L, R$. The Zeeman splitting in the left and right dot is given by $B_{z,L}$ and $B_{z,R}$, respectively. The spin independent tunneling between dots is given by t_{LR}.

the AC field time correlations between dots. Thus, the phase difference creates an spatial asymmetry which can be also produced by different methods, as for example tuning the quantum dots g-factors[37], or by Overhauser fields via hyperfine interaction[38]. In what follows we consider just asymmetries between the dots in the Zeeman splitting, and in the phase difference $\phi = \phi_L - \phi_R$. Note that the phase difference ϕ could arise naturally when the wavelength of the magnetic field becomes comparable to the distance between dots – in this case the magnetic field would have a spatial dependence $B_{ac}(x,t)$. Figure 3.1.2 shows the different field configurations studied below, where the AC magnetic field in each dot is in phase ($\phi = 0$), or in phase opposition ($\phi = \pi$). The green arrows represent the magnetic field direction of the AC field at each dot, for a given instant of time. In previous works, it has

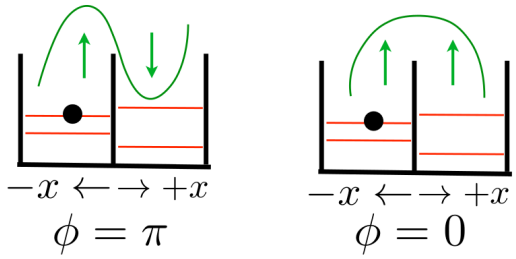

Figure 3.1.2: Different field configurations for phase differences $\phi = 0, \pi$. Left figure can be also thought as a magnetic field with half the wavelength than the one on the right. The green arrows illustrate the direction of the AC field at some fixed time. The case $\phi = \pi$ (left) shows a system which is invariant under generalized parity symmetry, while $\phi = 0$ (right) shows the case invariant under parity symmetry.

been shown that certain discrete $\mathbb{Z}_2$ symmetry conditions the existence of coherent destruction of tunneling[39, 40]. This is called *generalized parity symmetry* (GPS),

and consists in the inversion of the spatial coordinate and the evolution over a semi-period: $\{\mathbf{x}, t\} \rightarrow \{-\mathbf{x}, t + T/2\}$. This parity like operator labels the different states as even or odd, and following the Wigner-Von Neumann theorem, its existence allows crossings between quasi-energies with different symmetry[41]. Interestingly, *generalized parity symmetry can be thought as a natural extension of the parity symmetry defined in the initial Hilbert space, to the parity symmetry defined in the Sambe space.*

For the sake of clarity let us first consider symmetrical Zeeman splittings. In Figure 3.1.2 (left), it is shown that the effect of the parity symmetry operation is to move the particle from the left to the right at some fixed time. Thus, the phase difference makes the electron *feel* an opposite AC field and just if the evolution over a semi-period is included, the system remains invariant – i.e., it is invariant under GPS. On the other hand, in the right plot the system is parity invariant because the AC field is spatially homogeneous.

In general, if we apply the generalized parity symmetry operation to Equation 3.1.1, the system remains invariant for: $B_{z,L} = B_{z,R}$, $B_{ac,L} = B_{ac,R}$, $\epsilon_{g,L} = \epsilon_{g,R}$ and $\phi = \phi_R - \phi_L = \pi$ (in what follows we fix $\epsilon_{g,L} = \epsilon_{g,R} = 0$ for simplicity). Moreover, we can define another $\mathbb{Z}_2$ symmetry within a single dot if we flip the spins and evolve over a semi-period: $\{|\uparrow\rangle \leftrightarrow |\downarrow\rangle, t \rightarrow t+T/2\}$, this is an internal $\mathbb{Z}_2$ symmetry of the single dot Hamiltonian. We call this $\mathbb{Z}_2$ symmetry *generalized spin parity* (GSP)[1].

Note that although the case with $\phi = 0$ is not invariant under GPS, the Hamiltonian is parity invariant. Therefore, the difference of the phase parameter determines if the symmetry of the system corresponds to a parity invariant ($\phi = 0$) or to a GPS invariant ($\phi = \pi$) Hamiltonian. We will see below that degeneracies of the quasi-energies with opposite GPS gives rise to CDT, and degeneracies of quasi-energies with opposite GSP result in spin locking, where the spin projection is fixed in time.

Results:

As we discussed in Chapter 2, the present configuration with linear polarization is not analytically solvable. Thus, we shall use numerical methods and perturbation theory in the high frequency limit [40], considering the Zeeman splitting and the tunneling as the perturbation (up to first order), both in the same footing. By high frequency limit we mean that the quantum dots energy scales must fulfill $\omega \gg t_{LR}, B_z$. The following analytical expressions for the quasi-energies are obtained using the interaction picture described in the previous chapter (Equation 2.1.44), and the time evolution of the electronic states is obtained numerically.

Figure 3.1.3 (left) shows the quasi-energy spectrum in the high frequency limit with symmetric Zeeman splittings $B_{z,L} = B_{z,R}$ and $\phi = \pi$. The parameters considered

[1]This intrinsic $\mathbb{Z}_2$ symmetry is equivalent to the GPS of double well potentials driven by AC electric fields in[40, 39].

are of the order of those typical for transport experiments in QDs [42]. The corresponding quasi-energies obtained in perturbation theory are:

$$\varepsilon_{s,s'} = \frac{1}{2}\left(sB_z + s'2t_{LR}\right) J_0\left(\frac{B_{ac}}{\omega}\right), \quad (s, s' = \pm), \tag{3.1.6}$$

where $s^{(\prime)}$are referred to each parity symmetry (generalized spin parity and generalized parity symmetry respectively). The crossings of all the quasi-energies, according

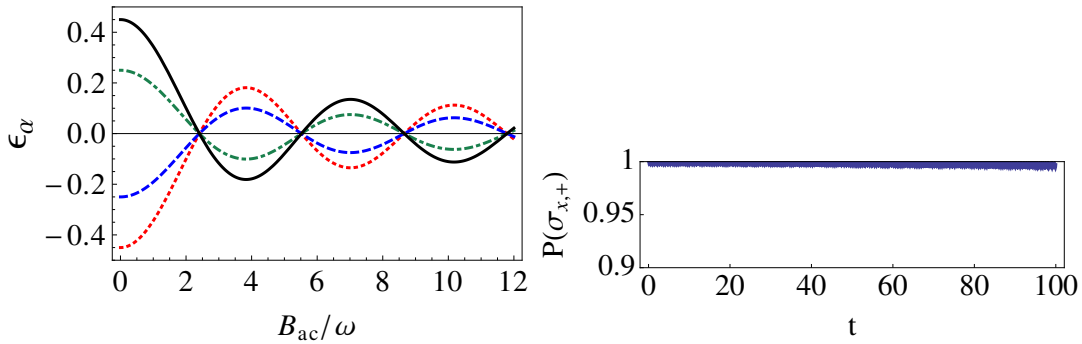

Figure 3.1.3: (Left) Quasi-energies vs B_{ac}/ω for $\phi = \pi$. The crossings of all the quasi-energies are allowed by the existence of the two $\mathbb{Z}_2$ symmetries. (Right) Occupation probability vs time for the initial state $|\Psi^L_{x,+}\rangle = (|\uparrow\rangle_L + |\downarrow\rangle_L)/\sqrt{2}$, at the first crossing of the quasi-energies ($B_{ac}/\omega \simeq 2.404$). The electron remains in a well defined spin projection and spatially localized at the left dot. Parameters: $B_{z,L} = B_{z,R} = 0.7$, $\omega = 8$ and $t_{LR} = 0.1$ in units $\mu_B = \hbar = 1$. This parameters correspond to a $\omega = 16\mu$eV, $B_z = 1.4\mu$eV and $t_{LR} = 0.2\mu$eV.

to the Wigner-Von Neumann theorem[41], are related to quasi-energies that belong to different symmetry groups. This fact allows the classification of the quasi-energies in terms of a $\mathbb{Z}_2 \otimes \mathbb{Z}_2$ symmetry group (GSP and GPS), where all the Floquet states are orthogonal to each other. Both coherent destruction of tunneling and dynamical spin locking have been found in this configuration (Figure 3.1.3, right) for frequency and intensity values such that $J_0\left(B_{ac}/\omega\right) = 0$ (Equation 3.1.6). Crossings between quasi-energies with opposite GPS result in charge localization at the left or at the right dot, while crossings between quasi-energies with opposite GSP result in dynamical spin locking[2]. Obviously, points where the quasi-energies vanish are those in which both, the tunneling and the Zeeman splitting are renormalized to zero.

If we instead consider that $\phi = 0$, the quasi-energy spectrum changes, and the multiple crossings vanish as a consequence of the Wigner Von-Neumann theorem (Figure 3.1.4). The numerical calculation of the occupation probabilities shows that charge localization does not occur in this case, but dynamically induced spin locking

[2]These states are localized in eigenstates of the σ_x matrix because the effective time-independent Hamiltonian in high frequency is obtained in the interaction picture after a rotation $\propto e^{i\int H^B_{ac}(t_1)dt_1}$. In conclusion, by tuning the AC field direction it is possible to select the locking direction.

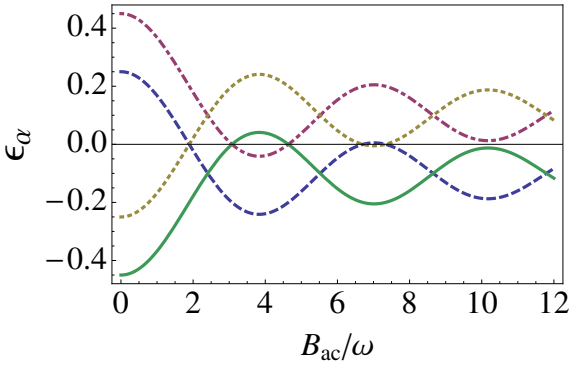

Figure 3.1.4: Quasi-energies vs B_{ac}/ω for $\phi = 0$. Crossings between quasi-energies with opposite GSP remain, but the quasi-energies with opposite parity now have a $2t_{LR}$ splitting due to the lack of GPS. In consequence, charge localization is not found and the electron performs Rabi oscillations between $|\Psi^L_{x,+}\rangle$ and $|\Psi^R_{x,+}\rangle$ (left and right dot) conserving the initial spin projection. Parameters: $B_{z,L} = B_{z,R} = 0.7$, $\omega = 8$ and $t_{LR} = 1/10$.

is found. These results indicate that CDT strongly depends on the spatial anisotropy induced by the phase difference ϕ, while spin locking does not. Moreover, charge localization is found just when the generalized parity symmetry is present.

Now we consider a spatial inhomogeneity for the Zeeman splittings ($B_{z,L} \neq B_{z,R}$), such that both parity and generalized parity symmetry are broken. As expected, it results in avoided crossings between the quasi-energies that previously had opposite generalized parity symmetry. The quasi-energies for arbitrary Zeeman splittings and phase difference ϕ can be obtained by means of perturbation theory:

$$\begin{aligned}\varepsilon_{i,j} &= \pm\frac{1}{2}\frac{B_{z,L}+B_{z,R}}{2}J_0\left(\frac{B_{ac}}{\omega}\right) \\ &\pm\frac{1}{2}\sqrt{\Delta_Z^2 J_0^2\left(\frac{B_{ac}}{\omega}\right)+\left(2t_{LR}\right)^2 J_0^2\left(\frac{B_{ac}}{\omega}\sin\left(\phi/2\right)\right)},\end{aligned} \tag{3.1.7}$$

where the indices $i, j = \pm, \pm$ label the parity according to each symmetry group (i refers to GPS, which is present if $B_{z,L} = B_{z,R}$, and j refers to the GSP), and $\Delta_Z = (B_{z,L} - B_{z,R})/2$. In order to analyze the ϕ dependence at fixed intensity, we consider the set of states $|\Psi^{L,R}_{x,\pm}\rangle = (|\uparrow\rangle_{L,R} \pm |\downarrow\rangle_{L,R})/\sqrt{2}$ and define the measure P^k_{min}, which characterizes the minimum of the occupation probability over one hundred periods to be in either the initial state $|\Psi^L_{x,+}\rangle$ ($k = 1$), the left dot ($k = 2$), or at the initial spin state projection, delocalized between the left and right dot ($k = 3$), when the system time evolves from the initial state. It can be formally defined as:

$$P^k_{min} = \min\left\{\sum_i \left|\langle\Psi^i_k|U\left(t,0\right)|\Psi^L_{x,+}\rangle\right|^2,\ t\in[0,100T]\right\}, \tag{3.1.8}$$

where $U(t,0)$ is the time evolution operator numerically obtained from the Floquet states and i labels the number of states in the subspace in which the measure projects. For example, the case $k=1$ projects into the initial state and this is coincident with the projection subspace, then $k=1 \to i=1$ where $|\Psi_1^1\rangle = |\Psi_{x,+}^L\rangle$. For the case $k=2$ we measure the probability to remain at the initial dot, and as it contains two spin projections, the subspace of projection contains these two states which are given by $|\Psi_2^{1,2}\rangle = |\Psi_{x,\pm}^L\rangle$. Finally, for the case $k=3$ we measure the locking of the initial spin projection which requires to consider the two states $|\Psi_3^{1,2}\rangle = |\Psi_{x,+}^{L,R}\rangle$, delocalized between the dots but with the same spin projection. In Figure 3.1.5 we show the measure P_{min}^k as a function of the phase difference ϕ between the two dots. It shows how spatial localization is destroyed as GPS is broken by the tuning of ϕ, while the spin locking is not affected. Importantly, in

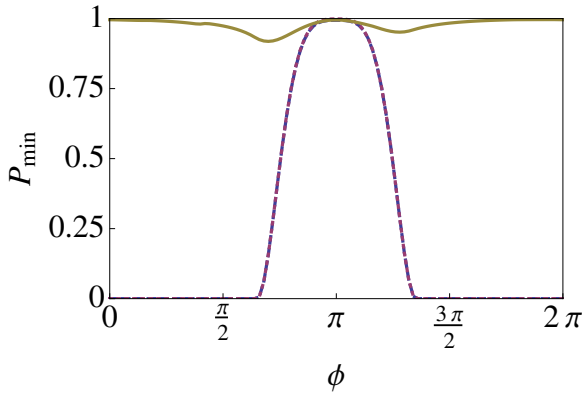

Figure 3.1.5: P_{min}^k vs ϕ for the first zero of $J_0(B_{ac}/\omega)$. Dashed red line shows initial state localization P_{min}^1, dotted blue line shows the spatial localization P_{min}^2, while the continuous brown line shows the spin locking P_{min}^3. For this case P_{min}^1 and P_{min}^2 are coincident. As the phase ϕ moves away from π, $P_{min}^{k=1,2}$ decreases, even destroying spatial localization. Spin locking P_{min}^3 holds for all ϕ because, although GPS symmetry is broken as ϕ varies from π, generalized spin parity remains invariant. Parameters: $\omega = 8$, $B_{z,L} = B_{z,R} = 0.7$, and $t_{LR} = 1/10$.

Equation 3.1.7 the Bessel functions have different arguments due to the phase difference ϕ. In consequence, their zeros shift and they match again for intensity values where $J_0(B_{ac}/\omega) = J_0(B_{ac}\sin(\phi/2)/\omega) = 0$. At these values of the field amplitude the spin locking and charge localization are recovered. Using an asymptotic expansion for the Bessel functions we find that for $B_{ac} > \omega > t_{LR}, B_z$ these values are given by:

$$\frac{B_{ac}}{\omega} = \frac{\pi(4n-1)}{4\sin(\phi/2)},\ n \in \mathbb{Z}^+. \tag{3.1.9}$$

Where we have used the asymptotic limit $J_0(x) \underset{x\gg 1}{\sim} \sqrt{2/(\pi x)}\sin(x+\pi/4)$. The case $n=2$ is shown in Figure 3.1.6 for $B_{ac}/\omega \simeq 8.8$.

In general, for the case $\phi \neq 0, \pi$ we can also consider nearby avoided crossings

between quasi-energies, which can happen at different positions than the zeros of $J_0\left(B_{ac}/\omega\right)$ – the inset in Figure 3.1.6, shows the avoided crossing between $\varepsilon_{+,\pm}$ and $\varepsilon_{-,\pm}$. At these points, although full spatial localization does not happen due to the small splitting between quasi-energies, the dynamics become almost frozen and for short time intervals it can be considered as charge localization regime – Figure 3.1.5 can be also interpreted as a measure of charge and spin localization vs quasi-energies splitting. In Figure 3.1.6 we show a quasi-energy spectrum for $\phi = 3\pi/7$ in which a

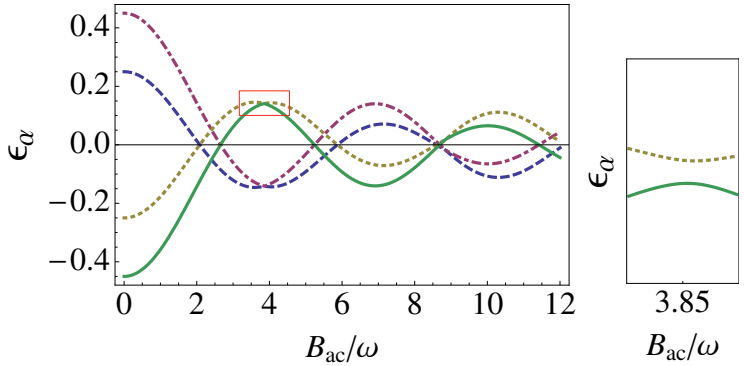

Figure 3.1.6: Quasi-energies vs B_{ac}/ω for $\phi = 3\pi/7$. The avoided crossings are due to the phase difference $\phi \neq \pi$. There, long time spatial localization is found at for example $B_{ac}/\omega = 3.85$ due to the nearby degeneracy. At $B_{ac} \simeq 5.5$ the crossing of quasi-energies gives rise to dynamically induced spin locking. For $B_{ac} \simeq 8.8$ CDT and spin locking are obtained due to the nearby degeneracy between all four quasi-energies. This is in good agreement with Equation 3.1.9 for $n = 2$. Parameters: $B_{z,L} = B_{z,R} = 0.7$, and $t_{LR} = 1/10$. Right figure shows a zoom of the avoided crossing.

tuning of the field intensity allows to switch between spatial localization ($B_{ac}/\omega \simeq 3.8$), dynamical spin locking ($B_{ac}/\omega \simeq 5.5$) and both ($B_{ac}/\omega \simeq 8.8$). The values for the measures P_k at the avoided crossings in Figure 3.1.6 for $B_{ac}/\omega \simeq 3.8$ are: $P^2_{min} = 0.98$ and $P^3_{min} = 0$, confirming the effective charge localization at the avoided crossings.

According to these results, driving DQDs with AC magnetic fields at high frequency regime allows to independently obtain charge localization and dynamical spin locking. In particular, modifying the intensity or the phase difference of the AC magnetic fields it is possible to select spatial localization, dynamical spin locking or both regimes simultaneously, giving rise to a coherent control of the electronic states. In fact, small changes of frequency – constrained to $\omega \gg B_z, t_{LR}$ – can be used to modify the wavelength of the AC field and the corresponding phase difference ϕ between the dots. This can be used to tune the difference of phase of the AC magnetic fields between spatially separated dots.

3.2 Transport properties of non-equilibrium quantum systems

Here we address the problem of charge transport through a system periodically driven out of equilibrium by means of AC fields. This is an important issue in the solid state community, because transport is one of the main methods used to obtain information from the system. On the other hand, out of equilibrium systems are difficult to characterize, since the electrons does not follow the usual distributions functions of equilibrium systems. The results obtained in this section will allow us to characterize and understand the population of Floquet states, as well as the charge localization in double quantum dots.

3.2.1 Periodically driven systems coupled to leads

When a quantum system is driven out of equilibrium, and we are interested in observables such as the current through the system, the calculation is far from being trivial. The main problems arise from the fact that in a closed system which is periodically driven, energy is ill defined. It means that in general, a Fermi level cannot be defined as in static systems. Nevertheless, if the system is coupled to leads, and these are unaffected by the periodic driving, they will fix the energy of the incoming electrons. Thus, a relation between the initial energy of the electrons, the processes within the periodically driven system – where the electrons can interact with the AC field – and the outgoing electrons can be stablished. In order to address this question, we describe in density matrix formalism the transport equations for a system out of equilibrium, coupled to contacts. We shall follow previous works [22, 21], considering the Liouville equation for the density matrix and weak coupling with the leads. The reduced density matrix is obtained by tracing out the bath degrees of freedom. For an adequate analytical approach we require an approximate factorization of the density matrix between bath and system[43], and the Markov approximation – no memory effects in the bath. Therefore, the density matrix of the leads can be described by a fermionic thermodynamical ensemble in equilibrium.

A quantum system, interacting with an external magnetic field and coupled to metallic reservoirs, can be described by the next Hamiltonian:

$$\begin{aligned} H(t) &= H_S(t) + \sum_{i,\sigma,K} \left(\Upsilon_{i\sigma} b_{i\sigma K} d^{\dagger}_{i\sigma} + h.c. \right) + \sum_{i,\sigma,K} \gamma_{i\sigma K} b^{\dagger}_{i\sigma K} b_{i\sigma K} \\ &= H_S(t) + V + H_B \end{aligned} \tag{3.2.1}$$

where $H_S(t)$ corresponds to the closed system interacting with the AC magnetic field, V takes in account the coupling with the environment – in our case tunneling to metallic leads – and H_B describes the leads as a set fermions with spin σ, K momentum, and energy $\gamma_{i\sigma K}$ (in general the energy of the level K can depend on

the lead position, spin projection σ and K). The operator $b_{i\sigma K}$ annihilates a fermion in the i-th lead with K momentum and spin σ, and the operator $d_{i\sigma}$ annihilates an electron in the i-th quantum dot with spin projection σ. The tunneling coefficients $\Upsilon_{i\sigma}$ can depend on the lead position i, and on the spin projection σ.

In order to find the master equation for the reduced density matrix we make use of the interaction picture, which allow us to easily study the coupling between system and leads. The density matrix for the whole system is given by:

$$\begin{aligned} \rho(t) &= \mid \Psi(t)\rangle\langle\Psi(t) \mid & (3.2.2)\\ \mid \Psi(t)\rangle &\equiv U(t,t_0) \mid \Psi(t_0)\rangle, & (3.2.3)\end{aligned}$$

where $U(t,t_0)$ is the time propagator. The transformation to the interaction picture for a state $\mid \Psi(t)\rangle$ and an observable A is :

$$\begin{aligned} \mid \tilde{\Psi}(t)\rangle &= e^{i\int H_0(t)dt+iH_Bt} \mid \Psi(t)\rangle & (3.2.4)\\ \tilde{A}(t,t_0) &= e^{i\int_{t_0}^{t} H_0(t)dt+iH_B(t-t_0)} A e^{-i\int_{t_0}^{t} H_0(t)dt-iH_B(t-t_0)} & (3.2.5)\\ &= U_0^{\dagger}(t,t_0)\, A U_0(t,t_0) = U_S^{\dagger}(t,t_0)\, U_B^{\dagger}(t,t_0)\, A U_B(t,t_0)\, U_S(t,t_0). \end{aligned}$$

where we have defined $U_0(t,t_0) \equiv e^{-i\int_{t_0}^{t} H_0(t)dt-iH_B(t-t_0)}$, $U_S(t,t_0) \equiv e^{-i\int_{t_0}^{t} H_0(t)dt}$, and $U_B(t,t_0) \equiv e^{-iH_B(t-t_0)}$, as the two Hamiltonians $H_0(t)$ and H_B commute. The time evolution of the density matrix in the interaction picture is obtained from the quantum Liouville equation in the initial frame:

$$\begin{aligned} \rho(t) &= U_0(t,t_0)\,\tilde{\rho}(t)\,U_0^{\dagger}(t,t_0), & (3.2.6)\\ i\dot{\tilde{\rho}}(t) &= \left[\tilde{V}(t,t_0), \tilde{\rho}(t)\right]. & (3.2.7)\end{aligned}$$

Integrating the last equation we obtain the recurrence relation:

$$\tilde{\rho}(t) = \tilde{\rho}(t_0) - i\int_{t_0}^{t} dt' \left[\tilde{V}(t',t_0), \tilde{\rho}(t')\right], \tag{3.2.8}$$

which depends on the system at intermediate times t'. Iteratively up to second order the solution is:

$$\begin{aligned} i\dot{\tilde{\rho}}(t) &= \left[\tilde{V}(t,t_0), \tilde{\rho}(t_0) - i\int_{0}^{t} dt' \left[\tilde{V}(t',t_0), \tilde{\rho}(t')\right]\right] & (3.2.9)\\ &= \left[\tilde{V}(t,t_0), \tilde{\rho}(t_0)\right] - i\int_{t_0}^{t} dt' \left[\tilde{V}(t,t_0), \left[\tilde{V}(t',t_0), \tilde{\rho}(t')\right]\right] \end{aligned}$$

$$\dot{\tilde{\rho}}(t) = -i \left[\tilde{V}(t,t_0), \tilde{\rho}(t_0)\right] - \int_{t_0}^{t} dt' \left[\tilde{V}(t,t_0), \left[\tilde{V}(t',t_0), \tilde{\rho}(t')\right]\right] \tag{3.2.10}$$

We now assume the Born-Markov approximation, in which $\tilde{\rho}(t') \simeq \tilde{\rho}(t)$. Then, the evolution of the density matrix only depends on its present value, and memory

effects are neglected. In addition, we consider that the coupling Hamiltonian V is off-diagonal in the bath operators. Thus, the first commutator of Equation 3.2.10 vanishes when we trace out the bath degrees of freedom[3]. Finally, we perform a change of variables: $t' = t - \tau \rightarrow d\tau = -dt'$, such that the integration limits become $\int_{t_0}^{t} dt' \rightarrow \int_{0}^{t-t_0} d\tau$ (it allows to rewrite the expressions in terms of time differences rather than absolute times). The commutator can be expressed in the Schrödinger picture as:

$$\left[\tilde{V}\left(t', t_0\right), \tilde{\rho}\left(t\right)\right] = \left[U_0^{\dagger}\left(t', t_0\right) V U_0\left(t', t_0\right), U_0^{\dagger}\left(t, t_0\right) \rho\left(t\right) U_0\left(t, t_0\right)\right]. \quad (3.2.11)$$

Expanding $\left[\tilde{V}\left(t, t_0\right), \left[\tilde{V}\left(t-\tau, t_0\right), \tilde{\rho}\left(t\right)\right]\right]$ and using $U\left(t, t'\right) U\left(t', t_0\right) = U\left(t, t_0\right)$ and $U\left(t, t'\right) = U^{\dagger}\left(t', t\right)$, we finally arrive to:

$$\dot{\rho}\left(t\right) + i\left[H_S\left(t\right) + H_B, \rho\left(t\right)\right] = -\int_0^{t-t_0} d\tau \left\{\left[V, \tilde{V}\left(t-\tau, t\right)\rho\left(t\right)\right] + \left[\rho\left(t\right)\tilde{V}\left(t-\tau, t\right), V\right]\right\}. \quad (3.2.12)$$

At this point, we can approximate the upper limit for the integral by infinity – implies that the decay time τ_c for the bath correlations is shorter than the evolution of the density matrix. Finally, in order to obtain the reduced density matrix, we have to trace out the bath degrees of freedom, leading to:

$$\begin{aligned} \dot{\rho}_S\left(t\right) + i\left[H_S\left(t\right), \rho_s\left(t\right)\right] &= -\int_0^{\infty} \{\mathrm{Tr}_B\left[V, \tilde{V}\left(t-\tau, t\right)\rho_s\left(t\right) \otimes \rho_B\right] \\ &\quad + \mathrm{Tr}_B\left[\rho_s\left(t\right) \otimes \rho_B \tilde{V}\left(t-\tau, t\right), V\right]\} d\tau, \quad (3.2.13) \end{aligned}$$

where we have chosen the Feynman-Vernon initial condition for the density matrix[43] – i.e., bath and system initially uncorrelated $\rho\left(0\right) = \rho_s\left(0\right) \otimes \rho_B$ – and that the reservoirs are larger than the system and hence their state is unchanged in time due to the interactions with the central system. In addition, note that the left hand side of Equation 3.2.13 does not contain the bath Hamiltonian within the commutator. The reason is that we have assumed an off-diagonal tunnel Hamiltonian in the bath operators, and then, the trace over the reservoirs degrees of freedom gives zero value (this is proved in Appendix A).

Up to this point, the treatment is the standard one for density matrix formalism. However, we now describe how to deal with the time dependence of the density matrix rates and we express the master equation in Floquet basis.

If we consider the right hand of Equation 3.2.13, the elements of the commutator which are affected by the trace can be written as two different terms:

$$G_1\left(t-\tau, t\right) = \sum_{j,l,K,K'} Tr_B\left\{F_{j,K}\tilde{F}_{l,K'}\left(t-\tau, t\right)\rho_B\right\}, \quad (3.2.14)$$

$$G_2\left(t-\tau, t\right) = \sum_{j,l,K,K'} Tr_B\left\{\tilde{F}_{l,K'}\left(t-\tau, t\right)F_{j,K}\rho_B\right\}, \quad (3.2.15)$$

[3]Note that if the coupling Hamiltonian contains some diagonal elements these can be introduced in H_B.

which fulfill $G_2(t-\tau) = G_1^*(t-\tau)$, being $j,l = (\sigma, i, p)$ a multi-index, where $p = 1,2$ labels if the operator creates or annihilates a particle respectively, σ labels the spin degree of freedom and i the additional degrees of freedom characterizing the central system properties. These are called thermal coefficients, as they contain information of the thermodynamical properties of the reservoirs.

Then, the master equation for the reduced density matrix can be written in a more compact form as:

$$\begin{aligned}\dot{\rho}_S(t) + i\left[H_S(t), \rho_s(t)\right] &= -\int_0^\infty d\tau \sum_{j,l,K,K'} G_1(t-\tau,t)\left[Q_j, \tilde{Q}_l(t-\tau,t)\,\rho_s(t)\right] \\ &\quad -\int_0^\infty d\tau \sum_{j,l,K,K'} G_1^*(t-\tau,t)\left[\rho_s(t)\,\tilde{Q}_l(t-\tau,t), Q_j\right],\end{aligned}$$

where $\tilde{F}_j(t,t_0) = U_B(t-t_0)^\dagger F_{j,K} U_B(t-t_0)$, and $\tilde{Q}_j(t,t_0) = U_S(t-t_0)^\dagger Q_j U_S(t-t_0)$.

Finally, if we choose the Floquet basis $\{|\phi_\alpha(t)\rangle\}$ for the representation of the reduced density matrix and expand in Fourier series the time dependence of the master equation rates (and integrate in τ), we arrive at the full master equation in Floquet basis (all the details of the calculation are in Appendix A):

$$\begin{aligned}(\partial_t + i\varepsilon_{\alpha\beta})\,\rho(t)_{\alpha\beta} &= -\sum_{jl,\mu\nu,nm} e^{-i\omega t(n+m)} \sum_{K,K'} \\ &\quad \times\{g_1(m\omega - \varepsilon_{\mu\nu})\,\rho(t)_{\nu\beta}\,Q(n)_{j,\alpha\mu}\,Q(m)_{l,\mu\nu} \\ &\quad -g_1(m\omega - \varepsilon_{\alpha\mu})\,\rho(t)_{\mu\nu}\,Q(n)_{j,\nu\beta}\,Q(m)_{l,\alpha\mu} \\ &\quad +g_1^*(m\omega - \varepsilon_{\mu\nu})\,\rho(t)_{\alpha\mu}\,Q(n)_{j,\nu\beta}\,Q(m)_{l,\mu\nu} \\ &\quad -g_1^*(m\omega - \varepsilon_{\nu\beta})\,\rho(t)_{\mu\nu}\,Q(n)_{j,\alpha\mu}\,Q(m)_{l,\nu\beta}\},\end{aligned} \tag{3.2.16}$$

where $Q(n)_{j,\mu\nu}$ is the n-th coefficient of the Fourier series expansion of $Q(t)_{j,\mu\nu} = \langle\phi_\mu(t)|Q(t)_j|\phi_\nu(t)\rangle$, greek indexes label Floquet states, and $g_1^{(*)}(m\omega - \epsilon_{\mu\nu})$ label the thermal coefficients:

$$\begin{aligned}g_1(m\omega - \varepsilon_{\mu\nu}) &= \pi \sum_{K,K'} \sum_{|K''\rangle} |\langle i''K''\sigma''|N_{\sigma'p'i',K'}|i''K''\sigma''\rangle| e^{-\beta(E_{K''}-\mu_{i''})} \\ &\quad \times\delta_{K,K'}\delta_{\sigma,\sigma'}\delta_{i,i'}(1-\delta_{p,p'})\,\delta(m\omega - \varepsilon_{\mu\nu} + E_{K''} - E_{K^{(3)}}),\end{aligned} \tag{3.2.17}$$

$$\begin{aligned}g_1^*(m\omega - \varepsilon_{\mu\nu}) &= \pi \sum_{K,K'} \sum_{|K''\rangle} |\langle i''K''\sigma''|N_{\sigma,p,i,K}|i''K''\sigma''\rangle| e^{-\beta(E_{K''}-\mu_{i''})} \\ &\quad \times\delta_{K,K'}\delta_{\sigma,\sigma'}\delta_{i,i'}(1-\delta_{p,p'})\,\delta(m\omega - \varepsilon_{\mu\nu} - E_{K''} + E_{K^{(3)}}).\end{aligned} \tag{3.2.18}$$

Note that both thermal coefficients $g_1^{(*)}$ are real functions, and we keep the superscript * just to differentiate between the two functions. Importantly, Equation 3.2.16 resembles the master equation of a time independent system with an important difference, ***the Fermi-Dirac distributions are in this case weighted by all the harmonics of the field*** $m\omega$. This is the main difference with undriven systems.

3.2.2 Transport in double quantum dots:

Now let us consider the case of a double quantum dot coupled to two leads. For this system, the multi-index notation introduced above becomes: $i = L, R$, $\sigma = \uparrow, \downarrow$ and $p = 1, 2$, and the coupling to the leads is described by the next Hamiltonian term:

$$\begin{aligned} V &= \Upsilon \sum_{i,\sigma,K} \left(b^{\dagger}_{\sigma,i,K} d_{\sigma,i} + d^{\dagger}_{\sigma,i} b_{\sigma,i,K} \right) \\ &= \Upsilon \sum_{i,\sigma,K} \left(b^{\dagger}_{\sigma,i,K} d_{\sigma,i} - b_{\sigma,i,K} d^{\dagger}_{\sigma,i} \right) \\ &= \Upsilon \sum_{i,\sigma,K,p} F_{p,\sigma,i,K} Q_{p,\sigma,i} \end{aligned} \tag{3.2.19}$$

where Υ represents a constant hopping to the leads, which for simplicity, we have assumed independent of the spin projection, lead position, and momentum of the incoming electron K. The index i is referred to the left/right lead, such that in our notation:

$$Q_{1,\sigma,i} = d_{\sigma,i},\ Q_{2,\sigma,i} = -d^{\dagger}_{\sigma,i},\ F_{1,i,\sigma,K} = b^{\dagger}_{\sigma,i,K},\ F_{2,i,\sigma,K} = b_{\sigma,i,K}\ . \tag{3.2.20}$$

Then, the number of particles operator in the leads are in this notation:

$$N_{p\sigma iK} = F^{\dagger}_{p\sigma iK} F_{p\sigma iK} = \begin{cases} p = 1 \rightarrow & N_{1,\sigma iK} = b_{\sigma iK} b^{\dagger}_{\sigma iK} = n_{\sigma iK} \\ p = 2 \rightarrow & N_{2,\sigma iK} = b^{\dagger}_{\sigma iK} b_{\sigma iK} = 1 - n_{\sigma iK} \end{cases} \tag{3.2.21}$$

and the energy differences $E_{K''} - E_{K^{(3)}}$ and thermal coefficients are:

$$\begin{aligned} g_1 \left(m\omega - \varepsilon_{\mu\nu} \right)_{p=1} &= \pi \sum_K |\langle iK\sigma | 1 - n_{\sigma,i,K} | iK\sigma \rangle| e^{-\beta(E_K - \mu_i)} \delta \left(m\omega - \varepsilon_{\mu\nu} - E_K \right), \\ g_1^{*} \left(m\omega - \varepsilon_{\mu\nu} \right)_{p=1} &= \pi \sum_K |\langle iK\sigma | n_{\sigma,i,K} | iK\sigma \rangle| e^{-\beta(E_K - \mu_i)} \delta \left(m\omega - \varepsilon_{\mu\nu} - E_K \right), \\ g_1 \left(m\omega - \varepsilon_{\mu\nu} \right)_{p=2} &= \pi \sum_K |\langle iK\sigma | n_{\sigma,i,K} | iK\sigma \rangle| e^{-\beta(E_K - \mu_i)} \delta \left(m\omega - \varepsilon_{\mu\nu} + E_K \right), \\ g_1^{*} \left(m\omega - \varepsilon_{\mu\nu} \right)_{p=2} &= \pi \sum_K |\langle iK\sigma | 1 - n_{\sigma,i,K} | iK\sigma \rangle| e^{-\beta(E_K - \mu_i)} \delta \left(m\omega - \varepsilon_{\mu\nu} + E_K \right). \end{aligned}$$

The sum in K can be reduced to an integral in energy multiplying by the density of states at each lead (we consider the density of states constant in our regime):

$$\begin{aligned} g_1 \left(m\omega - \varepsilon_{\mu\nu} \right)_{p=1,i} &= \pi \int_{-\infty}^{+\infty} dE_{K,i} D\left(E_{K,i} \right) |\langle iK\sigma | 1 - n_{\sigma,i,K} | iK\sigma \rangle| \\ &\quad \times e^{-\beta(E_K - \mu_i)} \delta \left(m\omega - \varepsilon_{\mu\nu} - E_K \right) \\ &= \pi D\left(E_{K,i} \right) \left(1 - n_F \left(m\omega - \varepsilon_{\mu\nu} - \mu_i \right) \right) \qquad (3.2.22) \\ &= g_1^{*} \left(m\omega - \varepsilon_{\mu\nu} \right)_{p=2,i} \qquad (3.2.23) \end{aligned}$$

$$g_1^* \left(m\omega - \varepsilon_{\mu\nu}\right)_{p=1,i} = \pi D\left(E_{K,i}\right) n_F\left(m\omega - \varepsilon_{\mu\nu} - \mu_i\right) \quad (3.2.24)$$

$$= g_1 \left(m\omega - \varepsilon_{\mu\nu}\right)_{p=2,i} \quad (3.2.25)$$

In consequence, the thermal coefficients are independent of the microscopic details of the leads (energy levels E_K), and for a given system, we can now plug all the parameters in Equation 3.2.16 in order to obtain the full master equation in Floquet basis.

Nevertheless, the full master equation is still very complicated, as it consists on a set differential equations, including an infinite sum over all Fourier harmonics $n, m \in (-\infty, \infty)$. Thus, a cutoff must be introduced in order to truncate these terms. The cutoff will be strongly dependent on the driving regime considered, as we prove next.

Including a cutoff in the master equation rates

The idea of the cutoff is to identify the dominant harmonics of the Fourier expansion depending on the regime we are interested in. For that purpose we consider a mathematical analysis of Floquet solutions following [22].

The solution for the density matrix of a system with periodic rates $R(t)$ can be written using the Floquet theorem. This ensures that the solution is of the form:

$$\rho_{ij}(t) = \sum_n a_n e^{\lambda_n t} r_{ij;n}(t) \quad (3.2.26)$$

with time-periodic functions $r_{ij;n}(t+T) = r_{ij;n}(t)$, and $e^{\lambda_n T}$ an eigenvalue of the time evolution operator for all density matrix elements over one period (λ_n is assumed to be here non-degenerate). *This solution is in general not periodic in time.* In our problem we are interested in solutions for large time scales, and because all solutions with $\Re(\lambda_n) < 0$ decay to zero in this limit, we are not interested on them. From the general properties of the density matrix, $0 \leq \rho_{ii} \leq 1$ and $|\rho_{ij}|^2 \leq \rho_{ii}\rho_{jj} \leq 1$, it follows that solutions with $\Re(\lambda_n) > 0$ are impossible. So we are left discussing solutions with $\Re(\lambda_n) = 0$ – note that the imaginary part $\Im(\lambda_n)$ can take any value.

For the trace of the density matrix to be 1, i.e., time independent and non-zero, $\lambda_0 = 0$ must be a solution. This is a stationary solution for the density matrix elements $\rho_{ij}(t) = r_{ij;0}(t)$, which is time periodic, and at least contains some diagonal components with non zero time average. If we now expand in Fourier series this solution:

$$\rho_{ij}(t) = \sum_K \rho_{ij}(K) e^{iK\omega t}, \quad (3.2.27)$$

and rewrite the periodic rates as $R_{\alpha\beta;\mu\nu}(t) = \sum_M e^{-iM\omega t} R_{\alpha\beta;\mu\nu}(M)$, we can write a master equation for each Fourier component as:

$$-i\left(K\omega + \varepsilon_{ij}\right)\rho_{ij}(K) = -\sum_{M,k,l} \left\{R^1_{ik;lk}(M)\,\rho_{lj}(K-M) + R^2_{lj;lk}(M)\,\rho_{ik}(K-M)\right\} + \sum_{M,k,l} \left(R^1_{lj;ki}(M) + R^2_{ik;jl}(M)\right)\rho_{kl}(K-M) \quad (3.2.28)$$

Now we must notice that in Equation 3.2.28, the right hand side is second order in the system-bath coupling constant Υ. As in the weak coupling regime $\omega \gg \Upsilon^2$, the left side of Equation 3.2.28 must be small as well. Thus, if $K \neq 0$ the density matrix components $\rho_{ij}\,(K \neq 0)$ must be also small. Therefore, it is consistent to neglect the components $\rho_{ij}\,(K \neq 0) \simeq 0$, and consider just $\rho_{ij}\,(K = 0)$, which is by definition time independent.

In order to identify the Equation 3.2.28 with Equation 3.2.16, we rewrite $R_{\alpha\beta;\mu\nu}\,(M)$ in terms of its matrix elements :

$$R_{\alpha\beta;\mu\nu}\,(M) = \Upsilon^2 \sum_{i,p,\sigma,m} Q\,(M+m)_{i\sigma p,\alpha\beta}\, Q\,(m)^*_{i\sigma p,\nu\mu}\, g_1^*\,(\varepsilon_{\nu\mu} - m\omega)_{p,i}\,,$$

where the index $M \equiv m + n$, and we have used $Q\,(-m) = Q\,(m)^*$.

Finally, note that if ρ_{ij} is time independent, as it is a function of the rates, it also implies that the rates $R^{1,2}_{ijkl}\,(M)$ must be time independent, i.e., $M = 0$. Then, they can be safely approximated by their time average.

Nevertheless, note that for a quasi-energies difference $\varepsilon_{ij} \approx \pm\omega$, the previous statement is not exactly correct and we must choose $K = \pm 1$ for this large quasi-energies difference – Otherwise $\rho_{i,j}$ does not have to be small. Although in the case of nearly degenerated quasi-energies, where coherent destruction of tunneling is found, is a correct assumption.

Thus, if the rates are time averaged their explicit expression is given by:

$$\begin{aligned}
R_{\alpha\beta;\mu\nu}\,(t) &\simeq R_{\alpha\beta;\mu\nu}\,(R=0)\,, && (3.2.29)\\
R^1_{\alpha\beta;\mu\nu}\,(0) &= \Upsilon^2 \sum_{i,p,\sigma,m} Q\,(m)_{i\sigma p,\alpha\beta}\, Q\,(m)^*_{i\sigma p,\mu\nu}\, g_1\,(\varepsilon_{\mu\nu} - m\omega)_{p,i}\,, && (3.2.30)\\
R^2_{\alpha\beta;\mu\nu}\,(0) &= \Upsilon^2 \sum_{i,p,\sigma,m} Q\,(m)_{i\sigma p,\alpha\beta}\, Q\,(m)^*_{i\sigma p,\mu\nu}\, g_1^*\,(\varepsilon_{\mu\nu} - m\omega)_{p,i}\,, && (3.2.31)
\end{aligned}$$

These set of assumptions allows to find the steady state solution of the system very easily:

$$i\varepsilon_{ij}\rho_{ij} = \sum_{k,l} \left\{ R^1_{ik;lk}\rho_{lj} + R^2_{lj;lk}\rho_{ik} - \left(R^1_{lj;ki} + R^2_{ik;jl} \right) \rho_{kl} \right\}. \qquad (3.2.32)$$

Further approximations can be assumed to study the system, as for example that the system-bath coupling Υ is very small compared with the quasi-energies splitting $\varepsilon_{\alpha\beta}$. Then the off-diagonal density matrix elements can be safely neglected and we end up with the density matrix master equation:

$$\begin{aligned}
0 &= \rho_{ii} \sum_k \left(R^1_{ik;ik} + R^2_{ki,ki} \right) - \sum_k \rho_{kk} \left(R^1_{ki;ki} + R^2_{ik;ik} \right) \\
&= \rho_{ii} \sum_k R^1_{ik;ik} - \sum_k \rho_{kk} R^1_{ki;ki}. && (3.2.33)
\end{aligned}$$

Importantly, note that these systems are described, in the steady state, by a master equation equivalent to the one of time independent systems. However, the rates $R^i_{jk,lr}$ contain a sum over all Fourier harmonics (see Equation 3.2.29), which can drastically change the system properties. The number of Fourier components

3.3 Analysis of a double quantum dot coupled to circularly polarized fields

In the first section, we have shown how linearly polarized AC magnetic fields can be used to achieve coherent destruction of tunneling and dynamical spin locking in a double quantum dot system. In order to address the question of how different field polarizations can modify the charge localization and the dynamical spin locking, we now consider a double quantum dot driven by circularly polarized magnetic fields. We will show that the circular polarization is able to induce charge localization () for arbitrary field intensity at electron spin resonance (ESR) configuration. This localization effect depends critically on the symmetries of the system and its appearance can also occur in larger size systems such as arrays of quantum dots, linear ions traps[44], optical lattices[45], and more generally, in tunnel coupled systems with a pseudo-spin degree of freedom. In addition, we perform the calculation of the current when the DQD when it is coupled to metallic leads, which allows to characterize the localization by means of a physical observable. The analysis of the open system is performed by means of the Density Matrix formalism described in the previous section, in the framework of Floquet theory [13]. We consider that

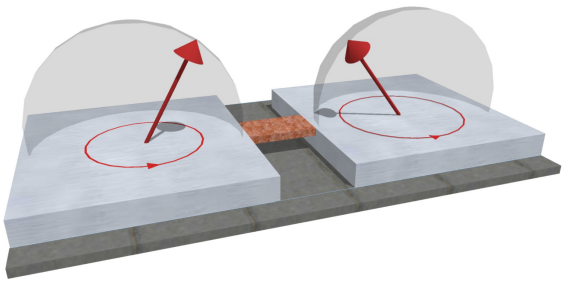

Figure 3.3.1: Schematic figure of a DQD coupled to circularly polarized magnetic fields oscillating in phase opposition

the double quantum dot is in strong Coulomb blockade regime, such that single electron occupancy is just allowed – as in the previous case with linearly polarized fields. We also include the metallic leads, which supply the electrons, in the system's description. The states spanning the Hilbert space of the double quantum dot are: $\{|\uparrow_L\rangle,\ |\downarrow_L\rangle,\ |\uparrow_R\rangle,\ |\downarrow_R\rangle, |0\rangle\}$, where now the empty state needs to be included in order to properly describe the transport. The AC magnetic fields

$\mathbf{B}^i = \left(B^i_x(t), B^i_y(t), B^i_z\right)$ couple to the electron's spin by magnetic dipole interaction $g\mu_B \mathbf{S}\cdot\mathbf{B}(t)$, where $i = L, R$. The Zeeman splitting can be different for each dot due to different g-factors, differences in the nuclei polarization or inhomogeneities in the applied field. Finally, the AC magnetic fields are circularly polarized: $B^i_x(t) = B^i_{ac,x}\cos(\omega t + \phi_i)$, $B^i_y(t) = B^i_{ac,y}\sin(\omega t + \phi_i)$, and both include a parameter ϕ_i characterizing the relative phase difference between them (Figure 3.3.1). The full Hamiltonian reads:

$$\begin{aligned} H(t) &= H_S(t) + H_B + V \\ H_S(t) &= H_0 + H^B_{ac}(t) + H^B_{dc} + H_{t_{LR}} \end{aligned} \tag{3.3.1}$$

where $H_0 = \sum_{i,\sigma}\epsilon_i d^\dagger_{\sigma,i} d_{\sigma,i}$ is the Hamiltonian for the i dot, $H^B_{ac}(t) = \sum_{i,\mu} B^i_{ac,\mu}(t,\phi_i) S_{\mu,i}$, $(\mu = x, y)$ is the coupling of the electronic spin with the external AC field, $H^B_{dc} = \sum_i B^i_z S_{z,i}$ is the Zeeman splitting at the i dot, and $H_{t_{LR}} = t_{LR}\sum_{\sigma,i\neq j} d^\dagger_{\sigma,j} d_{\sigma,i}$ is the inter-dot tunneling Hamiltonian ($\mu_B = g = \hbar = 1$). The bath Hamiltonian $H_B = \sum_{i,\sigma,K}\epsilon_{i,K} b^\dagger_{i,K,\sigma} b_{i,K,\sigma}$ represents the reservoirs with fermionic operators $b^\dagger_{i,K,\sigma}/b_{i,K,\sigma}$ for electrons with ϵ_K energy and K momentum. Finally, $V = \sum_{i,\sigma,K}\Upsilon\left(b^\dagger_{i,\sigma,K} d_{i,\sigma} + h.c.\right)$ weakly couples the double quantum dot with the reservoirs by means of a linear tunnel Hamiltonian.

Symmetries: Let us first analyze the symmetries defined in the double quantum dot. We study the parity symmetry $\Pi : \{x \to -x\}$ and the generalized parity symmetry $\Pi_T : \{x \to -x,\ t \to t + T/2\}$, which had play an important role in driven systems as we have shown for the linearly polarized case, and allows to classify the solutions according to $\mathbb{Z}_2$ groups[13]. Applying the parity transformation to Equation 3.3.1, we obtain the next condition for parity invariance: $B_{z,L} = B_{z,R}$, $\epsilon_L = \epsilon_R = 0$, $\phi = 0$, and $B^L_{ac,\mu} = B^R_{ac,\mu}$. Note that if we consider instead the generalized parity operation, an extra minus sign coming from the time dependent term shows up, leading to a non invariant Hamiltonian. To obtain Π_T invariance we must require $\phi = \phi_2 - \phi_1 = \pi$, i.e. a π difference of phase between the AC fields in each dot. Clearly, as in the linearly polarized case, the phase difference controls the existence of parity/GPS symmetry. First, we now fix the AC field amplitudes in each dot to $B^L_{ac,x} = B^R_{ac,y}$, and later on we shall include the case of asymmetric Zeeman splittings – where both parity symmetry and generalized parity symmetry are broken.

Importantly, in the first section we proved for the linearly polarized case, that an internal symmetry for a single quantum dot can also be defined. However, in contrast with the discrete $\mathbb{Z}_2$ symmetry, present due to the time dependence of the field intensity $|\vec{B}(t)|$, for the circularly polarized case the intensity $|\vec{B}|$ is constant and the system presents a continuous symmetry for rotations along the z-axis $U_R(\theta) = e^{-i\theta S_z}$. Furthermore, in this last case a time translation $t \to t'$ is equivalent to a rotation along the z axis. This difference in the internal symmetry of the single dot in the presence of magnetic fields with different polarizations leads to the lack of dynamical spin locking in the circularly polarized case as we will show below.

Master equation description:

For the analysis of the current through the quantum dots we consider the master equation formalism developed in the previous section. It describes a periodically driven quantum system coupled to a dissipative bath, such as a fermionic reservoir, in which the exchange of energy and information with the central system leads to decoherence and to a deviation from the unperturbed Floquet eigenstates. The Floquet spectrum of the closed system is obtained from the eigenvalue equation: $\mathcal{H} \mid \phi_\alpha(t)\rangle = \varepsilon_\alpha \mid \phi_\alpha\rangle$, and the operators $Q_{\sigma,i,p}$, defined in Equation .0.3, are just the creation or annihilation operators of the spin state σ in the i dot:

$$\begin{aligned} Q_{1,1,2} &= -d^\dagger_{\uparrow,L}, \quad Q_{1,2,2} = -d^\dagger_{\uparrow,R}, \quad Q_{2,1,2} = -d^\dagger_{\downarrow,L}, \\ Q_{2,2,2} &= -d^\dagger_{\downarrow,R}, \quad Q_{1,1,1} = d_{\uparrow,L}, \quad Q_{1,2,1} = d_{\uparrow,R}, \\ Q_{2,1,1} &= d_{\downarrow,L}, \quad Q_{2,2,1} = d_{\downarrow,R}. \end{aligned} \tag{3.3.2}$$

For the calculation of the master equation we first need to calculate the matrix elements $Q_{\alpha,\beta,p,\sigma,m}$ from Equation 3.2.16 and the thermal coefficients from Equation 3.2.22 and Equation 3.2.24. The thermal coefficients, as a function of a variable $x = \varepsilon_{\mu,\nu} - m\omega$ are given by:

$$\begin{aligned} g_1(x)_{i,p} &= \pi D_i N_1(x)_{i,p}\,, \; g_1^*(x)_{i,p} = \pi D_i N_1(x)^*_{i,p}\,, \\ N_1(x)_{i,1} &= \pi D\left(1 - \frac{1}{1+e^{(x-\mu_i)/T}}\right) = N_1(x)^*_{i,2}\,, \\ N_1(x)^*_{i,1} &= \pi D\left(\frac{1}{1+e^{(x-\mu_i)/T}}\right) = N_1(x)_{i,2}\,. \end{aligned} \tag{3.3.3}$$

Being D_i the density of states in each lead. Its behavior is plotted in Figure 3.3.2, and clearly the sum over all different harmonics leads to a sum of successive Fermi functions at multiples of the driving frequency. As we already know the Floquet

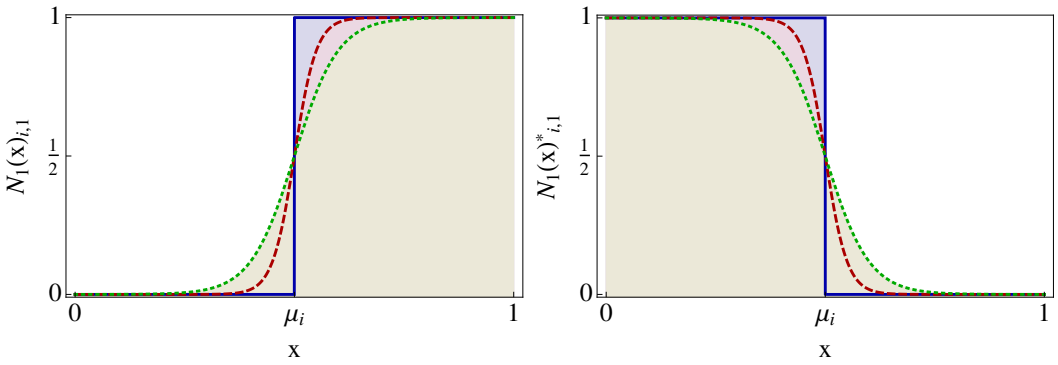

Figure 3.3.2: Thermal coefficients for three different temperatures $T = 10^{-5}$, 2.5×10^{-2}, and 5×10^{-2} (blue, red and green respectively) in energy units.

states, the quasi-energies from the closed system, as well as the thermal coefficients,

we can calculate the different rates that characterize the system:

$$R^{1}_{\alpha\beta,\mu\nu} = \Upsilon^{2} \sum_{i,p,\sigma,m} Q\left(m\right)_{i\sigma p,\alpha\beta} Q\left(m\right)^{*}_{i\sigma p,\mu\nu} g_{1}\left(\varepsilon_{\mu,\nu} - m\omega\right)_{p,i} \ , \tag{3.3.4}$$

$$R^{2}_{\alpha\beta,\mu\nu} = \Upsilon^{2} \sum_{i,p,\sigma,m} Q\left(m\right)_{i\sigma p,\alpha\beta} Q\left(m\right)^{*}_{i\sigma p,\mu\nu} g^{*}_{1}\left(\varepsilon_{\mu,\nu} - m\omega\right)_{p,i} \ . \tag{3.3.5}$$

Numerical solution for fixed intensity: As a check, we first calculate the full numerical solution of the master equation for the next set of parameters: $B_{ac} = 1$, $D_1 = D_2 = 1$, $\Upsilon = 10^{-2}$, $\mu_R = -\mu_L = 1$, $T = 10^{-4}$, $B_{z,L} = 1/2$, $B_{z,R} = 1$, $\omega = \omega_{\rm Av} = 3/4$, $\epsilon_{g,L} = \epsilon_{g,R} = 0$, $t_{LR} = 0.1$ and $\phi = \pi$. This configuration for the external fields is referred as the *average frequency configuration:* $\omega_{\rm Av} = \frac{B_{z,L}+B_{z,R}}{2}$, in which the average Zeeman splitting is in resonance with the field frequency ω. We have selected this configuration because, it will be an important one for the circularly polarized case. We also consider a generalized parity invariant Hamiltonian by requiring $\phi = \phi_L - \phi_R = \pi$, and assume $B_{ac} > \omega \gg t_{LR}$ – i.e., weak coupling limit to the reservoirs.

The quasi-energies for the closed system are plotted in Figure 3.3.3. The plot shows a degeneracy between states with opposite generalized parity symmetry, as the one found in Figure 3.1.3 for linearly polarized fields, which results in charge localization as we show next. In contrast with the linearly polarized case, the quasi-energies are degenerated for all values of the field amplitude B_{ac}, as far as the average frequency configuration $\omega = \omega_{Av}$ holds. Nevertheless, we will show that dynamical spin locking is not obtained for circular polarization due to the continuous circular symmetry of the field. Let us consider as the initial condition for $t = 0$ a localized state in the

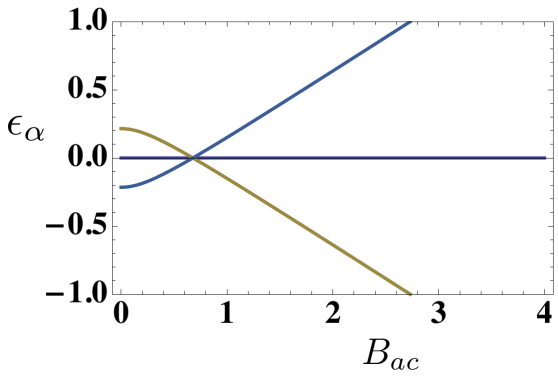

Figure 3.3.3: Quasi-energies as a function of the intensity B_{ac} for the average frequency $\omega_{\rm Av}$ and parameters: $\phi = \phi_R - \phi_L = \pi$, $B_{z,L} = 1/2$, $B_{z,R} = 1$, $t_{LR} = 1/10$ and $\epsilon_{g,L} = \epsilon_{g,R} = 0$. The double degeneracy between quasi-energies with opposite generalized parity symmetry allows localization at each dot.

left dot:

$$|\Psi_0\rangle = \frac{1}{\sqrt{2}}\left(|\uparrow_L\rangle + |\downarrow_L\rangle\right) \ . \tag{3.3.6}$$

Note that we have considered a chemical potential configuration in which the electrons flow from the right to the left lead. Then, when the system evolves in time, the electron initially placed at the left dot can jump to the left reservoir, however, as the system is in charge localization regime, a new electron coming from the right lead will populate the right dot and remain localized in time. This is shown in Figure 3.3.4, where it is shown the time evolution of the occupation probabilities. There, an inversion of the initial population, from the left to the right dot, with an intermediate increase of the vacuum state population confirms the localization process. For clarity we also plot in Figure 3.3.5 the occupation probabilities in each

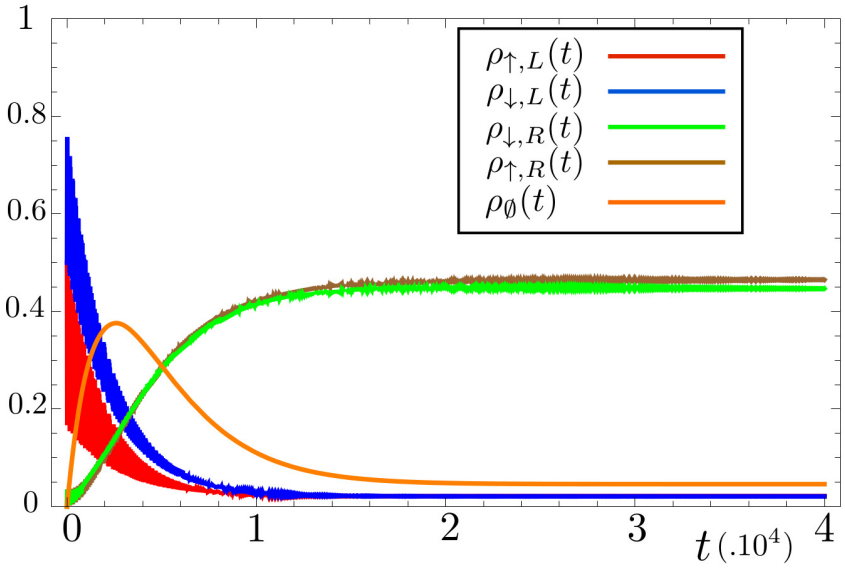

Figure 3.3.4: Diagonal elements of the density matrix vs t for the parameters chosen at the beginning of the section. Note that the vacuum state population increases (orange) as the initial electron tunnels to the left lead. Later on, a new electron coming from the right lead enters the system and remains localized in a superposition of spin up/down, which is precisely the localized Floquet state of the closed system.

dot as a function of time. Clearly the initial electron tunnels to the left lead and the right dot becomes occupied and localized as the system evolves in time. In addition, we can observe the small oscillations during the time evolution which represent the short time dynamics due to the high accuracy of the numerical approach. Finally, the calculation of the steady state solution by means of Equation 3.2.32 shows excellent agreement with the numerical calculation. Further, the temperature dependence could also be obtained with our formalism in order to understand how the charge localization is affected.

Current formula: Here we establish a relation between the dynamics of the system and the physical observables by means of the current operator. The current through

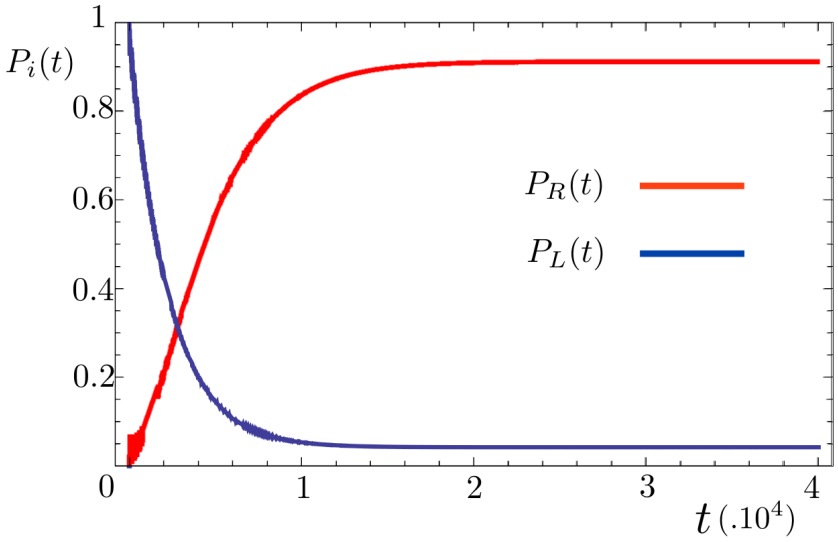

Figure 3.3.5: Time evolution of the occupation probabilities in each dot for an initially occupied left dot and charge localization regime. As the system evolves, the electron in the left dot jumps to the left lead, and a new electron is injected into the right dot. Thus, due to the charge localization regime, the current is blocked and the right dot remains occupied.

system can be computed in many different ways, depending on the different surfaces chosen to account of the current flow. The standard method considers the variation of the number of particles in one of the leads. However, the calculation for the case of a double quantum dot can be easily simplified when the charge considered encloses half the system, i.e., a single dot plus its neighboring lead. Then, we consider the charge conservation in the left-lead plus left dot for this system. It allows to define a current operator which does not depend on the bath operators, simplifying the calculation of the trace. The total charge in the left lead/dot is (for $-e = 1$):

$$Q_L = -e\left(N_L + N_{dot,L}\right), \tag{3.3.7}$$

$$N_L = \sum_{K,\sigma} b^\dagger_{LK\sigma} b_{LK\sigma}, \tag{3.3.8}$$

$$N_{dot,L} = \sum_{\sigma'} d^\dagger_{\sigma',L} d_{\sigma',L}, \tag{3.3.9}$$

The current is characterized by the change in time of the charge $\langle I\rangle = \left\langle \dot{Q}\right\rangle = i\left\langle [H,Q]\right\rangle = i\left\langle [H_{t_{LR}} + V, Q]\right\rangle = i\left\langle [H_{t_{LR}}, Q]\right\rangle$, and the resulting current operator is given by:

$$I = i\Upsilon \sum_{\sigma} \left(d^\dagger_{\sigma R} d_{\sigma L} - d^\dagger_{\sigma L} d_{\sigma R}\right), \tag{3.3.10}$$

which importantly, does not depend on the bath operators. The observable current is finally obtained by means of the next average:

$$\begin{aligned} \langle I \rangle &= Tr_{S+B}\left(\rho_{tot} I\right) \\ &= Tr_S\left\{\sum_{|B\rangle}\langle B|\rho_{tot}|B\rangle I\right\} , \end{aligned} \tag{3.3.11}$$

where $|B\rangle$ is an eigenstate of the bath Hamiltonian. Plugging the definition of reduced density matrix $\rho = Tr_B\left(\rho_{tot}\right)$ in the previous expression, we finally arrive at:

$$\begin{aligned} \langle I \rangle &= Tr_S\left(\rho I\right) = \sum_{|S\rangle,|S'\rangle}\langle S|\rho|S'\rangle\langle S'|I|S\rangle \\ &= i\Upsilon \sum_{|S\rangle,|S'\rangle}\sum_{\sigma}\left\{\rho\left(t\right)_{S,S'}\langle S'|\left(d^{\dagger}_{\sigma R}d_{\sigma L} - d^{\dagger}_{\sigma L}d_{\sigma R}\right)|S\rangle\right\} , \end{aligned} \tag{3.3.12}$$

where $|S\rangle$ and $|S'\rangle$ are the eigenstates of the central system Hamiltonian. This formula is the one we need, together with the steady state solution, to obtain the current through the system at different field configurations.

3.3.1 Results:

Now we explore in detail the different field configurations, the corresponding quasi-energies and the current flow for both, the open and closed system.

First, we consider two limiting cases, both in the resonance condition: $B_{z,L} = B_{z,R} = \omega$. For the closed system the closed system is exactly solvable due to the circularly polarized AC magnetic field. Thus, it is possible to analyze the quasi-energy structure in great detail.

For the case of a Π invariant Hamiltonian ($\phi = 0$), the quasi-energies are not degenerate for all B_{ac}, as it is shown in Figure 3.3.6, left. The isolated crossings, at certain values of the field intensity B_{ac}, are allowed by the rotational symmetry of the circular field. However, the time evolution of the occupation probabilities in the closed system indicates that charge localization does not happen for this field configuration, independently of the field intensity and frequency considered. The difference with the linear field is that the crossings are no longer between quasi-energies of states related by a discrete $\mathbb{Z}_2$ symmetry (i.e., states related by the generalized parity symmetry), but for states related by a continuous rotational symmetry. For the open system, the numerical calculation shows that at finite voltage gate $\mu_L - \mu_R \gg T, B_z, B_{ac}$, the current reaches a finite constant value for the long time dynamics, which confirms the lack of charge localization (see Figure 3.3.7). If we consider instead a generalized parity symmetry invariant Hamiltonian ($\phi = \pi$), the quasi-energies become degenerate in pairs for all B_{ac} (see Figure 3.3.6, right). This degeneracy is obtained by the restoration of the generalized parity symmetry.

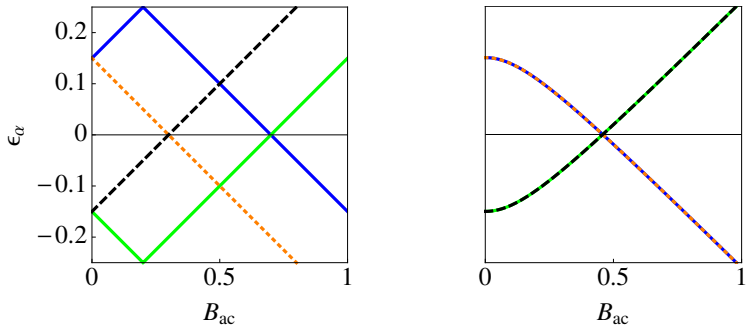

Figure 3.3.6: Quasi-energies vs B_{ac} for $\phi = 0$ (left) and $\phi = \pi$ (right), in resonance condition. The absence (presence) of generalized parity symmetry for $\phi = 0$ ($\phi = \pi$), leads to non-degenerate (doubly degenerate) quasi-energies. The degeneracy, present for all B_{ac} in the right figure, drives the system to charge localization. $t_{LR} = 1/10$, and $B_{z,L} = B_{z,R} = \omega = 1/2$.

In addition, the exact crossing at $B_{ac} = \omega$ is still allowed by the continuos rotational symmetry. The calculation of the occupation probabilities for both the open and closed system shows that the system is in charge localization regime, because the incoming electrons from the left lead cannot tunnel to the right dot (see Figure 3.3.8). In conclusion, by looking at Figure 3.3.6 we can differentiate two types of crossings

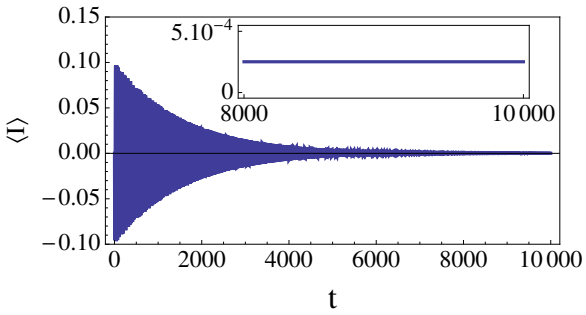

Figure 3.3.7: Current vs t for the presence of parity symmetry ($\phi = 0$) at resonance condition. The parameters considered in energy units are: $B_{zL} = B_{zR} = \omega = 0.5$, $B_{ac} = 0.5$, $t_{LR} = 0.1$, $\Upsilon = 0.01$, $T = 10^{-3}$ and $\mu_L - \mu_R \gg T, B_z, B_{ac}$. The inset shows the current vs time in the steady state with value $\langle I \rangle \simeq 2.5 \times 10^{-4}$.

between quasi-energies. On the one hand, the existence of the discrete GPS, allows a $\mathbb{Z}_2$ classification of the quasi-energies, leading to a degeneracy in pairs for all field amplitude B_{ac}, as it shown for the case $\phi = \pi$. This results in the presence of charge localization for resonant frequency, but dynamical spin locking is never obtained. On the other hand, both plots present isolated crossings between quasi-energies with the same parity or generalized parity symmetry (e.g., the ones present in Figure 3.3.6, left). They are allowed by the Wigner-Von Neumann theorem because of the continuous rotational symmetry of a single dot in a circularly polarized magnetic field, but they do not affect the occupation probabilities of the Floquet states.

We conclude that the continuous rotational symmetry is the one that differentiates the circular field polarization with the case of a linear one (which possess a $\mathbb{Z}_2$ symmetry), and it is responsible of the absence of dynamical spin locking in the former. In addition, as the discrete GPS can still be present in both field configurations, we have shown that charge localization can be obtained in both field configurations.

Nevertheless, for circularly polarized fields, we have found an important difference with linearly polarized fields besides from the absence of dynamical spin locking: Charge localization is obtained for all values of B_{ac} when the resonance condition is fulfilled. The reason is that the quasi-energies manifold is degenerated for all B_{ac}. However, localization is improved by increasing the field amplitude, as we show next. It can be seen, by direct comparison of Figure 3.3.8 and the inset, that

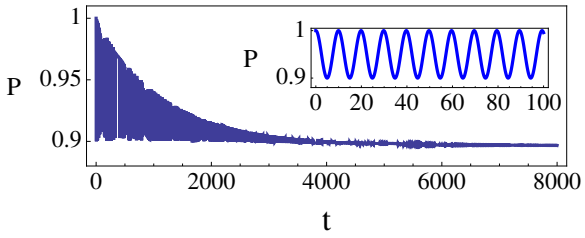

Figure 3.3.8: Occupation probability in the left dot P vs time for $B_{ac} = 0.6$, in presence of decoherence due to the leads. Note the charge localization induced as a consequence of the quasi-energies degeneracy between Floquet states with opposite GPS. The inset shows the time evolution (Equation 3.3.13) for the closed system. Parameters: $B_{z,L} = B_{z,R} = \omega = 1/2$, $\Upsilon = 0.01$, $T = 10^{-3}$, $t_{LR} = 1/10$ and $\phi = \pi$ in energy units for $\mu_L - \mu_R \gg 0$.

the decoherence effect due to the leads removes the coherent oscillations without breaking the localization induced by the AC field. In order to get a better insight on the charge localization at the resonance condition, we obtain analytically the localization probability for the closed system ($\phi = \pi$ and $B_{z,L} = B_{zR} = \omega$):

$$\begin{aligned} P(t) &= |\langle\uparrow_L |\Psi(t)\rangle|^2 + |\langle\downarrow_L |\Psi(t)\rangle|^2 \\ &= 1 + \frac{2t_{LR}^2\left(\cos\left(t\sqrt{B_{ac}^2 + 4t_{LR}^2}\right) - 1\right)}{B_{ac}^2 + 4t_{LR}^2}, \end{aligned} \tag{3.3.13}$$

Equation 3.3.13 shows that charge localization depends on the ratio B_{ac}/t_{LR}. Then, following Figure 3.3.8, if we assume that in presence of decoherence the probability of localization is given by the minimum value of the coherent oscillations in the closed system, we can characterize the degree of localization for the open system as: $P_{\min} = \min(P(t)) = \Lambda^2/(1+\Lambda^2)$, where $\Lambda = B_{ac}/(2t_{LR})$. This is plotted in Figure 3.3.9.

Thus, from the symmetrical Zeeman field configuration, we conclude that the existence of generalized parity symmetry drives the system to charge localization regime,

as far as ω is in resonance with the Zeeman splitting. If the system is tuned off resonance, the quasi-energies split, and charge localization is destroyed. Now let us

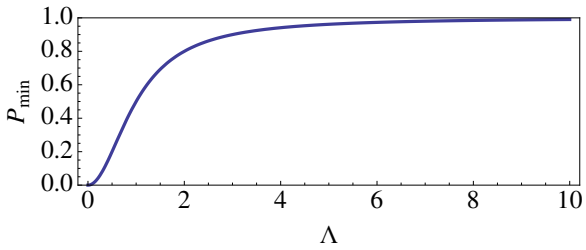

Figure 3.3.9: $P_{\min}$ vs Λ in presence of coupling with the leads for the steady state ($\phi = \pi$).

consider asymmetric Zeeman splittings. This is a very common situation in real experiments, where Overhauser fields or different g-factors make difficult to achieve a symmetric configuration. If we calculate the Floquet spectrum for the Hamiltonian $H_S(t)$ (Equation 3.3.1), it can be shown that the necessary condition to obtain a quasi-energies degeneracy is given by $\omega = \omega_{\text{Av}} \equiv \frac{B_{z,L}+B_{z,R}}{2}$. Note that in this configuration, generalized parity symmetry is always broken because of the asymmetric Zeeman splittings. Then, this degeneracy can be interpreted in terms of the renormalization by the AC field at frequency ω_{Av}, which restores the asymmetry in the Zeeman splittings, and recovers the generalized parity symmetry in the system. Remember that in Section 2 we have shown that the Hamiltonian, in the co-rotating frame, had a Zeeman splitting which is renormalized by the frequency.

In order to characterize the charge localization for asymmetric Zeeman splittings, Figure 3.3.10 shows the current $\langle I \rangle$ vs ω for $\phi = \{0, \pi\}$ and $B_{z,L} = B_{z,R}/2$. In the plot can be seen that the current drops to zero as the frequency reaches the value ω_{Av}. Figure 3.3.10 summarizes all the results for the circularly polarized case.

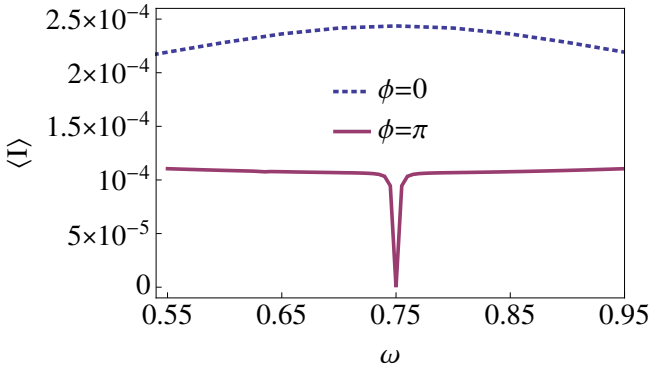

Figure 3.3.10: Current vs ω in the steady state for asymmetric Zeeman splittings. $\langle I \rangle$ drops to zero at $\omega = \omega_{\text{Av}}$ ($\omega_{\text{Av}} = 0.75$) for $\phi = \pi$, while for $\phi = 0$ the current is finite. $B_{z,L} = 0.5$, $B_{z,R} = 1$,$B_{ac} = 0.55$, $t_{LR} = 0.1$, and $\Upsilon = 0.01$.

It demonstrates the critical difference in the current behavior for phase difference $\phi = 0,$ and π, as well as the renormalization of the Zeeman splittings and the charge localization at resonance condition $\omega = \omega_{\mathrm{Av}}$.

In summary, we have analyzed the electron dynamics and the current through a double quantum dot attached to contacts, when it is driven by a circularly polarized magnetic field. We proved, numerically and based in symmetry arguments, that by tuning the phase difference ϕ between the AC magnetic fields applied each dot, it is possible to achieve charge localization when the system is near resonance. This effect is robust and perdure in presence of decoherence, induced by the coupling with contacts.

3.4 Adiabatic and non adiabatic phases

Geometric phases in quantum physics is a fundamental issue which has been studied during the last decades. Since Berry's discovery of geometric phases in quantum systems [23], and their further applications to different branches of physics – e.g. condensed matter and optics – geometry, topology and nature seem to be mixed at a highly complex level. The characterization of different physical properties in purely geometrical and topological terms, such as quantized transport[46] and electric polarization[47], has lead to the understanding of some undergoing processes governing the physical properties of these systems [48]. An important characteristic of geometrical and topological properties in physics, arises in their strength against different perturbations. Some examples of those are backscattering in edge states and fault tolerant quantum computation[49, 50, 51, 31].

Theory of Principal Fiber Bundles (PFB) has also played an important role in quantum mechanics due to its suitability to describe the underlying geometrical and topological properties[52, 24]. Its relation with condensed matter systems was pointed out by Simon [53], and the existence of an universal PFB [54, 25], which is a purely geometric object, shows that non-adiabatic processes can be used for practical purposes in a similar way than their adiabatic partners.

The interplay between geometry and AC fields is a very promising field with a huge activity in the last years. The tuning of geometrical properties by the application of AC fields offers a very interesting scenario, where non-equilibrium systems show quantum phase transitions, and the possibility to create topologically protected states[10, 11, 55, 56].

As Berry demonstrated, the phase acquired during the cyclic evolution of a general quantum system can be expressed as a combination of two terms, a dynamical phase γ_D and a geometric phase γ_G, being the latter obtained due to the parallel transportation of the vector state through the base manifold[57, 54]. The parallel transportation is obtained by means of the 1-form connection $A^n := i\langle n|d|n\rangle$ (d is the exterior derivative operator, and $|n\rangle$ is the instantaneous eigenstate), and the

geometric phase acquired is given by $\gamma_G^n = \int_C A^n$, that only depends on the path followed in the parameter space.

These geometric quantities describe the evolution of the system as the external parameters are varied, but other quantities, such us Chern numbers (topological invariants) can also be defined through the 1-form A^n, characterizing the topological properties of the whole base manifold. Motivated by the results of the previous

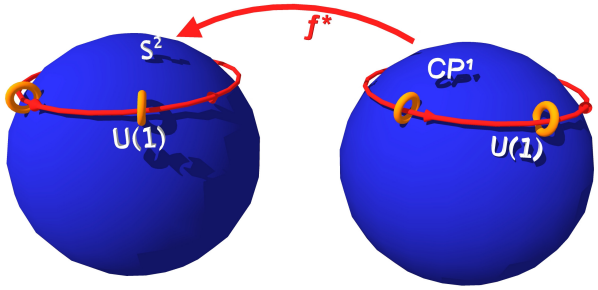

Figure 3.4.1: Schematic figure for the relation between adiabatic and non-adiabatic regimes. The function f^* maps curves $\mathcal{C}$ from the Bloch sphere (projective Hilbert $\mathbb{C}P^{N-1}$) into curves C in the parameter space $\mathcal{S}^2 = \{\theta, \varphi\}$. The $U(1)$ fibers attached to each point due to the phase invariance of quantum mechanics are represented by small circles. We consider $\mathbb{C}P^{N-1}$ with $N = 2$ for the schematic figure – $\mathbb{C}P^1$ corresponds to the Bloch sphere for a single qubit.

section, here we study an extension of the classical model considered by Berry[23], including the spatial degree of freedom due to the tunneling between dots, inhomogeneous magnetic fields and non-adiabatic evolution. The Hamiltonian describing this model directly applies to the double quantum dots in strong Coulomb blockade regime coupled to AC magnetic fields that we studied in the previous section. We will show that the interplay between the spin and spatial degree of freedom is remarkably relevant for the topological properties when the AC field varies between different sites. In order to characterize these properties, we will calculate the geometric phase and the Chern number for both adiabatic and non-adiabatic evolution. Our results can be extended to other experimental setups and to larger size systems, such as atomic arrays with a pseudo-spin degree of freedom. Importantly, in this section we will demonstrate that the AC field parameters allows for tunable geometric phases and the addition of new topological phases, which only appear out of the adiabatic regime.

Model: The Hamiltonian for a spin-full electron tunneling between two sites (L, R) and coupled to an AC field is given by:

$$\begin{aligned} H(t) &= \sum_{i=L,R} B\cos(\theta) S_z^i + \sum_{\sigma,i\neq j} t_{LR} c_{\sigma,i}^{\dagger} c_{\sigma,j} + \\ &\quad \sum_{i=L,R} B\sin(\theta)\left[\cos(\varphi_i(t)) S_x^i + \sin(\varphi_i(t)) S_y^i\right]. \end{aligned} \tag{3.4.1}$$

The coupling between sites is characterized by t_{LR}, B_z is the static field Zeeman which splits the spin levels, and the AC field $\vec{B}_{ac}(t)$ couples the different states of the qubit (perpendicular to B_z). In this Hamiltonian, the field has been parametrized according to the angles of a 2-sphere $\mathcal{S}^2 = \{\theta, \varphi\}$, being $B_z \equiv B\cos(\theta)$, $B_{ac}^x \equiv B\sin(\theta)\cos(\varphi_i(t))$ and $B_{ac}^y \equiv B\sin(\theta)\sin(\varphi_i(t))$. This is a very appropriate parametrization for a circularly polarized AC field, whose time dependence is considered to be linear $\varphi_i(t) = \Omega t + \phi_i$. For simplicity for the analytical calculation we consider symmetrical B_z and $B_{ac}(t)$ at each site.

For this Hamiltonian, we now calculate the geometric and topological properties by means of the connection 1-form A^n. We consider both, the adiabatic and non-adiabatic time evolution for phase differences $\phi = \phi_L - \phi_R \in \{0, \pi\}$ (i.e., magnetic fields in phase or in phase opposition respectively), and calculate the phase diagram demonstrating that non-adiabatic evolution leads to the appearance of new topological phases.

Adiabatic case: The adiabatic case considers slow time evolution. As we discussed in the introduction, it allows to approximate the solutions by the instantaneous eigenstates and neglect the transitions to other energy levels. The instantaneous energies $E_n(\phi)$ can be characterized by two indexes after the diagonalization $n \equiv (m_1 = \pm 1, m_2 = \pm 1)$:

$$\begin{aligned} E_n(0) &= -\frac{B}{2}(m_1 + m_2\lambda) \\ E_n(\pi) &= -\frac{m_1 B}{2}\sqrt{1 + \lambda^2 - 2m_2\lambda\cos(\theta)}, \end{aligned} \tag{3.4.2}$$

being $\lambda = 2t_{LR}/B$. Importantly, we can observe that both instantaneous energies are φ independent. The case $\phi = 0$ reflects the classical result obtained by Berry (i.e., flat bands without θ dependence), with an extra hybridization due to the tunneling t_{LR}. However, the case $\phi = \pi$ shows a θ dependence which has not been previously analyzed, consequence of the spatial anisotropy. In this case, the instantaneous energies now depend on the ratio between the AC field and the Zeeman splitting through θ (Figure 3.4.2), and not just on the total intensity $B = |\vec{B}| = \sqrt{B_{ac}^2 + B_z^2}$. Due to the fact that the points on the surface of a sphere cannot be directly mapped to a plane (this can be proved by stroboscopic projection from the sphere to a two dimensional plane), we need to consider two different charts to describe the parametric dependence of the instantaneous eigenstates. The transformation between the

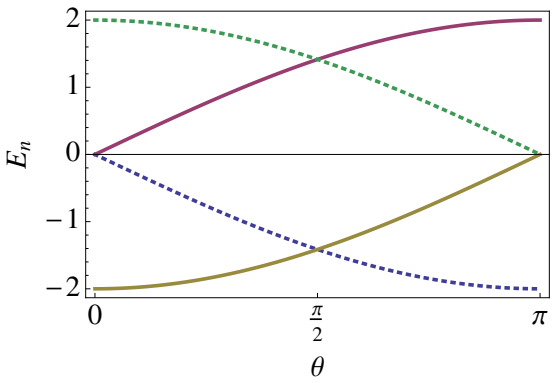

Figure 3.4.2: Instantaneous energies $E_n(\pi)$ vs θ for $t_{LR} = 1$, $\phi = \pi$ and $B = 2$ (dashed lines: $E_{\pm,\pm}(\pi)$ and continuous lines: $E_{\mp,\pm}(\pi)$).

instantaneous eigenstates in different charts is given by phase factors as can be seen in Ref.[24]. This is a signature of non-trivial geometrical and topological properties, and it is equivalent to an space-time curvature in general relativity – in geometric terms it can be described as a constriction against the use of flat coordinates. Fortunately for the present case, we do not need to worry this transformations between different charts, as we are interested in the geometric phase and the curvature tensor $F^n = dA^n$ (needed for the calculation of the Chern number), which are globally defined for the case of Abelian theories.

In order to obtain the geometric phase we calculate, using the instantaneous eigenvectors in a single chart, the connection 1-form $\mathbf{A}^n = \left(A^n_\varphi, A^n_\theta\right)$. It can be proved that the calculation into a different chart gives the same result for the geometric phase γ^n_G, which is obtained by the integral of the Berry connection along $\varphi(t)$. Importantly, the result shows that the phase difference ϕ strongly modifies the geometric phase (Figure 3.4.3), which is t_{LR} dependent for the case of $\phi = \pi$:

$$\gamma^n_G(\phi = 0) = \pi(1 - m_1 \cos(\theta)) \tag{3.4.3}$$

$$\gamma^n_G(\phi = \pi) = \pi \frac{m_1(\lambda m_2 - \cos(\theta)) + f_{m_2}(\lambda, \theta)}{f_{m_2}(\lambda, \theta)}, \tag{3.4.4}$$

being $f_{m_2}(\lambda, \theta) \equiv \sqrt{1 + \lambda^2 - 2m_2\lambda\cos(\theta)}$. Note that for $\phi = 0$ (spatially homogeneous field) γ^n_G does not depend on t_{LR}. This fact, implies that it remains invariant for several tunnel coupled two level systems as long as $\phi = 0$ – i.e., if the field is spatially homogeneous there is no interplay between spin and spatial degree of freedom and the classical Berry's result still applies. Once we consider the spatial anisotropy due the phase difference $\phi \neq 0$, Berry's result is modified, because it now includes an interplay between the tunneling and the AC field.

The next step is the calculation of the curvature 2-form $F^n = dA^n = \left(\frac{\partial}{\partial\varphi}A^n_\theta - \frac{\partial}{\partial\theta}A^n_\varphi\right) d\varphi\wedge$

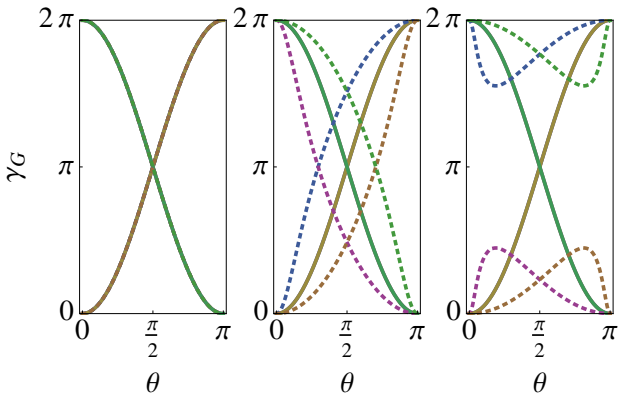

Figure 3.4.3: Geometric phase in the adiabatic limit γ_G vs θ for different λ ($\lambda = 0$ (left), $\lambda = 0.6$ (center) and $\lambda = 1.2$ (right)). Dashed (continuous) lines: $\phi = \pi$ ($\phi = 0$). Note that as $\lambda = 2t_{LR}/B$ is increased, a gap appears for the case $\phi = \pi$. The value at which the topological phase transition occurs is exactly where the gap opens ($\lambda = 1$).

$d\theta$, that will be used for the calculation of the Chern numbers:

$$F^n_{\phi=0} = m_1 \frac{\sin(\theta)}{2} \tag{3.4.5}$$

$$F^n_{\phi=\pi} = m_1 \frac{\sin(\theta)}{2} \frac{1 - \lambda m_2 \cos(\theta)}{(1 + \lambda^2 - 2\lambda m_2 \cos(\theta))^{3/2}}. \tag{3.4.6}$$

The result shows that for $\phi = \pi$, the original curvature (Equation 3.4.5) is renormalized by a factor which depends on t_{LR} and m_2 (Equation 3.4.6). For $\lambda = 1$, the curvature 2-form changes its value, and at the limit of large tunneling $t_{LR} \gg B$ the curvature tends to zero for all θ, evolving towards a flat space. The first Chern number is given by:

$$c_1^n(\lambda) = \int_{\mathcal{S}^2} \frac{F^n}{2\pi} = \begin{cases} m_1 \Theta(1 - \lambda) & \text{for } \phi{=}\pi \\ m_1 & \text{for } \phi{=}0 \end{cases} \tag{3.4.7}$$

being $\Theta(x)$ the Heaviside step function. Hence, for $\phi = \pi$, the system undergoes a transition from a topological phase $\mathbb{Z}$ ($c_1 \neq 0$) to a trivial phase ($c_1 = 0$) at $\lambda = 1$ by tuning the ratio between the hopping t_{LR} and the intensity of the AC field $|\vec{B}|$.

All results in this section has been obtained under the adiabatic assumption, but this is an approximation for ideal slow evolution, as we discussed in the first chapter. Therefore a natural question arises: How do the previous results change when we consider non-adiabatic evolution?.

Non-adiabatic case: Here we discuss the non-adiabatic case. As we previously argued, adiabaticity is a rather ideal limit for the time evolution, and corrections

due to non adiabatic processes are sometimes required. Aharonov and Anandan (A-A) proposed a generalization of the Berry phase to non-adiabatic processes, the A-A phase $\gamma_{\text{A-A}}$ [57]. As later was pointed out, this generalization corresponds to a universal connection $\mathcal{A}$ in a universal PFB $\mathbb{C}P^{\infty}$ or A-A bundle[4]. It establishes a general relation between the classification of $U(1)$ PFB and quantum mechanical systems[25]. The relation between Berry's and Anadan's result is stablished through a function f_n^* (pullback bundle), that maps curves $\mathcal{C}$ defined in $\mathbb{C}P^{\infty}$ to curves C in the parameter space, i.e. $C = f_n^*(\mathcal{C})$, then f_n^* has all the information for the computation of the geometric phase (the explicit form of the Hamiltonian determines f_n^*). Importantly, this is very connected with the next chapter of this thesis, where we describe the topological classification of insulators and superconductors. The classification is obtained in terms of K-theory, and it is closely related to the universal bundles. The difference is that the K-theory classification includes the presence of extra symmetries, such as time reversal and particle-hole.

By means of a unitary transformation to a co-rotating frame with the AC field, we obtain the static Hamiltonian which can be exactly diagonalized. The unitary transformation is given by $U(t) = \exp\left\{-i\Omega t\left(S_z^L + S_z^R\right)\right\}$, and the transformed Hamiltonian $\tilde{H} = U^{\dagger}HU - iU^{\dagger}\dot{U}$ reads:

$$\begin{aligned}\tilde{H} &= \sum_{i=L,R}\left(B\cos(\theta) - \Omega\right)S_z^i + \sum_{\sigma,i\neq j} t_{LR}c_{\sigma,i}^{\dagger}c_{\sigma,j} \\ &\quad + \sum_{i=L,R} B\sin(\theta)\left[\cos(\phi_i)\,S_x^i + \sin(\phi_i)\,S_y^i\right].\end{aligned} \tag{3.4.8}$$

which is independent of time, and contains a renormalized Zeeman splitting by Ω. The diagonalization of the Hamiltonian leads to the energies $\mathcal{E}_n(\phi)$:

$$\begin{aligned}\mathcal{E}_n(0) &= -m_1\frac{B}{2}\sqrt{1+\mu^2-2\mu\cos(\theta)} - m_2 t_{LR} \\ \mathcal{E}_n(\pi) &= -m_1\frac{B}{2}\sqrt{1+\Delta_{m_2}^2-2\Delta_{m_2}\cos(\theta)}\end{aligned} \tag{3.4.9}$$

being $\mu \equiv \Omega/B$ and $\Delta_{m_2} \equiv (\Omega + 2m_2 t_{LR})/B$. Note that in both cases, the limit $\Omega \to 0$ matches the adiabatic case studied above. In addition, Equation 3.4.2 is related with Equation 3.4.9 by including corrections in which the different parameters are renormalized by the frequency Ω. Interestingly, the energies present degeneracy points for both $\phi = 0, \pi$. Our calculations show that the geometric phases are also Abelian at the degeneracy points due to the structure of the Floquet operator, which is in agreement with the results of [58].

The solutions to the Schrödinger equation are given by the transformation of the eigenvectors $|\tilde{\psi}\rangle$ obtained by diagonalizing Equation 3.4.8 to the original frame, i.e.

[4] $\mathbb{C}\text{P}^N$ is the complex projective space of N dimension. This is the set of equivalence classes $P(H)$ for states $|\psi\rangle \in H$, such that the equivalence relation is given by $|\psi\rangle \sim c|\psi\rangle$, where H is the Hilbert space of dimension N and c a complex number.

$|\psi(t)\rangle = U(\varphi(t))\,|\tilde{\psi}\rangle$. Thus, the calculation of the 1-form $\mathcal{A}_\varphi$ gives:

$$\mathcal{A}_\varphi = i\langle\psi(t)\,|\partial_\varphi|\psi(t)\rangle d\varphi = \langle\tilde{\psi}|S_z|\tilde{\psi}\rangle d\varphi,$$

where the A-A geometric phase is given by $\gamma_{\text{A-A}} = \oint_{\mathcal{C}} \mathcal{A}_\varphi = 2\pi\mathcal{A}_\varphi$. Each of the ϕ configurations finally result in:

$$\gamma^n_{\text{A-A}}(0) = m_1\pi\frac{(\mu - \cos(\theta))}{\sqrt{1+\mu^2-2\mu\cos(\theta)}}\,, \tag{3.4.10}$$

$$\gamma^n_{\text{A-A}}(\pi) = m_1\pi\frac{(\Delta_{m_2} - \cos(\theta))}{\sqrt{1+\Delta^2_{m_2}-2\Delta_{m_2}\cos(\theta)}}\,, \tag{3.4.11}$$

with the associated curvatures:

$$F^n(0) = m_1\frac{\sin(\theta)}{2}\frac{1-\mu\cos(\theta)}{(1+\mu^2-2\mu\cos(\theta))^{3/2}} \tag{3.4.12}$$

$$F^n(\pi) = m_1\frac{\sin(\theta)}{2}\frac{(1-\Delta_{m_2}\cos(\theta))}{\left(1+\Delta^2_{m_2}-2\Delta_{m_2}\cos(\theta)\right)^{3/2}}$$

We can see that the geometric properties for the case $\phi = 0$ does not depend on t_{LR} nor on m_2 – in addition, a degeneracy is always present for states with different m_2. By contrary, the $\phi = \pi$ case presents different curvature for each state, but as the functions $\Delta_\pm$ are not independent (both depend on combinations of B, Ω and t_{LR}), the geometric phases and curvatures cannot be independently tuned. The Chern numbers can be calculated through the curvature, and then, obtain the phase diagrams as a function of Δ_{m_2} or μ:

$$\begin{aligned} c^n_1(0) &= \frac{m_1}{2}(1+\text{sign}(1-\mu)) \\ c^n_1(\pi) &= m_1\Theta(1-|\Delta_{m_2}|) \\ &= m_1\Theta(1-|\Omega+2m_2t_{LR}|/B) \end{aligned} \tag{3.4.13}$$

The results obtained for the geometric phase show certain interesting features. For the $\phi = 0$ case, the non-adiabatic phases $\gamma_{\text{A-A}}$ present some corrections in μ to the adiabatic case (this is precisely the adiabatic parameter), but they remain degenerate in pairs, and the variation of μ modifies all geometric phases simultaneously. Also we must note that $\gamma^n_{\text{A-A}}(\phi = 0)$ (Equation 3.4.10), as in the adiabatic case (Equation 3.4.3), does not depend on m_2 nor on t_{LR}, meaning that systems with a larger number of coupled spins would have the same geometric phase.

Regarding the phase diagram, the $\phi = 0$ case just contains two phases: The topologically trivial and the $\mathbb{Z}$ phase. The trivial phase appears when we reach the non-adiabatic regime by increasing the frequency ($\mu = \Omega/B > 1$), while the $\mathbb{Z}$ phase governs the whole adiabatic regime.

Concerning the $\phi = \pi$ case in the non-adiabatic regime, the geometric phases (Equation 3.4.11) depend on two functions Δ_{m_2}, and hence on both indexes (m_1, m_2) of the state vector. This allows to modify the geometric and topological properties differently for each state. This is an important difference with the $\phi = 0$ case, because now, the geometric phase for each state behaves differently when we vary t_{LR}, Ω and B for $\phi = \pi$. This is reflected in the phase diagram, where two new topological phases appear: $(0, \mathbb{Z})$ and $(\mathbb{Z}, 0)$ (first index labels states with $m_2 = +1$ and second index states with $m_2 = -1$) in which only two of the states have non-vanishing Chern number. More interestingly, at arbitrary high frequencies Ω we show that states with non-vanishing Chern number can appear (Figure 3.4.4).

As the functions $\Delta_\pm$ depend both on the system parameters, we plot the phase diagram as a function of B and Ω for fixed t_{LR}. Interestingly, the $(\mathbb{Z}, 0)$ phase is not accessible (Figure 3.4.4). This is due to dependence on B, t_{LR} and Ω of the functions $\Delta_\pm$. Note that for a different dependence on the parameters, the $(\mathbb{Z}, 0)$ phase could appear. We also notice that the variation of the parameter t_{LR} only modifies the width of the $(0, \mathbb{Z})$ phase, such that in the limit $t_{LR} \to 0$ we obtain the phase diagram for the $\phi = 0$ case.

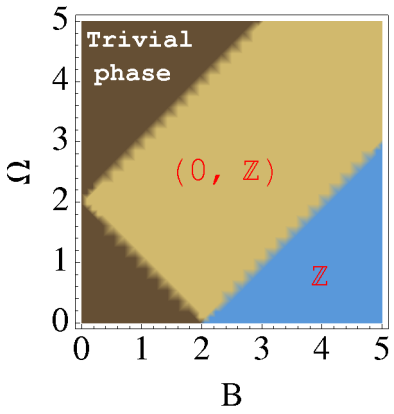

Figure 3.4.4: Topological phases diagram vs (B, Ω) for fixed $t_{LR} = 1$ and $\phi = \pi$. The phase diagram shows the three different topological regions which can be realized due to the addition of a tunneling process. The adiabatic limit is found by choosing $\Omega = 0$ with the trivial and non-trivial topological phases described above. In addition, for non adiabatic processes (i.e. $\Omega > 0$) a new phase $(0, \mathbb{Z})$ appears, in which just half of the states are characterized by a non vanishing Chern number.

Summarizing, we have analyzed the geometric and topological phases of tunnel coupled systems with an on-site pseudo-spin degree of freedom, and driven by AC fields. We have considered the case of an electron spin, tunneling between two different sites, which is coupled to an AC magnetic field that produces transitions between the spin up/down levels. The interplay between the spatial and spin degree of freedom due to the AC magnetic field, as well as its dependence with the external field

parameters B, Ω and ϕ, has been analyzed from a geometrical point of view. The existence of phases with non-vanishing Chern number implies a non-trivial bundle, and therefore holonomy elements different from the identity. It means that it is impossible to avoid the geometric phases in the study of these systems. The geometric phases are local, in difference with the Chern numbers, and can be different from zero even for regions where $c_1 = 0$.

We have found that a system presenting a spatial anisotropy – in our case due to the phase difference ϕ between the external AC driving fields in different sites – leads to a more complex behavior compared with Berry's classical result for a localized spin in the adiabatic regime. The results generalize the well known Aharonov-Anandan phase for localized spins, resulting in a novel topological phase diagram (Figure 3.4.4). Although the topological phase transition can be difficult to be directly measured in this setup, the measurement of geometric phases could indirectly show the topological phase transition (see Figure 3.4.3). Setups involving quantum dots in slanting magnetic fields [42] and quantum circuits[28] can be used for this purpose. Also, the non-adiabatic analysis shows how the topological invariants change out of the adiabatic regime, leading to possible applications in non-adiabatic quantum computation.

In summary to conclude this chapter, we have studied the dynamical and topological properties of double quantum dots, including measurable transport signatures. We have developed a master equation in which the current characterizes the charge localization induced by the AC magnetic fields. In addition, we have discussed the topological properties of the system and the effect of non-adiabatic corrections.

In the next chapter, we will study further the topological properties of periodically driven systems, including larger size systems and the presence of extra symmetries such as time reversal and particle-hole.

4 Topological Band theory and Floquet-Bloch states

In this chapter, we first review the topological band theory for time independent systems, and briefly explain its connection with K-theory. Finally we discuss the influence of time dependent fields in D-dimensional lattices from a topological point of view.

4.1 Time independent topological band theory

The topological classification of time independent systems[59, 60, 61] has become a very powerful tool in the last years. It was first developed by Altland and Zirnbauer[59] using random matrix theory, while later on, Kitaev[60] proved that this classification is directly connected with K-theory.

The recent interest in this field started due to the remarkable electronic properties systems with topological features. They contain gapless boundary modes as a consequence of the non trivial topology of the bulk structure, while at the same time, the bulk is insulating. This relation is known as the *bulk to boundary correspondence*, and importantly, the presence of these boundary modes is very robust, and they can be removed only when the bulk gap is closed. Some examples of these boundary modes are the edge states appearing in quantum Hall effect (see e.g. [62, 63] and references there in), or in topological insulators[49, 64, 65]. The combination of insulating materials in the bulk with Weyl semi-metallic states at the boundary provides new applications for nano-electronics and quantum computation among others.

The topological classification of non-interacting quantum systems has been proved to be related with a set of discrete symmetries defined in the system. These symmetries are: time reversal symmetry (TRS), and particle-hole symmetry (PHS). To understand why these symmetries are special we start with a description of all possible symmetries in quantum mechanics.

In general, in quantum mechanics a symmetry is defined as the operation that leaves the observables invariant, i.e., $|\langle\psi|\hat{O}|\psi\rangle| = |\langle\psi'|\hat{O}|\psi'\rangle|$, where $|\psi'\rangle = S|\psi\rangle$, and S is the symmetry transformation. This constrain allows two possibilities, R is either unitary or anti-unitary. An important difference between unitary and anti-unitary matrices is that the former has determinant $+1$ while the latter has determinant

-1. This difference means that unitary symmetries can be smoothly connected to the identity, while the anti-unitary ones cannot[1]. This fact reflects that they are discrete symmetries, and this is related with the existence of a gap which remains even for the thermodynamical limit.

A further analysis of these symmetries allows to classify them as follows: An anti-unitary operator A can commute or anti-commute with the Hamiltonian. Then, we can differentiate two kinds of anti-unitary operators:

$$\Theta^{-1}H\Theta = H \rightarrow \Theta: \text{ Time reversal symmetry,} \tag{4.1.1}$$

$$\Xi^{-1}H\Xi = -H \rightarrow \Xi: \text{ Particle-hole symmetry.} \tag{4.1.2}$$

In addition, each of this possibilities can square to $A^2 = \pm 1$. Thus, we have shown that in general two different anti-unitary operations can be defined for a quantum system, which are called generalized TRS and PHS. Besides, each of these symmetry transformations can square to ± 1 which is related with the specific system under consideration. For example a TRS operator Θ of a system of spin $\frac{1}{2}$ particles will square to -1, while for the case of spin-less particles squares to $+1$. This difference comes from the fact that the spin is an angular momentum, and then it changes in sign when time is reversed. Thus, even though the spin is an intrinsic degree of freedom, time reversal also acts within the spin sub-space leading to the -1 sign. For the case of particle hole symmetry the difference in sign is more subtle, but in superconductors it can be interpreted with the $SU(2)$ symmetry of the wave function (singlet superconductors have -1, while triplets have $+1$)[61].

Importantly, there is a third symmetry operation which can be defined for systems with both TRS and PHS. This is chiral symmetry[2], which can be made by the product of both $\mathcal{C} = \Theta\Xi$. Then, chiral symmetry is a unitary symmetry transformation, which anti-commutes with the Hamiltonian:

$$\mathcal{C}^{-1}H\mathcal{C} = -H, \ \mathcal{C}^2 = 1. \tag{4.1.3}$$

All possible combinations of these three symmetry operations define the full classification of single particle Hamiltonians, summarized in Table 4.1.1.

Table 4.1.1 contains ten different classes, depending on the system symmetries. The topological invariant for each symmetry class depends on the dimensionality of the parameter space. Up to this point, this is a formal classification of the topological properties, but in order to physically understand how the non trivial topology arises, let us connect the previous concepts with a the concepts of band theory in solid state physics.

[1]Note that the determinant cannot change under smooth transformations.

[2]Chiral symmetry is also known as sub-lattice symmetry in the condensed matter community.

Class	***TRS***	***PHS***	***SLS***	***d=0***	***d=1***	***d=2***	***d=3***
A	0	0	0	$\mathbb{Z}$	-	$\mathbb{Z}$	-
AI	+1	0	0	$\mathbb{Z}$	-	-	-
AII	-1	0	0	$2\mathbb{Z}$	-	$\mathbb{Z}_2$	$\mathbb{Z}_2$
AIII	0	0	1	-	$\mathbb{Z}$	-	$\mathbb{Z}$
BDI	+1	+1	1	$\mathbb{Z}_2$	$\mathbb{Z}$	-	-
CII	-1	-1	1	-	$2\mathbb{Z}$	-	$\mathbb{Z}_2$
D	0	+1	0	$\mathbb{Z}_2$	$\mathbb{Z}_2$	$\mathbb{Z}$	-
C	0	-1	0	-	-	$2\mathbb{Z}$	-
DIII	-1	+1	1	-	$\mathbb{Z}_2$	$\mathbb{Z}_2$	$\mathbb{Z}$
CI	+1	-1	1	-	-	-	$2\mathbb{Z}$

Table 4.1.1: Periodic table of topological insulators and superconductors in d-dimensions. This table associates a topological invariant to each symmetry class. The symmetry class only depends on the discrete symmetries of the system and the dimensionality of the parameter space.

Typically, a crystal Hamiltonian can be described in terms of a tight binding model (TB). Its most general form in $\mathbf{k}$-space, when periodic boundary conditions are assumed is:

$$H(\mathbf{k}) = \sum_{\alpha,\beta}\sum_{j,l} t_{j,l}^{\alpha,\beta} e^{i\mathbf{k}\cdot(\mathbf{R}_j-\mathbf{R}_l)} c_{\alpha,\mathbf{k}}^{\dagger} c_{\beta,\mathbf{k}}, \tag{4.1.4}$$

where $t_{j,l}^{\alpha,\beta}$ is the hopping from site $l \to j$, $c_{\alpha,\mathbf{k}}$ annihilates a particle with $\mathbf{k}$ momentum, and α represents some extra degrees of freedom, such as spin, or sub-lattice.

Anti-unitary operators can always be written as the product of a unitary matrix U and the complex conjugation K, i.e., $A = UK$. Then, considering their action on Equation 4.1.4, the resulting Hamiltonian will be rotated by the unitary transformation, but in addition the complex exponential will change sign due to the complex conjugation. Then, for a band Hamiltonian in $\mathbf{k}$-space, TRS, PHS and chiral symmetry are defined as:

$$\Theta^{-1} H(\mathbf{k}) \Theta = H(-\mathbf{k}) \to \Theta: \text{ Time reversal symmetry,} \tag{4.1.5}$$

$$\Xi^{-1} H(\mathbf{k}) \Xi = -H(-\mathbf{k}) \to \Xi: \text{ Particle-hole symmetry,} \tag{4.1.6}$$

$$\mathcal{C}^{-1} H(\mathbf{k}) \mathcal{C} = -H(\mathbf{k}) \to \mathcal{C}: \text{ Chiral symmetry.} \tag{4.1.7}$$

The topology for a band Hamiltonian is then characterized by the behavior of the eigenstates of $H(\mathbf{k})$ when they are transported along the FBZ (parameter space). In addition, we show below that this can also be understood in terms of the Anderson vector which characterizes the band Hamiltonian.

As an example, let us consider a one dimensional two band system without TRS or PHS. The parameter space or FBZ is given by a circle $\mathbb{T} = k \in [0, 2\pi/a] \simeq S^1$, and the topological invariant classifies the topologically different mappings from k

to the family of parametric Hamiltonians $H(k) = \vec{g}(k) \cdot \vec{\sigma}$, where $\vec{g}(k)$ is a three dimensional real Bloch vector, and $\vec{\sigma}$ are the generators of the $SU(2)$ algebra. If we assume that the Hamiltonian is always gapped, we have that $\vec{g}(k) \neq 0$ for all k. Then, the family of Hamiltonians $H(k)$ can be described by the surface of a sphere $\mathbb{R}^3 - \{0\} \simeq S^2$. The mappings from the FBZ to $H(k)$ are then equivalent to mappings $S^1 \to S^2$. According to Table 4.1.1 the A class in one dimension does not have a topological invariant, and all mappings should be equivalent. Fig.Figure 4.1.1 shows that all the mappings are actually trivial. Therefore, we have proved that

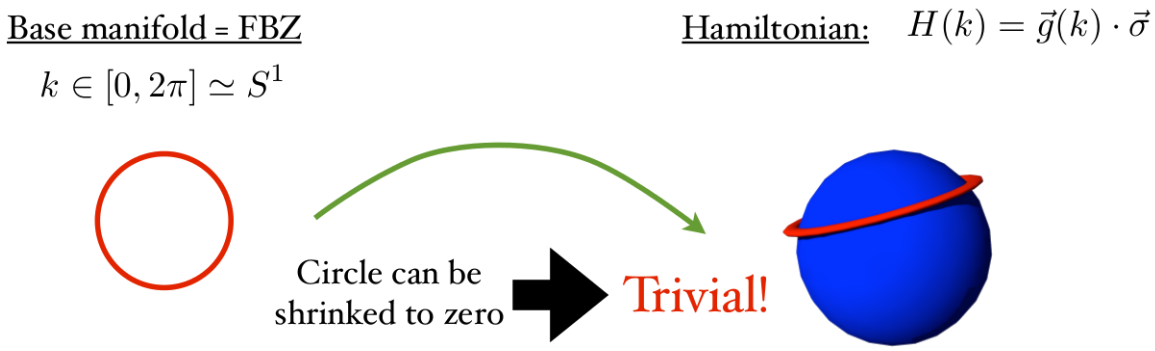

Figure 4.1.1: Mapping from a one dimensional FBZ to a family of parametric Hamiltonians $H(k)$ in the A class. All mappings are equivalent because they can be smoothly connected by deformations of the circle over the 2-sphere surface.

the topological classification of non-interacting systems just takes into account the presence or absence of certain anti-unitary symmetries and the dimensionality of the FBZ. Importantly, other discrete symmetries such as inversion are also important, but they play a different role[66]. However, in combination with TRS and PHS they can have important consequences. An example corresponds to the one of topological insulators in three dimensions, where the Hamiltonian belongs to the simplectic class[3], and just the existence of inversion symmetry allows to reach the topological transition to a non trivial phase[67]. In addition, some discrete crystal symmetries allow to emulate TRS or PHS, and this has allowed to experimentally obtain the called crystal topological insulators (cTI)[68]. Finally, we have not discussed the topological classification of gapless phases. This is out of the scope of this thesis, but their classification is also obtained by means of the topological classification of defects. This is based on the same approach as to gapped phases, but the degeneracy points are included as defects in **k**-space[69, 70].

[3]This class requires five parameters to be varied simultaneously in order to fin an accidental degeneracy.

4.1.1 K-Theory classification

It was noticed that the classification obtained in Table 4.1.1 had some symmetry or repetition pattern, and the table could be written in the form of an 8-hours clock (Figure 4.1.2), where the non-chiral classes lie at the corners of the clock, while the chiral ones are at the edges[69]. This periodicity is easily explained in terms of K-theory, and it is commonly called Bott periodicity[71]. For the classification

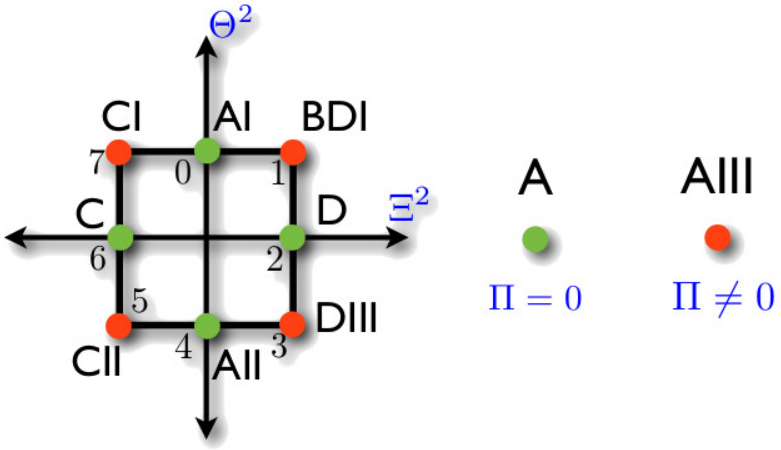

Figure 4.1.2: Eight hours clock for the topological classification of non-interacting systems (real classes). They are arranged in terms of the existence of TRS Θ and PHS Ξ. Green color labels chiral classes while red color labels non chiral ones. On the right is written the two hour clock for the complex classes (the ones without TRS and PHS).

using K-theory one needs to notice that the direct sum of matrices leads to an additional structure of equivalence between Hamiltonians. We shall follow [69] for the introduction: The set of Hamiltonians that conserve the gap separating positive and negative energy states can be simplified without losing any topological information. Consider the transformation of a Hamiltonian $H(\mathbf{k})$ to a simpler Hamiltonian whose eigenvalue spectrum is "flattened", so that the positive and negative energy states all have the same energy $\pm E_0$. Note that this flattened Hamiltonian contains the same topological properties as the initial one, because the gap is not closed when the bands are flattened. This Hamiltonian is specified the set of all n eigenvectors –classified according to a $U(n)$ matrix– modulo unitary rotations within the m conduction bands or the $n-m$ valence bands. The flattened Hamiltonian can thus be identified with a point in the Grassmanian manifold (*classifying space*)

$$G_{n,m} = U(n)/U(m) \times U(n-m). \tag{4.1.8}$$

Next, we can extend the notion of topological equivalence: Two families of Hamiltonians are *stably equivalent* if they can be transformed into one another after adding

an arbitrary number of trivial bands. Stable equivalence can be implemented by considering an expanded classifying space that includes an infinite number of extra conduction and valence bands

$$\mathcal{C}_0 = U/U \times U = \cup_{m=0}^{\infty} G_{\infty,m}. \tag{4.1.9}$$

The addition of two classes, $[\mathcal{H}_1] + [\mathcal{H}_2]$ it is simply given by the direct matrix sum $[\mathcal{H}_1 \oplus \mathcal{H}_2]$, while the subtraction is obtained by reversing conduction and valence bands (change of sign of the bands) $[\mathcal{H}_1] - [\mathcal{H}_2] = [\mathcal{H}_1 \oplus -\mathcal{H}_2]$. The trivial class is then given by $[\mathcal{H} \oplus -\mathcal{H}] = [0]$.

All properties described above for the *stable equivalence classes* allow to form an Abelian group, which is the key element of K-theory. The equivalence among all the gapped Hamiltonians obtained by addition forms a group $K_s\left(BZ\right)$, as it depends on the symmetries and FBZ dimension. If one considers just the long wave length of the theory, and then assumes that the torus of the first Brillouin zone is an sphere, the group can be finally denoted as $K_s\left(S^d\right)$. The advantage of this approach is that it does not rely on the matrix dimensions. Finally, this group has the property:

$$K_{\mathbb{R}}\left(s, S^d\right) = K_{\mathbb{R}}\left(s, S^{d+8}\right), \tag{4.1.10}$$

$$K_{\mathbb{C}}\left(s, S^d\right) = K_{\mathbb{C}}\left(s, S^{d+2}\right), \tag{4.1.11}$$

leading to the two/eight periodicity for complex/real groups (more details in[69]). It is important to comment that in this approach, due to the long wave length approximation, some topological information is missing. This is related with the so called weak topological insulators[72], which can be understood as weakly coupled copies of lower dimensional topological insulators[73].

4.2 Topological properties of time dependent systems

Periodically driven quantum systems has been a fastly growing research field in the last years. The development of effective Hamiltonians describing AC driven systems at certain regimes has allowed to predict novel properties such as topological phases[74, 75, 76, 10, 77], and quantum phase transitions[55, 78] that otherwise would be impossible to achieve in the undriven case. Therefore, the application of AC fields has become a very promising tool to engineer quantum systems. On the other hand, the obtention of effective Hamiltonians can be a difficult task, depending on the driving regime to be considered.

Since the appearance of the firsts proposals to control the topological properties of solid state systems by means of time dependent fields, different approaches have been considered to take advantage of the tunability of the external electric fields and to classify the topological properties of periodically driven systems[11, 79]. The main problem for this classification has been that in time dependent systems the

energy is not a conserved quantity. Thus, the Bloch vector is not defined in terms of the time independent Schrödinger equation, and a different formulation is required. Furthermore, the different approaches to obtain effective Hamiltonians which describe AC driven system are not clearly connected. Next we shall provide a general procedure which connects all these different approaches and allows a complete topological classification. In addition our method establishes a connection between the adiabatic and diabatic regime in terms of a dimensional reduction mechanism.

4.2.1 Dimensional reduction

Here we will prove that time dependent problems with time translational symmetry can be mapped into time independent ones in a higher dimension, in which the time variable can be considered as an additional parameter defined over a compact manifold which can lead to non-trivial topological structures –i.e., it provides an extra direction for the winding. For simplicity, we first illustrate the mechanism of dimensional reduction with a time independent example in a 2 dimensional lattice.

Let us consider a rectangular lattice with periodic boundary conditions in both x, y directions. Then, our system FBZ is defined over a torus $(k_x, k_y) \in FBZ = \left\{\frac{-\pi}{a}, \frac{\pi}{a}\right\} \cup \left\{\frac{-\pi}{b}, \frac{\pi}{b}\right\} = \mathbb{T}^2$ (see Figure 4.2.1(a)). The single particle Bloch Hamiltonian

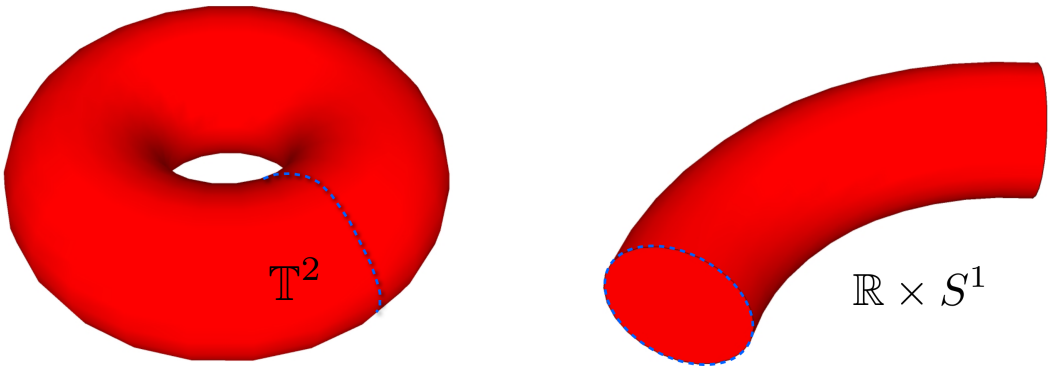

Figure 4.2.1: (a) Torus FBZ for a 2D system with periodic boundary conditions in all directions. (b) Cylinder topology corresponding to a 2D system with a finite boundary in one direction. The blue dotted line shows how the torus is transformed into the cylinder by a cut.

in $\mathbf{k}$ space for this system is diagonal in the annihilation/creation operators $\left\{c_{\mathbf{k}}, c_{\mathbf{k}}^\dagger\right\}$. Then it can be written as:

$$H = \sum_{\mathbf{k}} E_{\mathbf{k}} c_{\mathbf{k}}^\dagger c_{\mathbf{k}}. \tag{4.2.1}$$

Performing a transformation to real space (Wannier basis) by means of inverse Fourier transformations:

$$c_{\mathbf{k}} = \frac{1}{N}\sum_{\mathbf{n}} e^{-i\mathbf{k}\cdot\mathbf{R_n}} c_{\mathbf{n}}, \tag{4.2.2}$$

$$c^{\dagger}_{\mathbf{k}} = \frac{1}{N}\sum_{\mathbf{n}} e^{-i\mathbf{k}\cdot\mathbf{R_n}} c^{\dagger}_{\mathbf{n}}, \tag{4.2.3}$$

we obtain the real space representation or tight binding Hamiltonian:

$$\begin{aligned} H &= \sum_{\mathbf{n},\mathbf{m}} c^{\dagger}_{\mathbf{n}} c_{\mathbf{m}} \sum_{\mathbf{k}} N^{-2} E_{\mathbf{k}} e^{-i\mathbf{k}\cdot(\mathbf{R_n}-\mathbf{R_m})} \\ &= \sum_{\mathbf{n},\mathbf{m}} c^{\dagger}_{\mathbf{n}} c_{\mathbf{m}} \tau_{\mathbf{n},\mathbf{m}}, \end{aligned} \tag{4.2.4}$$

being $\mathbf{R_n}$ the position of the electron and $\tau_{\mathbf{n},\mathbf{m}}$ the hopping energy from site $\mathbf{m} \to \mathbf{n}$. For simplicity we restrict the infinite sum to nearest neighbors:

$$\begin{aligned} H &= \sum_{\langle \mathbf{n},\mathbf{m} \rangle} c^{\dagger}_{\mathbf{n}} c_{\mathbf{m}} \tau_{\mathbf{n},\mathbf{m}} \\ &= \sum_{\mathbf{k}} c^{\dagger}_{\mathbf{k}} c_{\mathbf{k}} \sum_{\langle \mathbf{n},\mathbf{m} \rangle} N^{-2} \tau_{\mathbf{n},\mathbf{m}} e^{-i\mathbf{k}\cdot(\mathbf{R_n}-\mathbf{R_m})} \\ &= \sum_{\mathbf{k}} c^{\dagger}_{\mathbf{k}} c_{\mathbf{k}} \left(\tau_x e^{-ik_x a} + \tau_x e^{ik_x a} + \tau_y e^{-ik_y b} + \tau_y e^{ik_x b} \right) \\ &= \sum_{\mathbf{k}} c^{\dagger}_{\mathbf{k}} c_{\mathbf{k}} 2 \left(\tau_x \cos\left(k_x a\right) + \tau_y \cos\left(k_y b\right) \right), \end{aligned} \tag{4.2.5}$$

where we have used the inverse Fourier transformation to reciprocal space. Comparing Equation 4.2.1 and Equation 4.2.5 we can finally obtain the dispersion relation:

$$E_{\mathbf{k}} = 2 \left(\tau_x \cos\left(k_x a\right) + \tau_y \cos\left(k_y b\right) \right). \tag{4.2.6}$$

Next we calculate the tight binding of the same Hamiltonian, but this time considering a finite stripe in one direction (lets say y-axis). If the stripe is finite along the y-axis, Equation 4.2.4 is Fourier transformed to k space only for the k_x component. Hence, we end up in a mixed representation for the annihilation and creation operators in terms of the real and reciprocal space:

$$\begin{aligned} H &= \sum_{\langle \mathbf{n},\mathbf{m} \rangle} c^{\dagger}_{\mathbf{n}} c_{\mathbf{m}} \tau_{\mathbf{n},\mathbf{m}} \\ &= \sum_{k_x} \sum_{\langle n_y, m_y \rangle}^{N} c^{\dagger}_{k_x,n_y} c_{k_x m_y} \sum_{\langle n_x, m_x \rangle} N^{-1} \tau_{\mathbf{n},\mathbf{m}} e^{-i\mathbf{k}_x\cdot(\mathbf{R_n}-\mathbf{R_m})} \\ &= \sum_{k_x} \sum_{\langle n_y, m_y \rangle}^{N} c^{\dagger}_{k_x,n_y} c_{k_x m_y} \left(\tau_x \delta_{n_y,m_y} e^{-ik_x a} + \tau_x \delta_{n_y,m_y} e^{ik_x a} + \tau_y \delta_{n_y,m_y+1} + \tau_y \delta_{n_y,m_y-1} \right) \\ &= \sum_{k_x} \sum_{\langle n_y, m_y \rangle}^{N} c^{\dagger}_{k_x,n_y} c_{k_x m_y} \left(2\tau_x \delta_{n_y,m_y} \cos\left(k_x a\right) + \tau_y \left(\delta_{n_y,m_y+1} + \delta_{n_y,m_y-1} \right) \right). \end{aligned} \tag{4.2.7}$$

Equation 4.2.7 represents the Hamiltonian of a finite stripe. Its matrix form consists in $N \times N$ matrix (where N is the length of the stripe) which can be considered as a quasi-1D system:

$$H_{N\times N} = \begin{pmatrix} \ddots & \tau_y & 0 & 0 & \iddots \\ \tau_y & 2\tau_x \cos(k_x a) & \tau_y & 0 & 0 \\ 0 & \tau_y & 2\tau_x \cos(k_x a) & \tau_y & 0 \\ 0 & 0 & \tau_y & 2\tau_x \cos(k_x a) & \tau_y \\ \iddots & 0 & 0 & \tau_y & \ddots \end{pmatrix}, \tag{4.2.8}$$

The diagonalization of Equation 4.2.8 leads to the energy spectrum of the stripe, which in general –and depending on the stripe length– will show finite size effects simultaneously with the bulk band structure. Note that the addition of higher neighbors couplings would include new off-diagonal couplings between the diagonal elements.

Finally, let us assume that the periodicity in the y axis is recovered somehow. In topological terms this is very intuitive, and corresponds to gluing up a cylinder in order to make a torus (Figure 4.2.1, (b)). The mathematical formulation only requires to assume that now k_y is a good quantum number, and Fourier transform the operators to reciprocal space:

$$\begin{aligned} H &= \sum_{k_x} \sum_{\langle n_y, m_y \rangle}^{N} c^\dagger_{k_x,n_y} c_{k_x m_y} \left(2\tau_x \delta_{n_y,m_y} \cos(k_x a) + \tau_y \left(\delta_{n_y,m_y+1} + \delta_{n_y,m_y-1} \right) \right) \\ &= \sum_{k_x,k_y} c^\dagger_{k_x,k_y} c_{k_x,k_y} \sum_{\langle n_y, m_y \rangle}^{N} N^{-1} e^{-i\mathbf{k}_y \cdot (\mathbf{R_n} - \mathbf{R_m})} \\ &\quad \times \left(2\tau_x \delta_{n_y,m_y} \cos(k_x a) + \tau_y \left(\delta_{n_y,m_y+1} + \delta_{n_y,m_y-1} \right) \right) \\ &= \sum_{\mathbf{k}} c^\dagger_{\mathbf{k}} c_{\mathbf{k}} \left(2\tau_x \cos(k_x a) + \tau_y \left(e^{-ik_y b} + e^{ik_y b} \right) \right) \\ &= \sum_{\mathbf{k}} c^\dagger_{\mathbf{k}} c_{\mathbf{k}} 2 \left(\tau_x \cos(k_x a) + \tau_y \cos(k_y b) \right). \end{aligned} \tag{4.2.9}$$

Note that we have recovered Equation 4.2.5 as we should expect. This process is roughly the so called *dimensional reduction*, in which if one imposes open boundary conditions along one direction, it is possible to go from a D dimensional parameter space $\{k_x, k_y\}$, to a D-1 parameter space, or the other way around.

4.2.2 Topological properties of time dependent systems

Now let us consider time dependent systems. Here we propose a method which allows to solve with arbitrary accuracy the time evolution and obtain effective Hamiltonians for the different driving regimes. It is based in solutions in Floquet-Bloch form due to

the system symmetries, and the quasi-energies are their corresponding eigenvalues. As we will see below, it allows to formally describe the AC driven D dimensional lattice as analogous to a time independent D+1 dimensional lattice. This description enlightens the underlaying structure of periodically driven systems, in which the initial Bloch band splits into several copies (Floquet-Bloch bands), and the coupling between them directly depends on the driving regime. Interestingly, the isolated Floquet-Bloch bands have the same topological properties as the Bloch bands of the undriven system, now tuned by the external field parameters. Thus, the topological invariants for the isolated Floquet-Bloch bands can be obtained following the general classification of time independent systems – the AZ classes[59, 61] described above. However, we shall also prove that lowering the frequency, the bands couple to each other. In that case the topological structures are classified according to a base manifold of dimension D+1.

Importantly, our procedure is valid for arbitrary dimension and allows to independently analyze the effect of the field amplitude and frequency. We shall show that the field amplitude controls the renormalization of the system parameters, while the frequency acts analogously to a DC electric field along the extra dimension. In particular, this last property relates the high frequency regime with the existence of Bloch oscillations and Landau-Zener transitions between bands[80], establishing a direct relation between diabatic regime and localization[81]. We illustrate the formalism with the analysis of an AC driven homogeneous[8] chain and a dimerized chain[82, 83, 84].

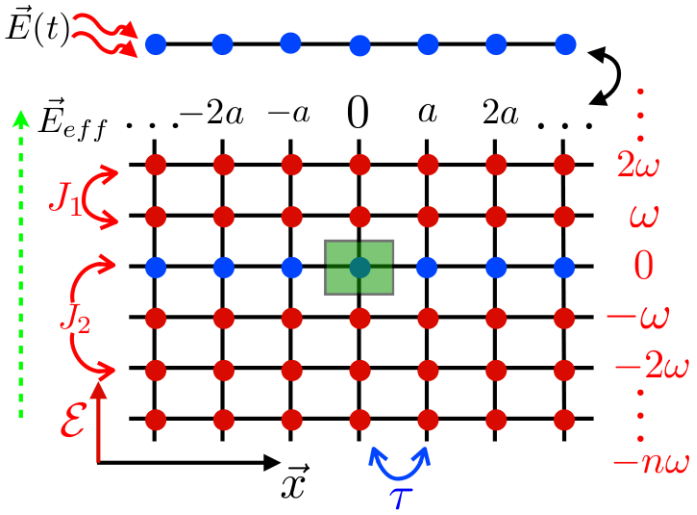

Figure 4.2.2: Equivalence between a periodically driven 1D chain, and the effective static lattice in 2D. Blue dots show the positions of the undressed states at sites ra, $r \in \mathbb{Z}$. Each site is coupled to a set of dressed states (red dots), with coupling $\propto \tau J_p\left(A_0\right)$, being $p = n - m$ the difference in the number of photons, and A_0 the vector potential amplitude. We draw the Wigner-Seitz unit cell (green), and the effective DC electric field along the energy axis $\mathcal{E}$ (green dotted arrow).

Theory: Let us consider a Hamiltonian with lattice and time translation invariance: $H(\mathbf{x}+\mathbf{a}_i, t+T) = H(\mathbf{x}+\mathbf{a}_i, t) = H(\mathbf{x}, t+T)$, characterized by lattice vectors $\mathbf{a}_i$ and time period $T = 2\pi/\omega$. Under these assumptions, we use the Floquet-Bloch ansatz $|\Psi_{\alpha,\mathbf{k}}(\mathbf{x},t)\rangle = e^{i\mathbf{k}\cdot\mathbf{x}-i\epsilon_{\alpha,\mathbf{k}}t}|u_{\alpha,\mathbf{k}}(\mathbf{x},t)\rangle$, being $\epsilon_{\alpha,\mathbf{k}}$ the quasi-energy for the Floquet state, α the pseudo-spin index, and $\mathbf{k}$ the wave-vector. The Floquet-Bloch states $|u_{\alpha,\mathbf{k}}(\mathbf{x},t)\rangle$ are periodic in both $\mathbf{x}$ and t, and map the time dependent Schrödinger equation to an eigenvalue equation for the Floquet states, in which t and $\mathbf{k}$ are both parameters:

$$\begin{aligned} \mathcal{H}(\mathbf{k},t)|u_{\alpha,\mathbf{k}}\rangle &= \epsilon_{\alpha,\mathbf{k}}|u_{\alpha,\mathbf{k}}\rangle, && (4.2.10)\\ \mathcal{H}(\mathbf{k},t) &\equiv e^{-i\mathbf{k}\cdot\mathbf{x}}(H(t)-i\partial_t)e^{i\mathbf{k}\cdot\mathbf{x}} \\ &= H_{\mathbf{k}}(t)-i\partial_t\ , && (4.2.11)\end{aligned}$$

where $\mathcal{H}(\mathbf{k},t)$ is the Floquet operator. Note that the assumption of the Floquet ansatz allowed to map the time dependent Schrödinger equation into an eigenvalue equation, solving one of the initial issues in time dependent systems. Nevertheless, the Floquet operator $\mathcal{H}(\mathbf{k},t)$ contains a time derivative and the treatment of the eigenvalue equation still requires to solve a differential equation. However, due to the time periodicity, the Floquet states can be expressed in terms of its Fourier components $|u_{\alpha,\mathbf{k},n}\rangle$. It allows to consider the composed Hilbert space $\mathcal{S} = \mathscr{H}\otimes\mathcal{T}$[33] for the basis $\{|u_{\alpha,\mathbf{k},n}\rangle\}$, where $\mathcal{T}$ is the space of T-periodic functions and $\mathscr{H}$ the initial Hilbert space. We also define the composed scalar product $\langle\langle\ldots\rangle\rangle = \int_0^T\langle\ldots\rangle dt/T$, which allows to get rid of the time dependence, and the Floquet-Bloch annihilation and creation operators $c(t)_{\alpha,\mathbf{k}}, c(t)^\dagger_{\alpha,\mathbf{k}}$, which satisfy the usual commutation relations $\left[c(t)^\dagger_{\alpha,\mathbf{k}}, c(t)_{\beta,\mathbf{k}'}\right]_\pm = \delta_{\mathbf{k},\mathbf{k}'}\delta_{\alpha,\beta}$ for boson and fermions. Now we demonstrate that an exact mapping between a D dimensional AC driven system and a D+1 undriven one can be established, in which $\mathcal{H}(\mathbf{k},t)$ is equivalent to an static Hamiltonian. It will allow to classify the topological invariants in terms of the mappings from the parameter space to the set of Floquet operators $\mathcal{H}(\mathbf{k},t)$, being the parameter space now given by $S^1\times\mathbb{T}^n$, where n is the dimension of the First Brillouin zone (FBZ).

We first define the Fourier transforms:

$$\begin{aligned} c(t)_{\alpha,\mathbf{k}} &= N^{-D/2}\sum_{j=1}^{N}\sum_{n=-\infty}^{\infty} c_{\alpha,j,n}e^{i\mathbf{k}\cdot\mathbf{R}_j+in\omega t} && (4.2.12)\\ c(t)^\dagger_{\alpha,\mathbf{k}} &= N^{-D/2}\sum_{j=1}^{N}\sum_{n=-\infty}^{\infty} c^\dagger_{\alpha,j,n}e^{-i\mathbf{k}\cdot\mathbf{R}_j-in\omega t}, \end{aligned}$$

where N is the number of sites in the the lattice with periodic boundary conditions and D the dimension of the undriven system. For a time dependent Hamiltonian in the dipolar approximation, the relation between undriven and driven system is given by the minimal coupling $\mathbf{k}\to\mathbf{K}(t) = \mathbf{k}+\mathbf{A}(t)$, where $\mathbf{A}(t)$ is the vector potential (see Appendix B for a formal proof). Thus, one can obtain the time dependent

tight binding by using the minimal coupling in the inverse Fourier transformation, leading to the time dependent hoppings $\tau\left(t\right)_{j,l}^{\alpha,\beta} = \tau_{j,l}^{\alpha,\beta} e^{i\mathbf{A}(t)\cdot(\mathbf{R}_j - \mathbf{R}_l)}$, and being the Hamiltonian:

$$H_{\mathbf{k}}\left(t\right) = \sum_{\alpha,\mathbf{k}} \sum_{j,l} \tau\left(t\right)_{j,l}^{\alpha,\beta} e^{i\mathbf{k}\cdot(\mathbf{R}_j - \mathbf{R}_l)} c\left(t\right)_{\beta,\mathbf{k}}^{\dagger} c\left(t\right)_{\alpha,\mathbf{k}}, \tag{4.2.13}$$

where the time dependence in the operators is now included. Next we expand in Fourier series $c\left(t\right)_{\alpha,\mathbf{k}}$ and $c\left(t\right)_{\alpha,\mathbf{k}}^{\dagger}$ using Equation 4.2.12:

$$H_{\mathbf{k}}\left(t\right) = \sum_{\alpha,\mathbf{k}} \sum_{n,m} \sum_{j,l} \tau\left(t\right)_{j,l}^{\alpha,\beta} c_{\beta,\mathbf{k},n}^{\dagger} c_{\alpha,\mathbf{k},m} e^{i\kappa(t)\cdot\left(\rho_{n,j} - \rho_{m,l}\right)}, \tag{4.2.14}$$

where we have defined the quadrivectors $\kappa\left(t\right) \equiv \left(-t, \mathbf{k}\right)$ and $\rho_{n,j} \equiv \left(n\omega, \mathbf{R}_j\right)$. Equation 4.2.14 gives a description of the time dependent Hamiltonian in terms of the time independent operators $\left\{c_{\alpha,\mathbf{k},n}, c_{\alpha,\mathbf{k},n}^{\dagger}\right\}$. Finally, the use of the composed scalar product allows to obtain the quasi-energies by diagonalization of the matrix:

$$\left\langle\left\langle u_{\beta,\mathbf{k},n} \middle| \mathcal{H}\left(\mathbf{k}, t\right) \middle| u_{\alpha,\mathbf{k},m} \right\rangle\right\rangle = \tilde{\tau}_{n,m}^{\alpha,\beta} - n\omega\delta_{n,m}\delta_{\alpha,\beta}, \tag{4.2.15}$$

$$\tilde{\tau}_{n,m}^{\alpha,\beta} \equiv \frac{1}{T}\int_0^T \sum_{j,l}^{N} \tau\left(t\right)_{j,l}^{\alpha,\beta} e^{i\kappa(t)\cdot\left(\rho_{n,j} - \rho_{m,l}\right)} dt, \tag{4.2.16}$$

where $n\omega\delta_{n,m}$ is the Fourier space representation of $-i\partial_t$. Equation 4.2.15 is analogous to a time independent tight binding in D+1 dimensions with a constant electric field of unit intensity applied along the extra dimension (see Figure 4.2.2). Also, the full Floquet operator would contain a summation over all sites labeled by (n, m), which exactly resembles the mixed representation discussed in Equation 4.2.7. Here, the $\mathbf{k}$ dependence due to the sum over all real space sites (j, l) results in the axis with periodic boundary conditions. On the other hand, the sum in (m, n) represents the axis with a finite size (whenever we consider a finite cut-off for the Floquet side-bands). Finally, note that the effective electric $n\omega$ field breaks translational symmetry along the $\mathcal{E}$ axis, and one can differentiate two regimes: Low and high frequency.

In the low frequency regime ($\omega \ll \tau_{j,i}^{\alpha,\beta}$), it is a good approximation to neglect the effect of the time derivative in the Floquet operator (Equation 4.2.11), or equivalently, the Stark shift due to the effective electric field. Then, we restore the $\mathcal{E}$ axis translational symmetry, and the Floquet operator can be diagonalized by Fourier transformation of Equation 4.2.15 to t domain for an infinite set of Floquet side-bands – This is equivalent to the gluing procedure explained in the previous section for the torus. The obtained $\mathcal{H}\left(\mathbf{k}, t\right)$ is analog to a Hamiltonian over a D+1 compact base manifold, that we define as the First Floquet Brillouin Zone (FFBZ), parametrized by $\{t, \mathbf{k}\} \in S^1 \times \mathbb{T}^n$. Hence, the system topology is classified according to the AZ class of D+1 static Hamiltonians. Note in addition that the low frequency regime resembles the adiabatic approximation, since now the Floquet operator $\mathcal{H}\left(\mathbf{k}, t\right)$ can be identified with an adiabatic Hamiltonian, and its eigenvalues/eigenstates with the instantaneous energies/states. In addition, this approach

contains renormalized hoppings due to the field amplitude in opposition to the fully adiabatic assumption. Then, it can provide new insights into the effect of the AC field on the lattice hoppings.

For high frequency ($\omega \gg \tau_{j,l}^{\alpha,\beta}$), the effective electric field produces Bloch-Zener transitions and Bloch oscillations[80, 81], inducing localization in $n\omega$, and decoupling the Floquet bands. Then, Equation 4.2.15 becomes almost block-diagonal in Fourier space, and the effective Floquet operator becomes approximately time independent. In consequence, it is defined over a D dimensional base manifold $\mathbf{k} \in \mathbb{T}^n$ (FBZ), and the topological classification is given in terms of the AZ classes for time independent systems in D dimensions. The transition from a D+1 to a D dimensional base manifold (equivalently, from the FFBZ to the FBZ), as one increases the frequency ω, is driven by the non-adiabatic processes in time[15].

Importantly, note that in general the hopping between n, m neighbors depends on the amplitude of the vector potential (Equation 4.2.16). It allows to design "effective lattices" by tuning the hoppings with the AC field[85].

4.2.3 Periodically driven linear quantum chain

As a first example, let us consider the case of a quantum linear chain in the x direction, with nearest neighbors coupling $\tau_{ij} = \tau$ for $i \pm 1 = j$ and $\tau_{ij} = 0$ otherwise. This is a model previously studied by Holthaus[8] in the context of coherent destruction of tunneling in superlattices. Although he mainly studied the electron dynamics in the high frequency regime, some of his results will be useful to check our approximations, and we shall also describe the low frequency regimes. The tight binding Hamiltonian of the undriven system for spinless electrons is:

$$\begin{aligned} H &= \sum_{k}^{\mathrm{FBZ}} N^{-1} c_k^\dagger c_k \sum_{\langle i,j \rangle} e^{ik\cdot(R_i - R_j)} \tau_{ij} \\ &= \tau \sum_{k}^{\mathrm{FBZ}} c_k^\dagger c_k \left(e^{ika_0} + e^{-ika_0} \right) \\ &= 2\tau \sum_{k}^{\mathrm{FBZ}} \cos\left(ka_0\right) c_k^\dagger c_k, \end{aligned}$$

and its energy dispersion relation is given by:

$$E_k = 2\tau \cos\left(ka_0\right). \tag{4.2.17}$$

Next, let us consider the application of the AC electric field under the dipolar approximation $A\left(x,t\right) \simeq A\left(x_0,t\right)$, being x_0 the position of the region we are studying. We can couple the system to the field by means of the minimal coupling

$k \to K(t) = k + A(x_0, t)$, as we previously described, leading to the time dependent Hamiltonian:

$$\begin{aligned} H(t) &= 2\tau \sum_{k}^{\text{FBZ}} \cos\left(ka_0 + qE_0 a_0 \sin(\omega t)/\omega\right) c_k^{\dagger}(t)\, c_k(t), && (4.2.18)\\ &= \sum_{k} H_k(t)\, c_{k\sigma}^{\dagger}(t)\, c_{k\sigma}(t), && (4.2.19)\\ A(t) &\equiv qE_0 \sin(\omega t)/\omega, && (4.2.20) \end{aligned}$$

where q is the charge of the particle, and $E(t) = -\partial_t A(t)$ the AC electric field. To obtain the quasi-energies we need to calculate the matrix elements in Sambe space:

$$\begin{aligned} H_p = \frac{1}{T}\int_0^T H_k(t)\, e^{ip\omega t} dt = 2\tau \cos(ka_0)\, J_{p=\text{even}}\left(\frac{qE_0 a_0}{\omega}\right) \\ - 2i\tau \sin(ka_0)\, J_{p=\text{odd}}\left(\frac{qE_0 a_0}{\omega}\right), \end{aligned} \quad (4.2.21)$$

where $p = n - m$, and we have used $J_p\left(\frac{qE_0}{\omega}a_0\right) = \frac{1}{2\pi}\int_0^{2\pi} e^{iqE_0 a_0 \cos\theta/\omega} e^{-ip\theta} d\theta$, $J_p(-x) = J_p(x)\ \ \forall p$ even, and $J_p(-x) = -J_p(x)\ \ \forall p$ odd. The resulting matrix corresponds to the Fourier space representation of the Hamiltonian. The Floquet operator is given by $\mathcal{H}_p = H_{n,m} - n\omega\delta_{n,m}$ and its eigenvalues are the quasi-energies. In order to obtain simple analytical results we shall consider first the high frequency regime, which restricts the couplings between Floquet side-bands assuming that they are decoupled – physically restricts the number of photons which can be exchanged with the external field in a single process. For $p = 0$ we obtain the quasi-energies:

$$\epsilon_{\beta,k}^{(0)} = 2\tau J_0\left(\frac{qE_0}{\omega}a_0\right)\cos(ka_0), \quad (4.2.22)$$

where we have selected the side-band $n = 0$ – note that in this approximation all side-bands are decoupled and equivalent. As we can see from Figure 4.2.3, the k dependence of the quasi-energies has been obtained as well as their dependence on the ratio between the field amplitude and the frequency E_0/ω, which renormalizes the hopping by Bessel functions $\tau \to \tau J_0\left(\frac{qE_0}{\omega}a_0\right)$. In agreement with [8], we have obtained the mini bands collapse for the zeroes of the Bessel function (Figure 4.2.3, b). At $qE_0 a_0/\omega = 2.404$ the quasi-energy becomes flat, meaning infinite effective mass and charge localization. Besides, our result allow us to determine the full evolution of the tight binding system, as this is a complete solution when more side-bands are included.

Before we discuss the effect of lower frequencies, note that this system contains just a single atom per unit cell, and the solutions are not spinors. It implies that we do not transport a vector frame over the FBZ or the FFBZ. Thus, special topological features are not expected and we shall not analyze them in this example.

Figure 4.2.3 shows the dependence on k and on the external field parameters for the quasi-energies at the high frequency regime. As we vary the value of the intensity

E_0, the energy dispersion relation is renormalized by $J_0\left(qE_0a_0/\omega\right)$. Importantly, the Bessel function can change its sign, inverting the dispersion relation. This will play an important role in the topological properties in terms of band inversions. The

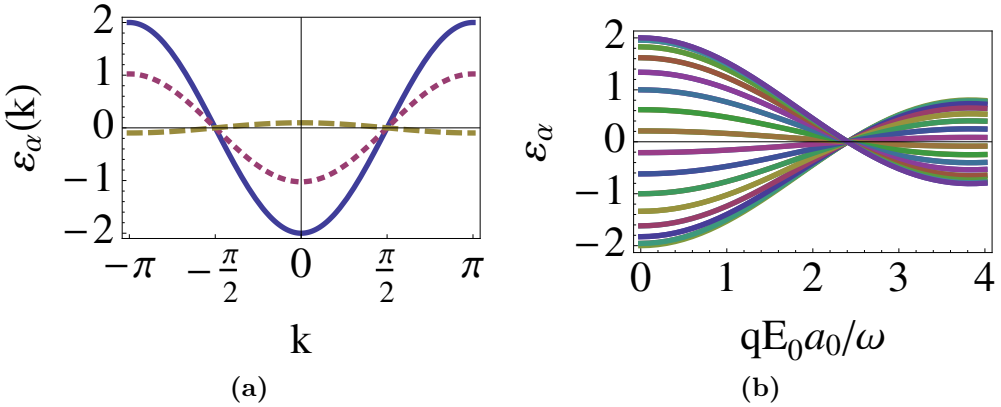

Figure 4.2.3: (a) Quasi-energy renormalization vs k. The blue solid line shows the limit $E_0 = 0$ without renormalization (undriven system). Yellow and red lines show the renormalization at non zero field and high frequency. Parameters: $qE_0a_0/\omega = 1.5$ (red dotted), $qE_0a_0/\omega = 2.5$ (yellow dashed), $\omega = 10$ and $\tau = -1$. (b) Quasi-energies vs qE_0a_0/ω for different k values equally spaced within the FBZ and $\tau = -1$. Note the mini bands collapse at the first zero of the Bessel function.

use of lower frequencies increases the photon mediated transitions, and reduces the size of the Floquet side-bands $\epsilon_{\alpha,k} \in [-\omega/2, \omega/2]$. Further, the side-bands cannot be considered as decoupled, as they interact through the couplings $J_{p>0}\left(A_0a_0\right)$. The addition of higher order processes leads to a Floquet Hamiltonian given by:

$$\epsilon_{\beta,k} = 2\tau \begin{pmatrix} \ddots & \vdots & \vdots & \vdots & \iddots \\ \dots & J_0\left(A_0\right)\cos\left(k\right) - \omega & -iJ_1\left(A_0\right)\sin\left(k\right) & J_2\left(A_0\right)\cos\left(k\right) & \dots \\ \dots & iJ_1\left(A_0\right)\sin\left(k\right) & J_0\left(A_0\right)\cos\left(k\right) & -iJ_1\left(A_0\right)\sin\left(k\right) & \dots \\ \dots & J_2\left(A_0\right)\cos\left(k\right) & iJ_1\left(A_0\right)\sin\left(k\right) & J_0\left(A_0\right)\cos\left(k\right) + \omega & \dots \\ \iddots & \vdots & \vdots & \vdots & \ddots \end{pmatrix}. \tag{4.2.23}$$

Note that the Floquet bands coupling just depends on the ratio qE_0a_0/ω, while ω shifts the on site energy of the different Floquet side-bands. Therefore, a change in frequency reduces the FFBZ size and does not affect the couplings if we keep the same value for the ratio E_0/ω. In Figure 4.2.4 we show a comparison between the zeroth order approximation (red) and the exact calculation (blue) where the FFBZ has been plotted in green color. The fact that the near resonant regime is described very accurately by the decoupled bands limit is very particular for this case and will be analyzed below.

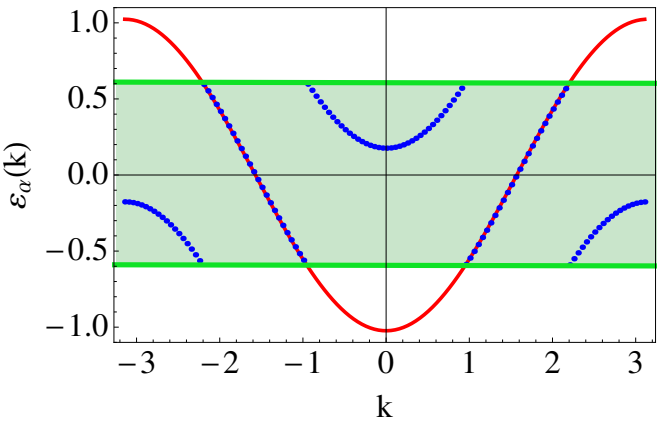

Figure 4.2.4: Quasi-energy dispersion for $qE_0a_0/\omega = 1.5$, $\omega = 1.2$ and $\tau = -1$. The plot shows the zeroth order approximation (red solid line), and the numerical calculation with $p_{max} = 10$ and 50 sidebands (blue dotted line). The filled area $\epsilon_{\alpha,k} \in [-0.6, 0.6]$ corresponds to the FFBZ of the system. Note that the decrease of the frequency leads to a mix of Floquet bands inside the FFBZ.

Comparison with finite tight binding models

In this section we consider a finite tight binding model in a different gauge. It will allow to compare our previous results, check the gauge invariance, and include the finite size effects. The system is described by the well known and commonly used Hamiltonian for AC driven systems[40]:

$$H_F(t) = \sum_{j=1}^{M} \{\Delta|j\rangle\langle j+1| + \text{h.c.} + qE_0x_j\cos(\omega t)\,|j\rangle\langle j|\}\,, \tag{4.2.24}$$

where j labels the site, and x_j is the position operator. Note that this Hamiltonian is in a different gauge, and then it allows to compare the Peierls substitution with the position dependent coupling term of the Hamiltonian. We consider the Floquet Hamiltonian $\mathcal{H}(t) = H(t) - i\partial_t$ and its description in Sambe space given by:

$$\mathcal{H} \equiv \sum_{n,m=-\infty}^{\infty}\sum_{j=1}^{M}\left\{(\Delta|j\rangle\langle j+1| + \text{h.c.} - \omega n)\,\delta_{n,m} + q\frac{E_0a_0}{2}j|j\rangle\langle j|\,(\delta_{n+1,m} + \delta_{n-1,m})\right\},$$

In Figure 4.2.5, (a) we show the quasi-energies vs qE_0a_0/ω obtained by diagonalization of the Floquet operator for the model with periodic boundary conditions. Figure 4.2.5, (b) shows the spectrum for the finite tight binding model. An excellent agreement between both is obtained in the high frequency regime, with the advantage that the analytical calculation for the model with periodic boundary conditions just requires to diagonalize a 2x2 matrix (Equation 4.2.22), while the numerical calculation for the finite model requires 65 side-bands to reach convergence. In Figure 4.2.6 we show the previous comparison but now for the case $\omega = 1.5|\tau|$,

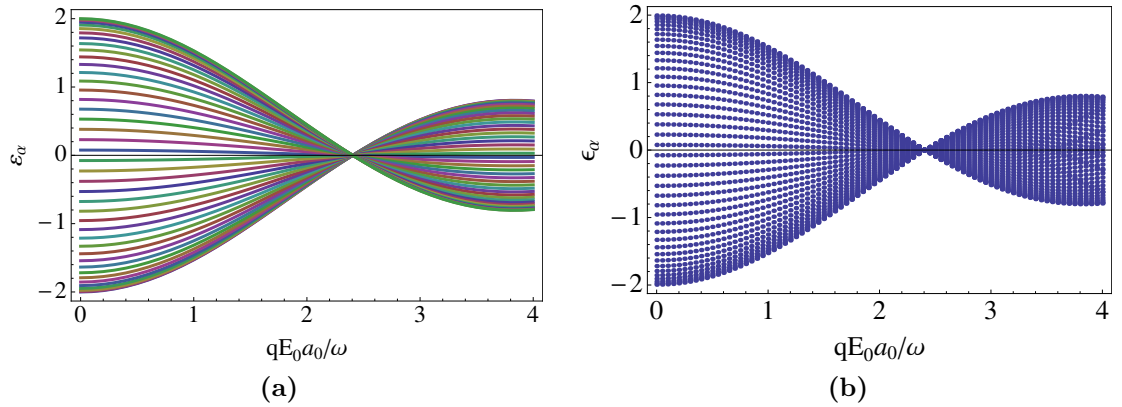

Figure 4.2.5: Comparison between the analytical model with periodic boundary condition and the direct calculation of the spectrum for a finite chain, both at high frequency regime. (a) Shows the analytical result using 40 equally spaced k vectors within the FBZ, while (b) shows the case of a finite chain with 40 sites. We have considered $\tau = -1$ and $\omega = 10|\tau|$.

where the high frequency regime does not hold. The decrease of the frequency mixes the different side-bands and in consequence, the finite tight binding model at this frequency regime requires a much larger number of side-bands to reach convergence (we have considered 150 side-bands). Interestingly, finite size effects are observed in Figure 4.2.6, (b), in the form of two states which does not collapse at the first zero of the Bessel function. In addition, for Figure 4.2.6, (a) we have checked that the avoided crossings between quasi-energies become exponentially reduced as we increase the size of the chain. It is also important to observe that zero energy modes –linked to the topological properties– does not arise in this system due to the lack of a spinor solution.

Stark effect along the extra dimension

Here we discuss in detail the interpretation of the Floquet operator in terms of a higher dimensional lattice coupled to a constant electric field. As we argued above, the Floquet operator can be considered as a time independent tight binding Hamiltonian in a higher dimensional system. There, the time derivative operator plays the role of a constant electric field, producing a Stark shift along the extra dimension, tilting the on-site energy. For simplicity we shall restrict the couplings between Floquet bands up to a maximum number of neighbors, depending on the field intensity.

If we consider low intensity, the Bessel functions fulfill $J_1(A_0) \gg J_{p>1}(A_0)$. Then, we can assume first neighbors coupling between Floquet side-bands and the Floquet

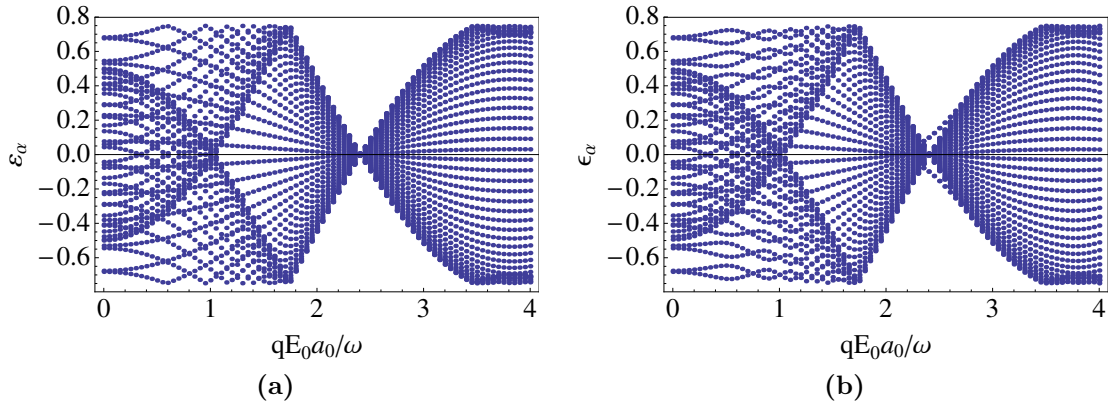

Figure 4.2.6: Comparison for $\omega = 1.5|\tau|$ between the finite chain with $M = 40$ (b) and the chain with periodic boundary conditions (a) considering 40 equally spaced k vectors within the FBZ. The avoided crossings between quasi-energies within the band for the finite chain are due to finite size effects, and the increase of the number of atoms in the chain makes these gaps tend to zero. We have considered $\tau = -1$, and 150 sidebands for the finite tight binding model.

operator reads:

$$\mathcal{H}(k,t) = 2\tau J_0(a_0 A_0)\cos(ka_0) + 4\tau J_1(A_0 a_0)\sin(k)\sin(\omega t) - i\partial_t. \quad (4.2.25)$$

Fortunately, in the present single band model we can exactly solve the Floquet equation by direct integration of the Floquet operator, leading to the exact quasi-energies:

$$\epsilon_{m,k} = \omega m + 2\tau J_0(A_0 a_0)\cos(ka_0), \quad (4.2.26)$$

The eigenstates are also obtained by integration:

$$\phi_m(t) = \exp\{im\omega t + 4i\tau J_1(A_0 a_0)\sin(ka_0)\cos(\omega t)/\omega\}, \quad (4.2.27)$$

and importantly, they can be interpreted as Wannier-Stark states for the Floquet operator $\mathcal{H}(k,t)$, which belong to the Sambe space. We can Fourier transform this state to obtain its frequency distribution, and it can be seen that is proportional to:

$$|\phi_m\rangle \propto \sum_n J_{m-n}(4\tau J_1(A_0 a_0)\sin(ka_0)/\omega)|n\rangle. \quad (4.2.28)$$

The frequency representation shows the spreading of the wave function along the different harmonics of the field – or equivalently, the distribution of photons dressing the electron – which depends on the ratio τ/ω. Thus, it is clear that for high frequency $\tau \ll \omega$ just the $m = n$ level is occupied, meaning localization in a single Floquet side-band as we stated above. In general, just the levels $|m - n| < 4\tau J_1(A_0 a_0)\sin(ka_0)/\omega$ have significant occupation.

It is important to comment that this result generalizes Holthaus analysis for all driving regimes – higher field amplitudes just require to include a larger number of couplings. However, as we shall show below for the dimer chain, it is not common to find an exact solution for the Floquet equation in models with two or more bands.

In summary, the comparison shows that the solutions of Floquet systems have similar properties to Stark ladders: spreading in position depending on the ratio between the field intensity and the hopping parameter. We have shown the efficiency of the calculation for time dependent systems when periodic boundary conditions are included, and how to relate the undriven system with the driven. Finally, we have shown how to perform the calculations in Sambe space. However, this case with a single band is too simple for our purposes, because it does not contain topological structures. For such purpose, we need to consider a spinor solution, and hence, a system with at least two bands.

4.2.4 Dimers chain

Here we consider a dimers chain coupled to an AC electric field. The undriven system has been tediously studied in the physical context of soliton waves in Polyacetilene[82, 83, 84]. The tight binding is characterized by the hoppings τ and τ' (Figure 4.2.7), and the AC electric field considered in this work $E(t) = -\partial_t A(t)$ is defined in terms of the vector potential $A(t) = A_0 \sin(\omega t)$, where $A_0 \equiv qE_0/\omega$. The tight binding

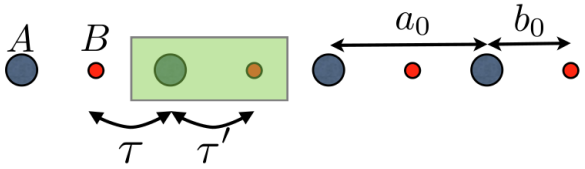

Figure 4.2.7: Schematic figure for a dimers chain with two inequivalent atoms (A, B) for unit cell (green area). b_0 is the intra-dimer distance, a_0 the lattice translation vector, and $\tau'(\tau)$ the intra(inter) dimer hopping.

model for the undriven system in the nearest neighbors approximation is given by:

$$\begin{aligned} H_k &= \begin{pmatrix} 0 & \rho(k) \\ \rho(k)^* & 0 \end{pmatrix}, \\ \rho(k) &\equiv \tau' e^{-ikb_0} + \tau e^{ik(a_0 - b_0)}, \end{aligned} \tag{4.2.29}$$

$$E_\pm = \pm\tau\sqrt{\lambda^2 + 1 + 2\lambda\cos(ka_0)}, \tag{4.2.30}$$

in the spinor basis $\Psi = (\Psi_{A,k}, \Psi_{B,k})^T$, and with $\lambda \equiv \tau'/\tau$ (see Figure 4.2.7). Importantly, the dispersion relation in Equation 4.2.30 does not depend on b_0, and for the condition $b_0 = a_0/2$, and $\tau = \tau'$ in H_k one recovers the energy spectrum of the

linear chain – performing a Peierls transition. By means of the minimal coupling $k \to k + A(t)$ we arrive at the time dependent Hamiltonian:

$$\begin{aligned} H_{K(t)} &= \tau \begin{pmatrix} 0 & \rho(k,t) \\ \rho(k,t)^* & 0 \end{pmatrix}, \\ \rho(k,t) &\equiv \lambda e^{-i(k+A_0\sin(\omega t))b_0} + e^{i(k+A_0\sin(\omega t))(a_0-b_0)}. \end{aligned}$$

Note that here the vector potential only acts along the x-axis. The reason is that perpendicular electric fields would not affect the electron dynamics, since this are restricted to move just along one dimension. In order to calculate $\tilde{\tau}^{\alpha,\beta}_{n,m}$, we use the identity $J_n(x) = \frac{1}{T}\int_0^T e^{ix\sin(\omega t) - in\omega t}dt$, leading to:

$$\tilde{\tau}^{\alpha,\beta}_{n,m} = \tau \begin{pmatrix} 0 & \rho_F(k) \\ \tilde{\rho}_F(k) & 0 \end{pmatrix}, \tag{4.2.31}$$

$$\begin{aligned} \rho_F(k) &\equiv \lambda e^{-ikb_0} J_{n-m}(A_0 b_0) \\ &\quad + e^{ik(a_0-b_0)} J_{m-n}(A_0(a_0-b_0)), \\ \tilde{\rho}_F(k) &\equiv \lambda e^{ikb_0} J_{m-n}(A_0 b_0) \\ &\quad + e^{-ik(a_0-b_0)} J_{n-m}(A_0(a_0-b_0)). \end{aligned} \tag{4.2.32}$$

Where the matrix elements of the Floquet operator are given by:

$$\mathcal{H}^{(n,m)}_{k,(\alpha,\beta)} = \tilde{\tau}^{\alpha,\beta}_{n,m} - n\omega\delta_{n,m}\delta_{\alpha,\beta}. \tag{4.2.33}$$

Note that the last term of Equation 4.2.33 is just the Fourier transform of the time derivative operator. As we discussed before, the Floquet operator in Sambe space is an infinite dimensional matrix, because $(n,m) \in \mathbb{Z}$. In the high frequency regime ($\omega \gg \tau, \tau'$), the second term in the right hand side of Equation 4.2.33 dominates, and the matrix is approximately block diagonal. Thus, we select the Floquet band $m = n = 0$ for simplicity, and the effective Hamiltonian is given by the 2×2 matrix:

$$\begin{aligned} \mathcal{H}^{(0)}_k &= \tau \begin{pmatrix} 0 & \rho^{(0)}_F \\ \left(\rho^{(0)}_F\right)^* & 0 \end{pmatrix}, \\ \rho^{(0)}_F &\equiv \lambda J_0(A_0 b_0) + e^{ika_0} J_0(A_0(a_0-b_0)). \end{aligned} \tag{4.2.34}$$

Note that we have considered $\rho^{(0)}_F$ in a different basis than in Equation 4.2.32. Both basis differ in a phase factor $e^{\pm ikb_0}$, and the reason is that in order to properly obtain the topological properties we must consider the closed lifts basis[86, 24]. The quasi-energy spectrum at high frequency is:

$$\epsilon^0_{\pm,k} = \pm\tau\sqrt{\lambda^2 J_0^2(x) + J_0^2(y) + 2\lambda\cos(ka_0) J_0(x) J_0(y)}, \tag{4.2.35}$$

In contrast with the undriven case, the spectrum now depends on the intra-dimer distance b_0 and the hoppings are renormalized by the field amplitude. Importantly,

note that for the limit $A_0 \to 0$ the quasi-energies match the energies of the undriven system. Figure 4.2.8 shows the quasi-energy spectrum in high frequency regime for periodic boundary conditions. We have included in green dotted lines the regions of existence of edge states, obtained from the numerical calculation of the finite size system with Hamiltonian $H(t) = H_0 + qE(t)x$, being H_0 the time independent tight binding Hamiltonian and $qE(t)x$ the coupling with the electric field term. The appearance of zero energy modes is a finite size effect linked to the underlaying

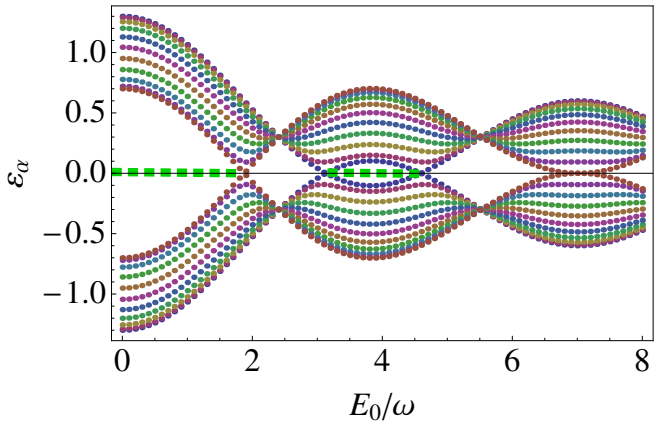

Figure 4.2.8: Quasi-energy spectrum vs E_0/ω for $\lambda = 0.3$, and $b_0 = 0$, considering Equation 4.2.36 (high frequency). The band structure is obtained by taking 10 k vectors equally spaced within the FBZ. We also included in green color the gapless modes obtained from the numerical calculation with $\omega = 10\tau$.

topology of the system. The bulk to edge correspondence relates the number of zero energy modes at the boundary, carrying a topological number, with the bulk topological invariants[87]. Therefore, the calculation of the topological invariants of $\mathcal{H}_k^{(0)}$ should predict their existence in this regime (Figure 4.2.8). The Floquet operator in the high frequency regime can be rewritten in terms of the Anderson vector as follows:

$$\mathcal{H}_k^{(0)} = \tau \vec{g}(k) \cdot \vec{\sigma}, \tag{4.2.36}$$

where $\vec{g}(k) = (\Re(\tilde{\rho}_F), \Im(\tilde{\rho}_F), 0)$ for $n = m = 0$, and $\vec{\sigma} = (\sigma_x, \sigma_y, \sigma_z)$ are the Pauli matrices. $\mathcal{H}_k^{(0)}$ belongs to the BDI class (as the one corresponding to the undriven system), with time reversal, particle-hole, and chiral symmetry[61]. In 1D, the BDI class is characterized by a winding number ν_1, which classifies mappings $\mathbb{T}^1 = S^1 \to \mathbb{R}^2 - \{0\} \simeq S^1$, from the FBZ to the family of Hamiltonians $\mathcal{H}_k^{(0)}$:

$$\begin{aligned} \nu_1 &= \oint \langle u_{\alpha,k} | i\partial_k | u_{\alpha,k} \rangle dk \\ &= \frac{\pi}{2}\left(1 + \text{sign}\left(J_0^2(y) - \lambda^2 J_0^2(x)\right)\right), \end{aligned} \tag{4.2.37}$$

where $y \equiv A_0 (a_0 - b_0)$, $x \equiv A_0 b_0$, and $|u_{\alpha,k}\rangle$ are the eigenstates of $\mathcal{H}_k^{(0)}$. Equation 4.2.37 shows that in contrast with the undriven case[84], one can create non-trivial topological phases even for $\lambda > 1$, where the undriven system is in the trivial phase (Figure 4.2.9, a). This is an example of topology induced by the driving in the high frequency regime.

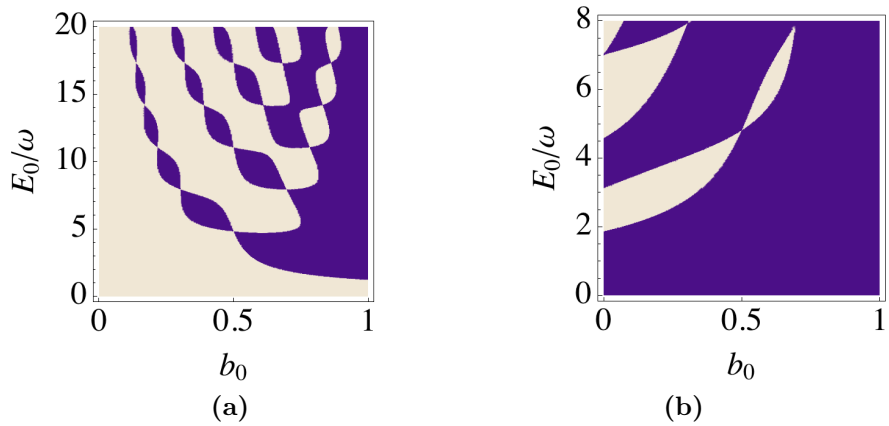

Figure 4.2.9: Topological phase diagram at high frequency for an AC driven dimers chain with $\lambda = 1.5$ (a), and $\lambda = 0.3$ (b). Dark blue color represents $\nu_1 = \pi$ areas, while light areas represent $\nu_1 = 0$. Note that even for $\lambda > 1$ we can induce a non-trivial topology, in contrast with the undriven case. Further, the phase diagram for $\lambda = 0.3$ (b) agrees with the existence of edge states in Figure 4.2.8 (line $b_0 = 0$).

In Figure 4.2.9 (b) we plot the phase diagram for $\lambda = 0.3$, which correctly predicts the existence of edge states for Figure 4.2.8. Then, we have shown that in the high frequency regime, the topological properties can be obtained using an effective static Hamiltonian $\mathcal{H}_k^{(0)}$, and that they can be tuned by the field amplitude. In addition, in the high frequency regime it is possible to obtain an effective Hamiltonian including corrections by finite coupling between Floquet bands –This will be analyzed for the case of two dimensional systems in the next chapter. However, in for the current setup the corrections are not very important.

As we decrease the frequency, the different Floquet bands couple to each other, and the isolated band picture is not accurate. In this regime, one must consider the full Floquet operator (Equation 4.2.15), which for this system is not exactly solvable. Nevertheless, some general features can be obtained as we described above. Due to the coupling between Floquet bands, two different but related effects happen as ω is reduced: Bands inversions due to gap closures, and the emergence of the D+1 parameter space.

Band inversions: The concept of band inversions will be further analyzed in the next section. However, we will briefly discuss here the main characteristics of Floquet

bands describing periodically driven system.

As we have seen above, a time dependent system with, for example two bands, becomes a system with infinite number of bands when this is mapped to Sambe space. Importantly, these bands appear as a consequence of the multivaluedness of the quasi-energies and they are just copies shifted $m\omega$ $\forall m \in \mathbb{Z}$. This allows to study all Floquet states properties within a single side-band. However an important difference with the two initial bands happens: two inequivalent gaps can be defined now. We shall call them Δ_0 when the gap lies *between the valence and conduction band within the same side-band* (this can be considered as the usual gap in the undriven system), or Δ_π when the gap lies *between the valence and conduction band of neighboring side-bands*. Note that these two gaps are inequivalent as they cannot be connected through a ω shift. Importantly, the high frequency regime corresponds to the atomic limit for the gap Δ_π – meaning that topologically protected states will not cross this gap – while the Δ_0 is the one which can be tuned by the field amplitude and can host topological states. The topological transition from diabatic to adiabatic regime obtained in Chapter 2 corresponds to the one happening when the gap Δ_π is closed due to a frequency decrease.

Bands inversions correspond to crossings of the bands, in which the symmetry of the associated eigenvectors changes – it occurs in quantum wells of HgTe/CdTe as the well thickness reaches a critical value[9, 67]. This effect happens in AC driven systems as we decrease the frequency, because the distance between Floquet bands is proportional to ω and thus the gaps $\Delta_{0,\pi}$ can be affected and closed by the frequency decrease. If the width of an isolated Floquet band, for a given field amplitude, is given by $\delta\epsilon \leq \omega$, where $\epsilon_\alpha \in [-\omega/2, \omega/2]$, the Floquet bands at $\pm\omega$ close the gap $\Delta_{0,\pi}$ when $\omega_1 = \delta\epsilon/2$ and $\omega_2 = \delta\epsilon$. As a general rule band closures happen for every:

$$\omega_0(n) = \frac{\delta\epsilon}{2n},\ \omega_\pi(n) = \frac{\delta\epsilon}{2n-1},\ n \in \mathbb{Z}^+, \tag{4.2.38}$$

where $\mathbb{Z}^+$ denotes the set of positive integers. Therefore, at $\omega_{0,\pi}(n)$ the $\pm n\omega$ Floquet bands close the gap $\Delta_{0,\pi}$ modifying the topological properties. Note that this picture is based on the assumption that the Floquet bands are weakly interacting. Then, corrections proportional to ω and A_0 can change the exact frequency values, although the order of the gap closures would still be correctly described.

In addition, it is possible to track the bands inversions in terms of the band structure of the undriven system, considering the band width $\delta\epsilon$ for $A_0 \to 0$. The width $\delta\epsilon$ of the dimers chain for $b_0 = 0$, $\lambda = 0.5$ and $A_0 = 0$ is given by $\delta\epsilon = \delta E = 2\tau\sqrt{1+\lambda^2+2\lambda} = 3\tau$. Then, according to Equation 4.2.38 the first band inversion would happen at $\omega_\pi = 3\tau$, and a second one at $\omega_0 = 1.5\tau$. Figure 4.2.10 shows the band structure of the dimers chain for $\omega = 2\tau$ and τ. Importantly for this model, the closure of the gap Δ_π does not lead to the appearance of zero energy modes within that gap (Figure 4.2.10, left). However, the closure at $\omega_0 = 1.5\tau$ has exchanged the order of appearance of zero energy modes, and as an example, if our system is

initially at $E_0/\omega \simeq 2$ in the high frequency regime, for $\omega = 1.5\tau$ a transition to a non trivial phase happens and zero energy modes arise . Then, it is clear that the decrease of frequency can also drive topological phase transitions.

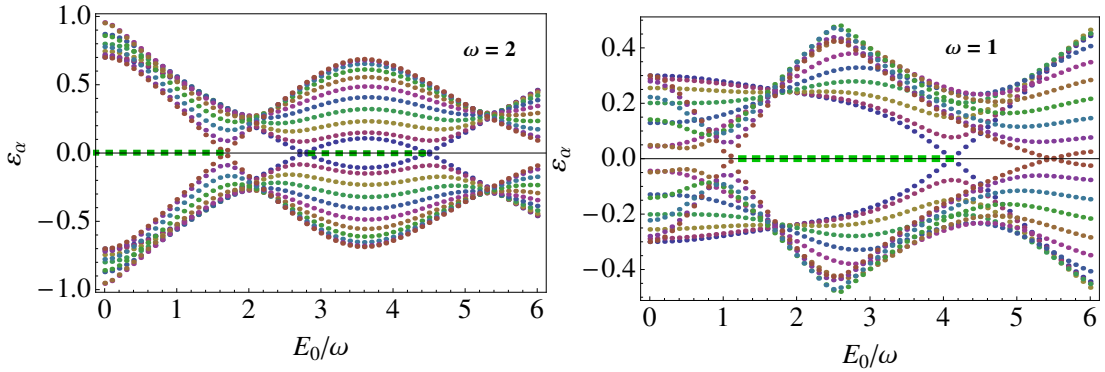

Figure 4.2.10: Quasi-energies vs $A_0 = E_0/\omega$ for different frequencies considering periodic boundary conditions. In dotted green color we plot the boundary states, which has been obtained using a finite tight binding model. Left figure shows the quasi-energies for $\omega = 2\tau$, where the Δ_0 gap is not yet inverted. The right figure considers a lower frequency ($\omega = 1\tau$) where the gap Δ_0 has been inverted. Importantly, the comparison between left and right figures shows that the order in which the boundary states appear as a function of A_0 is exchanged.

For $\omega \ll \tau, \tau'$, a large number of bands inversions occur, being difficult to track all of them. In addition, the presence of a D+1 base manifold becomes important. For the treatment of such a low frequency regimes let us start from the Floquet operator in time domain:

$$\left(H\left(k,t\right) - i\partial_t\right)\left|u_{\alpha,k}\right\rangle = \epsilon_{\alpha,k}\left|u_{\alpha,k}\right\rangle. \tag{4.2.39}$$

To carry out the explicit calculation of $\mathcal{H}\left(k,t\right)$, we can notice in Equation 4.2.32 that the coupling between different Floquet bands depends just on the amplitude of the vector potential A_0 and not in the frequency ω. If we assume $A_0 \leq 1$, we can safely neglect the contributions from $J_{p>2}\left(A_0\right)$, leading to an effective time dependent Hamiltonian up to next nearest neighbors:

$$\begin{aligned} H\left(k,t\right)_{\text{NNN}} &= \tau \begin{pmatrix} 0 & \rho_F\left(k,t\right) \\ \rho_F\left(k,t\right)^* & 0 \end{pmatrix}, \\ \rho_F\left(k,t\right) &\equiv \lambda J_0\left(x\right) + 2i\lambda J_1\left(x\right)\sin\left(\omega t\right) \\ &\quad +2\lambda J_2\left(x\right)\cos\left(2\omega t\right) + e^{ika_0}J_0\left(y\right) \\ &\quad -2e^{ika_0}\left(iJ_1\left(y\right)\sin\left(\omega t\right) - J_2\left(y\right)\cos\left(2\omega t\right)\right), \end{aligned} \tag{4.2.40}$$

which, in the limit $A_0 \to 0$, becomes the energy dispersion of the undriven system. Unfortunately, Equation 4.2.39 is not exactly solvable for the time dependent Hamiltonian $H\left(k,t\right)_{\text{NNN}}$. However, for frequency values $\omega \ll \tau, \tau'$ we can neglect

the time derivative (or equivalently neglect the last term of Equation 4.2.33) and approximate $\mathcal{H}(k,t) \simeq H(k,t)_{\mathrm{NNN}}$. This effective Hamiltonian resembles the adiabatic evolution of a periodically driven dimers chain at low field amplitudes. Then, Equation 4.2.39 describes an eigenvalue equation, and we can classify the mappings $(k,t) \to \mathcal{H}(k,t)$, from the FFBZ to the set of Floquet operators:

$$\mathcal{H}(k,t) = \tau \vec{g}(k,t) \cdot \vec{\sigma}. \tag{4.2.41}$$

The calculation of the first Chern number using Equation 4.2.41 gives $c_1 = 0$, because the Hamiltonian still belongs to the BDI class at low frequency, and it does not have a topological invariant in 2 dimensions. It means that all changes in the topological properties will be reflected in ν_1. By a procedure of dimensional reduction we can fix a random time value and obtain the corresponding topological class. This is given by the AIII class, which is also a chiral Hamiltonian, but now with both TRS and PHS broken. In chiral Hamiltonians one can compute the 1 dimensional winding number graphically[84], in terms of the divergences of the phase $\phi(k,t) = \arctan(g_y/g_x)$ over the FFBZ (Figure 4.2.11), being $g_{x,y}$ the components of the vector:

$$H(k,t)_{\mathrm{NNN}} = \tau \vec{g}(k,t) \cdot \vec{\sigma}. \tag{4.2.42}$$

Note that in difference with Equation 4.2.36, $\vec{g}(k,t)$ now depends on t, and ν_1 can be defined along the two inequivalent axis of the torus

$$\nu_1(\eta) = \frac{1}{2} \oint \frac{\partial}{\partial \mu} \phi(\mu,\eta)\, d\mu, \quad \mu,\eta = k,t. \tag{4.2.43}$$

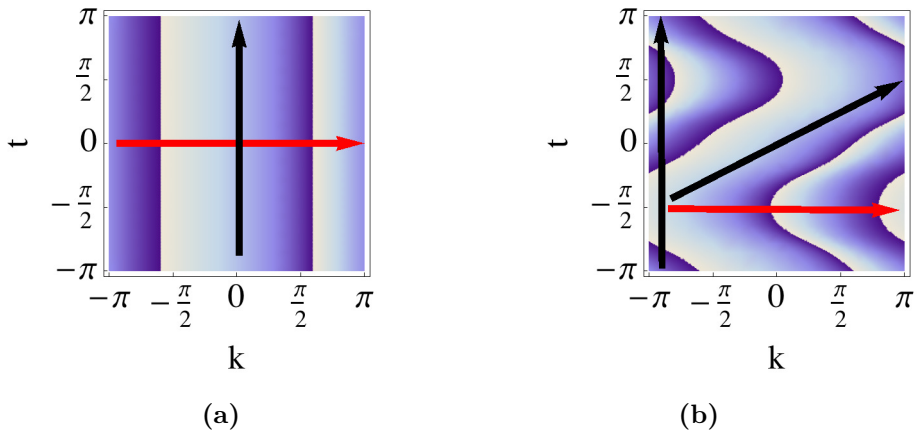

Figure 4.2.11: Plot of $\phi(k,t)$ all over the FFBZ for $A_0 = 0$ (a) and $A_0 = 2$ (b). Paths parallel to k cross two discontinuities meaning $\nu_1 = \pi$ (red arrow), on the other hand, paths parallel to t have $\nu_1 = 0$ because they wind back and forth (black arrow).

For the case of a finite chain, the existence of boundary states at the end of the chain, depend on the loops along the k axis, i.e., on $\nu_1(t)$[84]. In Figure 4.2.11

$\nu_1(t) = \pi$ for all t, independently of the value of E_0/ω – the trajectories always cross two discontinuities. Thus, band inversions are not relevant for the existence of edge states at low frequency, because now an adiabatic evolution picture is more appropriate. This can be seen numerically in the finite size system, in which zero energy modes are present independently on the gap inversions (see Figure 4.2.12, right).

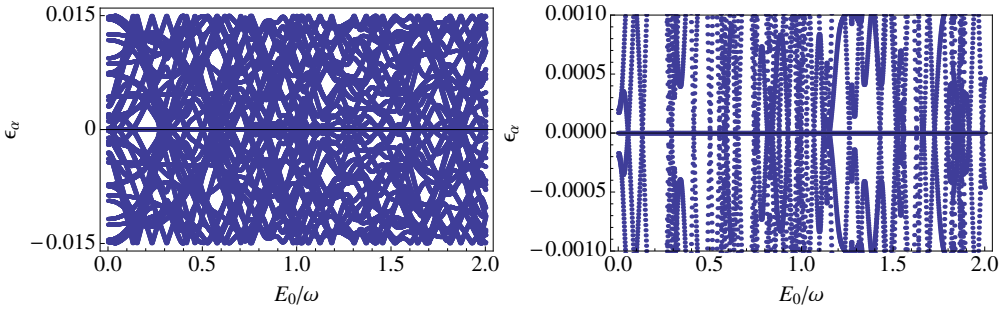

Figure 4.2.12: (Left) Quasi-energy spectrum within $(-\omega/2, \omega/2)$ for a finite dimers chain in the low frequency regime ($\omega \ll \tau, \tau'$). Right plot shows a zoom of the zero energy mode. The plots show a large number of crossings between the quasi-energies. However, the existence of zero energy modes is not affected by these crossings, and they exists for all values of E_0/ω. We have considered a finite chain of 20 dimers, $n, m = 105$, $\omega = 3.10^{-2}$, and $\lambda = 0.3$ in units of τ.

Finally, we shall discuss the properties of the zero energy modes arising on the dimers chain system when it is driven out of equilibrium. Importantly, this model just contains zero energy modes in the Δ_0 gap. Thus we cannot study all range of possibilities. For the analysis we will solve the finite tight binding and characterize the end states by computing its spatial distribution and its time evolution. Let us first consider a 20 dimers chain in the first non-trivial topological region. Figure 4.2.13, left, shows the spatial distribution at long times (when the steady state of the system is reached) of a particle which is initially placed at the boundary of the chain (A atom). Clearly the particle remains well localized at the end of the chain as we would expect for a system with topologically protected states. On the other hand, when the particle is initially placed in the middle of the chain, for long times the wave function spreads as it is expected for a particle in the bulk, which tends to a Bloch state. Next, we compare the previous results with a system in a trivial topological phase. The lack of end states in the system should be reflected in the absence of solutions with exponential decay, and therefore an initially placed electron at the end of the chain should also spread in time. This can be observed in Figure 4.2.14, where it is plotted the time evolution of a particle initially placed at the end of the chain (atom A) for the system in the trivial topological phase. Therefore, in a trivial topological region the end-states are not formed, and all the solutions are delocalized in the bulk. Calculations of the edge states, increasing the b_0 parameter and for different topological regions, are also in agreement with

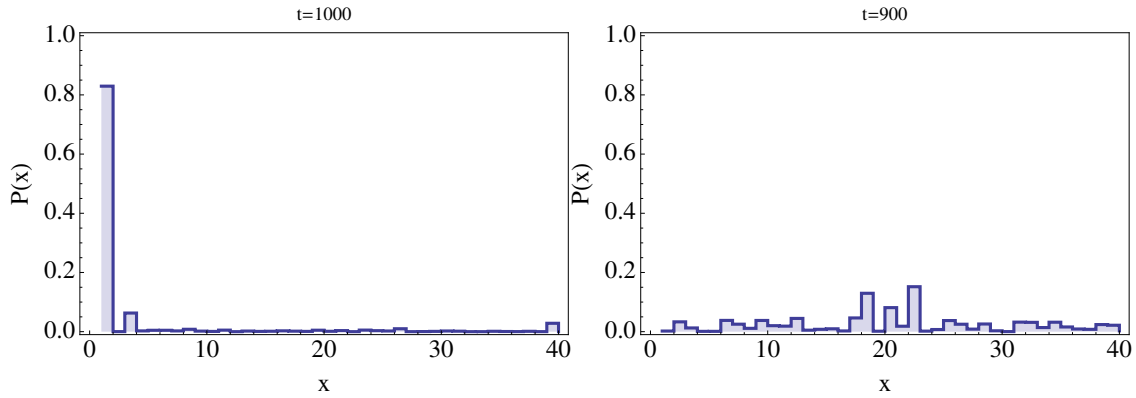

Figure 4.2.13: (Left) Long time spatial distribution of a particle initially placed at the first A atom of the chain. We have considered a non-trivial topological phase for the system, i.e. $\lambda = 0.3$, $E_0/\omega = 0.5$, $a_0 = 1$, $b_0 = 0$ and $\omega = 10\tau$ (see Figure 4.2.9). (Right) Long time spatial distribution of an electron initially placed in the middle of the chain. The electron spreads in time and remains delocalized according to a Bloch state.

our predictions in the phase diagrams (Equation 4.2.37). Note that we have not discussed the case of zero energy modes lying in the Δ_π gap. These states behave differently as the ones in the Δ_0 gap and contain intrinsic time correlations which will be briefly discussed in the last chapter.

In summary, we have derived a general approach to solve periodically driven D dimensional lattices. It allows to obtain effective Hamiltonians for the different driving regimes and a complete topological classification in terms of AZ classes. We show that even for high frequency, the underlying topology of the undriven system is present due to the time periodicity with important applications for non-adiabatic quantum computation. In addition, we show that for low frequency, the Floquet operator is analog to the one of a static system in D+1 dimensions, leading to interesting topological states of matter which otherwise would be inaccessible. Finally, we also described the mechanism of bands inversion in AC driven systems and its relation with the topology of the system.

For the case of the linear homogeneous chain, we have obtained a full analytical solution for the AC driven problem. It generalizes the previous work of Holthaus and establishes a connection between Stark ladder systems and periodically driven ones. For the dimers chain, we have obtained exact expressions in Fourier space for the quasi-energies, without invoking a low energy approximation, which accounts with both the lattice and field symmetries. It allows to obtain the effective Hamiltonian at low frequency, which in difference with the one in high frequency, presents boundary states for a wide range of field amplitudes. In addition, the simplicity of the system and its relation with other systems such as graphene[84] motivates its study. In addition, our results have large consequences and can be studied experimentally e.g., by measuring the electric polarizability[81] or the appearance of boundary states.

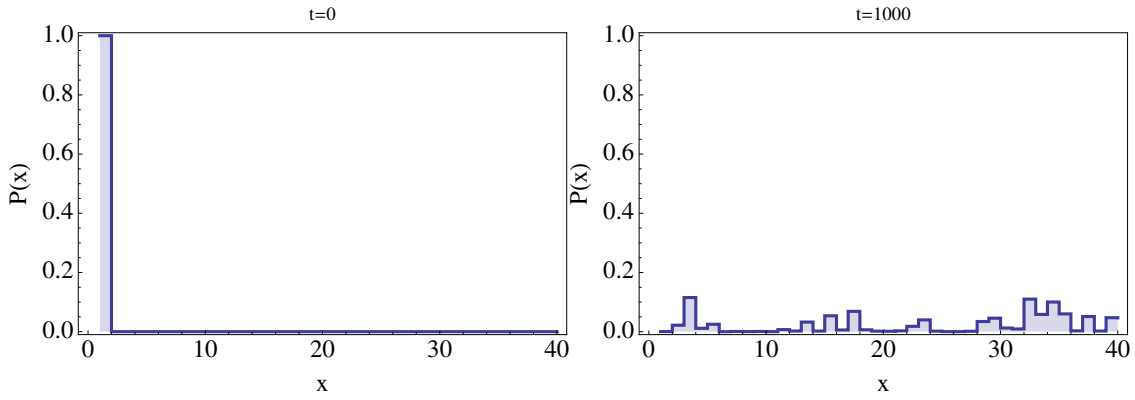

Figure 4.2.14: Spatial distribution at $t = 0$ and for the steady state $t \to \infty$, for a particle initially placed at the boundary (atom A). The system is in the trivial topological region, i.e. $\lambda = 0.3$, $E_0/\omega = 2.2$, $a_0 = 1$, $b_0 = 0$ and $\omega = 10$ (see Figure 4.2.9). The state evolves according to a Bloch wave function, spatially spreading in time. The reason is that in the trivial topological region, exponentially decaying solutions do not exist.

The driving allows to simulate properties of undriven systems in higher dimensions and the obtention of new topological phases due to tunable hoppings[85]. One could also think in more exotic types of zero energy modes in the low frequency regime, as for example those in the boundary between a driven and undriven materials.

5 Periodically driven graphene

In this chapter, we first review the honeycomb lattice and its condensed matter realization in graphene, describing the main features of this system. Next, we analyze in terms of Floquet theory, the effect of an AC electric field coupled to the system. We will show that the AC electric field allows to renormalize the microscopic parameters of the model, and then its band structure in a controllable way. Finally, we will discuss the effect of different field polarizations and the topological phases which can be found in the system.

5.1 Undriven graphene

Graphene is one of the most promising solid state candidates for electronic applications. Since its discovery in 2004 by A. Geim and K. Novoselov[88], applications in many different branches of physics such as optics, electronic transport and topological insulators among others have been proposed. In this material, the electrons obey the dispersion relation analogous to the one of relativistic particles, allowing high mobilities at room temperature and extraordinary effects such as the Klein tunneling[89]. In order to understand the stunning properties of graphene, one must pay attention to its electronic structure. Graphene consist on a two dimensional plane of carbon atoms arranged according to a honeycomb lattice. Each carbon atom contains one electron in a free p_z orbital perpendicular to the plane, which can bind covalently with neighboring carbon atoms leading to the formation of a π-band which is half filled. Then, the electronic structure can be accurately described in terms of a tight binding model for the electrons of the π-band. The lattice is described in terms of a primitive unit cell with two inequivalent atoms (A,B) and unit cell translation vectors $\mathbf{a}_1 = \frac{a}{2}\left(3, \sqrt{3}\right)$ and $\mathbf{a}_2 = \frac{a}{2}\left(3, -\sqrt{3}\right)$, being a the distance between the atom A and B (Figure 5.1.1, (a)). Each A atom has three nearest neighbors (B type) at positions $\vec{\delta}_1 = a\,(1, 0)$, $\vec{\delta}_2 = \frac{a}{2}\left(-1, \sqrt{3}\right)$ and $\vec{\delta}_3 = \frac{a}{2}\left(-1, -\sqrt{3}\right)$. In k-space, the reciprocal lattice vectors are given by $\mathbf{b}_1 = \frac{2\pi}{3a}\left(1, \sqrt{3}\right)$, and $\mathbf{b}_2 = \frac{2\pi}{3a}\left(1, -\sqrt{3}\right)$, and the energy spectrum shows two inequivalent gapless points at $\mathbf{K} = \frac{2\pi}{3a}\left(1, \frac{1}{\sqrt{3}}\right)$ and $\mathbf{K}' = \frac{2\pi}{3a}\left(1, -\frac{1}{\sqrt{3}}\right)$ called Dirac cones (Figure 5.1.1, (b)). We also plot the Time Reversal Invariant Momentum (TRIM) points in blue color, which will be used later

on in this chapter. These are given by:

$$\begin{aligned} M_0 &= (0,0) && (5.1.1)\\ M_1 &= \frac{\pi}{3a}\left(1,-\sqrt{3}\right), && (5.1.2)\\ M_2 &= \frac{\pi}{3a}\left(1,\sqrt{3}\right), && (5.1.3)\\ M_3 &= \frac{2\pi}{3a}(1,0). \end{aligned}$$

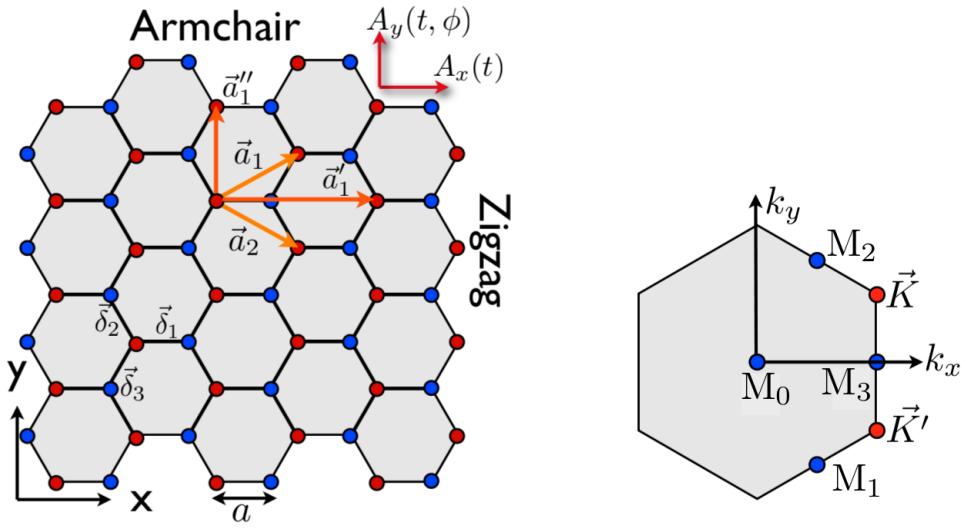

(a) **(b)**

Figure 5.1.1: (a) Reference frame considered and orientation of the different edges according to this frame. We also included the time dependent vector potential components considered in this thesis A_x and A_y. (b) First Brillouin Zone for the honeycomb lattice with the two inequivalent Dirac points in red color and blue dots at the high symmetry points (Time reversal symmetric points).

The undriven tight binding Hamiltonian, describing up to nearest neighbors coupling the honeycomb lattice, is given by:

$$H^B(\mathbf{k}) = \begin{pmatrix} 0 & \rho(\mathbf{k})^* \\ \rho(\mathbf{k}) & 0 \end{pmatrix}, \ \rho(\mathbf{k}) = \sum_{i=1}^{3} t_i e^{i\mathbf{k}\cdot\vec{\delta}_i}, \tag{5.1.4}$$

where t_i is referred to the hopping along the $\vec{\delta}_i$ direction. Explicitly, $\rho(\mathbf{k}) = \sum_{i=1}^{3}\rho_i(\mathbf{k})$ is given by:

$$\begin{aligned} \rho_1(\mathbf{k}) &\equiv t_1 e^{ik_x a}, && (5.1.5)\\ \rho_2(\mathbf{k}) &\equiv t_2 e^{-i\frac{a}{2}\left(k_x-\sqrt{3}k_y\right)}, \\ \rho_3(\mathbf{k}) &\equiv t_3 e^{-i\frac{a}{2}\left(k_x+\sqrt{3}k_y\right)}. \end{aligned}$$

The spectrum of $H^B(\mathbf{k})$ has two bands with dispersion relation given by:

$$E(\mathbf{k})_{\pm} = \pm|\rho(\mathbf{k})| = \pm\sqrt{t_1^2 + t_2^2 + t_3^2 + f(\mathbf{k})}, \tag{5.1.6}$$

$$\begin{aligned} f(\mathbf{k}) \equiv\ & 2t_2t_3\cos\left(\sqrt{3}k_y a\right) + 2t_1t_2\cos\left(\frac{3}{2}k_x a - \frac{\sqrt{3}}{2}k_y a\right) \\ & + 2t_1t_3\cos\left(\frac{3}{2}k_x a + \frac{\sqrt{3}}{2}k_y a\right). \end{aligned} \tag{5.1.7}$$

Figure 5.1.2 shows the energy dispersion of the honeycomb lattice with the two inequivalent Dirac cones $\mathbf{K}$ and $\mathbf{K}'$. Near these points (i.e., in the low energy approximation) the electrons fulfill the Dirac equation and behave relativistically as we show below. Note that for graphene all hoppings are equal $t_i = t\ \forall i$ which makes inversion symmetry to be present – inversion symmetry can be described in terms of the exchange of the different hoppings $t_i \leftrightarrow t_j$.

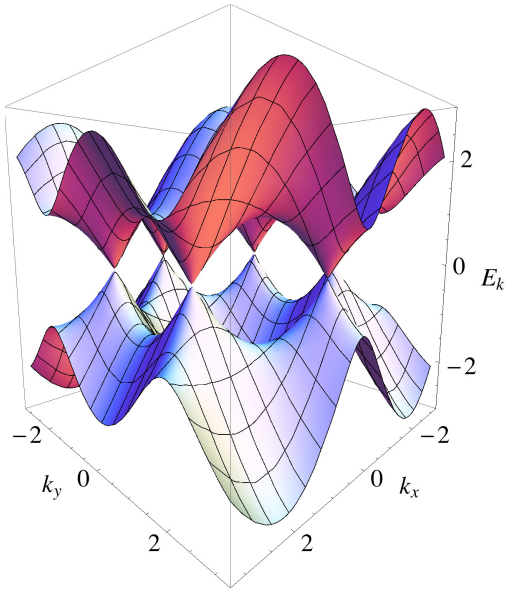

Figure 5.1.2: Graphene energy dispersion ($t_i = t_j = 1$) with exact crossings at the two inequivalent K and K' points.

5.1.1 Low energy approximation and the emergence of massless electrons

In graphene, the most interesting properties arise near the Dirac points, where the electrons obey a two dimensional Dirac equation, analogous to the one of relativistic particles in two dimensional QED[90]. In order to describe the electronic properties

for the electrons near these points, we will obtain the effective Hamiltonian at low energies. Then, we linearize the Hamiltonian near the K and K' points, starting from the tight binding Hamiltonian:

$$H = \begin{pmatrix} 0 & \rho(\mathbf{k})^* \\ \rho(\mathbf{k}) & 0 \end{pmatrix},$$

where $\rho(\mathbf{k}) = \sum_j t_j e^{i\vec{k}\cdot\vec{\delta}_j}$. We use a Fourier expansion of the matrix elements near the K (K') point up to linear order:

$$\begin{aligned} \rho(K+\vec{q}) &= \rho(K) + \nabla_{\vec{k}}\rho\left(\vec{k}\right)\Big|_{\vec{k}=\vec{K}} \cdot \vec{q} + O\left(\vec{q}^2\right) \\ &= -\sum_j t_j \left(\sin\left(K\cdot\vec{\delta}_j\right) - i\cos\left(K\cdot\vec{\delta}_j\right)\right)\vec{\delta}_j \cdot \vec{q} \\ &= -(\vec{v}_1 - i\vec{v}_2)\cdot\vec{q}, \\ \vec{v}_1 &\equiv \sum_j t_j \sin\left(K\cdot\vec{\delta}_j\right)\vec{\delta}_j, \\ \vec{v}_2 &\equiv \sum_j t_j \cos\left(K\cdot\vec{\delta}_j\right)\vec{\delta}_j. \end{aligned} \tag{5.1.8}$$

Similarly, for the other matrix element we find that $\rho(K+\vec{q})^* = -(\vec{v}_1 + i\vec{v}_2)\cdot\vec{q}$, while for the other Dirac cone we just substitute K for K' – this is equivalent to complex conjugation, as they are related by time-reversal symmetry. Then, the effective Hamiltonian is:

$$H_K = -\begin{pmatrix} 0 & (\vec{v}_1 + i\vec{v}_2)\cdot\vec{q} \\ (\vec{v}_1 - i\vec{v}_2)\cdot\vec{q} & 0 \end{pmatrix} = (H_{K'})^*. \tag{5.1.9}$$

Explicitly for the case of graphene where $t_i = t$, the velocities are given by:

$$\begin{cases} \vec{v}_1 = \frac{3}{4}at\left(\sqrt{3}, 1\right), \\ \vec{v}_2 = \frac{3}{4}at\left(-1, \sqrt{3}\right). \end{cases} \tag{5.1.10}$$

Finally, the equivalence with a 2 dimensional QED theory requires to rewrite the Hamiltonian as:

$$\begin{aligned} H_K &= \frac{3}{4}at_1\left\{\begin{pmatrix} 0 & i-\sqrt{3} \\ -i-\sqrt{3} & 0 \end{pmatrix} q_x + \begin{pmatrix} 0 & -1-i\sqrt{3} \\ -1+i\sqrt{3} & 0 \end{pmatrix} q_y\right\} \\ &= -iv_F\vec{\sigma}\cdot\vec{q}, \end{aligned} \tag{5.1.11}$$

being $v_F \equiv 3at/4$ the Fermi velocity, and where we have used the next representation for the Pauli matrices:

$$\sigma_x = \frac{1}{2}\begin{pmatrix} 0 & -1-i\sqrt{3} \\ 1-i\sqrt{3} & 0 \end{pmatrix}, \tag{5.1.12}$$

$$\sigma_y = \frac{1}{2}\begin{pmatrix} 0 & -i+\sqrt{3} \\ -i-\sqrt{3} & 0 \end{pmatrix}, \tag{5.1.13}$$

$$\sigma_z = \begin{pmatrix} -1 & 0 \\ 0 & 1 \end{pmatrix}, \tag{5.1.14}$$

which agree with the commutation relation of the $SU(2)$ algebra $[\sigma_x, \sigma_y] = i\sigma_z$. Note that as this is a low energy approximation for electrons next to the Dirac cones, the effective Hamiltonian will be valid for the typical energies considered in condensed matter experiments and small doping.

5.1.2 Dirac cones merging

In this section we introduce a description of the Dirac cones merging. This is an important process which happens in graphene when the hoppings are tuned asymmetrically[91, 92, 93]. When a hopping anisotropy is introduced in the honeycomb lattice, inversion symmetry breaks down, and the Dirac cones move in **k**-space. Importantly, if the pair of Dirac points (PDP) meet, they annihilate and the gapless phase results in an gaped phase. We shall follow [91] to describe the merging process.

First, let us fix the reference frame at the mass center between the Dirac cones. In this frame their coordinates are given by $\pm\vec{D}$, highly simplifying the results. When an anisotropy in the hoppings is considered, the position of the Dirac cones can be anywhere in the FBZ, because they move as the hoppings are varied. Around the Dirac cones, the functions $\rho\left(\vec{k}\right)$ change linearly in $\vec{q}$ as we described above, and at the merging point, the two Dirac cones touch. When this happens, their position are given by $\vec{D} = -\vec{D}$ (modulo a reciprocal lattice vector). Thus, there are four inequivalent points in the Brillouin zone A, B, C and Γ, at which the merging can happen – see Figure 5.1.1, (b). Explicitly the coordinates of the merging points are given in Equation 5.1.1. At these points $\vec{v}_1 = 0$ and $\vec{v}_2 = \sum_j (-1)^{\beta_j} t_j \vec{\delta}_j$. Then the effective Hamiltonian becomes purely imaginary:

$$H_{\vec{D}_0} = \begin{pmatrix} 0 & -i\vec{v}_2 \cdot \vec{q} \\ i\vec{v}_2 \cdot \vec{q} & 0 \end{pmatrix}, \tag{5.1.15}$$

being $\vec{D}_0$ the merging point. Importantly at these points it is required to expand up to second order the dispersion relation, resulting in a linear energy dispersion in one axis, and quadratic dispersion in the perpendicular one.

5.1.3 Berry connection and topological invariants in graphene

Finally, for completeness of the introduction, we discuss the different topological invariants which can be defined on the honeycomb lattice – these are the 1D winding number and the 2D Chern number. For that purpose it is useful to work in the next parametrization of the Hamiltonian:

$$H(\mathbf{k}) = \vec{g} \cdot \vec{\sigma} = |\vec{g}| (\cos(\phi), \sin(\phi)), \tag{5.1.16}$$

$$\vec{g} = (\Re(\rho), \Im(\rho), 0) = (g_x, g_y, 0), \tag{5.1.17}$$

$$\phi = \arctan\left(\frac{g_y}{g_x}\right), \tag{5.1.18}$$

where the Hamiltonian can be written as:

$$H(\mathbf{k}) = |\vec{g}| \begin{pmatrix} 0 & e^{-i\phi} \\ e^{i\phi} & 0 \end{pmatrix}, \tag{5.1.19}$$

and its eigenvalues and eigenvectors are given by:

$$E_{\pm} = \pm|\vec{g}|, \quad |\psi_{\pm}\rangle = \frac{1}{\sqrt{2}} \begin{pmatrix} \pm e^{-i\phi} \\ 1 \end{pmatrix}. \tag{5.1.20}$$

This parametrization allows to define the Berry connection 1-form in a very simple way:

$$\begin{aligned} \hat{A}_{\pm} &= \langle\psi_{\pm}|id|\psi_{\pm}\rangle \\ &= \langle\psi_{\pm}|i\partial_x|\psi_{\pm}\rangle dk_x + \langle\psi_{\pm}|i\partial_y|\psi_{\pm}\rangle dk_y \\ &= \partial_x \frac{\phi}{2} dk_x + \partial_y \frac{\phi}{2} dk_y, \end{aligned} \tag{5.1.21}$$

which is required for the calculation of the geometrical and topological properties. We can define winding numbers at each of the inequivalent directions, but it is important to note that the Berry curvature, defined as $B = dA$, will always vanish because of the vanishing component σ_z. Therefore in graphene the first Chern number is always zero, as it is always for time reversal symmetric systems. Then, we are left with the calculation of winding numbers along the two inequivalent directions k_x and k_y, which are given by:

$$\begin{aligned} \gamma_x(k_y) &= \oint_{BZ} A_{x,\pm} = \begin{cases} \pi & \text{for } k_y \in \left(\frac{-2\pi}{3\sqrt{3}}, \frac{2\pi}{3\sqrt{3}}\right), \\ 0 & \text{otherwise,} \end{cases} \\ \gamma_y(k_x) &= \oint_{BZ} A_{y,\pm} = 0 \ \forall k_x \in BZ, \end{aligned} \tag{5.1.22}$$

where $\oint_{BZ}$ indicates a 1D loop along the FBZ in the direction of integration. Importantly the non-contractible loops – those with non zero winding number – appear along the k_x direction. This result has physical consequences in the form of localized edge states at the boundaries of the graphene ribbons, depending on the edge properties. In Figure 5.1.3 and Figure 5.1.4 it is shown this dependence for armchair and zigzag ribbons. Note that the use of open boundary conditions along some axis is equivalent to a projection of the FBZ (Figure 5.1.1) in $\mathbf{k}$ space – armchair ribbons is equivalent to a projection on the k_x axis, while zigzag is equivalent to a projection on the k_y axis. In addition, note that a pair zero energy modes appear for the zigzag ribbon (Figure 5.1.4) approximately in the range $k_y \in \left(\frac{-2\pi}{3\sqrt{3}}, \frac{2\pi}{3\sqrt{3}}\right)$, i.e., between the Dirac cones position, while for the armchair ribbon they do not exist. This is a finite size effect, consequence of the open boundary conditions imposed in the system. One way to easily understand the effect of the different edge configurations consists in a description along the finite axis in terms of planes of projection

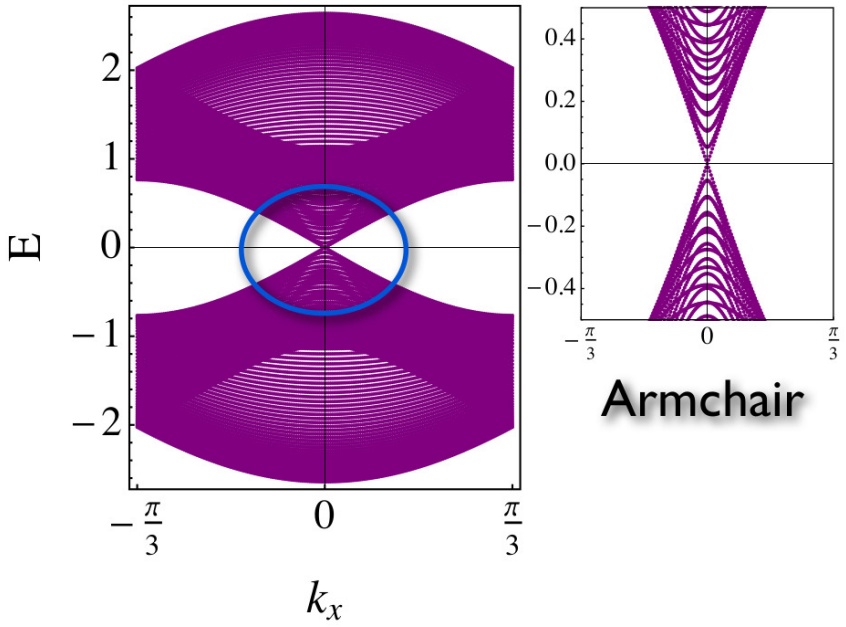

Figure 5.1.3: Edge states appearance for armchair ribbons in graphene. Note that in this projection of the FBZ structure the two cones are aligned and just a single one is visible. The inset of the figure shows a zoom of the Dirac cone and the absence of edge states.

– e.g., for a finite system along the y-axis, each discrete $k_y \in$ FBZ vector defines a plane of projection. Each plane of projection can be thought as a 1D insulating phase which is classified according to the AZ topological classification, explained in Chapter 4. Note that this description allows to relate the gapped phases of the projected Hamiltonian in 1D to the gapless structure of graphene. The resulting 1D insulator at each plane of projection belongs to a chiral class[1] whose topological properties are described in terms of a winding number. This is schematically shown in Figure 5.1.5, were $k_y \in \left(\frac{-\pi}{\sqrt{3}}, \frac{-2\pi}{3\sqrt{3}}\right) \cup \left(\frac{2\pi}{3\sqrt{3}}, \frac{\pi}{\sqrt{3}}\right)$ represents the trivial phase and in consequence does not have zero energy modes, while $k_y \in \left(\frac{2\pi}{3\sqrt{3}}, \frac{-2\pi}{3\sqrt{3}}\right)$ has inverted the bands and contains the corresponding zero energy modes. In addition, we must comment that the symmetry protecting the Dirac cones/gapless structure of the honeycomb lattice is a combination of TRS and inversion symmetry, and unless any of them is broken, the zero energy modes remain. In the next sections we shall explore the effects associated with the breaking of each of these symmetries and the resulting topological phases.

As a comment for this section, we could repeat the previous calculation but this time considering the low energy approximation (Equation 5.1.11) instead of the full Hamiltonian. This procedure adds a cut-off to low energy scales, and has important

[1]The reason is that the effective projected Hamiltonian can be written in chiral form, i.e., as a combination of $\sigma_{x,y}$ components.

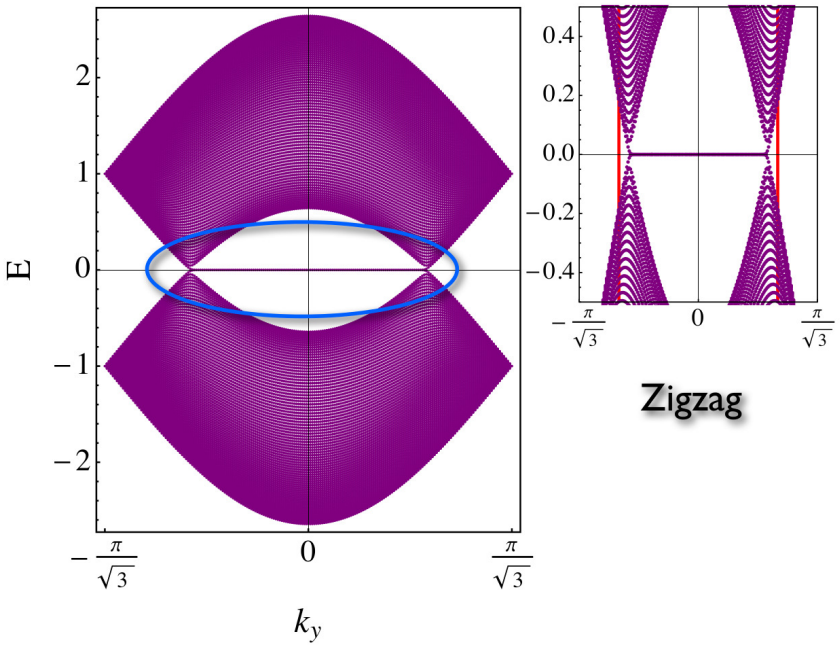

Figure 5.1.4: Edge states appearance for zigzag ribbons in graphene. In this projection both inequivalent Dirac cones are observed. In addition the inset shows the appearance of edge states connecting both cones as a consequence of finite size effects. The red thick lines indicate the points $k_y = \pm\frac{2\pi}{3\sqrt{3}}$.

consequences due to the lost on information regarding higher lattice symmetries (hexagonal for the case of graphene). As an example, the calculation of the winding number does not show the boundary condition dependence of the zero energy modes – i.e., its **k** dependence. Even further, we will show in the next sections the important consequences of the energy cut-off in relation with the tunability of the Chern number for irradiated graphene. In summary of the introduction to undriven graphene, we have discussed the extraordinary electronic structure associated to the honeycomb lattice and its physical realization in graphene. We have shown that it provides a very rich playground for electronics and even for testing effects associated to relativistic field theories. In addition, we have explained its topological properties and the existence of zero energy modes for the different ribbons.

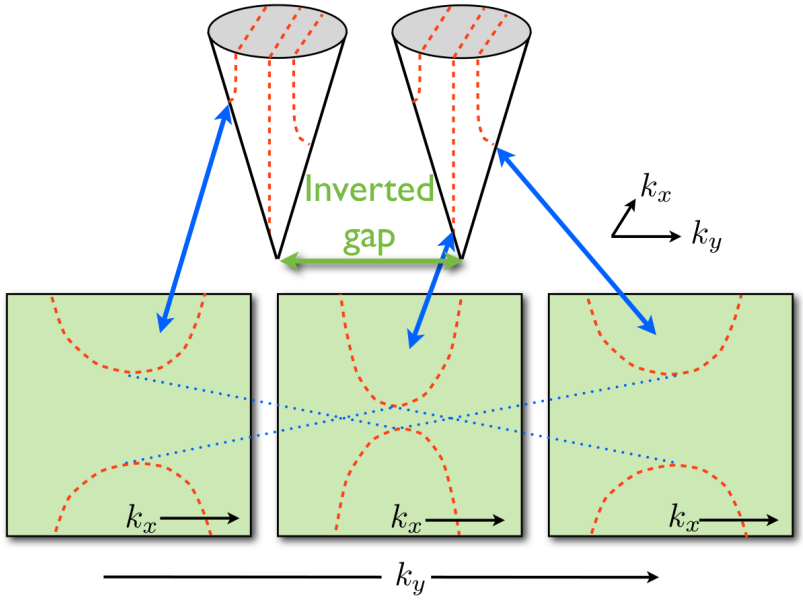

Figure 5.1.5: Gap inversions mechanism in terms of the AZ classification. Each discrete k_y vector for the finite axis corresponds to a section of the FBZ at fixed k_y. Each section is then a gapped phase of a chiral Hamiltonian unless $k_y = \frac{\pm 2\pi}{3\sqrt{3}}$ where it becomes gapless. This can be interpreted as a gap inversion in which the 1D winding number becomes non zero. This is the reason why in Figure 5.1.4 zero energy modes appear within the two Dirac cones. In this figure the blue dotted lines show the continuos transformation of the bands and the gap closures as a function of k_y.

5.2 AC driven graphene

In this section we obtain the tight binding Hamiltonian of electrons in the honeycomb lattice coupled to an in plane AC electric field. We follow the procedure described in Chapter 4 to obtain the Sambe space representation of the tight binding bulk Hamiltonian. Then, we describe the topological properties of graphene in the high frequency regime, and prove that the AC electric field allows to merge the Dirac cones by an appropriate field configuration. The merging of a pair of Dirac points is an important concept from both theoretical and experimental point of view, since it allows to transform the semi-metallic phase into an insulator, and it is also a process in which a pair of topological defects annihilate.

Several ideas to induce topological states of matter by means of time periodic external potentials have been proposed in the last years[76, 10, 74, 77, 16]. Importantly, these phases have been recently observed in temporal modulated photonic crystals [94]. This approach renews considerably the possibilities of inducing new topological phases. However, as we described above, in graphene it is possible to find another topological transition between a Dirac semi-metallic (SM) phase and an insulating (I) phase by merging the pair of Dirac points[93, 91]. The resulting I phase is

not a Chern insulating phase, but may nevertheless hosts zero-energy modes whose topological origin is well understood in terms of a one-dimensional bulk winding number, namely the Zak phase[95, 84, 83]. The search for this transition has stimulated experimental efforts beyond the solid state community, and the merging of the Dirac points as well as the emergence of zero-energy edge states have been recently observed in anisotropic traps of cold atoms[96, 97] and in microwave tight-binding analogue experiments of a honeycomb lattice[98]. However, the merging transition has not been observed yet in electronic systems. In particular its achievement in graphene itself[92], by means of mechanical manipulations like stretching, is unfortunately out of reach, because the graphene sheet would be destroyed far before the expected transition[99].

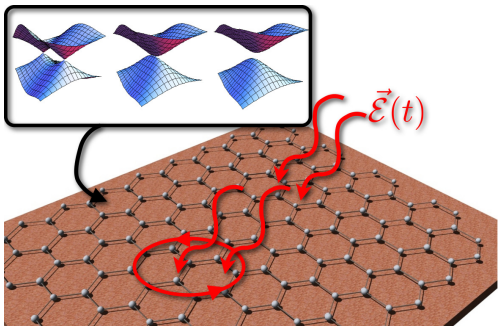

Figure 5.2.1: Graphene sheet irradiated by an AC electric field with arbitrary polarization. The inset shows the merging of the Dirac points induced by the external field.

In this section we will prove that, in the high frequency regime, the AC field acts similarly to a mechanical strain, and therefore allows for the manipulation of the Dirac points, their annihilation and their creation, in a controllable way. Furthermore, the AC field is able to induce the localization of the electrons in specific directions, which marks another topological transition between two insulating or two semi-metallic phases. Our analysis, when restricted to linear polarization and high frequency regime, agrees with the results obtained in shaken optical lattices[100]. In addition, we shall also consider different field polarizations and finite frequency effects. As we will see, they play a crucial role for lower frequencies by breaking time reversal symmetry. At lower frequencies, we find that the coupling between the Floquet bands, that characterize the properties of the driven system, leads to Floquet bands inversions. This gives rise to out-of-equilibrium phases with no analog in the static system in which e.g., multiple pairs of Dirac points appear. Importantly, this approach does not rely neither on low energy models nor on approximations valid just close to resonance (as the rotating wave approximation)[101, 74, 10]. In particular, it allows for keeping track of the relative position between the Dirac points due to the interplay between lattice and field symmetries. In addition, the results are valid for arbitrary field amplitudes and phase polarizations.

As we discussed in Chapter 4, the Hamiltonian of a T-periodic driven system fulfills $H(\tau+T) = H(\tau)$, and its eigenvectors can be written in Floquet form: $|\psi(\tau)\rangle = e^{-i\epsilon\tau}|\Phi(\tau)\rangle$ ($\hbar = 1$), being ϵ the quasi-energy, and $|\Phi(\tau)\rangle = |\Phi(\tau+T)\rangle$ the Floquet state[16]. This ansatz, consequence of the time translation invariance, maps the time-dependent Schrödinger equation to the eigenvalue equation $\mathcal{H}(t)|\Phi(\tau)\rangle = \epsilon|\Phi(\tau)\rangle$, in which the quasi-energies and the Floquet states are the eigenvalues and eigenvectors of the Floquet operator $\mathcal{H}(\tau) \equiv H(\tau) - i\partial_\tau$, respectively. As we discussed in previous chapters, in order to deal with the time dependence of the Floquet operator $\mathcal{H}(\tau)$ we introduce the Sambe space representation, which consists in a composed Hilbert space with time independent basis states[33]. In this space, the quasi-energies are given by:

$$\epsilon = \sum_{p,p'} \langle \Phi_{p'}|H_{p'-p}|\Phi_p\rangle - \ \delta_{p,p'} p\omega \tag{5.2.1}$$

where $H_{p'-p} = \int_0^T \frac{d\tau}{T} e^{i\omega\tau(p'-p)} H(\tau)$ with $\omega = 2\pi/T$, and where $\Phi_{p^{(\prime)}}$ is the $p^{(\prime)}-$th $\in \mathbb{Z}$ Fourier component of the Floquet state. The coupling between the Floquet sidebands is encoded into the Fourier components $H_{p'-p}$ of the Hamiltonian.

For a honeycomb lattice embedded in a periodic time dependent in-plane electric field $\mathcal{E}(\tau)$ (Figure 5.2.1), the Peierls substitution leads to the time dependent Hamiltonian:

$$H(\tau,\mathbf{k}) = \begin{pmatrix} 0 & \rho(\tau,\mathbf{k}) \\ \rho^*(\tau,\mathbf{k}) & 0 \end{pmatrix}, \tag{5.2.2}$$

where $\rho(\tau,\mathbf{k}) = \sum_j t_j(\tau) e^{i\mathbf{k}\cdot\mathbf{a}_j}$, $t_j(\tau) = te^{i\mathbf{d}_j\cdot\mathbf{A}(\tau)}$, $\mathbf{a}_1 = a\left(-3,\sqrt{3}\right)/2$, $\mathbf{a}_2 = -a\left(3,\sqrt{3}\right)/2$ and $\mathbf{a}_3 = (0,0)$ are the basis vectors of the Bravais lattice, and the vectors joining the nearest neighbors $\mathbf{d}_j$ are given by $\mathbf{d}_1 = \frac{a}{2}\left(-1,\sqrt{3}\right)$, $\mathbf{d}_2 = \frac{a}{2}\left(-1,-\sqrt{3}\right)$ and $\mathbf{d}_3 = a(1,0)$. We consider electric fields with arbitrary amplitude and polarization, and write the vector potential as $\mathbf{A}(\tau) = (A_x\sin(\omega\tau), A_y\sin(\omega\tau+\varphi))$. The analytical calculation of the different Fourier components $H_{q=p'-p}(\mathbf{k})$ gives:

$$H_q(\mathbf{k}) = \begin{pmatrix} 0 & \rho_q(\mathbf{k}) \\ \rho^*_{-q}(\mathbf{k}) & 0 \end{pmatrix}, \tag{5.2.3}$$

where $\rho_q(\mathbf{k}) = \sum_j t^F_{j,q} e^{i\mathbf{k}\cdot\mathbf{a}_j}$, and where we have defined the time independent Floquet hoppings $t^F_{j,q} = tJ_{-q}(\mathcal{A}_j)e^{iq\Psi_j}$, being $J_q(x)$ the q^{th} order Bessel function of the first kind. For the previous calculation we have used the identity:

$$e^{-i\nu\Psi}J_\nu(\Gamma) = \sum_{m=-\infty}^{\infty} J_{\nu+m}(\alpha)\,J_m(\beta)\,e^{-i\varphi m}, \tag{5.2.4}$$

$$\Gamma \equiv \sqrt{\alpha^2+\beta^2-2\alpha\beta\cos(\varphi)}, \tag{5.2.5}$$

$$\Psi \equiv \arctan\left(\frac{\beta\sin(\varphi)}{\alpha-\beta\cos(\varphi)}\right). \tag{5.2.6}$$

Importantly, the dimensionless functions $\mathcal{A}_j$ and Ψ_j encode all the information of the field configuration:

$$\begin{aligned}\mathcal{A}_{2,1} =& \frac{a}{2}\sqrt{A_x^2 + 3A_y^2 \pm 2\sqrt{3}A_x A_y \cos(\varphi)},\\ \Psi_{2,1} =& \pm \arctan\left[\frac{\sqrt{3}A_y \sin(\varphi)}{A_x \pm \sqrt{3}A_y \cos(\varphi)}\right],\\ \mathcal{A}_3 =& A_x a, \quad \Psi_3 = 0,\end{aligned} \tag{5.2.7}$$

and as a consequence, the spatial anisotropy can be tuned by varying the polarization or the amplitude of the field since the Floquet hoppings $t^F_{j,q}$ will be affected differently.

We first focus on the high frequency regime $\omega \gg t$. In this limit, Equation 5.2.1 is almost block-diagonal in the Fourier space, and simply consists in a collection of 2×2 time-independent Hamiltonians separated in energy by ω. As the Floquet bands are decoupled we can consider just the zeroth Fourier component $\mathcal{H}_{q=0}$ of the Floquet operator to correctly describe the system. The quasi-energy of a side-band α, is then simply given by $\epsilon_\alpha(\mathbf{k}; A_x, A_y, \varphi) = \pm|\rho_{q=0}(\mathbf{k}; A_x, A_y, \varphi)| + \alpha\omega$, which shows that the quasi-energy of each Floquet band is, in the high-frequency regime, identical to the energy bands of undriven graphene with renormalized hopping parameters $t^F_{j,0}(A_x, A_y, \varphi) = tJ_0(\mathcal{A}_j)$.

5.2.1 Manipulation of the Dirac points by the AC field: merging and localization

A direct consequence of the anisotropy of the hopping parameters, induced by the AC field, is to change the location of the Dirac points breaking inversion symmetry. The two Dirac points, related by time-reversal symmetry will move as the anisotropy is modified, and merge at one of the four time-reversal symmetric points of the Brillouin zone M_i, whenever a specific relation between the hopping parameters is fulfilled [93, 91]:

$$\begin{aligned}&\mathrm{M}_0, \quad t_1^F + t_2^F + t_3^F = 0 \qquad && \mathrm{M}_1, \quad t_1^F = t_2^F + t_3^F\\ &\mathrm{M}_2, \quad t_2^F = t_1^F + t_3^F && \mathrm{M}_3, \quad t_3^F = t_1^F + t_2^F\end{aligned} \tag{5.2.8}$$

where the index 0 from $t^F_{j,0}$, which refers to the intra-side band hopping, has been dropped out for clarity. The merging transition corresponds to the creation/annihilation of the pair of Dirac points. As we have shown in the introduction, at the transition the dispersion relation is quadratic in one direction, but remains linear in the other one, leading to the prediction of striking properties such as an unusual temperature dependence of the specific heat and magnetic field dependence of the Landau levels[92]. Such transitions can now be achieved for specific values of amplitude (A_x, A_y) and polarization φ of the electric field.

AC driven graphene exhibits several distinct semi-metallic and insulating phases that we now describe. Figure 5.2.2 shows a typical example of a semi-metallic/insulating phase diagram obtained in the high frequency regime when the amplitude and the polarization of the field are varied. The colors filling the different areas represent inequivalent phases in topological terms. The creation/annihilation of a pair of Dirac points at a M_i point is represented by a continuous *merging line* that separates a semi-metallic phase from an insulating phase. The color code in given by:

Renormalization	Merging point
$t_1^F + t_2^F + t_3^F = 0$	M_0 (Green)
$t_1^F = t_2^F + t_3^F$	M_1 (Brown)
$t_2^F = t_1^F + t_3^F$	M_2 (Red)
$t_3^F = t_2^F + t_1^F$	M_3 (Blue)

Thus, there are four different merging lines, one for each point M_i. It follows that distinct semi-metallic or insulating phases may emerge when different merging lines are crossed. This distinction can be made in terms of both the points M_i and topological (winding) numbers: Each semi-metallic phase can be labeled by a point M_i where a pair of Dirac points *cannot* be annihilated. For instance, a pair of Dirac points cannot be annihilated at M_0 (green line) from the semi-metallic phase SM_0 (which is the one connected to the undriven graphene phase). The reason is that all the hopping parameters in the SM_0 phase have the same sign, so that the merging at M_0 would require first a change in sign of any of them, and according to Equation 5.2.8, it would fulfill the merging conditions at other $M_{i\neq 0}$ point. Therefore, one can distinguish four semi-metallic phases, denoted as SM_i, one for each M_i point where the merging transition cannot happen.

In addition, two winding numbers can be introduced to characterize the topology of these four semi-metallic phases. The first one is the quantized Berry phase around a Dirac point, giving rise to a topological charge $\frac{1}{2\pi}\oint d\mathbf{k}\cdot\nabla_{\mathbf{k}}\theta_{\mathbf{k}} = \pm 1$ assigned to each Dirac point, where $\theta_{\mathbf{k}} = \arg\rho(\mathbf{k})$ is the polar angle parameterizing the Bloch sphere. The two Dirac points of graphene carry opposite topological charges that annihilate at the merging transition [92]. Besides, the topological transition is accompanied with a change of a second winding number, *the Berry phase evaluated across a reduced one-dimensional Brillouin zone*, namely the Zak phase $Z = \frac{1}{2\pi}\int_{-\mathbf{G}/2}^{\mathbf{G}/2}\{d\mathbf{k}\cdot\nabla_{\mathbf{k}}\theta_{\mathbf{k}}\}$, where $\mathbf{G}$ is a vector of the reciprocal lattice. Chiral symmetry guaranties integer values of the Zak phase [83] which depend on the direction in the reciprocal space. This reflects the edge orientations dependence for the density of zero-energy edge modes [84]. Thus, the four semi-metallic phases differ by the set of values the Zak phase takes for all directions in the reciprocal space, and therefore by the range of existence in k-space of edge zero-energy modes for a given edge orientation. Similarly, different insulating phases can be distinguished as well by the set of values the Zak phase takes in all possible directions, even though a pair

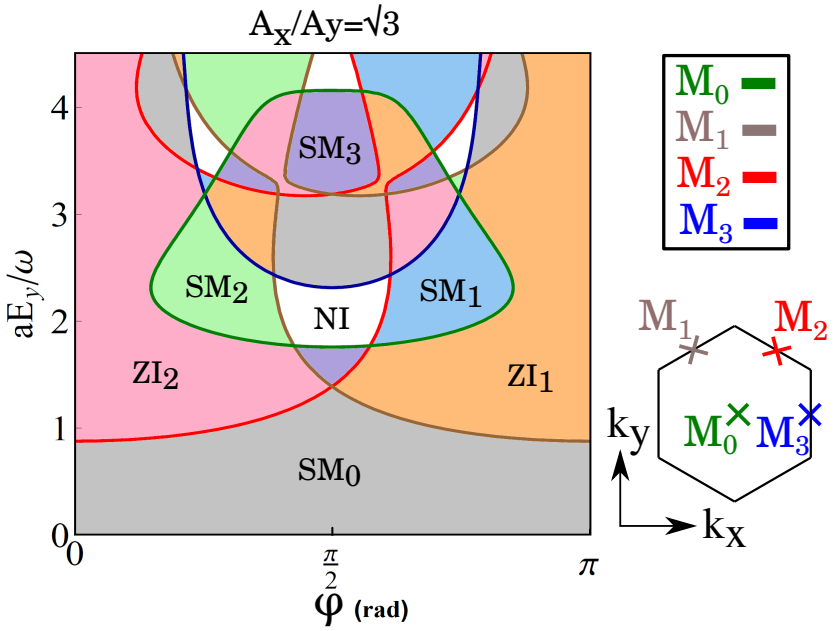

Figure 5.2.2: SM/I phase diagram (φ, aA_y) in the high frequency regime for fixed $A_x/A_y = \sqrt{3}$, with a the lattice spacing. The different phases are separated by four distinct merging lines corresponding to the four M_i points of the first Brillouin zone (shown on the right) where a PDP can be created/annihilated.

of Dirac points can, in principle, be created at any of the four points M_i. We find one normal insulating (NI) phase for which the Zak phase is zero in every directions (meaning the absence of zero-energy edge states), and, for polarizations different than $\varphi = \pi/2$, two *Zak insulating* (ZI) phases for which the Zak phase is non zero in different directions. The Zak insulating phases reflect, in 2D, the underlying non-trivial topology expected for a BDI symmetry class in 1D[61].

Interestingly, the phase diagrams also show multiple crossings between the merging lines, meaning that a pair of Dirac points *can be created and annihilated simultaneously at two different M_i points*. Following Equation 5.2.8, such crossings actually imply the vanishing of one of the three hopping parameters t_j^F, which directly implies localization of the electrons along the $\mathbf{d}_j$ direction. This striking feature corresponds to a transition between two insulating or two semi-metallic phases. At the transition, the gap closes along lines parallel to the $\mathbf{d}_j$ direction that passes through the two distinct merging points. Unlike a single merging transition, it follows that the dispersion relation is flat along the $\mathbf{d}_j$ direction but remains linear in the other one, as shown in Figure 5.2.3, (c). At the transition, the system is then reduced to an array of uncoupled one-dimensional chains, hosting one-dimensional massless Dirac fermions. Remarkably, for phase polarization $\varphi = \pi/2$, the merging at M_1 and M_2 is always coincident. This gives rise to critical *localization lines* that separate two semi-metallic phases as shown in Figure 5.2.3. At the transition between two semi-metallic phases, the topological charges assigned to the Dirac points change sign

(see Figure 5.2.3, (b) and (d)). In that sense, the localization (or double merging) transition is also a topological transition. Finally, the phase diagram for polarization $\varphi = \pi/2$ also exhibits crossings between the four merging lines simultaneously[2]. At such critical points, all the hopping parameters t_j^F vanish and the quasi-energy of each side-band is perfectly flat which leads to full charge localization in all directions.

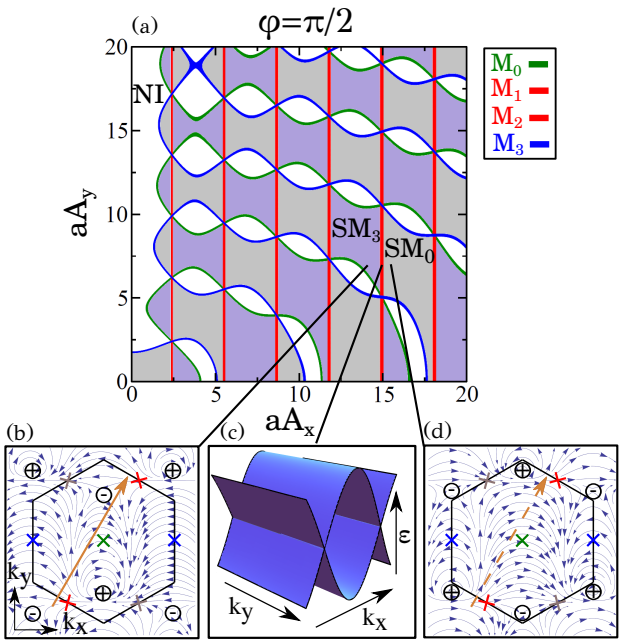

Figure 5.2.3: (a) Phase diagram in the high frequency regime for $\varphi = \pi/2$, where only three phases appear due to the overlap between the M_1 and M_2 merging lines. (c) Localization lines separate two semi-metallic phases. In addition, at the transition between these phases, the topological charges assigned to each Dirac point change sign ((b) and (d)). This topological transition goes together with a change of the value of the Zak phase, which is 1 (0) in the SM_3 (SM_0) phase along the path represented by a full (dashed) arrow.

Finally for completeness, we show the phase diagrams associated to different AC field configurations in the high frequency regime. They show the competition between the lattice and the electric field symmetries by modifying the different merging lines and the possible emergent phases.

[2](According to Equation 5.2.8, the crossing of three merging lines only is not possible.)

5.2.2 Phase diagrams for other field configurations

First we consider the variation of the functions $\mathcal{A}_j$ and Ψ_j with the constrain $A_y = A_x/\sqrt{3}$. Importantly, this condition highly simplifies the functions $\mathcal{A}_j$ and Ψ_j:

$$\begin{aligned} \mathcal{A}_{2,1} &= \frac{A_x a}{\sqrt{2}},\ \mathcal{A}_3 = A_x a, \\ \Psi_{2,1} &= \arctan\left(\frac{\sin(\varphi)}{[1 \pm \cos(\varphi)]}\right),\ \Psi_3 = 0. \end{aligned}$$

The renormalized hoppings are then given by: $t_3^F = tJ_0(A_x a)$, $t_2^F = tJ_0\left(aA_x \cos\left(\frac{\varphi}{2}\right)\right)$, and $t_1^F = tJ_0\left(aA_x \sin\left(\frac{\varphi}{2}\right)\right)$. In Figure 5.2.4 it is shown its phase diagram.

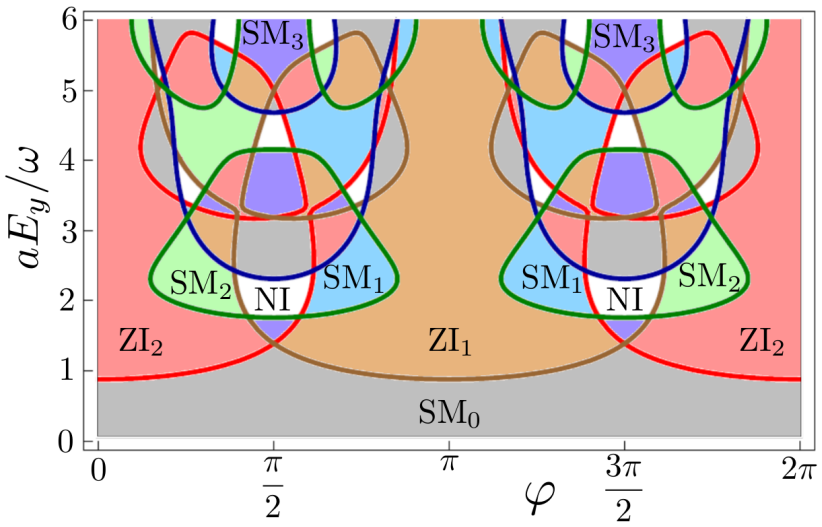

Figure 5.2.4: Phase diagram as a function of the external AC electric field parameters ϕ and E_y for the condition $A_x = \sqrt{3}A_y$. The different colored lines label the four inequivalent M_j points for the merging, and the colored areas the inequivalent phases.

Note that this field configuration allows to merge two or four Dirac points simultaneously and also contains all possible semi-metallic and insulating phases described above.

If we now fix the phase difference to $\varphi = \pi/2$ and vary the amplitude of each component the functions $\mathcal{A}_j$ and Ψ_j become:

$$\begin{aligned} \mathcal{A}_{2,1} &= \frac{a}{2}\sqrt{A_x^2 + 3A_y^2}, \\ \Psi_{2,1} &= \arctan\left(\frac{\sqrt{3}A_y}{A_x}\right),\ \mathcal{A}_3 = A_x a,\ \Psi_3 = 0. \end{aligned}$$

Importantly, for $\varphi = \pi/2$ polarization the functions $\Psi_{1,2}$ are equal, which is the main feature of circular fields. This can be also described in terms of the couplings in Sambe space, where the hoppings between different ω harmonics now carrie symmetrical complex phases. The phase diagram is plotted in Figure 5.2.5, and shows double and quadruple merging points. Even further, the phase diagram contains just three different phases: A trivial insulating phase and two semi-metallic phases $\mathrm{SM}_{0,3}$. Also, note that the case of circular polarization is obtained by tracing a line $E_x = E_y$ in Figure 5.2.5.

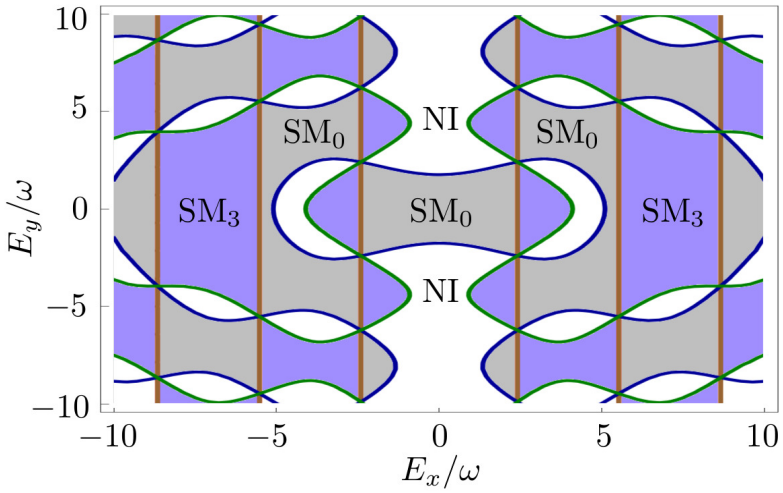

Figure 5.2.5: Phase diagram as a function of the external AC electric field parameters E_x and E_y for the condition $\varphi = \pi/2$. Note that in this case the merging lines M_1 and M_2 overlap, giving rise to crossings of two and four merging lines.

The case of linear polarization ($\varphi = 0$) is an important one, since it is the only field polarization which does not break time reversal symmetry. This can be seen in the expression for the Ψ_j functions, which are given by:

$$\begin{aligned} \mathcal{A}_{2,1} &= \frac{a}{2}\sqrt{A_x^2 + 3A_y^2 \pm 2\sqrt{3}A_x A_y}, \\ \Psi_{2,1} &= 0,\ \mathcal{A}_3 = A_x a,\ \Psi_3 = 0. \end{aligned}$$

The invariance under time reversal transformations is thus guaranteed by the vanishing of Ψ_j, which for non-linear fields contribute with a complex hopping element, breaking time reversal symmetry. The corresponding phase diagram is plotted in Figure 5.2.6. It is clear that for linear fields a three-fold crystal symmetry (hexagonal pattern around the SM_0 phase at $E_j = 0$, invariant under π rotations) naturally arises in Figure 5.2.6, due to the interplay between the direction of the field and the one of each of the three hoppings. Finally, we can see certain similarities between this phase diagram and the one in Figure 5.2.4.

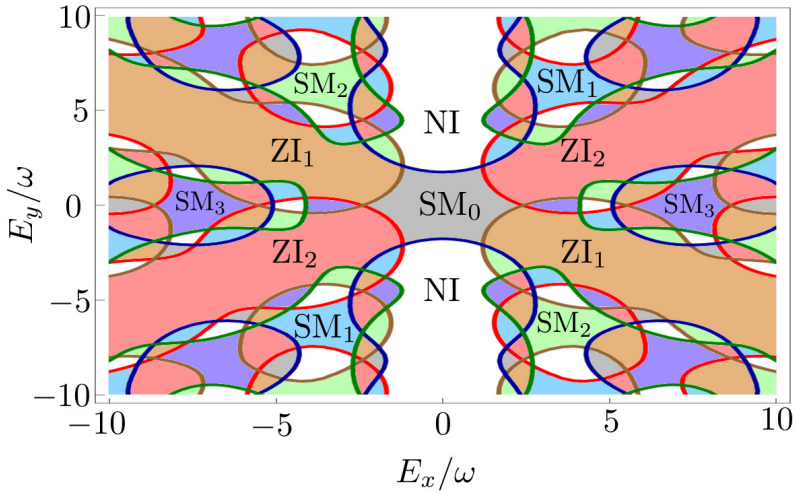

Figure 5.2.6: Merging lines as a function of the external AC electric field parameters E_x and E_y for the condition $\varphi = 0$.

5.2.3 Multi side-bands effects and topological transitions

When the frequency is decreased from the high frequency limit, the different Floquet bands couple and the isolated Floquet band picture is not accurate – we consider, for the honeycomb lattice, that the high frequency limit is the one in which the ratio between the frequency and the bandwidth fulfills $\frac{\omega}{6t} > 1$, i.e., when the Δ_π gap has not yet been closed and the topological properties should remain invariant. In addition, as non-linearly polarized fields lead to complex phase factors attached to the hoppings in Sambe space which break TRS, we shall consider in this section just linear fields (see a formal proof in Appendix C). The case of TRS breaking field configurations will be explored further in the next section, since the Hamiltonian belongs to a different AZ class and the band structure is always gapped[3].

For the linearly polarized case ($\phi = 0$) the system is time reversal invariant and the mergings can happen as in high frequency. Note that, according to Figure 5.2.6, the phase diagram for linearly polarized fields contains all the different semi-metallic and insulating phases, thus, it is still possible to explore the effect of a frequency decrease in all phases.

For frequencies of $3t < \omega \lesssim 6t$, the Floquet band $\alpha = 0$ overlaps the two nearest side-bands $\alpha = \pm 1$, as schematically illustrated in Figure 5.2.7 for a non interacting bands picture. The overlap between the Floquet side-bands can be interpreted as the emergence of new hoppings which now include the absorption or the emission

[3]Similarly to the Boron Nitride model, for non-linearly polarized fields at high frequency a small gap opens. Nevertheless, the topological charges assigned to the non-trivial Berry phases in each valley remain, so that their annihilation/creation can still be achieved by varying the parameters of the field

of photons during the hopping process. In this situation, the coupling between the Floquet side-bands becomes relevant, and the simple high frequency effective theory is not accurate anymore.

We have numerically calculated the phase diagrams using the full Floquet operator, revealing only small qualitative changes for $\omega > 3t$, in comparison with those obtained in the high frequency regime. However, the phase diagrams are largely modified when the overlap between side-bands $\alpha = \pm 1$ happens.

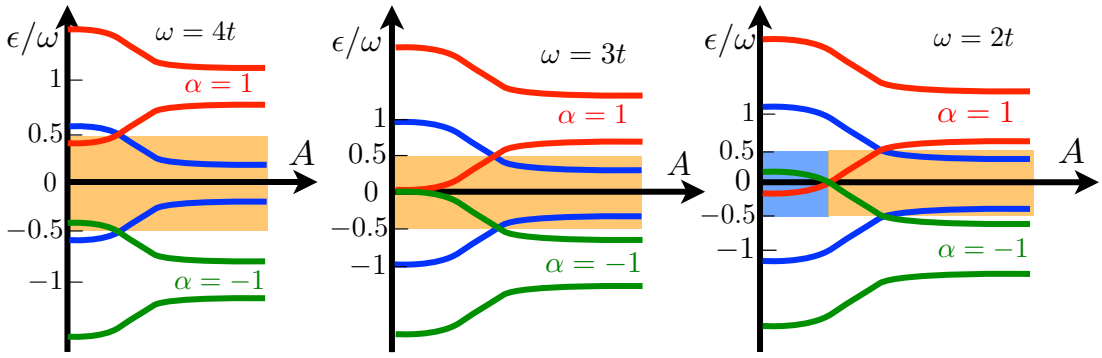

Figure 5.2.7: Schematic figure for the quasi-energies overlap considering the side-bands $\alpha = -1, 0, +1$, as a function of the field amplitude A for three different frequencies. The side-band $\alpha = 0$ is enhanced by a colored area ($[-\omega/2; \omega/2]$). For $\omega = 4t$ (left), the nearest neighboring side-bands weakly couple, slightly modifying the merging phase diagram. For $\omega = 3t$ (center) a band crossing between side-bands $\alpha = +1$ and $\alpha = -1$ happens at $\epsilon = 0$, leading to a band inversion that changes the insulating or semi-metallic state of the system. For $\omega = 2t$ (right) we show in blue color the inverted band region.

At $\omega = 3t$, the side-bands $\alpha = +1$ and $\alpha = -1$ touch at the Δ_0 gap for $A_{x,y} = 0$ amplitude, giving rise to a new crossing at the M_0 point (Figure 5.2.7). This new crossing corresponds to a band inversion, in which the symmetry of the conduction and valence band is exchanged. The quasi-energy band structure for the zeroth side-band in this case is displayed in Figure 5.2.8. This phase reveals the emergence of a new pair of Dirac points related with photon mediated transitions.

Importantly, it is possible to confirm that the emergence of a new PDP is related with a merging transition, since Figure 5.2.8 (center) shows that the dispersion relation is linear along the k_x axis and quadratic along the k_y. Thus, a change in frequency for fixed field amplitude also allows to reproduce the merging process, without the requirement of a high frequency and intensity field. Interestingly, a further decrease of the frequency leads to a second crossing between the side-bands at the M_3 point which allows one to create a *second PDP*, also associated with a photon mediated transition, as shown in Figure 5.2.9. The appearance of new pairs of Dirac cones is an important property of intermediate frequency regimes, produced by photon

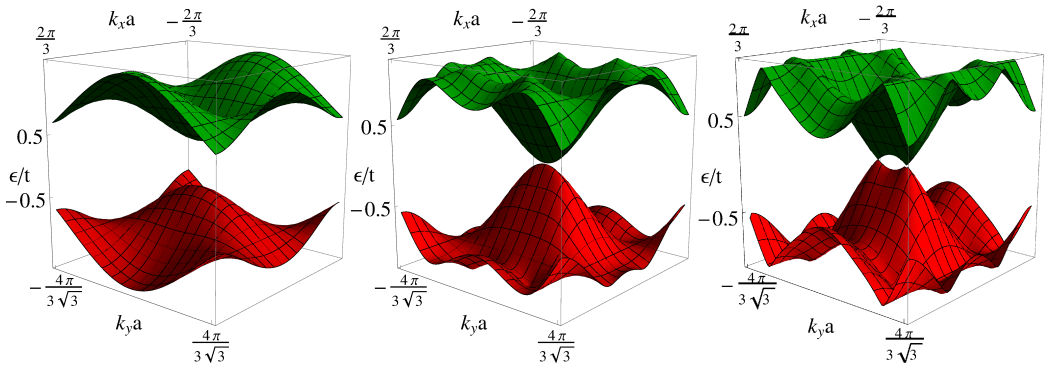

Figure 5.2.8: Appearance of a PDP at the M_0 point when the frequency is decreased from the high frequency limit. We fix $A_y = 3.6$, $A_x = 0$, and $\phi = 0$ such that the system is initially in the NI phase. Left plot shows the FBZ at high frequency ($\omega = 10t$) in the normal insulating phase. Center shows the gap closure due to a frequency decrease ($\omega = 2.5t$), where the dispersion relation is linear in one direction and quadratic in the perpendicular one, as it is expected for the merging process. Right shows the appearance of a new PDP when the frequency is further decreased ($\omega = 2.1t$).

mediated transitions/multi-photon resonances. This will be related with the results of the next section, where the obtention of a plateau structure for the quantum anomalous Hall effect is obtained using a frequency decrease.

In conclusion, we have shown that the merging of the Dirac points in the honeycomb lattice can be driven in a controllable way by an AC electric field. We have obtained rich phase diagrams in which distinct topological semi-metallic and insulating phases emerge. At high frequency, $\omega \gg t$, the behavior is easily described by an effective Floquet operator, equivalent to the Hamiltonian of undriven graphene, but with renormalized hoppings tuned by the field amplitude and the phase polarization. The resulting phases reflect interesting topological features, and the critical lines in which pairs of Dirac points are created and annihilated simultaneously show unexpected localization properties for which electrons behave relativistically in one direction, while they are localized in the other one.

Importantly, we have shown that for linearly polarized fields and intermediate frequency regimes ($\omega \sim t$), a change in frequency can drive a novel transition with the emergence of new pairs of Dirac points, although it does not necessarily correspond to a transition between an insulating and a semi-metallic phase. This new transition lies on multi-side-bands couplings, or in other words, multi-photon assisted transitions. The resulting new semi-metallic phase with four Dirac points could clearly be distinguished from the one with two Dirac points by transport measurements. For instance, a Hall conductance measurement would provide a direct signature of the two additional Dirac points, since each valley brings a contribution $e^2/h\,(1/2 + n)$ to the total transverse conductivity, where n is the number of Landau levels. The

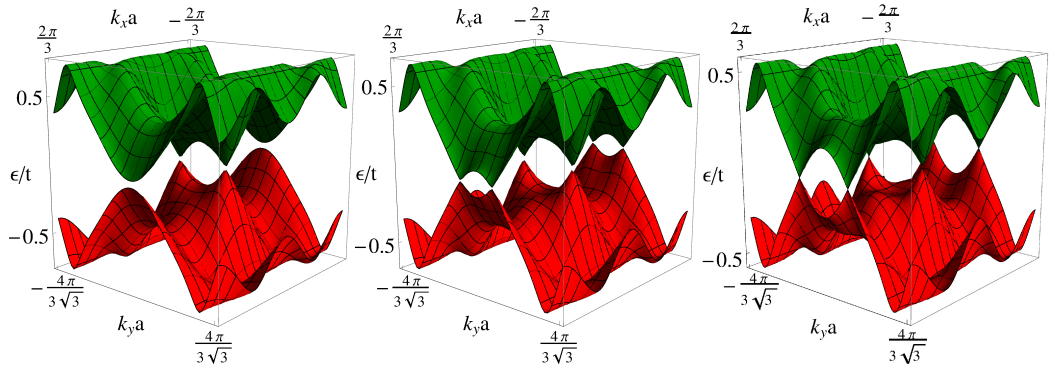

Figure 5.2.9: Creation of a new PDP at M_3 in addition to the initial ones by a further decrease of the frequency. Left plot shows the case were initially a single PDP is in the FBZ ($\omega = 1.7t$). Center plots shows the case $\omega = 1.6t$, where the gap is closing at M_3. Right plots shows the case $\omega = 1.5t$, where a PDP has appeared.

conductivity measurements would be accomplished by considering the Floquet sum rule obtained in Ref.[102], due to the far from equilibrium situation of the setup at intermediate frequencies.

For the realization in graphene, the high frequency regime requires field frequencies in the near ultraviolet and field amplitudes at least of the order ~ 3.4V/Å[103, 104, 105]. The energy corresponding to this electric field is about half the ionization energy of carbon atoms. However, real graphene also possesses s-orbitals which can be affected by such a high frequency field. Thus, in order to achieve the high frequency regime, a frequency larger than the actual band width of the graphene bands should be considered. In addition, for fields of both high frequency and high amplitude, the heating of the sample will certainly be an issue because of the dissipative processes due to phonons and electron-electron scattering. One way to partially avoid these issues can be the use of alternative platforms with similar properties, such as artificial graphene[106]. This would help in two different ways: The increase of the lattice parameter allows to consider lower frequencies and then lower the field intensities, while in addition, the s-orbitals contribution vanish. Finally, we expect that the results obtained in the intermediate frequency regime to be more easily achievable in real graphene, if only because the undesirable heating of the sample will be reduced. Furthermore, this regime also allows to create new pairs of Dirac points just by tuning the frequency which is a new feature not previously studied.

5.3 Graphene Ribbons and Edge States

Before we discuss the effect of time reversal symmetry breaking field configurations, we proceed to discuss the properties of graphene ribbons. It is known that for the case of graphene ribbons we can obtain a Hamiltonian which is equivalent to the one used for the description of a dimers chain[84]. This mapping intuitively explains why different ribbons possess different zero energy modes. The dimers chain belongs to the BDI class of Hamiltonians, and defines a 1D winding number topologically protected by chiral symmetry – exactly as we shown in the introduction of this chapter. The winding number value only depends on the ratio between the intra-dimer and the inter-dimer hoppings, and this mapping explicitly shows its relation with the ribbon configuration. Here we build this mapping for periodically driven graphene in order to calculate the quasi-energy spectrum of irradiated graphene ribbons.

5.3.1 Armchair ribbons

In order to obtain the armchair ribbon Hamiltonian, we first define an appropriate basis for the mapping between the edge of the graphene ribbon and the dimers chain (see Figure 5.1.1 for a definition of the x and y directions considered). The most appropriate one for this case is:

$$\vec{a}_1' = 3a\,(1,0)\,, \quad \vec{a}_2 = \frac{a}{2}\left(3,-\sqrt{3}\right), \tag{5.3.1}$$

where we have chosen the $\vec{a}_1$ unit vector parallel to the armchair edge. Next we write the tight binding Hamiltonian by assuming that the x coordinate is referred to the direction with periodic boundary conditions (meaning that k_x is a well defined quantum number):

$$H^x_{AC}\,(k_x) = \begin{pmatrix} 0 & \rho\,(k_x)^* \\ \rho\,(k_x) & 0 \end{pmatrix}, \tag{5.3.2}$$

$$\rho\,(k_x) = \sum_{m_y,n_y} t_1 e^{ik_x a}\delta_{m_y,n_y} + t_2 e^{-ik_x a/2}\delta_{m_y+1,n_y} + t_3 e^{-ik_x a/2}\delta_{m_y-1,n_y}. \tag{5.3.3}$$

The (m_y, n_y) indices label the tunneling processes along the y direction (finite length), between the unit cells at sites m_y and n_y. The finite sum of Equation 5.3.2 for all $m_y,\ n_y$ is the ribbon Hamiltonian for the case of an undriven armchair ribbon of graphene.

When the armchair ribbon is coupled to an AC electric field we can describe its effect by means of the minimal coupling with the k_x crystal momentum, and with an on-site energy term in the y direction. Usually these are different representations related by a gauge transformation[107], but in the present case we can use both of

them, since the vector potential $\mathbf{A}(\tau)$ commutes with $\hat{p}$. The AC driven Hamiltonian is:

$$\begin{aligned} H_{AC}(\tau) &= H^x_{AC}(k_x + A_x(\tau)) + H^y_{AC}(\tau) && (5.3.4)\\ H^y_{AC}(\tau) &\equiv \sum_{m_y} E_y(\tau)\, y|m_y\rangle\langle m_y|\delta_{m_y,n_y} && (5.3.5)\\ E_y(\tau) &\equiv E_y \cos(\omega\tau+\varphi) = A_y\omega\cos(\omega\tau+\varphi), && (5.3.6)\\ A_x(\tau) &\equiv A_x \sin(\omega\tau) = \frac{E_x}{\omega}\sin(\omega\tau), && (5.3.7) \end{aligned}$$

and its matrix elements are:

$$\begin{aligned} H_{AC}(\tau) &= \begin{pmatrix} \sum_{m_y,n_y} \frac{a\sqrt{3}}{2} m_y E_y(\tau)\,\delta_{m_y,n_y} & \rho(k_x,\tau)^* \\ \rho(k_x,\tau) & \sum_{m_y,n_y} \frac{a\sqrt{3}}{2} m_y E_y(\tau)\,\delta_{m_y,n_y} \end{pmatrix},\\ \rho(k_x,\tau) &= \rho(k_x + A_x(\tau)). && (5.3.8) \end{aligned}$$

For the calculation of the quasi-energies we use the Sambe space scalar product. This leads to the Fourier decomposition of the Hamiltonian:

$$\begin{aligned} \frac{1}{T}\int_0^T H_{AC}(\tau)\, e^{i\omega(p-q)\tau} d\tau &= \begin{pmatrix} 0 & \rho(k_x,A_x)^* \\ \rho(k_x,A_x) & 0 \end{pmatrix} && (5.3.9)\\ &\quad + \sum_{m_y,n_y} \frac{a\sqrt{3}}{2} m_y E_y \delta_{m_y,n_y} \left(\frac{e^{i\varphi}\delta_{p+1,q} + e^{-i\varphi}\delta_{p-1,q}}{2}\right)\mathcal{I}_{2\times 2}, \end{aligned}$$

where

$$\begin{aligned} \rho(k_x,A_x) &\equiv \tilde{t}_1 e^{ik_x a}\delta_{m_y,n_y} + \tilde{t}_2 e^{-ik_x a/2}\delta_{m_y+1,n_y} + \tilde{t}_3 e^{-ik_x a/2}\delta_{m_y-1,n_y},\\ \tilde{t}_1 &= t_1 J_{q-p}(A_x a),\\ \tilde{t}_2 &= t_2 J_{p-q}(A_x a/2),\\ \tilde{t}_3 &= t_3 J_{p-q}(A_x a/2). && (5.3.10) \end{aligned}$$

As previously, the matrix element ρ^* is now obtained by complex conjugation and a change $(p,q) \to -(p,q)$. Note that φ is just present in the real space components $E_y(\tau,\varphi)\, y$ due to the vector potential configuration $\mathbf{A}(\tau) = (A_x \sin(\omega\tau), A_y \sin(\omega\tau+\varphi))$.

5.3.2 Zigzag ribbons

For the case of a zigzag ribbon it is simpler to introduce a new reference frame, in which the zigzag edge is parallel to the translation vector ($\vec{a}_1''$ in Figure 5.1.1), where the calculations are simplified. The basis is given by:

$$\vec{a}_1'' = a\left(0,\sqrt{3}\right),\ \vec{a}_2 = \frac{a}{2}\left(3,-\sqrt{3}\right). \qquad (5.3.11)$$

In this case, we just need to repeat the same procedure than for the armchair ribbon, but now considering the new basis. It leads to the matrix elements:

$$H_{AC}^{y}\left(k_y\right) = \begin{pmatrix} 0 & \rho\left(k_y\right)^* \\ \rho\left(k_y\right) & 0 \end{pmatrix}, \tag{5.3.12}$$

$$\rho\left(k_y\right) \equiv \sum_{m_x,n_x} t_1 \delta_{m_x,n_x} + \left(t_2 e^{i\sqrt{3}k_y a/2} + t_3 e^{-i\sqrt{3}k_y a/2}\right)\delta_{m_x-1,n_x}, \tag{5.3.13}$$

being the whole Hamiltonian given by:

$$H_{AC}\left(\tau\right) = H_{m_x,n_x}^{B}\left(k_y + A_y\left(\tau,\varphi\right)\right) + H_{AC}^{x}\left(\tau\right), \tag{5.3.14}$$

$$H_{AC}^{x}\left(\tau\right) \equiv \sum_{m_x,nx} E_x\left(\tau\right) x|m_x\rangle\langle m_x|\delta_{m_x,n_x}, \tag{5.3.15}$$

$$E_x\left(\tau\right) \equiv E_x \cos\left(\omega\tau\right) = -A_x\omega\cos\left(\omega\tau\right), \tag{5.3.16}$$

$$A_y\left(\tau\right) \equiv A_y \sin\left(\omega\tau+\varphi\right) = \frac{E_{0,y}}{\omega}\sin\left(\omega\tau+\varphi\right), \tag{5.3.17}$$

$$H_{AC}^{B}\left(\tau\right) = \begin{pmatrix} \sum_{m_x,nx} a\frac{3}{2}m_x E_x\left(\tau\right)\delta_{m_x,n_x} & \rho\left(k_y\left(\tau\right)\right)^* \\ \rho\left(k_y\left(\tau\right)\right) & \sum_{m_x,nx} a\left(\frac{3}{2}m_x+1\right)E_x\left(\tau\right)\delta_{m_x,n_x} \end{pmatrix},$$

$$\rho\left(k_x\left(\tau\right)\right) \equiv \rho\left(k_y + A_y\left(\tau\right)\right). \tag{5.3.18}$$

Time averaging the matrix elements to obtain the Sambe space representation of the Hamiltonian we finally obtain:

$$\frac{1}{T}\int_0^T H_{AC}\left(\tau\right)e^{i\omega(p-q)\tau}d\tau = \begin{pmatrix} 0 & \rho\left(k_y, A_{0,y}\right)^* \\ \rho\left(k_y, A_{0,y}\right) & 0 \end{pmatrix} + \sum_{m_x,n_x} aE_{0,y}\delta_{m_x,n_x}\left(\delta_{p+1,q}+\delta_{p-1,q}\right)\begin{pmatrix} \frac{3}{4}m_x & 0 \\ 0 & \frac{3}{4}m_x+\frac{1}{2} \end{pmatrix}, \tag{5.3.19}$$

where

$$\rho\left(k_y, A_{0,y}\right) \equiv t_1\delta_{m_x,n_x}\delta_{p,q} + \left(\tilde{t}_2 e^{i\sqrt{3}k_y a/2} + \tilde{t}_3 e^{-i\sqrt{3}k_y a/2}\right)\delta_{m_x-1,n_x}, \tag{5.3.20}$$

$$\tilde{t}_2 \equiv t_2 J_{q-p}\left(\sqrt{3}A_{0,y}a/2\right)e^{i\varphi(q-p)}, \tag{5.3.21}$$

$$\tilde{t}_3 \equiv t_3 J_{p-q}\left(\sqrt{3}A_{0,y}a/2\right)e^{i\varphi(q-p)}. \tag{5.3.22}$$

As in the previous case, the matrix element ρ^* is now obtained by complex conjugation and a change $(p,q) \to -(p,q)$ in the Bessel functions arguments. In addition, for the zigzag ribbon, the phase difference φ is now encoded in the components along the direction with periodic boundary conditions.

5.4 Circular polarization and the quantum anomalous Hall effect

In the previous section we have shown that AC electric fields coupled to electrons in a honeycomb lattice allow to merge the Dirac cones for linearly polarized fields. We also proved that non linear field polarizations break time reversal symmetry when couplings between side-bands are considered. Here we analyze in detail the time reversal symmetry broken phases and discuss the effect of lower frequencies using a full numerical approach. Importantly, we show that the insulating phase corresponds to a physical realization of a Chern insulator predicted by Haldane in 1988[108]. This topological phase is characterized by the first Chern number c_1, as for the case of the quantum Hall effect, but importantly it is obtained in the absence of external magnetic fields. The first experimental realization of the quantum anomalous Hall effect (QAHE) has been recently reported by magnetic doping of a topological insulator[109].

Here we propose an alternative procedure to obtain the QAHE by using non-linearly polarized fields in graphene, instead of magnetic impurities in a topological insulator. Even further, we show that the mechanism which allows to gap the Weyl semimetallic phases is general and can be used in a wider range of setups. Finally, we prove that by tuning the AC field parameters it is possible to obtain a plateaus structure for the conductivity and the density of states. This represents a Floquet analog of the plateau structure of the quantum Hall effect.

5.4.1 Bulk Model

The bulk model will allow us to derive the full phase diagram of the QAHE by explicitly calculating the Chern number of the Floquet bands, beyond the single Dirac cone approximation and for arbitrary amplitude and polarization of the field. We shall consider the same Hamiltonian as in the previous section (Equation 5.2.3) due to its generality. It considers electrons on a honeycomb lattice coupled to an in-plane, spatially homogeneous, AC electric field of period $T = \frac{2\pi}{\omega}$. We stress that the previous derivation is exact and therefore correctly describes a uniform AC electric field with arbitrary polarization, amplitude and frequency. Besides, the low energy approximation for a single Dirac cone is not needed, which would add a constrain on the field amplitude values. In addition, in our approach the effect of the field amplitude $A_{x,y}$ and frequency ω are separated, then it is clear how the band structure changes: The frequency ω shifts the distance between Floquet side-bands and the field amplitude renormalizes the hoppings t.

5.4.2 Phase diagram of the lattice model

In the high frequency regime ($\omega \gg t$) the Floquet operator (Equation 5.2.3) is approximately block diagonal, meaning that photon absorption/emission are not very likely. Then, as we discussed above, one can choose a single block as the effective Floquet operator. In this limit, the system fulfills both time reversal and particle-hole symmetries, and its Hamiltonian is analogous to the one of undriven graphene with renormalized anisotropic hoppings $t^F_{j,0} = tJ_0(\mathcal{A}_j)$. The hopping anisotropy breaks inversion symmetry and moves the relative position of the Dirac points. When the anisotropy fulfills $\pm t^F_{i,0} \pm t^F_{j,0} \pm t^F_{k,0} = 0$ $(i \neq j \neq k)$, the Dirac points merge, leading to an insulating state. The resulting phase diagram in terms of the electric field parameters was analyzed in terms of different merging processes in the previous section. It contains several Dirac semi-metallic (SM) and Zak insulating phases (ZI), as illustrated in Figure 5.4.1 (left) for $A_x = A_y$.

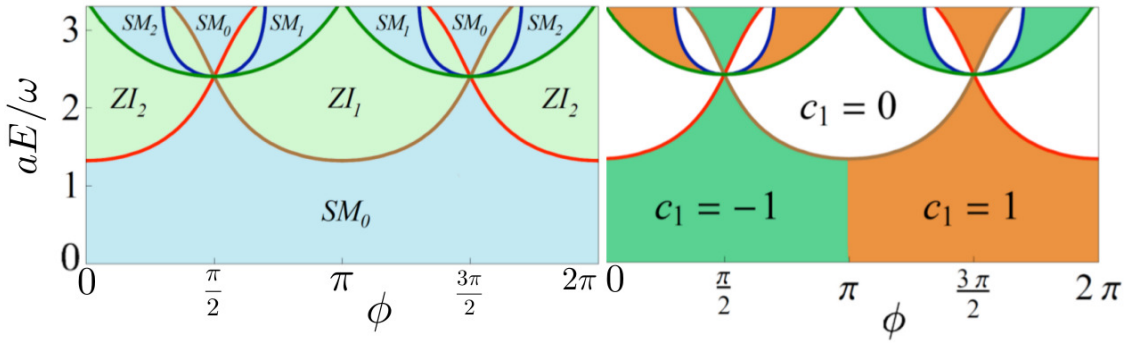

Figure 5.4.1: (Left) Phase diagram of semi-metallic SM_i (light blue) and insulating phases ZI_i (light green) obtained by merging the Dirac points at the different time reversal symmetric points of the first Brillouin zone. (Right) Calculation of the first Chern number of the valence Floquet band for $\omega = 10t$ when first order coupling among the Floquet side-bands is considered. The transitions between two Chern phases occur when the Dirac points of the unperturbed Hamiltonian merge, or when TRS is restored.

Nevertheless, in this section we are interested in changes of the phase diagram when TRS is broken by non linear field polarizations. This is included, even at high frequency, due to a finite coupling between the Floquet side-bands. If this coupling breaks time reversal symmetry – as for the case of non-linearly polarized fields – an inverted gap opens[77]. This can be understood by noticing that the renormalized hoppings contain complex phases Ψ_i for non-linearly polarized fields. In order to take into account the effect of this small coupling, we now use first order perturbation theory in t/ω and derive an effective time independent Bloch Hamiltonian as it is described in Appendix D, leading to:

$$H_{\text{eff}}(\mathbf{k}) = H_0 - \frac{1}{\omega}\left([H_0, H_{-1}] - [H_0, H_1] + [H_{-1}, H_1]\right), \tag{5.4.1}$$

where $H_{0,\pm1}$ are the 0, and ±1 Fourier components of the time dependent Hamiltonian obtained in Equation 5.2.3. It worth mentioning that we have also derived Equation 5.4.1 by using the more rigorous Magnus expansion, and the similarities between this result and the one obtained for example in [77]. However, as we did not require a low energy approximation to a single Dirac cone, we are not restricted to small values of the field amplitude. This feature allows us to fully address the phase diagram and the Chern number dependence on the external parameters. In Figure 5.4.2 we plot the exact gap obtained in a system with periodic boundary conditions when non linear polarization is considered. In contrast, a gapless phase is developed when linear polarization is considered and the merging of the Dirac points has not happened yet.

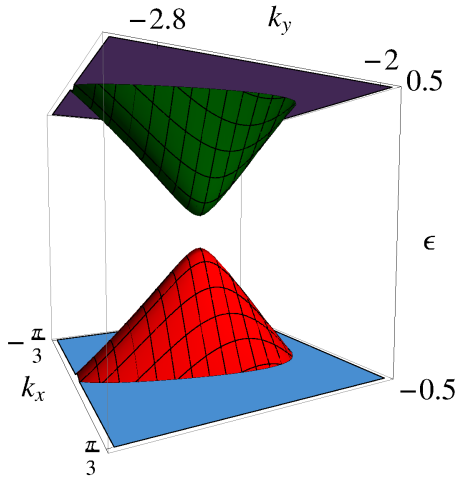

Figure 5.4.2: Quasi-energy spectrum in units of t for AC driven graphene. We have considered $\omega = 10t$, $\varphi = \pi/2$ and $A_y = A_x = 1$. According to Figure 5.4.1, this phase corresponds to a Weyl semi-metal (SM_0), but the finite coupling between Floquet bands opens a gap. In opposition, the case with $\varphi = 0$ still is a gapless phase (not shown).

The correction to $H_0 = H_0(\mathbf{k})$ in Equation 5.2.3 is proportional to $t\sigma_z/\omega$, where σ_z is the Pauli matrix, and opens a quasi-energy gap at the Dirac points if $\varphi \neq 0, \pi$. Besides, this correction is $\mathbf{k}$ dependent, unlike what is found within the single Dirac cone approximation[77, 110, 111]. This will now allow us to take into account the motion of the Dirac points in the calculation of the the Chern number for arbitrary polarization and field amplitude.

We characterize the topology of the AC driven lattice by the explicit calculation of the Chern number using the effective Hamiltonian H_{eff}. The Chern number of a Floquet band n is defined as the integration over the Brillouin zone of the Berry curvature $\nabla \wedge \mathbf{A}_n$:

$$c_n = -\frac{1}{2\pi} \int dk_x dk_y \nabla \wedge \mathbf{A}_n \tag{5.4.2}$$

where $\mathbf{A}_n = \langle u_n(\mathbf{k},t)\,|i\nabla|\,u_n(\mathbf{k},t)\rangle$. We follow the elegant method of the Brouwer degree developed in Ref.[112] to evaluate the Chern number. This analytical approach especially requires to know the positions of the Dirac points for any value of the field, which is obtained by means of the expression of the dressed hoppings $t^F_{j,0}(A_x, A_y, \varphi)$. Note that the inequivalent Floquet bands resulting from a periodically driven two-bands system necessarily have opposite Chern numbers[79], so that we only need to compute the Chern number of one of them.

We show in Figure 5.4.1 (right) the values of the Chern number for the valence band in the case where $A_x = A_y$. This phase diagram is the first main result of the present work. It is interesting to compare the two phase diagrams of Figure 5.4.1, where we find that the Chern number remains zero in the regions related with insulating phases in the high frequency limit, but becomes ± 1 in the ones related with semimetallic phases in the same limit. This agrees with the Brouwer degree picture, in which for the existence of a Chern number it is a necessary condition to find a gapless phase when the Hamiltonian is projected onto an arbitrary plane (e.g., $\sigma_z \to 0$). Importantly, the phase diagram also shows how the Chern number value can be tuned by the field amplitude or by the phase polarization in this frequency regime. In contrast, within the single Dirac cone approximation, the analysis is restricted to the weak amplitude regime, where it is stated that the value of the Chern number $c_1 = +1$ or -1 only depends on the chirality of the field. The less restrictive approach used here shows that the phase polarization φ does not fix by itself the value of the Chern number. Indeed, any value of $c_1 = 0, \pm 1$ can in principle be implemented for a given phase φ. It is worth mentioning that we also have checked the phase diagram of Figure 5.4.1 by performing an alternative and exact approach based on a lattice gauge theory [113] showing full agreement. In addition, the calculation of the system's spectrum in a finite geometry exhibits chiral edge states when the Floquet bands have a non zero Chern number. This is shown for armchair and zigzag ribbons and parameters $A_x = A_y = 1$ and $\varphi = \frac{\pi}{2}$ in Figure 5.4.3. As expected, these spectra clearly show that the existence of the Floquet chiral edge states is independent of the ribbons boundary. We shall see in the following that such a statement becomes more subtle for lower frequencies. For completeness, when the system is in a phase with Chern number $c_1 = 0$, the chiral edge states does not appear (see Figure 5.4.4). Instead, the existence of localized end states is restricted by whether the system is in a Zak insulating phase or a trivial phase. Note that these states can be removed by a shift of the "Fermi energy level" and they are not dispersive. In opposition, the edge states arising from a non zero Chern number phase are chiral and propagate along the boundaries. Finally, we stress that the edge states arising in a non-zero Chern number phase connect both bands, representing a condensed matter realization of the AQHE.

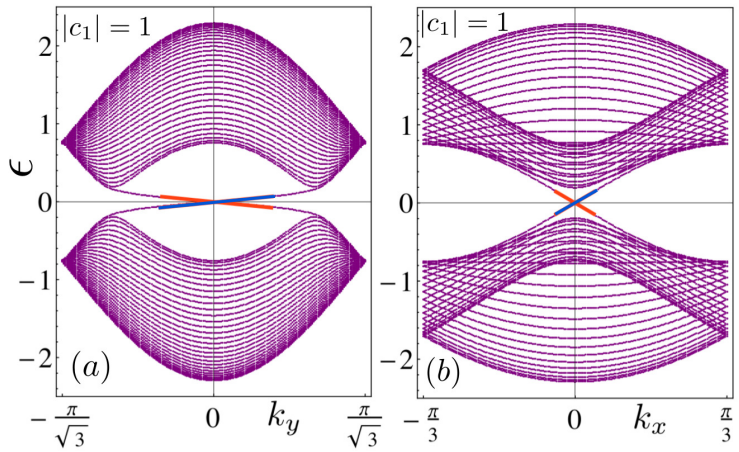

Figure 5.4.3: Edge states for the high frequency regime ($\omega = 10t$). (a) shows the zigzag ribbon spectrum with two chiral edge states propagating along the right/left (red/blue) boundary, while (b) shows the armchair spectrum. Parameters considered: 30 unit cells of length for the ribbons, $t = 1$, $\varphi = \pi/2$ and $A_x = A_y = 1$.

5.4.3 Multi-photon resonances and the emergence of plateaus

We now ask whether the driving can induce topological phases with Chern numbers larger than 1. One way to address this question is to notice that in order to obtain larger Chern numbers, it is necessary to have more than one pair of Dirac points. In the previous section, we have shown that multi-photon resonances, occurring when the Floquet bands overlap, can induce additional pairs of Dirac points, provided that TRS holds [17, 114]. Such an overlap can be achieved by decreasing the frequency, which brings the Floquet side-bands closer to each other. It is therefore natural to investigate the effect of a frequency decrease on the topological properties of the system, for TRS breaking driving fields.

On the other hand, a decrease in frequency increases the number of bands involved in the description of the system, and as one approaches $t \sim \omega$ the validity of H_{eff} breaks down. In this regime the system's dynamics becomes highly non-linear, and a numerical treatment is required. Let us first describe how the system is affected when the side-bands overlap. As we discussed in Chapter 4, for periodically driven systems we must distinguish two inequivalent gaps: the one between the conduction and the valence bands *within* the same Floquet side-band Δ_0, and the one separating two *different* side-bands Δ_π as depicted in Figure 5.4.5. Note that the gap Δ_π was assumed to be infinite at high frequency. This is commonly referred as the atomic limit for the system, in which the gap is always trivial. The consequence is that for the high frequency limit just edge states within the Δ_0 gap can exist. When neighboring side-bands touch due to a frequency decrease, the gap Δ_π closes and a topological phase transition can happen from the atomic limit. Figure 5.4.6 (a-b) shows the quasi-energy spectra for zigzag and armchair ribbons after the gap Δ_π has

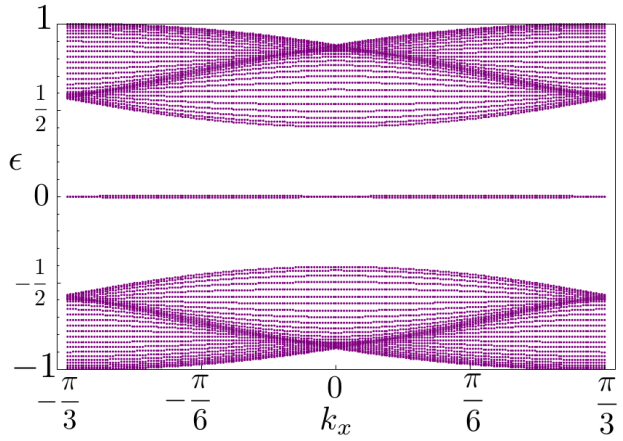

Figure 5.4.4: Quasi-energy spectrum for graphene armchair ribbon in a topologically trivial region. The parameters are: $A_x = A_y = 2$, $\varphi = 0.6$, $\omega = 10t$, and 20 unit cells for the ribbon. For a zigzag ribbon also the not topologically protected edge states are found (not shown).

closed and re-opened by decreasing the frequency to $\omega = 2.5t$. There, two chiral edge states with opposite chirality to the pre-existing one in the gap Δ_0 have emerged along each boundary. This also illustrates that in Floquet Chern insulators the chiral edge states at a given boundary can propagate in opposite directions. Note that because of the quasi-energy shift of $\pm\omega/2$, the *new* states in the gap Δ_π differ from the ones in the gap Δ_0 by their time evolution [75, 102] as they contain a time dependent correlation between the spinor components. It is therefore important to know whether two edge states with opposite chirality lie in the same gap or not. The Chern number of the new phase can be deduced from $c_1 = W_0 - W_\pi$ where $W_{0/\pi}$ is the total chirality of the edge states lying in the gap $\Delta_{0/\pi}$[79]. This leads to $c_1 = 1 - (-2) = 3$ for the present phase. Next, we use lattice gauge theory [113] to explicitly compute the Chern number for arbitrary frequencies. We plot the (absolute) value of the Chern number as the frequency is decreased in Figure 5.4.7. This is the second main result of this work. It shows a plateau structure with oscillations, which reflects the alternating closures and re-openings of the gaps Δ_0 and Δ_π as the frequency is tuned. Importantly, for a given plateau, it is still possible to change the Chern number by tuning the field amplitude or polarization, as it is shown in Figure 5.4.1. Note that the period of the Chern number oscillations decreases with the frequency as it is expected due to the folding of the Floquet side-bands. Obviously, one cannot deduce the total chirality of the edge states in the system $W = W_0 + W_\pi$ from the Chern number, but just the minimal amount of edge states which is consistent with the total chirality. However, a change of Chern number necessarily involves a change in the total chirality W. Actually, W is another topological invariant of the system and can be expressed as a 3D winding number in the extended $(\mathbf{k}, t)$ space [79]. It follows that the total chirality in each gap $W_{0/\pi}$ is also an invariant. In contrast, the number of edge states – in total, as

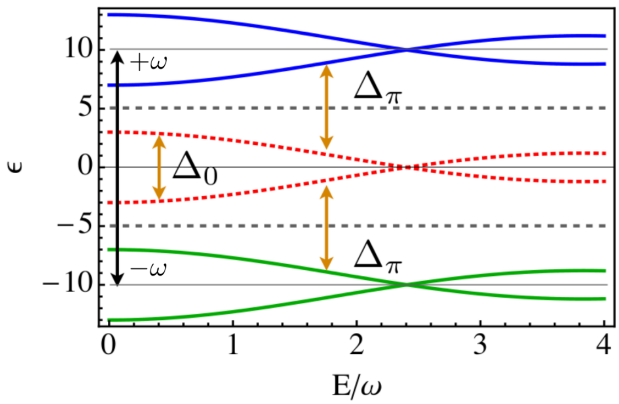

Figure 5.4.5: Schematic representation of three equivalent side-bands (red, blue and green) separated by an ω shift, and the two inequivalent gaps $\Delta_{0,\pi}$. Dashed lines show the boundaries of each side-band.

well as in each gap – is not an invariant. Indeed, for sufficiently weak frequency, we show in Figure 5.4.6 (c-d) that the number of edge states depends on the edge geometry, although it is always in agreement with the value of the Chern number ($|c_1| = 4$) as well as with the chirality in each gap $W_0 = 0$ and $|W_\pi| = 4$.

The measurement of a density of states for an out-of-equilibrium system is a non trivial problem currently under intense theoretical study. Recently, the transport signatures of zero energy modes in periodically driven system have been discussed for all frequency regimes [102]. The main result is the existence of a Floquet sum rule which states that the quantized conductivity corresponds to the sum of the conductivities at $V + n\omega$ where V is the voltage bias. Thus, a quantized conductivity is finally obtained for each of the inequivalent edge states at the $\Delta_{0/\pi}$ gaps. This result allows us to connect the previous plateau structure with changes in the conductivity due to variations of the winding number W, and with the minimum number of edge states lying in the gaps $\Delta_{0,\pi}$, which reproduces a plateau structure for the QAHE**.** However, note that the plateaus for the conductivity and for the density of states at each boundary will have different quantized values in general.

In conclusion, we have obtained a general Hamiltonian for electrons coupled to an AC electric field on the honeycomb lattice, which includes TRS breaking terms for non linearly polarized field configurations. We have studied high and intermediate frequency regimes, showing that the bulk Hamiltonian can be highly modified tuning the external field parameters. It allows to obtain a complete phase diagram of the Chern number as a function of the external parameters with arbitrary Chern number value. In addition, we have studied numerically the quasi-energy spectrum when finite couplings between Floquet side-bands are considered for different open boundary conditions. It leads to successive topological phase transitions in both, the $\Delta_{0,\pi}$ gaps, with the emergence of the corresponding chiral edge states. We have proposed this mechanism as a general one to obtain Chern insulators from 2D Dirac

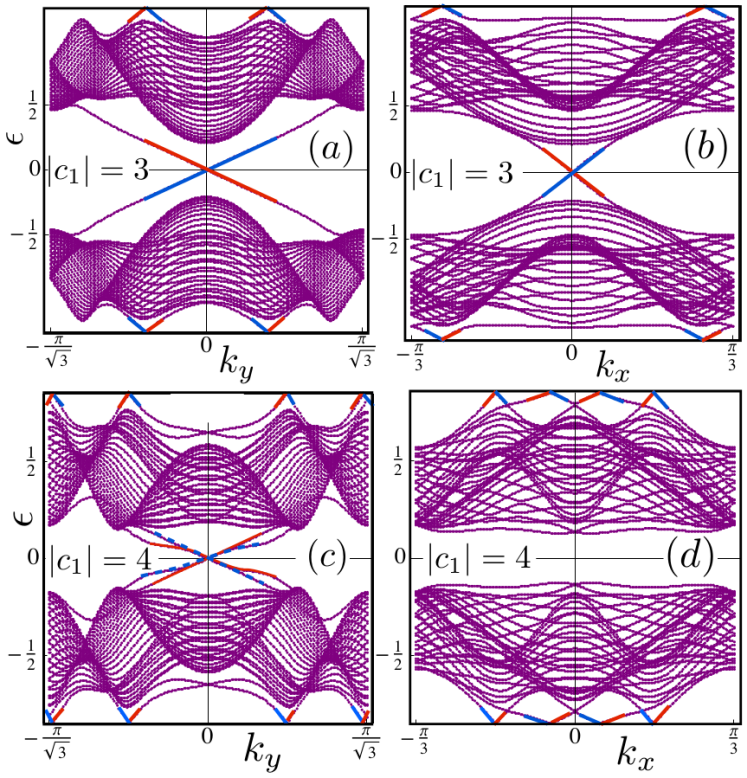

Figure 5.4.6: Quasi-energy spectra in units of t for zigzag (a, d), and armchair (b, d) ribbons at frequencies $\omega = 2.5t$ (top) and $\omega = 1.7t$ (bottom) respectively. The field amplitude and polarization are $A_x = A_y = 1$, and $\varphi = \pi/2$. Chiral edge states in thick red/blue color connect the valence and conduction band and propagate along the right/left boundary respectively. It is clear that for the case $\omega = 1.7t$ the number of chiral states in each gap is edge dependent, although the total chirality is invariant because the two edge states at Δ_0 counter propagate at the same edge.

semi-metallic phases, in which the coupling of the system to non linearly polarized AC electric fields breaks TRS opening a non topologically trivial gap.

Finally, we have shown how to control the Chern number value (for fixed field amplitude) with a decrease in frequency, yielding a plateau structure for the QAHE. This is a zero magnetic field analog of the plateaus in the quantum Hall effect. These plateaus reveal changes in the amount of chiral edge states that should directly affect the conductivity of the system. In contrast with the plateaus in time independent systems, we showed that the edge states arise in two inequivalent gaps $\Delta_{0/\pi}$ and that their total number depends on the geometry of the edge, although their total chirality does not. Our model finds a natural application in graphene irradiated by uniform THz electromagnetic fields, and a signature of the plateaus should be visible in ARPES measurements, as well as in the conductance measurement of a multi-terminal set-up. Nevertheless, the emergence of Chern number plateaus

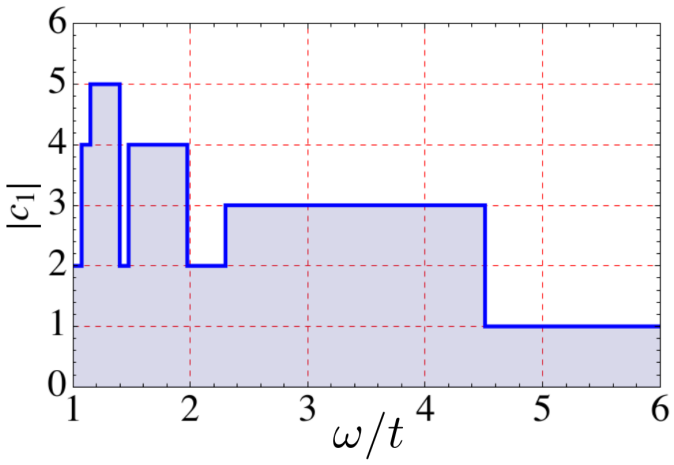

Figure 5.4.7: Chern number value vs ω. Note how the change in frequency creates a plateau structure in which every step is related with a closure of the gaps $\Delta_{0,\pi}$.

by multi-photon resonances is a general statement for any undriven gapless phase perturbed by non-linear AC electric fields, and could easily be applied to other 2D systems such as the surface of 3D topological insulators.

Appendix

Appendix A: Master equation

Here we provide all detailed calculations of the master equation approach to periodically driven systems.

First we prove that linear order term $[H_B, \rho(t)]$, at the left hand of Equation 3.2.12, vanishes when the trace over the reservoirs degrees of freedom is considered. This is due to the off diagonal form of the tunneling Hamiltonian.

Let us write the coupling Hamiltonian as a linear combination of system operators Q_j, and leads operators $F_{j,K}$:

$$V \equiv \sum_{j,K} F_{j,K} Q_j, \tag{.0.3}$$

where we have considered that the index j contains all the information of the central system states, (i.e., $j = \sigma, i, p$ is a multi-index, where $p = 1, 2$ labels if the operator creates or annihilates a particle respectively, σ labels the spin degree of freedom and i the additional degrees of freedom characterizing the central system properties), and K labels the momentum of the electron in the reservoir. In the interaction picture we write V as:

$$\begin{aligned} \tilde{V}(t, t_0) &= U_0^{\dagger}(t, t_0) \sum_{j,K} F_{j,K} Q_j U_0(t, t_0) \\ &= \sum_{j,K} \tilde{F}_{j,K}(t, t_0) \tilde{Q}_j(t, t_0) \end{aligned} \tag{.0.4}$$

where $\tilde{F}_j(t, t_0) = U_B(t - t_0)^{\dagger} F_{j,K} U_B(t - t_0)$, and $\tilde{Q}_j(t, t_0) = U_S(t - t_0)^{\dagger} Q_j U_S(t - t_0)$. The trace over the bath degrees of freedom can be rewritten as:

$$\begin{aligned} \mathrm{Tr}_B\left\{\tilde{F}_{j,K}(t, t_0)\rho_B\right\} &= \sum_{|j,K\rangle} \langle j, K \mid \tilde{F}_{j,K}(t, t_0)\rho_B \mid j, K\rangle \\ &= \sum_{|j,K\rangle} \langle j, K \mid \tilde{F}_{j,K}(t, t_0) \mid j, K\rangle \rho_{B,(j,K)} \end{aligned} \tag{.0.5}$$

where $\mid j, K\rangle$ is a complete basis that diagonalizes the leads Hamiltonian H_B, and $\rho_{B,(j,K)}$ are the diagonal elements of the bath density matrix. Therefore, as we

required an off-diagonal V operator in $F_{j,K}$, the term proportional to H_B in the left hand of Equation 3.2.13 vanishes when the trace is performed.

To obtain the detailed rates of the master equation we proceed as follows: If we consider the right hand of Equation 3.2.13, the elements of the commutator which are affected by the trace can be written as two different terms:

$$G_1(t-\tau,t) = \sum_{j,l,K,K'} Tr_B\left\{F_{j,K}\tilde{F}_{l,K'}(t-\tau,t)\,\rho_B\right\}, \tag{.0.6}$$

$$G_2(t-\tau,t) = \sum_{j,l,K,K'} Tr_B\left\{\tilde{F}_{l,K'}(t-\tau,t)\,F_{j,K}\rho_B\right\}, \tag{.0.7}$$

which fulfill $G_2(t-\tau) = G_1^*(t-\tau)$, and $\tilde{F}_j(t,t_0) = U_B(t-t_0)^\dagger F_{j,K}U_B(t-t_0)$. It allows to write the master equation for the reduced density matrix in a more compact form:

$$\begin{aligned}\dot{\rho}_S(t) + i\left[H_S(t),\rho_s(t)\right] &= -\int_0^\infty d\tau \sum_{j,l,K,K'} G_1(t-\tau,t)\left[Q_j,\tilde{Q}_l(t-\tau,t)\,\rho_s(t)\right] \\ &\quad -\int_0^\infty d\tau \sum_{j,l,K,K'} G_1^*(t-\tau,t)\left[\rho_s(t)\,\tilde{Q}_l(t-\tau,t),Q_j\right],\end{aligned}$$

where $\tilde{Q}_j(t,t_0) = U_S(t-t_0)^\dagger Q_j U_S(t-t_0)$.

When we apply the Floquet basis for the master equation of the reduced density matrix, the left hand side of the master equation gives:

$$\langle\phi_\alpha(t)|\left(\dot{\rho}_S(t) + i\left[H_S(t),\rho_s(t)\right]\right)|\phi_\beta(t)\rangle = \left(\partial_t + i\varepsilon_{\alpha\beta}\right)\rho(t)_{\alpha\beta}, \tag{.0.8}$$

$$\langle\phi_\alpha(t)|\rho_S(t)|\phi_\beta(t)\rangle \equiv \rho(t)_{\alpha\beta}, \tag{.0.9}$$

$$\varepsilon_{\alpha\beta} \equiv \varepsilon_\alpha - \varepsilon_\beta, \tag{.0.10}$$

while the right hand side terms become:

$$\langle\phi_\alpha(t) \mid Q_j\tilde{Q}_l(t-\tau,t)\,\rho_s(t) \mid \phi_\beta(t)\rangle = \sum_{\mu\nu} Q(t)_{j,\alpha\mu}\,\tilde{Q}(t-\tau,t)_{l,\mu\nu}\,\rho(t)_{\nu\beta},$$

where greek indexes label Floquet states. In addition, the time dependent periodic functions $Q(t)_{j,\alpha\beta}$ and $\tilde{Q}(t-\tau,t)_{l,\mu\nu}$ can be expanded in Fourier series:

$$Q(t)_{j,\alpha\beta} = \sum_n e^{-in\omega t}Q(n)_{j,\alpha\beta}, \tag{.0.11}$$

$$\begin{aligned}\tilde{Q}(t-\tau,t)_{l,\mu\nu} &= \langle\phi_\mu(t) \mid U_s^\dagger(t-\tau,t)\,Q_l U_s(t-\tau,t) \mid \phi_\nu(t)\rangle \\ &= e^{-i\tau\varepsilon_{\mu\nu}}\langle\phi_\mu(t-\tau) \mid Q_l \mid \phi_\nu(t-\tau)\rangle \\ &= e^{-i\tau\varepsilon_{\mu\nu}}Q_{l,\mu\nu}(t-\tau).\end{aligned} \tag{.0.12}$$

leading to:

$$\begin{aligned}\sum_{\mu\nu} Q(t)_{j,\alpha\mu}\,\tilde{Q}(t-\tau,t)_{l,\mu\nu}\,\rho(t)_{\nu\beta} &= \sum_{\mu\nu nm} e^{-i(n+m)\omega t}e^{i\tau(m\omega-\varepsilon_{\mu\nu})} \\ &\quad \times Q(n)_{j,\alpha\mu}\,Q_{k,\mu\nu}(m)\,\rho(t)_{\nu\beta}.\end{aligned} \tag{.0.13}$$

Note that for the last expression we have considered the evolution of the Floquet states under the action of the propagator as follows:

$$\begin{aligned} U_s\left(t-\tau,t\right)\mid\phi_\alpha\left(t\right)\rangle &= \sum_\beta e^{-i\varepsilon_\beta(t-\tau-t)}\mid\phi_\beta\left(t-\tau\right)\rangle\langle\phi_\beta\left(t\right)\mid\phi_\alpha\left(t\right)\rangle \\ &= e^{i\varepsilon_\alpha\tau}\mid\phi_\alpha\left(t-\tau\right)\rangle. \end{aligned}$$

Then, the full master equation in Floquet basis is given by:

$$\begin{aligned} \left(\partial_t+i\varepsilon_{\alpha\beta}\right)\rho\left(t\right)_{\alpha\beta} &= -\sum_{jl,\mu\nu,nm} e^{-i\omega t(n+m)}\sum_{K,K'}\int_0^\infty e^{i\tau m\omega} \\ &\times\{G_1\left(t-\tau,t\right)\rho\left(t\right)_{\nu\beta}Q\left(n\right)_{j,\alpha\mu}Q\left(m\right)_{l,\mu\nu}e^{-i\tau\varepsilon_{\mu\nu}} \\ &-G_1\left(t-\tau,t\right)\rho\left(t\right)_{\mu\nu}Q\left(n\right)_{j,\nu\beta}Q\left(m\right)_{l,\alpha\mu}e^{-i\tau\varepsilon_{\alpha\mu}} \\ &+G_1^*\left(t-\tau,t\right)\rho\left(t\right)_{\alpha\mu}Q\left(n\right)_{j,\nu\beta}Q\left(m\right)_{l,\mu\nu}e^{-i\tau\varepsilon_{\mu\nu}} \\ &-G_1^*\left(t-\tau,t\right)\rho\left(t\right)_{\mu\nu}Q\left(n\right)_{j,\alpha\mu}Q\left(m\right)_{l,\nu\beta}e^{-i\tau\varepsilon_{\nu\beta}}\}d\tau \end{aligned} \tag{.0.14}$$

For the evaluation of integrals in τ we can use the identity:

$$\int_0^\infty e^{i\omega\tau}d\tau=\mathcal{P}\left(\frac{i}{\omega}\right)+\pi\delta\left(\omega\right), \tag{.0.15}$$

such that the thermal coefficients result in:

$$\begin{aligned} \int_0^\infty G_1\left(t-\tau\right)e^{i\tau(m\omega-\varepsilon_{\mu\nu})}d\tau &= \sum_{|K''\rangle,|K^{(3)}\rangle} F_{j,K''K^{(3)}}F_{l,K^{(3)}K''}\rho_B\left(E_{K''}\right) \\ &\times\int_0^\infty e^{i\tau\left(m\omega-\varepsilon_{\mu\nu}+E_{K''K^{(3)}}\right)}d\tau \\ &\simeq \pi\sum_{|K''\rangle,|K^{(3)}\rangle} F_{jK,K''K^{(3)}}F_{lK',K^{(3)}K''}e^{-\beta(E_{K''}-\mu_i)} \\ &\times\delta\left(m\omega-\varepsilon_{\mu\nu}+E_{K''K^{(3)}}\right), \end{aligned} \tag{.0.16}$$

where we have used:

$$\begin{aligned} \langle K^{(3)}\sigma^{(3)}i^{(3)}|\tilde{F}_l\left(t-\tau,t\right)|K''\sigma''i''\rangle &= \langle K^{(3)}\sigma^{(3)}i^{(3)}|U_B^\dagger\left(t-\tau,t\right)F_lU_B\left(t-\tau,t\right)|K''\sigma''i''\rangle \\ &= e^{i\tau\left(E_{K''}-E_{K^{(3)}}\right)}\langle K^{(3)}\sigma^{(3)}i^{(3)}|F_l|K''\sigma''i''\rangle. \end{aligned} \tag{.0.17}$$

Note, that in Equation .0.16 we have introduced the chemical potential μ_i which is related with the bias voltage $eV=\mu_L-\mu_R$ applied to the leads. At this point, we can consider the case of a linear coupling (first order tunneling processes). In this case, the sum of states $|K''\sigma''\rangle$ and $|K^{(3)}\sigma^{(3)}\rangle$ can be simplified, as the elements which does not vanish must fulfill $\left(F_{\sigma pi,K}\right)^\dagger=F_{\sigma'p'i',K'}$, i.e., we require $\delta_{K,K'}\delta_{\sigma,\sigma'}\delta_{i,i'}\left(1-\delta_{p,p'}\right)$. Finally, if we define: $N_{i'\sigma'K'p'}=F^\dagger_{i'\sigma'K'p'}F_{i'\sigma'K'p'}$, $|i^{(3)}K^{(3)}\sigma^{(3)}\rangle=F_{i'\sigma'K'p'}|i''K''\sigma''\rangle$,

and use the fact that for fermions $|\langle a|N|b\rangle|^2 = |\langle a|N|b\rangle|$ because the occupation number is always 1 or 0, we arrive at:

$$\begin{aligned} g_1\left(m\omega-\varepsilon_{\mu\nu}\right) &= \pi\sum_{K,K'}\sum_{|K''\rangle}|\langle i''K''\sigma''|N_{\sigma'p'i',K'}|i''K''\sigma''\rangle|e^{-\beta(E_{K''}-\mu_{i''})} \\ &\times\delta_{K,K'}\delta_{\sigma,\sigma'}\delta_{i,i'}\left(1-\delta_{p,p'}\right)\delta\left(m\omega-\varepsilon_{\mu\nu}+E_{K''}-E_{K^{(3)}}\right), \end{aligned} \tag{.0.18}$$

$$\begin{aligned} g_1^*\left(m\omega-\varepsilon_{\mu\nu}\right) &= \pi\sum_{K,K'}\sum_{|K''\rangle}|\langle i''K''\sigma''|N_{\sigma,p,i,K}|i''K''\sigma''\rangle|e^{-\beta(E_{K''}-\mu_{i''})} \\ &\times\delta_{K,K'}\delta_{\sigma,\sigma'}\delta_{i,i'}\left(1-\delta_{p,p'}\right)\delta\left(m\omega-\varepsilon_{\mu\nu}-E_{K''}+E_{K^{(3)}}\right). \end{aligned} \tag{.0.19}$$

Applying this result to Equation .0.14 we arrive at the master equation in Floquet basis:

$$\begin{aligned} \left(\partial_t+i\varepsilon_{\alpha\beta}\right)\rho\left(t\right)_{\alpha\beta} &= -\sum_{jl,\mu\nu,nm}e^{-i\omega t(n+m)}\sum_{K,K'} \\ &\times\{g_1\left(m\omega-\varepsilon_{\mu\nu}\right)\rho\left(t\right)_{\nu\beta}Q\left(n\right)_{j,\alpha\mu}Q\left(m\right)_{l,\mu\nu} \\ &-g_1\left(m\omega-\varepsilon_{\alpha\mu}\right)\rho\left(t\right)_{\mu\nu}Q\left(n\right)_{j,\nu\beta}Q\left(m\right)_{l,\alpha\mu} \\ &+g_1^*\left(m\omega-\varepsilon_{\mu\nu}\right)\rho\left(t\right)_{\alpha\mu}Q\left(n\right)_{j,\nu\beta}Q\left(m\right)_{l,\mu\nu} \\ &-g_1^*\left(m\omega-\varepsilon_{\nu\beta}\right)\rho\left(t\right)_{\mu\nu}Q\left(n\right)_{j,\alpha\mu}Q\left(m\right)_{l,\nu\beta}\}. \end{aligned} \tag{.0.20}$$

Appendix B: Relation between undriven and AC driven Hamiltonians

Here we prove the relation between a time independent tight binding Hamiltonian and a periodically driven one. We shall assume that the system is driven by an AC electric field under the dipolar approximation: $\mathbf{A}\left(\mathbf{x},\tau\right)\simeq\mathbf{A}\left(\tau\right)$, meaning that the AC electric field is spatially homogeneous. Usually, the relation between an undriven system and a driven one is obtained by means of the minimal coupling $\mathbf{p}\rightarrow\mathbf{p}+\mathbf{A}\left(\tau\right)$. This relation is mainly based in the fact that the Lorentz force equation is correctly obtained under this substitution in the Hamiltonian. Thus we use the minimal coupling for a general Hamiltonian as follows:

$$\begin{aligned} H &= \frac{\mathbf{p}^2}{2m}+V\left(\mathbf{x}\right), \\ H_{\mathbf{k}} &\equiv e^{-i\mathbf{k}\cdot\mathbf{x}}He^{i\mathbf{k}\cdot\mathbf{x}}=\frac{\left(\mathbf{p}+\mathbf{k}\right)^2}{2m}+V\left(\mathbf{x}\right), \\ H\left(\tau\right) &= \frac{\left(\mathbf{p}+\mathbf{A}\left(\tau\right)\right)^2}{2m}+V\left(\mathbf{x}\right), \\ H_{\mathbf{k}}\left(\tau\right) &\equiv e^{-i\mathbf{k}\cdot\mathbf{x}}H\left(\tau\right)e^{i\mathbf{k}\cdot\mathbf{x}}=\frac{\left(\mathbf{p}+\mathbf{k}+\mathbf{A}\left(\tau\right)\right)^2}{2m}+V\left(\mathbf{x}\right) \\ &= e^{-i(\mathbf{k}+\mathbf{A}(\tau))\cdot\mathbf{x}}He^{i(\mathbf{k}+\mathbf{A}(\tau))\cdot\mathbf{x}}. \end{aligned} \tag{.0.21}$$

Where in the last line we have explicitly related the time independent system with the time dependent one. We now consider the specific case of a tight binding Hamiltonian, in which the hoppings are defined through the Fourier transformation of the energies:

$$t_{j,l} \equiv N^{-D} \sum_{\mathbf{k}} E_{\mathbf{k}} e^{-i\mathbf{k}\cdot(\mathbf{R}_j - \mathbf{R}_l)}.$$

Importantly, they are $\mathbf{k}$ independent due to the sum in $\mathbf{k}$. This implies that the $\mathbf{k}$ space representation of the Hamiltonian can encode the full time dependence within the phase factors:

$$H_{\mathbf{k}}(\tau) = N^{-D} \sum_{j,l} t_{j,l} e^{i\mathbf{K}(\tau)\cdot(\mathbf{R}_j - \mathbf{R}_l)} c(\tau)^{\dagger}_{\mathbf{k}} c(\tau)_{\mathbf{k}}.$$

Which leads to the so called Peierls substitution. Importantly, the annihilation and creation operators now also depend on time, since they are Floquet states. Finally, one could define the time dependent hoppings as $t_{j,l}(\tau) = t_{j,l} e^{i\mathbf{A}(\tau)\cdot(\mathbf{R}_j - \mathbf{R}_l)}$, which are obtained in terms of the time independent ones.

Appendix C: Time reversal and particle-hole symmetry in periodically driven systems

For Bloch Hamiltonians, which are parametrized by a $\mathbf{k}$ dependence, a local symmetry is represented by a unitary ($U^{\dagger} = U^{-1}$) or an anti-unitary operator ($A^{\dagger} = A^{-1} = U^T K$, where K is the complex conjugate operator) that commute or anti-commute with the band Hamiltonian (we do not consider space group symmetries). That is, if one considers a symmetry $\mathcal{O}$ such that $\mathcal{O}^{\dagger} H \mathcal{O} = e^{i\phi} H$, hermiticity requires the phase factor to be real, i.e., $e^{i\phi} = \pm 1$. Thus, anti-unitary operators (which can be written as a product of a unitary operator and the complex conjugate operator), can be of two different types: $\Theta^{-1} H \Theta = +1$ (they commute), or $\Xi^{-1} H \Xi = -1$ (anti-commute), respectively called time reversal type or particle-hole type. For band Hamiltonians, which explicitly contains a $\mathbf{k}$ dependence due to the space periodicity, the action of complex conjugation acts in reciprocal space as $\Theta^{-1} e^{i\mathbf{k}\cdot\mathbf{x}} \Theta = e^{-i\mathbf{k}\cdot\mathbf{x}}$, and for Bloch Hamiltonians we obtain two types of anti-unitary operators:

$$\Theta^{-1} H(\mathbf{k}) \Theta = H(-\mathbf{k}) \quad \text{(Time Reversal)}, \tag{.0.22}$$

$$\Xi^{-1} H(\mathbf{k}) \Xi = -H(-\mathbf{k}) \quad \text{(Particle-Hole)}. \tag{.0.23}$$

For time independent tight binding Hamiltonians, TRS invariant requires the hoppings to be real, as we prove next. Let us start with a general tight binding model:

$$H(k) = \sum_{k \in FBZ} \sum_{j,l} c_k^{\dagger} c_k t_{j,l} e^{ik(R_j - R_l)}, \tag{.0.24}$$

where we have omitted additional degrees of freedom, such as spin, for simplicity. Hermiticity requires $t_{l,j} = t^*_{j,l}$ and if we define:

$$h\left(k\right) \equiv \sum_{j,l} e^{ik(R_j - R_l)} t_{j,l}, \tag{.0.25}$$

the effect of a time reversal symmetry operation on the Hamiltonian results in:

$$\Theta^{-1} h\left(k\right) \Theta = \sum_{j,l} e^{-ik(R_j - R_l)} t^*_{j,l}. \tag{.0.26}$$

Thus, if we write the complex hoppings as $t_{j,l} = |t_{j,l}| e^{i\eta}$, we see that in general:

$$\begin{aligned} \Theta^{-1} h\left(k\right) \Theta &= \sum_{j,l} e^{-ik(R_j - R_l)} |t_{j,l}| e^{-i\eta} \\ &\neq \sum_{j,l} e^{-ik(R_j - R_l)} |t_{j,l}| e^{i\eta} = h\left(-k\right). \end{aligned} \tag{.0.27}$$

Therefore, we must require real hoppings $t_{j,l}$, in order to have time-reversal symmetry present our band Hamiltonian. Is also important to comment that anti-unitary operators square to ± 1, i.e., $\Theta^2 = \pm 1$, and $\Xi^2 = \pm 1$. For the time reversal operator it distinguishes between integer and half integer particles, while for the particle-hole operator the interpretation depends on the system under consideration.

For our present case, in which time periodic systems are considered, the relevant operator for the full topological classification is $\mathcal{H}\left(k, \tau\right) = H\left(k, \tau\right) - i\partial_\tau$. As we have shown for general Floquet-Bloch Hamiltonians, the Floquet operator can be written as:

$$\mathcal{H}\left(k, \tau\right) = \sum_{n,m} \sum_{j,l} t^{n,m}_{j,l} e^{ik(R_j - R_l) - i\omega\tau(n-m)} - i\partial_\tau \ , \tag{.0.28}$$

$$t^{n,m}_{j,l} \equiv \frac{1}{T} \int_0^T e^{iA(\tau)(R_j - R_l) + i\omega\tau(n-m)} d\tau \ . \tag{.0.29}$$

The presence of time reversal symmetry and particle-hole is then given by:

$$\begin{aligned} \Theta^{-1} \mathcal{H}\left(\mathbf{k}, t\right) \Theta &= \mathcal{H}\left(-\mathbf{k}, -t\right) \qquad \text{(Time Reversal)}, \\ \Xi^{-1} \mathcal{H}\left(\mathbf{k}, t\right) \Xi &= -\mathcal{H}\left(-\mathbf{k}, -t\right) \qquad \text{(Particle-Hole)}, \end{aligned}$$

where the anti-unitary operators are in general given by:

$$\begin{aligned} \Theta &= U_\Theta K, \\ \Xi &= U_\Xi K. \end{aligned}$$

Thus, it is possible to define a chiral operator given by the product of TRS and PHS $\mathcal{C} = \Theta\Xi$, as we did for the case of time independent systems.

An important consequence from these results is that an analogous procedure to the one used above, to obtain the condition for systems invariant under TRS (i.e., real

hoppings $t_{j,l}$) can be applied in time dependent systems as well. It imposes that the Sambe space hoppings $t_{j,l}^{n,m}$ must be real in order to conserve TRS in the periodically driven system. Otherwise time reversal symmetry is broken and dynamical gaps will arise in the spectrum, as the ones found in the Chapter 5 of this thesis, for non linearly polarized fields in graphene.

Appendix D: High frequency effective Hamiltonian and $1/\omega$ corrections

Here we describe a general procedure to obtain effective Hamiltonians in high frequency regime. These Hamiltonians are valid for frequencies larger than the bandwidth of the system. The method is based on a perturbative expansion in $1/\omega$ and includes the effect of weak couplings with neighboring side bands. Here we present an intuitive approach based on physical arguments, however, the same result is obtained by means of a Magnus expansion, which has been formally stablished in solid mathematical grounds.

Let us first assume a description of the long time dynamics ($\tau \gg 1/\omega$). Next, consider a stroboscopic evolution operator for the time periodic Hamiltonian over a period T, and an approximate evolution operator described by a time independent effective Hamiltonian H_{eff}:

$$U(T) = \mathcal{T} e^{-i\int_0^T H(\tau)d\tau} \simeq e^{-iH_{eff}T}. \tag{.0.30}$$

Then, we can consider a Fourier expansion of the Hamiltonian due to its time periodicity:

$$H(\tau) = \sum_{n=-\infty}^{\infty} H_n e^{in\omega\tau} \simeq H_0 + H_1 e^{i\omega\tau} + H_{-1} e^{-i\omega\tau}, \tag{.0.31}$$

where we have considered just the first harmonic contribution. Next, expanding the exponential in Taylor series we obtain:

$$e^{-i\int_0^T H(\tau)d\tau} \simeq 1 - i\int_0^T H(\tau)\,d\tau + \frac{(-i)^2}{2}\int_0^T H(\tau_1)\,d\tau_1 \int_0^T H(\tau_2)\,d\tau_2 + \dots \tag{.0.32}$$

Therefore, in terms of the previous expansion, the stroboscopic evolution operator is given by:

$$\begin{aligned} U(T) &\simeq \mathcal{T}\left\{1 - i\int_0^T H(\tau)\,d\tau + \frac{(-i)^2}{2}\int_0^T H(\tau_1)\,d\tau_1 \int_0^T H(\tau_2)\,d\tau_2\right\} \\ &= 1 - i\int_0^T H(\tau)\,d\tau - \frac{1}{2}\int_0^T d\tau_1 \int_0^{\tau_1} d\tau_2 H(\tau_1) H(\tau_2) \\ &\quad -\frac{1}{2}\int_0^T d\tau_2 \int_0^{\tau_2} d\tau_1 H(\tau_2) H(\tau_1), \end{aligned} \tag{.0.33}$$

where in the last line we have applied the time ordering operator $\mathcal{T}$. Using Equation .0.31 we can finally perform the last integrals, and obtain the effective evolution operator:

$$\begin{aligned} U(T) &\simeq 1 - iH_0T - \frac{T}{\omega}\left\{\pi H_0^2 - i\left([H_0, H_{-1}] - [H_0, H_1] + [H_{-1}, H_1]\right)\right\} \\ &\simeq 1 - iH_{eff}T - \frac{1}{2}H_{eff}^2T^2 + \dots \end{aligned} \tag{.0.34}$$

By comparison, the effective Hamiltonian is:

$$H_{\text{eff}}(\mathbf{k}) = H_0 - \frac{1}{\omega}\left([H_0, H_{-1}] - [H_0, H_1] + [H_{-1}, H_1]\right), \tag{.0.35}$$

where we have neglected the term H_0^2 because it belongs to the second order term of the Taylor expansion. Importantly, note that this effective Hamiltonian does not require to use the Floquet theorem, meaning that if the system is in the high frequency regime, the filling of the bands can be assumed to follow the usual equilibrium distributions. This is more involved when the system cannot be considered in equilibrium (at lower frequencies) and the side-bands description is required, which complicates the filling distribution.

Appendix E: Energy scales for the electromagnetic spectrum

Here we include a table with the different energy scales of the electromagnetic spectrum:

Class	Frequency	Wavelength	Energy
ELF/SLF	300 Hz	10 Mm	124 feV
VF/ULF	3 kHz	100 km	12.4 peV
LF	300 kHZ	1 km	1.24 neV
MF	3 MHz	100 m	12.4 neV
HF	30 MHz	10 m	124 neV
UHF	3 GHz	1 dm	12.4 μeV
FIR	3 THz	100 μm	12.4 meV
MIR	30 THz	10 μm	124 meV
NIR	300 THz	1 μm	1.24 eV
VL	400-790 THz	380-760 nm	
NUV	3 PHz	100 nm	12.4 eV
EUV	30 PHz	10 nm	124 eV

Legend: MIR= Mid infrared, HF= High freq., FIR= Far infrared, MF= Medium freq., LF= Low freq., NUV= Near ultraviolet, VF/ULF= Voice freq., VL= Visible light, UHF= Ultra high freq., SLF= Super low freq., NIR= Near Infrared UHF= Ultra high freq. ELF= Extremely low freq., EUV= Extreme ultraviolet.

Bibliography

[1] F. Grossmann, T. Dittrich, P. Jung, and P. Hänggi, Phys. Rev. Lett. **67**, 516 (1991). pages 1, 5

[2] K. M. Fonseca-Romero, S. Kohler, and P. Hänggi, Phys. Rev. Lett. **95**, 140502 (2005). pages 1, 5

[3] H.-A. Engel and D. Loss, Phys. Rev. Lett. **86**, 4648 (2001). pages 1, 5

[4] F. H. L. Koppens et al., Nature , 766 (2004). pages 1, 5

[5] E. A. Laird et al., Phys. Rev. Lett. **99**, 246601 (2007). pages 1, 5

[6] F. H. L. Koppens et al., Phys. Rev. Lett. **99**, 106803 (2007). pages 1, 5

[7] R. Sánchez, C. López-Monís, and G. Platero, Phys. Rev. B **77**, 165312 (2008). pages 1, 5

[8] M. Holthaus, Zeitschrift für Physik B Condensed Matter **89**, 251 (1992). pages 1, 5, 82, 85, 86

[9] B. A. Bernevig, T. L. Hughes, and S.-C. Zhang, Science (New York, N.Y.) **314**, 1757 (2006). pages 1, 95

[10] N. Lindner, G. Refael, and V. Galitski, Nature Physics **7**, 490 (2011). pages 1, 63, 78, 109, 110

[11] T. Kitagawa, E. Berg, M. Rudner, and E. Demler, Phys. Rev. B **82**, 235114 (2010). pages 1, 63, 78

[12] F. Bloch and I. I. Rabi, Rev. Mod. Phys. **17**, 237 (1945). pages 2, 5, 25

[13] A. Gómez-León and G. Platero, Phys. Rev. B **84**, 121310 (2011). pages 2, 6, 53, 54

[14] A. Gómez-León and G. Platero, Phys. Rev. B **245319**, 1 (2012). pages 2, 6

[15] A. Gómez-León and G. Platero, Phys. Rev. B **86**, 115318 (2012). pages 2, 6, 15, 85

[16] A. Gómez-León and G. Platero, Phys. Rev. Lett. **110**, 200403 (2013). pages 2, 6, 109, 111

[17] P. Delplace, A. Gómez-León, and G. Platero, Arxiv Preprint , 1304.6272 (2013). pages 2, 6, 129

[18] A. Gómez-León, P. Delplace, and G. Platero, Arxiv Preprint , 1309.5402 (2013). pages 2, 6

[19] V. M. Bastidas et al., Arxiv Preprint , 1302.0781 (2013). pages 3, 6

[20] A. G. Grushin, A. Gómez-León, and T. Neupert, Arxiv Preprint , 1301.4433 (2013). pages 3, 6

[21] S. Kohler, J. Lehmann, and P. Hänggi, Physics Reports **406**, 379 (2005). pages 6, 46

[22] D. Hone, R. Ketzmerick, and W. Kohn, Phys. Rev. E **79**, 51129 (2009). pages 6, 46, 51

[23] M. V. Berry, Proceedings of the Royal Society of London. A. Mathematical and Physical Sciences **392**, 45 (1984). pages 6, 25, 63, 64

[24] A. Bohm, A. Mostafazadeh, H. Koizumi, Q. Niu, and J. Zwanziger, *The geometric phase in quantum systems*, Springer, 2003. pages 11, 12, 16, 63, 66, 92

[25] A. Bohm, L. Boya, A. Mostafazadeh, and G. Rudolph, Journal of Geometry and Physics **12**, 13 (1993). pages 12, 63, 68

[26] A. Mostafazadeh, Journal of Physics A: Mathematical and General **30**, 7525 (1997). pages 12

[27] D. Leibfried et al., Nature **422**, 412 (2003). pages 15

[28] P. J. Leek et al., Science (New York, N.Y.) **318**, 1889 (2007). pages 15, 71

[29] F. Nagasawa, J. Takagi, Y. Kunihashi, M. Kohda, and J. Nitta, Phys. Rev. Lett. **108**, 086801 (2012). pages 15

[30] M. Pechal et al., Phys. Rev. Lett. **108**, 170401 (2012). pages 15

[31] P. Zanardi and M. Rasetti, Physics Letters A **264**, 94 (1999). pages 15, 63

[32] B. Schutz, *A first course in general relativity*, Cambridge University Press, 2009. pages 17

[33] H. Sambe, Physical Review A **7**, 2203 (1973). pages 19, 83, 111

[34] A. A. Reynoso and D. Frustaglia, Phys. Rev. B **87**, 115420 (2013). pages 21

[35] A. G. Fainshtein, N. L. Manakov, and L. P. Rapoport, Journal of Physics B: Atomic and Molecular Physics **11**, 2561 (1978). pages 35

[36] F. Grossmann, T. Dittrich, P. Jung, and P. Hänggi, Phys. Rev. Lett. **67**, 516 (1991). pages 36

[37] S. M. Huang et al., Phys. Rev. Lett. **104**, 136801 (2010). pages 40

[38] J. Iñarrea, G. Platero, and A. MacDonald, Phys. Rev. B **76**, 085329 (2007). pages 40

[39] E. Kierig, U. Schnorrberger, A. Schietinger, J. Tomkovic, and M. Oberthaler, Phys. Rev. Lett. **100**, 190405 (2008). pages 40, 41

[40] M. Grifoni and P. Hänggi, Physics Reports **304**, 229 (1998). pages 40, 41, 88

[41] J. Von Neumann and E. Wigner, Phys. Z. , 467 (1929). pages 41, 42

[42] M. Pioro-Ladrière et al., Nature Physics **4**, 776 (2008). pages 42, 71

[43] R. Feynman and F. V. Jr., Annals of Physics **24**, 118 (1963). pages 46, 48

[44] J. Cirac and P. Zoller, Phys. Rev. Lett. **74**, 4091 (1995). pages 53

[45] J. Struck et al., Phys. Rev. Lett. **108**, 225304 (2012). pages 53

[46] D. Thouless, Phys. Rev. B **27**, 6083 (1983). pages 63

[47] R. King-Smith, Phys. Rev. B **47**, 1651 (1993). pages 63

[48] D. Xiao, M.-C. Chang, and Q. Niu, Rev. Mod. Phys. **82**, 1959 (2010). pages 63

[49] M. König et al., Science **318**, 766 (2007). pages 63, 73

[50] A. Kitaev, Annals of Physics **303**, 2 (2003). pages 63

[51] E. Dennis, A. Kitaev, A. Landahl, and J. Preskill, Journal of Mathematical Physics **43**, 4452 (2002). pages 63

[52] T. Wu and C. Yang, Phys. Rev. D **12**, 3845 (1975). pages 63

[53] B. Simon, Phys. Rev. Lett. **51**, 2167 (1983). pages 63

[54] J. Anandan and L. Stodolsky, Phys. Rev. D **35**, 2597 (1987). pages 63

[55] V. Bastidas, C. Emary, B. Regler, and T. Brandes, Phys. Rev. Lett. **108**, 043003 (2012). pages 63, 78

[56] M. Tomka, A. Polkovnikov, and V. Gritsev, Phys. Rev. Lett. **108**, 080404 (2012). pages 63

[57] Y. Aharonov and J. Anandan, Phys. Rev. Lett. **58**, 1593 (1987). pages 63, 68

[58] A. Mostafazadeh, Journal of Physics A: Mathematical and General **31**, 9975 (1998). pages 68

[59] A. Altland and M. R. Zirnbauer, Phys. Rev. B **55**, 1142 (1997). pages 73, 82

[60] A. Kitaev, ArXiv Preprint , 0901.2686 (2009). pages 73

[61] A. P. Schnyder, S. Ryu, A. Furusaki, and A. W. W. Ludwig, Phys. Rev. B **78**, 195125 (2008). pages 73, 74, 82, 93, 114

[62] D. J. Thouless, M. Kohmoto, M. P. Nightingale, and M. den Nijs, Phys. Rev. Lett. **49**, 405 (1982). pages 73

[63] Y. Hatsugai and M. Kohmoto, Phys. Rev. B **42**, 8282 (1990). pages 73

[64] M. König et al., Journal of the Physical Society of Japan **77**, 031007 (2008). pages 73

[65] A. Roth et al., Science (New York, N.Y.) **325**, 294 (2009). pages 73

[66] T. L. Hughes, E. Prodan, and B. A. Bernevig, Phys. Rev. B **83**, 245132 (2011). pages 76

[67] A. Bernevig and T. L. Hughes, *Topological insulators and topological superconductors*, Princeton University Press, 2013. pages 76, 95

[68] L. Fu, Phys. Rev. Lett. **106**, 106802 (2011). pages 76

[69] J. C. Y. Teo and C. L. Kane, Phys. Rev. B **82**, 115120 (2010). pages 76, 77, 78

[70] S. Matsuura, P.-Y. Chang, A. P. Schnyder, and S. Ryu, New Journal of Physics **15**, 065001 (2013). pages 76

[71] M. Stone, C.-K. Chiu, and A. Roy, Journal of Physics A: Mathematical and Theoretical **44**, 045001 (2011). pages 77

[72] L. Fu, C. L. Kane, and E. J. Mele, Phys. Rev. Lett. **98**, 106803 (2007). pages 78

[73] Z. Ringel, Y. E. Kraus, and A. Stern, Phys. Rev. B **86**, 045102 (2012). pages 78

[74] Z. Gu, H. A. Fertig, D. P. Arovas, and A. Auerbach, Phys. Rev. Lett. **107**, 216601 (2011). pages 78, 109, 110

[75] L. Jiang et al., Phys. Rev. Lett. **106**, 220402 (2011). pages 78, 130

[76] J.-i. Inoue and A. Tanaka, Phys. Rev. Lett. **105**, 017401 (2010). pages 78, 109

[77] T. Kitagawa, T. Oka, A. Brataas, L. Fu, and E. Demler, Phys. Rev. B **84**, 235108 (2011). pages 78, 109, 126, 127

[78] V. Bastidas and C. Emary, arXiv preprint arXiv: ..., 1 (2012). pages 78

[79] M. S. Rudner, N. H. Lindner, E. Berg, and M. Levin, Phys. Rev. X **3**, 031005 (2013). pages 78, 128, 130

[80] C. Zener, Proceedings of the Royal Society of London. Series A **137**, 696 (1932). pages 82, 85

[81] N. Marzari, A. Mostofi, J. Yates, I. Souza, and D. Vanderbilt, Rev. Mod. Phys. **84**, 1419 (2012). pages 82, 85, 99

[82] W. P. Su, J. R. Schrieffer, and A. J. Heeger, Phys. Rev. Lett. **42**, 1698 (1979). pages 82, 91

[83] S. Ryu and Y. Hatsugai, Phys. Rev. Lett. **89**, 077002 (2002). pages 82, 91, 110, 113

[84] P. Delplace, D. Ullmo, and G. Montambaux, Phys. Rev. B **84**, 195452 (2011). pages 82, 91, 94, 97, 99, 110, 113, 122

[85] W. Beugeling, J. Everts, and C. Morais Smith, Phys. Rev. B **86**, 195129 (2012). pages 85, 100

[86] C. Bena and G. Montambaux, New Journal of Physics **11**, 095003 (2009). pages 92

[87] M. Hasan and C. Kane, Rev. Mod. Phys. **82**, 3045 (2010). pages 93

[88] K. S. Novoselov et al., Science **306**, 666 (2004). pages 101

[89] A. H. Castro Neto, F. Guinea, N. M. R. Peres, K. S. Novoselov, and A. K. Geim, Rev. Mod. Phys. **81**, 109 (2009). pages 101

[90] G. Semenoff, Phys. Rev. Lett. **55**, 2449 (1984). pages 103

[91] P. Dietl, F. Piéchon, and G. Montambaux, Phys. Rev. Lett. **100**, 236405 (2008). pages 105, 109, 112

[92] G. Montambaux and F. Piéchon, The European Physical Journal B **72**, 509 (2009). pages 105, 110, 112, 113

[93] B. Wunsch, F. Guinea, and F. Sols, New Journal of Physics **10**, 103027 (2008). pages 105, 109, 112

[94] M. C. Rechtsman et al., Nature **496**, 196 (2013). pages 109

[95] J. Zak, Phys. Rev. **136**, A1647 (1964). pages 110

[96] L. Tarruell, D. Greif, T. Uehlinger, G. Jotzu, and T. Esslinger, Nature **483**, 302 (2012). pages 110

[97] L.-K. Lim, J.-N. Fuchs, and G. Montambaux, Phys. Rev. Lett. **108**, 175303 (2012). pages 110

[98] M. Bellec, U. Kuhl, G. Montambaux, and F. Mortessagne, Phys. Rev. Lett. **110**, 033902 (2013). pages 110

[99] V. M. Pereira and A. H. Castro Neto, Phys. Rev. Lett. **103**, 046801 (2009). pages 110

[100] S. Koghee, L.-K. Lim, M. O. Goerbig, and C. M. Smith, Physical Review A **85**, 023637 (2012). pages 110

[101] M. Busl, G. Platero, and A.-P. Jauho, Phys. Rev. B **85**, 155449 (2012). pages 110

[102] A. Kundu and B. Seradjeh, Phys. Rev. Lett. **111**, 136402 (2013). pages 121, 130, 131

[103] E. J. G. Santos and E. Kaxiras, Nano letters **13**, 898 (2013). pages 121

[104] J. Karch et al., Phys. Rev. Lett. **107**, 276601 (2011). pages 121

[105] S. Tani, F. m. c. Blanchard, and K. Tanaka, Phys. Rev. Lett. **109**, 166603 (2012). pages 121

[106] M. Polini, F. Guinea, M. Lewenstein, H. C. Manoharan, and V. Pellegrini, Nature Nanotechnology **8**, 625 (2013). pages 121

[107] M. O. Scully and M. S. Zubairy, *Quantum Optics*, Cambridge University Press, 2001. pages 122

[108] F. D. M. Haldane, Phys. Rev. Lett. **61**, 2015 (1988). pages 125

[109] C.-Z. Chang et al., Science **340**, 167 (2013). pages 125

[110] J. Cayssol, B. Dóra, F. Simon, and R. Moessner, Physica Status Solidi (RRL)-Rapid Research Letters **7**, 101 (2013). pages 127

[111] Y. T. Katan and D. Podolsky, Phys. Rev. Lett. **110**, 016802 (2013). pages 127

[112] D. Sticlet, F. Piéchon, J.-N. Fuchs, P. Kalugin, and P. Simon, Phys. Rev. B **85**, 165456 (2012). pages 128

[113] T. Fukui, Y. Hatsugai, and H. Suzuki, J. Phys. Soc. Jpn. , 1674 (2005). pages 128, 130

[114] B. M. Fregoso, Y. H. Wang, N. Gedik, and V. Galitski, Phys. Rev. B **88**, 155129 (2013). pages 129

Nomenclature

CDT	Coherent destruction of tunneling.
CL	Charge localization. The spatial localization of an electron induced by the ac field. We differenciate during this thesis charge localization from coherent destruction of tunnel, although the physical effect is the same.
cTI	Crystal Topological Insulator.
DQD	Double quantum dot.
ESR	Electron spin resonance.
FBZ	First Brillouin Zone.
FSB	Floquet side-band.
GPS	Generalized parity symmetry. It consists on the inversion of the spatial coordinate and the eovlution over a semiperiod: $x, t \to -x, t + T/2$.
GSP	Generalized spin parity. It consists on the inversion of the spin projection and the eovlution over a semiperiod: $\uparrow / \downarrow, t \to \downarrow / \uparrow, t + T/2$.
I	Insulating
PDP	Pair of Dirac points.
PHS	Particle-hole symmetry.
QAHE	Quantum anomalous Hall effect.
QED	Quantum electro dynamics.
RWA	Rotating wave approximation.
SM	Semi-metallic
TB	Tight binding.
TRIM	Time Reversal Invariant Momentum.
TRS	Time reversal symmetry, which is defined as the inversion of the time arrow $t \to -t$.